Covariance matrix of nucleon-nucleon potential parameters in few-nucleon studies

Yuriy Volkotrub

Ph.D. thesis
written under the supervision of dr. hab Roman Skibiński, prof. UJ
at the Jagiellonian University, Faculty of Physics, Astronomy
and Applied Computer Science, Kraków,
Friday 4$^{\text{th}}$ June, 2021

Abstract

The formalism of Faddeev equations is a consistent momentum space framework that allows performing rigorous calculations for three-nucleon scattering. Here I use it to predict, at energies up to 200 MeV, various observables employing two models of nucleon-nucleon interaction: the OPE-Gaussian potential and the chiral interactions with semilocal regularization in momentum space up to the N^4LO^+ chiral order. These models contain a number of free parameters whose values are typically fixed using the two-nucleon data. In addition to the central values of parameters also their covariance matrix has been determined. The knowledge of the covariance matrix of the potential parameters opens new possibilities in studies of few-nucleon systems.

In this thesis, I use such a covariance matrix to estimate uncertainties of 3N observables arising from the propagation of the uncertainties of the potential parameters. The magnitudes of such statistical uncertainties for the two models of interaction are found to be rather similar. In the case of the chiral potentials, we also show truncation errors estimated in two ways: via the EKM prescription or via the Bayesian approach. The statistical uncertainties occur to be usually much smaller than the truncation errors.

Another example of using the covariance matrix of potential parameters is investigation of correlations among various two- and three-nucleon observables as well as between observables and specific potential parameters. In the second part of my thesis, I present a systematic analysis of such correlations, basing on the relatively big sample of predictions. I found that most observables are uncorrelated one with the other, but there are exceptions showing up strong correlations. That piece of information may be useful in precise procedure to fix potential parameters and in finding the dependences and correlations between potential parameters and observables.

Streszczenie

Formalizm równań Faddeeva umożliwia wykonywanie rygorystycznych obliczeń dla procesów rozpraszania trzech nukleonów. W prezentowanej pracy używamy go, w przestrzeni pędowej, do przewidywania przy energiach do 200 MeV wartości obserwabli, wykorzystując dwa modele oddziaływania nukleon-nukleon: potencjał OPE-Gaussian i oddziaływanie chiralne z półlokalną regularyzacją w przestrzeni pędowej do rzędu N^4LO^+. Modele te zawierają szereg swobodnych parametrów, których wartości są zwykle ustalane na podstawie danych z sektora dwóch nukleonów. Oprócz wartości oczekiwanych tych parametrów wyznaczono także ich macierz kowariancji. Znajomość macierzy kowariancji parametrów potencjału otwiera nowe możliwości w badaniach układów kilkunukleonowych.

W niniejszej pracy wykorzystuję taką macierz kowariancji do oszacowania niepewności obserwabli w reakcji rozpraszania neutronu na deuteronie wynikających z propagacji niepewności parametrów potencjału. Jak wykazuję, wielkości takich niepewności statystycznych dla obu użytych modeli sił jądrowych są zbliżone. W przypadku potencjałów chiralnych pokazuję również oszacowane błędy obcięcia. Okazuje się, że niepewności statystyczne są zwykle znacznie mniejsze niż błędy obcięcia, które obliczam na dwa sposoby: poprzez metodę EKM lub używając podejścia analizy bayesowskiej.

Innym przykładem wykorzystania macierzy kowariancji parametrów potencjału jest badanie korelacji między różnymi obserwablami dwu- i trójnukleonowymi, a także między obserwablami a określonymi parametrami potencjału. W drugiej części mojej pracy doktorskiej przedstawiam systematyczną analizę takich korelacji w oparciu o stosunkowo dużą próbę losową. Odkryłem, że większość obserwabli jest nieskorelowana wzajemnie, ale istnieją wyjątki pokazujące silne korelacje. Ta informacja może być przydatna w precyzyjnym wykonaniu procedury dopasowania parametrów potenciału oraz w znalezieniu zależności i korelacji pomiędzy parametrami potencjału a obserwablami.

Contents

Overview

One of the main goals of theoretical low-energy nuclear physics is to establish the structure of the nuclear Hamiltonian. Up to now, a large set of experimental data has been accumulated, both from bound states and reactions, including elastic and inelastic nucleons scattering on nuclei over a wide range of energies. This is especially true for the elastic nucleon-deuteron (Nd) scattering and the nucleon-induced deuteron breakup processes. During many years of theoretical investigations of three-nucleon (3N) systems conducted among others, by the Kraków-Bochum group, it was demonstrated that using nucleon-nucleon (NN) force is not sufficient to provide an accurate description of such systems. An additional 3N force (3NF) is required to obtain a precise description of the 3N data [1]. Nowadays, unfortunately, the details of the 3N force are still poorly known and many efforts are undertaken to establish its properties. One example are calculations performed by the Kraków-Bochum group that enabled experimentalists to prepare measurements sensitive to specific features of the nuclear Hamiltonians: the role of particular NN force components, charge independence breaking, and the structure of the 3NF. Major important results obtained before the mid-1990s for the 3N system were summarized in a review paper [2], which is an important reference for a reader interested in 3N calculations.

In order to obtain reliable and accurate information from comparing 3N data with rigorous theoretical calculations it is necessary to estimate the uncertainties of theoretical predictions, in addition to the uncertainties of 3N data. Such estimation should start already when working with two-nucleon forces only. This would allow to estimate a contribution of 3NF in the description of various phenomena of nuclear physics. Of course, such estimations should be confirmed by calculations which explicitly take into account NN interactions combined with 3NFs.

In the past, for various reasons, the uncertainty budget for theoretical predictions in nuclear physics was not available or the estimated uncertainties did not offer a statistical interpretation. With the increasing accuracy of experimental data in all areas of physics, including the three-nucleon sector, see, e.g., Refs. [3, 4, 5, 6, 7], the question of the uncertainty of theoretical predictions has became very relevant in the last decade. For instance, the problem of uncertainty quantification of theoretical calculations was emphasized in an editorial in Physical Review A [8] journal which covers atomic, molecular, and optical physics. This guideline was also taken by the nuclear physics community. In order to facilitate intensive discussions, among others, the ISNET workshops (Information and Statistics in Nuclear Experiment and Theory) are organized to better understand issues related to the application of applied mathematics, information theory, and statistics in the analysis of experiments, and possibilities of calculating the uncertainties of corresponding theoretical calculations. The first workshop resulted in a special issue of the *Journal of Physics G: Nuclear and Particle Physics* (2015). This has been continued by the next special issue published in 2020. In my studies I would like to contribute to these

efforts and an important part of my thesis is devoted to studying selected theoretical uncertainties.

For the specific case of elastic Nd scattering, the *ab initio* theoretical studies of 3N observables are possible using any modern model of nuclear forces. NN force models used in such investigations contain a number of free parameters whose values are fixed from two-nucleon (2N) data. For my studies, the most important examples of such models are the new generation of the chiral interaction currently derived even beyond to the fifth-order (N^4LO) of the chiral expansion using the semilocal regularization in momentum space (SMS) by the Bochum-Bonn group [9] and the semi-phenomenological One-Pion-Exchange-Gaussian (OPE-Gaussian) potential, proposed by the Granada group [10]. This choice is dictated by the availability of the covariance matrix for the free parameters of these forces. The knowledge of the covariance matrix of the potential parameters opens new opportunities in studies of few-nucleon systems. One of them, realized in this thesis, is to determine the magnitude of the uncertainty (the so-called theoretical statistical error) of the investigated observables that arises from the propagation of uncertainty of NN potential parameters. Part of the results presented in the thesis have been shown in [11, 12]. Another possibility is to investigate correlations among various 2N and 3N observables as well as between observables and specific potential parameters. The information about correlations among such observables is particularly interesting in the context of determining free strength parameters present in the 3N interaction. The values of these parameters are traditionally obtained by fixing from 3N data. However, using correlated 3N observables in such an analysis may lead to an inaccurate determination of the sought parameters. In this thesis I determine the correlations among 3N observables in a statistically consistent way, based on a relatively big sample of predictions.

Summarizing, the main goal of this doctoral dissertation is the theoretical study of 3N observables for elastic and inelastic Nd scattering by using the newest semilocal momentum-space regularized chiral force. The first part of this work deals with various types of theoretical uncertainties of the 3N scattering observables. The statistical uncertainties obtained with the OPE-Gaussian potential and the chiral SMS interaction at different orders of the chiral expansion are the central part of my work. In addition, for the Nd elastic scattering, the statistical uncertainties are compared with the truncation errors arising from the restriction to a specific order of the chiral expansion, which can be done in two ways using a prescription suggested in [13, 14] or within the Bayesian method [15], and with the cutoff dependence of chiral predictions. The second part of my thesis is devoted to collecting information about the correlations among all 2N and 3N elastic scattering observables. Knowing if some observables are or are not correlated, can have a significant impact on future methods of fixing free parameters of the two- and many-body potentials. Especially the case of correlations in a 3N system should deliver information on possible restrictions on data sets used during fitting the 3NF parameters. In the case of correlations between potential parameters and 2N observables, the problem at hand is existence of observables that show strong sensitivity to a given part of the potential. If this is the case such an observable could be possibly used to fix this particular parameter. This, in turn, will reduce the number of remaining free parameters, which would simplify the rest of the fitting procedure.

In the next Chapter I give a more elaborate introduction to my studies while in Chapter 2 I describe the two-nucleon force models which are used in my investigations. In Chapter 3 I discuss various types of theoretical uncertainties and the usefulness of the covariance matrix of two-nucleon potential parameters. In Chapter 4 I show the essential

elements of our methods in computing the deuteron binding energy, the 2N scattering observable, and the framework of the 3N Faddeev equations in computing 3N scattering observables used in my research. Chapter 5 is devoted to results for elastic scattering and breakup reactions. In Chapter 6 I show results on correlations among various two- and three-nucleon observables. Finally, I summarize in Chapter 7. This thesis contains four appendices. The first one describes how to sample 50 sets sets of the chiral potential parameters at different orders in the chiral expansion. Appendix B is devoted to the dependence of truncation errors obtained within the Bayesian approach on the order of chiral NN potential. In Appendix C, I provide a table of the central values of LECs of the NN interactions for the N^2LO, N^3LO, N^4LO and N^4LO^+ chiral orders for the cutoff value of $\Lambda = 450$ MeV.

Chapter 1

Introduction

Modern physics tells that four fundamental forces describe the entire observable Universe. They are gravitational, electromagnetic, strong and weak interactions. Three of them are combined to the Standard Model, except the gravitational one. A scale comparable to a size of no more than the size of atomic nuclei is a field studied within the nuclear physics in close connection with the particle physics.

Nuclear physics studies the properties and structure of atomic nuclei and their reactions. Some of its main tasks are related to the analysis of the nature of nuclear forces acting between nucleons (protons and neutrons) that form nuclei and to identify and explain the properties of their motion. Understanding nuclear forces is fundamental for both theoretical and experimental nuclear physics as well as for applied nuclear physics. Currently, it is known that nuclear interaction between nucleons is a residual interaction of the strong interaction between even finer elements of matter — quarks and gluons and which is described by the Quantum Chromodynamics (QCD). As is well known, nowadays we are not able to solve QCD in the non-perturbative region (at the low-energy scale) and thus to describe processes at nuclear scale starting from quarks and gluons and their interactions. For the first ongoing attempts in lattice QCD, see e.g. Refs. [16, 17]. For example, the obtained deuteron binding energy is still much larger than the experimental value [18, 19]. Another advanced approaches, like the Lattice Effective Field Theory [20], also fail to deliver results of quality comparable with the standard nuclear physics techniques. By the latter ones we understand approaches based on the effective nuclear interactions defined as interactions among nucleons and relying mainly on meson exchange processes.

As a result, effective and phenomenological models of nuclear interactions are still of great importance in low-energy nuclear physics [1] and various *ab initio* techniques to obtain predictions have been derived. Calculations within the *ab initio* or *microscopic* techniques mean that the nuclear A-few body problem can be formulated in terms of the nonrelativistic Schrödinger equation using various NN local or non-local interactions with or without the inclusion of many-body forces. Independently on the problem in hand: the bound state of nucleons, nuclear reactions, production or decay processes, the starting point of research is a construction of the complete Hamiltonian of the system of interacting particles. This thesis is devoted to purely nucleonic processes, in particular to three-nucleon processes: the elastic and inelastic neutron-deuteron scattering.

[1] In my doctoral research, done as part of the investigations within the Kraków's group, low-energy nuclear physics is understood as nuclear physics at energies below the pion production threshold.

The general form of the nuclear Hamiltonian for the system A of nucleons is

$$H = \sum_{i=1}^{A} \frac{p_i^2}{2m_i} + \sum_{i,j}^{A} V_{ij}^{\mathrm{2N}} + \sum_{i,j,k}^{A} V_{ijk}^{\mathrm{3N}} + \ldots + V^{A\mathrm{N}} \ , \tag{1.1}$$

where the first term is the non-relativistic kinetic energy, m_i and p_i are the i-th nucleon mass and momentum, respectively, and V_{ij}^{2N}, V_{ijk}^{3N} and $V^{A\mathrm{N}}$ represent the two-, three and A-nucleon potentials, respectively. The definition (1.1) is used e.g. for a bound state $\left|\Psi^A_{\mathrm{bound}}\right\rangle$ in the time-independent Schrödinger equation formulated as an eigenvalue problem

$$H \left|\Psi^A_{\mathrm{bound}}\right\rangle = E \left|\Psi^A_{\mathrm{bound}}\right\rangle \ , \tag{1.2}$$

where E is the binding energy.

There are a few mathematical algorithms and *ab initio* approaches with well-controlled approximations for solving a A-nucleon Schrödinger equation for light nuclei. In general, this equation can be considered in coordinate or momentum space. Some examples of *ab initio* methods for study few-nucleon systems with $A \geq 4$ were listed and reported in an overview [21]. For example, one of these methods is approach basing on the Faddeev-Yakubovsky equation, which was used to calculate the binding energy and the wave function of ^{4}He [22]. I would like also to mention methods which are quite precise in describing the properties of light and medium mass nuclei up to $A = 12$, i.e. methods based on Monte Carlo algorithms, such as the Monte Carlo variational (VMC) or the Monte Carlo with Green's function (GFMC) methods, see Ref. [23]. It is also worth mentioning that there are approaches associated with the shell model of nuclei, as the no-core shell model (NCSM) [24], the No-Core Configuration Interaction (NCCI) [25] model, or the realistic shell model (RSM) [26]. In the last decade, many efforts have been made to use the Similarity Renormalization Group (SRG) approach with a combination of the chiral interaction, see e.g. Ref. [27]. The SRG approach is based on the unitary transformation of the many-body Hamiltonian system to decouple states with high and low momenta [28, 29]. Such transformed Hamiltonian can be next used in the above-mentioned computational schemes. In the case of $A \leq 4$ nuclear bound systems, the hyperspherical harmonic (HH) method has been developed and applied by the Pisa group [30].

The latter method has also been applied to describe the elastic Nd scattering at the very low ($\leq$ 10 MeV) incoming nucleon laboratory energies, working in coordinate or in momentum space [31, 32]. However, to study 3N scattering a few *ab initio* approaches based on the Faddeev equations scheme [33] are currently the most effective tools. The Kraków-Bochum group developed the Faddeev formalism for rigorous calculations applied to 3N continuum observables, see Ref. [2] for a general overview. Interesting computational technique based on the 3N continuum Faddeev calculations with lattice-like discretization in momentum space was developed in [34]. In 3N systems as well as beyond them, the Faddeev formalism can be realized in a couple of ways, like the Alt-Grassberger-Sandhas (AGS) equations [35] with the possibility to include the Coulomb interaction between protons [36] and the Faddeev-Yakubovsky for five-nucleon calculations [37]. Among the above-mentioned frameworks, the Density Functional Theory (DFT) is also interesting approach which can be used to compute ground-state and excited configurations of medium-mass and heavy nuclei to study nuclear structure. A brief description of the achievements and challenges within the framework of the DFT is described in Refs. [38, 39, 40, 41]. Another recent overview of state-of-the-art *ab ini-*

tio calculations of the bound state and scattering observables is given in Ref. [42] and references therein.

The deuteron is the only one stable bound state of two nucleons. Analyzing its properties, it was found that nuclear forces of short-range nature with a range of not more than $2 \div 3$ fm play a key role in nuclear physics. Experimental data on nuclei and nuclear reactions, including a huge amount of data on nucleon-nucleon (proton-proton and proton-neutron) scattering, led to the conclusion that nuclear forces can be considered in the first approximation as a two-particle interactions. Thus, the problem of describing nuclear interactions can be approximately formulated as a problem of determining the two-nucleon (2N) potential $V^{2\mathrm{N}}$.

In general, no matter what strategy (phenomenology, meson exchange picture, etc.) is chosen to build a model of nuclear interactions, the properties of nuclei are taken into account. With an increasing number of nucleons, the volume of nuclei increases proportionally to the mass number ($A > 4$), which is explained by the fact that the central nuclear force is a short-range interaction and strongly attractive at this range. This makes a saturation effect. The nuclear force depends not only on the range between nucleons (central force), but also on the mutual orientation of spins (spin-spin force), the mutual direction of the spin and the orbital angular momentum (spin-orbit force), and also on the orientation of the spins of each nucleon to the relative distance between them (tensor force). The existence of a spin-orbit force helps to explain the experimentally observed magic numbers for nucleons. The presence of a quadrupole moment in the deuteron is a result of the tensor force contribution. It is also often convenient to split the nuclear force to a sum of two (short- and long-range) or three (short-, intermediate- and long-range) terms.

The first non-trivial model of nuclear force was the NN potential developed by Hideki Yukawa [43]. Yukawa used the idea that nucleons interact via exchanges of an unknown particle, and combined it with the idea of the short-range interaction. He predicted that this intermediate particle should obey the Einstein-Bose statistics and estimated its mass. Today, we identify this particle as the π^0-meson pseudoscalar boson (with total spin 0 and odd parity). Further development of nuclear forces showed by the end of the 60s that the NN interaction includes not only a one-pion interaction but also processes with two pions, and much heavier meson exchanges depending on the inter-nucleon distance. In the 90s, the most known and frequently used the meson-exchange models were the Paris potential [44], the Bonn potential [45], and two potentials provided by the Nijmegen group — the non-local Nijmegen potential (Nijm I) and its local version (Nijm II) [46]. During works on their potential, the Nijmegen group collected 1787 *pp* data sets and 2514 *np* data sets. They performed partial-wave analysis (PWA93) below 350 MeV and the Nijmegen database (or the 1992-database) was obtained. Thanks to this approach, they were able to describe 2N scattering data using their potentials with $\chi^2/\mathrm{datum} \approx 1.08$. All the above-mentioned models combine the meson exchange theory with a more phenomenological approach in the derivation of NN potentials with a complex operator structure. In general, such a phenomenological NN potential consists of linear combinations of operators which are deduced from the nuclear properties and symmetries. The interested reader can find more detailed information on how the theory of nuclear structure has developed from a historical perspective, from the discovery of the neutron to the present day, as well as a review of NN interactions in Refs. [47, 48, 49, 50, 51].

At the beginning of the 21st century, the most successful *realistic* models of the NN force were the above-mentioned Nijmegen (I, II), the Argonne V18 (AV18) [52] and the

CD-Bonn [53] potentials which provided an accurate description of the 2N scattering data and deuteron properties. In the case of the AV18 the long-range part of the interaction, given by the one-pion-exchange (OPE), was supplemented by a purely phenomenological short-range part. For the CD-Bonn model the short-range part was described via exchanges of heavier mesons and processes with multiple meson exchanges. The AV18 and the CD-Bonn potentials have 40 and 43 potential force parameters, respectively. The AV18 potential parameters were fitted using the above-mentioned Nijmegen PWA93 results. Before the year 2000, the new sets of experimental 2N data were collected and together with the 1992-database built the 1999-database [53]. The resulting 1999-database was taken into account to construct the CD-Bonn potential. The quality of description can be quantified by the magnitude of χ^2/datum obtained from a comparison of theoretical predictions and experimental data. In the case of the AV18 potential $\chi^2/\text{PWA92} = 1.09$ and $\chi^2/\text{PWA99} = 1.21$. For the CD-Bonn model $\chi^2/\text{datum} = 1.02$ for both databases [53]. For both potentials, only the central values of the parameters were determined and to the best of our knowledge, no information about their uncertainties was published.

In the course of time, the expectations of improvements in the accuracy of the fitting as well as in establishing parameter uncertainties procedure grew. An important step in establishing the 2N potential parameters was taken by Rodrigo Navarro Pérez and his collaborators from the Granada group, who carefully revised the whole 2N database. They prepared a new database (Granada-2013 database) [54], removing from the previously used data, those for which the experimental uncertainties had been unknown or unclearly defined. They also excluded data sets that were inconsistent with other data, which led to the self-consistency of the final choice of data. This procedure is described in Chapter 2.1 in more detail. The extended statistical tests of this database, presented in [54], confirmed the internal consistency of the accepted data. The Granada-2013 database is currently a standard set of data used for fixing parameters of the NN forces which can be done by fitting parameters to the extracted phase shifts or to 2N data directly. The free parameters of the both models of the NN force used in this thesis: the OPE-Gaussian [10] and the family of the chiral SMS interactions from the Bochum group [9] have been fixed with the Granada-2013 database. Specifically the OPE-Gaussian potential has been derived already by R. Navarro Pérez and collaborators. This potential is discussed in Chapter 2.1 in detail.

Currently, the most sophisticated models of nuclear forces at the low-energy regime are chiral interactions. S. Weinberg was the first who proved, in his seminal papers [55, 56], that it is possible to build a Lagrangian for all possible interactions between pions and nucleons in agreement with the symmetries (including the broken chiral symmetry) and properties of low-energy QCD, and to construct an effective Hamiltonian in terms of nucleons and pions. In this construction an infinite number of terms corresponding to the Feynman diagrams for the Lagrangian can be rewritten as an pertubative expansion with respect to some parameter. Each term in this Lagrangian is multiplied by the corresponding coupling constants, the so-called low-energy constants (LECs), which need to be determined from experimental data in the nucleonic or π-N sector [9, 57]. The power counting scheme allows organizing a perturbative ordering of the Lagrangian terms and thus point terms dominant in the potential. The expansion parameter depends on the ratio between the low- and high-energy scales. It is assumed to have the form $Q = \max\left(\frac{p}{\Lambda_\chi}, \frac{m_\pi}{\Lambda_\chi}\right)$, where Λ_χ is the chiral symmetry breaking scale, whose value is a priori set to the order of the ρ-meson mass ($\Lambda_\chi = 770$ MeV), however, values in the

range 600 MeV [58] – 1 GeV [59] are also used [9], [60], [61]. Further $p \equiv |\vec{p}|$ is the typical magnitude of the external (nucleon) three-momenta in the center-of-mass system (c.m.s.), and m_π is the pion mass. An important feature of the chiral expansion in powers ν of (Q/Λ_χ) is the finite number of diagrams at a given order which makes theory computable. Finally, an effective potential can be derived from the effective Lagrangian with e.g. the method of unitary transformations [62, 57]. This leads to nuclear forces emerging as a hierarchy controlled by the ν parameter, see Figure 1.1, and gives a nice explanation of the different strengths of contributions to two- and many-body forces obtained within the Chiral Effective Field Theory (χEFT). In general, the expansion of the NN force has the form

$$V_{\rm 2N} = V_{\rm 2N}^{(0)} + V_{\rm 2N}^{(2)} + V_{\rm 2N}^{(3)} + V_{\rm 2N}^{(4)} + V_{\rm 2N}^{(5)} + \dots \ , \tag{1.3}$$

with the superscripts referring to the power ν of the expansion parameter $(Q/\Lambda_\chi)^\nu$. For example, in the lowest leading order ($\nu = 0$) the NN potential is made up by two terms, represented by the graphs in the first row of Figure 1.1. They are the static one-pion exchange ($V_{1\pi}$) and the contact interaction ($V_{\rm cont}$) between two nucleons. The latter plays role of a short-range interaction. For $\nu = 1$ all terms cancel and give no contribution to the NN interaction. At the higher orders of the chiral expansion more terms containing multiple mesons exchanges and various types of contact terms are present. At the next-to-next-to-leading order ($\rm N^2LO$), which corresponds to $\nu = 3$, the NN potential includes contributions from the one-, two-exchange and contact terms with up to three derivatives which enters new short-range interactions contributing at this order. In addition, for a 3N system a 3N force appears, for the first time, at this chiral order.

Nowadays, there are a number of groups engaged in the derivation of chiral forces and two of them have dominated the field: the Bochum-Bonn group (see Refs. [58, 63, 64, 65] and more recently [9]) and the Moscow (Idaho)-Salamanca group (see Refs. [59, 66, 67, 68, 69]). Both teams start from the same Lagrangian but due to various methods used, their final effective potentials differ.

The important difference between their approaches is using various ways of regularization of the chiral nuclear potential. In particular, the Moscow (Idaho)-Salamanca collaboration uses a non-local regularization procedure in momentum-space for both the long- and short-range contributions [59]. The regulator function of the initial p and final p' relative momentum of two nucleons is taken as

$$f(p', p) = \exp\left[-\left(\frac{p'}{\Lambda}\right)^{2n} - \left(\frac{p}{\Lambda}\right)^{2n} \right] \ , \tag{1.4}$$

where n depends on the chiral operators (e.g., $n = 4$ for the one-pion exchange potential). Three values of the cutoff parameter $\Lambda = 450$, 500, and 550 MeV were used while fitting potential parameters which resulted in three versions of this potential [59]. Obtained χ^2/datum values depend on the regularization parameter Λ, the order of the chiral expansion, the energy range, and the isospin channel. In the case of the next-to-next-to-next-to-next-to-leading order ($\rm N^4LO$) potential and $\Lambda = 500$ MeV, χ^2/datum = 1.15 for the fit of the 2016-database [2] (see [59] for details) of combined np and pp data in the energy range 0–290 MeV.

In their early works, the Bochum-Bonn group also proposed and used a non-local

[2] 2016 database bases on the 1999 database and consists of 2932 pp and 3058 np data and includes the data published between 2000 and 2016 which are not discarded by the Nijmegen criteria [70].

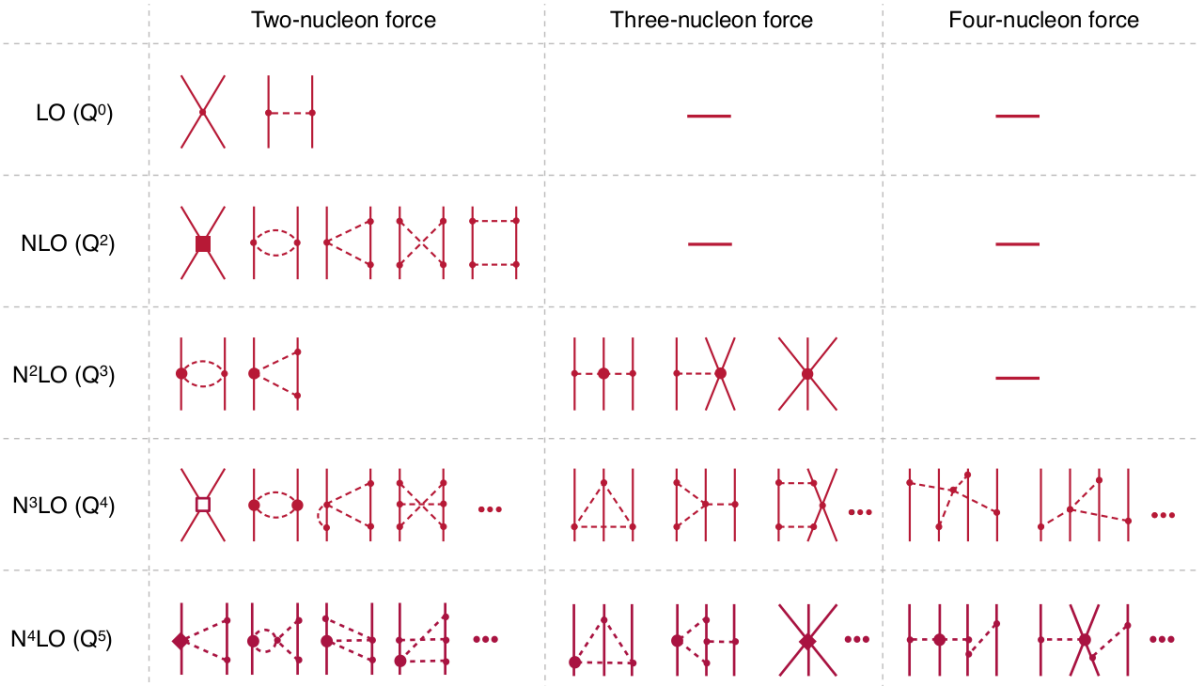

Figure 1.1: Hierarchy of nuclear forces in χEET at increasing orders in chiral expansion based on the Weinberg scheme. The figure is taken from Ref. [57]. Solid and dashed lines represent nucleons and pions, respectively. Solid dots, filled circles, filled squares, filled diamonds, and open squares denote vertexes arising at the corresponding order ν_i $(i = 0, 2, 3, 4, 5)$ of the effective Lagrangian, respectively. (Image source: https://www.frontiersin.org/files/Articles/515888/fphy-08-00098-HTML/image_m/fphy-08-00098-g002.jpg; use permitted under the Creative Commons Attribution License CC BY 4.0.)

regulator. However, due to observed strong artefacts the newest models of the Bochum-Bonn group, use the semilocal [3] regularization. It can be applied either in coordinate space with the regulator function,

$$f(r) = \left[1 - exp\left(-\frac{r^2}{R^2}\right)\right]^6 , \tag{1.5}$$

where r is the internucleon distance and R is the regulator parameter, [58, 65]; or in momentum space by changing the meson propagator, see Ref. [9].

In this thesis I use the chiral NN potentials up to N^4LO^+ order (the N^4LO potential supplemented by some terms from the sixth order N^5LO force) with regularization applied in momentum space (the SMS forces). This force is described in Chapter 2.2 in detail.

The understanding of nuclear systems is limited if only NN potentials are used in investigations of systems with more than two nucleons. In principle, the NN potentials can well describe 3N systems, and most of the results are in good agreement with the available experimental data at laboratory nucleon scattering energies of up to 100 MeV [2]. However, there are some large discrepancies between theory and experiment already in

[3]The term "semilocal" means that the nuclear force is regularized locally for the long-range part and non-locally for the short-range one.

the 3N system, for example, the triton binding energy problem [71, 72, 73], the A_y-puzzle (the problem of describing the nucleon analyzing power for the elastic Nd scattering up to 30 MeV) [74], and the description of the deuteron breakup cross section for the symmetric space star (SST) and quasi-free scattering (QFS) configurations [75, 76]. Therefore, in order to obtain a more accurate description of a 3N system, a NN interaction must be supplemented by a 3N force acting in this system.

Among all of the many-nucleon forces, the 3N force is the most intensively studied, but its structure is still unclear. Currently, the important models of 3NF are the semi-phenomenological ones: the Tucson-Melbourne [77, 78, 79] force, and the UrbanaIX [80] potential as well as models arising from χEFT. The latter have been derived mainly by the Bochum-Bonn group, starting from the seminal paper [81] where the 3NF effects in the nucleon-deuteron scattering up to the next-to-next-the leading order (N^2LO) were investigated. The 3N interaction, similarly to the two-nucleon one is derived within the chiral approach in a perturbative way [64, 66]. It occurs for the first time at the N^2LO and has at this order only two free parameters, (the low-energy constants commonly denoted c_D and c_E). Already in the work [81] the problem of fixing of these parameters had been addressed. The authors chose the ^{3}H binding energy and the nucleon-deuteron doublet scattering length $^2a_{nd}$ to find the c_D and c_E values. The same procedure to fix c_D and c_E was also used at the next (N^3LO) order of the chiral expansion with new diagrams for 3NF taken into account [82]. These new contributions to the 3NF do not introduce new free parameters, however at the next (N^4LO) order again several free parameters are expected [83]. Another strategy of fixing 3NF's parameters was used recently for the next generation of the chiral models — with semilocal regularization in coordinate space [27]. At the moment, the 3NF with regularization in coordinate space is available only up to N^2LO and this dominant 3NF contribution was used in [27]. Here, beside the ^{3}H binding energy, the total and differential cross sections at $E_{lab} = 70$ MeV and at $E_{lab} = 108$ MeV around its minimum were used to fix the c_D and c_E parameters. The use of the cross section instead of the nucleon-deuteron doublet scattering length was imposed by the strong correlation between the ^{3}H binding energy and the nucleon-deuteron doublet scattering length (the so-called Phillips line) [84], which could bias the fitting procedure and lead to incorrect c_D and c_E values. The choice of the cross section as the new observable was dictated by the fact that big 3NF effects are observed for this observable above $E_{lab} \approx 60$ MeV, thus a sensitivity of theoretical predictions to the values of free parameters had been expected. Another reason for using the cross section was the existence of very precise experimental data [85]. Nevertheless, the values of c_D and c_E obtained in [27] suffer from relatively large uncertainties and are (for the regulator parameter $R = 0.9$ fm): $c_D = 2.1 \pm 0.9$ and $c_E =$ -0.329 (+0.103, -0.106), so the uncertainty amounts up to 30%-40%, being quite substantial. The magnitudes of the free parameters and their uncertainties depend also on the value of the regulator parameter and for $R = 1$ fm one finds $c_D = 7.2 \pm 0.9$ and $c_E =$ -0.381 (+0.117, -0.122), so the uncertainty here reaches 12%–30%. Such big values of parameters' uncertainties suggest that the usefulness of other observables to fix 3NF free parameters is worth investigating as it can lead to a more precise determination of the c_D and c_E values.

Investigation of Nd scattering within the Faddeev equations in momentum space is an obvious method to study not only the NN potential but also the 3N force. A comprehensive overview of 3N calculations with various semi-phenomenological NN + 3N potentials is given in Ref. [1]. Similar works were recently conducted as part of the LENPIC (Low-Energy Nuclear Physics International Collaboration) project by applying

the chiral interaction [13, 14, 27] with the coordinate space semilocal regularization (the SCS potential) [58] and with the momentum space semilocal regularization (the SMS potential) [9, 61, 86].

Over the last ten years, in parallel with the development of nuclear force models, the question of how to estimate uncertainties has also been considered. For example, various ideas for estimating theoretical uncertainties have been proposed and discussed within the χEFT framework, see Refs. [15, 58, 60, 87, 88]. In Ref. [64] a simple approach for estimating the theoretical uncertainty in few-nucleon calculations by the cutoff dependence was suggested. However, as was shown by E. Epelbaum, H. Krebs, and Ulf-G. Meißner (EKM) [58], such a procedure has some disadvantages, namely does not allow one to precisely evaluate the effects of neglected interactions. Therefore in [58], they proposed and applied to 2N observables a new method ("EKM prescription") for estimating truncation errors, which are uncertainties arising from neglecting higher orders of the chiral expansion for the 2N potential. This algorithm was adopted also for many-nucleons systems, in the cases where predictions are based on a NN interaction [13, 14] only or on NN+3N force [27]. However, since the EKM prescription does not provide a statistical interpretation of truncation errors, a Bayesian approach for calculating the posterior probability distribution for predictions in the chiral EFT was developed, see Refs. [15, 60].

As mentioned above, there is one more additional source of theoretical errors — the statistical errors arising from the propagation of uncertainties of free parameters of a NN interaction. For the first time, it was studied with the OPE-Gaussian potential in the description of the elastic Nd observables [11]. In a recent paper [12] we investigated the magnitudes of statistical uncertainties of 3N observables of the elastic and inelastic Nd scattering at energies up to 200 MeV predicted by the chiral SMS potential at different orders of the chiral expansion up to N^4LO^+. Last but not least, there are the uncertainties arising from using the various models of nuclear interaction and the numerical uncertainties as well as the uncertainties bound to the computational scheme used. As was shown in Ref. [11] the two latter ones are small in the Faddeev approach we use. The study of the dependence of 3NF predictions on various potentials is out of scope of this thesis where we restrict ourselves only to the chiral SMS NN and the OPE-Gaussian interactions. The choice of these models is dictated by the fact that the authors quantified the statistical uncertainties of NN potential parameters and obtained not only their values but also their covariance matrices. For these forces I will discuss the dependence of prediction on used interactions as well.

Chapter 2

NN potentials

2.1 The OPE-Gaussian potential

The OPE-Gaussian force is a phenomenological NN potential which has been presented by R. Navarro Pérez, J. E. Amaro, and E. Ruiz Arriola in 2014 [10]. Customarily this potential is decomposed into the short-range $V_{\rm short}(r)$ and the long-range $V_{\rm long}(r)$ parts,

$$V(r) = V_{\rm short}(r)\theta(r_c - r) + V_{\rm long}(r)\theta(r - r_c) \ , \tag{2.1}$$

where r is the internucleon distance and for the OPE-Gaussian potential $r_c = 3$ fm.

The long-range force $V_{\rm long}(r)$ is, in turn, the sum of the one-pion exchange (OPE) force and the electromagnetic (EM) corrections:

$$V_{\rm long}(r) = V_{1\pi} + V_{\rm EM} \ . \tag{2.2}$$

The OPE potential $V_{1\pi}$ is the same as the charge-dependent OPE potential used in the PWA93 by the Nijmegen group [89] and the AV18 potential [52] which reads as

$$V_{1\pi}(r) \equiv V_{m,1\pi}(r) = \frac{1}{3} m f^2 \left(\frac{m}{m_s}\right)^2 \left[Y_m(r)\vec{\sigma}_1 \cdot \vec{\sigma}_2 + T_m S_{1,2}\right] \ , \tag{2.3}$$

where $\vec{\sigma}_1$ and $\vec{\sigma}_2$ denote the Pauli matrices of nucleons 1 and 2, respectively, $S_{1,2}$ is the tensor operator, and $Y_m(r)$ and $T_m(r)$ are the Yukawa and tensor functions,

$$\begin{aligned} S_{12} &= 3\,(\vec{\sigma}_1 \cdot \hat{r}\ \vec{\sigma}_2 \cdot \hat{r}) - \vec{\sigma}_1 \cdot \vec{\sigma}_2 \ , \ \hat{r} = \frac{\vec{r}_1 - \vec{r}_2}{|\vec{r}_1 - \vec{r}_2|} \ , \\ Y_m(r) &= \frac{e^{-mr}}{mr} \ , \\ T_m(r) &= \frac{e^{-mr}}{mr}\left(1 + \frac{3}{mr} + \frac{3}{(mr)^2}\right) \ . \end{aligned} \tag{2.4}$$

The scalling mass m_s in Eq. (2.3) is the charged-pion mass $m_{\pi^\pm}$, the average value of the pion mass $m = \frac{1}{3}(m_{\pi^0} + 2m_{\pi^\pm}) = 138.057$ MeV. Finally, $f = \sqrt{0.075} \approx 0.274$ is the pion coupling constant and the value of this parameter is the same for all pairs of nucleons (pp, np, nn). As a result, only the difference between the charged $m_{\pi^\pm}$ and neutral m_{π^0}

pion mass and leads to charge dependence

$$V_{1\pi}^{pp}(r) = V_{1\pi}^{nn} \neq V_{1\pi}^{np} \ . \tag{2.5}$$

The EM corrections contribute to the np and pp potentials. The np potential contains only a magnetic moment (MM) interaction

$$V_{\rm EM}^{np} = V_{\rm MM}^{np}(r) = -\frac{\alpha\mu_n}{2m_n r^3}\left(\frac{\mu_p S_{1,2}}{2m_p} + \frac{\vec{L}\cdot\vec{S}}{\mu}\right) \ , \tag{2.6}$$

where m_n and m_p are the neutron and proton masses, μ is the reduced mass of the nucleon, μ_n and μ_p are the neutron and proton magnetic moments, $\vec{L}$ and $\vec{S}$ denote the angular momentum and spin operator, respectively, and $\vec{L}\cdot\vec{S}$ is the 2N spin-orbit operator. The pp EM potential contains one- and two-photon exchange, vacuum polarization and a magnetic moment interaction

$$V_{\rm EM}^{pp} = V_{\rm C_1}^{pp}(r) + V_{\rm C_2}^{pp}(r) + V_{\rm VP}^{pp}(r) + V_{\rm MM}^{pp}(r) \ , \tag{2.7}$$

with detailed expressions given in Eqs. (9-12) of Ref. [54]

Below $r_c = 3$ fm the short-range part $V_{short}(r)$ of the OPE-Gaussian force is built from 18 spin-isospin operators $\hat{O}_n$, 16 of these operators are the same as in the AV18 model [46]. Among them 14 operators are charge-independent,

$$\begin{aligned}\hat{O}_{i\in[1,14]} =&\{\mathbb{1}, \vec{\tau}_1\cdot\vec{\tau}_2, \vec{\sigma}_1\cdot\vec{\sigma}_2, (\vec{\sigma}_1\cdot\vec{\sigma}_2)(\vec{\tau}_1\cdot\vec{\tau}_2), S_{12}, S_{12}(\vec{\tau}_1\cdot\vec{\tau}_2),\\ &\vec{L}\cdot\vec{S}, \vec{L}\cdot\vec{S}(\vec{\tau}_1\cdot\vec{\tau}_2), \vec{L}^2, \vec{L}^2(\vec{\tau}_1\cdot\vec{\tau}_2),\\ &\vec{L}^2(\vec{\sigma}_1\cdot\vec{\sigma}_2), \vec{L}^2(\vec{\sigma}_1\cdot\vec{\sigma}_2)(\vec{\tau}_1\cdot\vec{\tau}_2), (\vec{L}\cdot\vec{S})^2, (\vec{L}\cdot\vec{S})^2(\vec{\tau}_1\cdot\vec{\tau}_2)\} \ .\end{aligned} \tag{2.8}$$

The remaining operators

$$\hat{O}_{i\in[15,18]} =\{T_{12}, (\vec{\sigma}_1\cdot\vec{\sigma}_2), \vec{L}^2 T_{12}, \vec{L}^2(\vec{\sigma}_1\cdot\vec{\sigma}_2)T_{12}\} \ , \tag{2.9}$$

with $T_{12} = 3\tau_{z1}\tau_{z2} - \vec{\tau}_1\cdot\vec{\tau}_2$ introduce charge dependence. Each element of sets (2.8-2.9) is multiplied by a sum of four Gaussian functions $F_{i,n}(r) = V_{i,n} exp(-r^2/(2a_i^2))$, where $a_i = \frac{a}{1+i}$ and $V_{i,n}$ are the strength coefficients. Thus

$$V_{\rm short}(r) = \sum_{n=1}^{18} \hat{O}_n \left[\sum_{i=1}^{4} V_{i,n} F_{i,n}(r)\right] \ . \tag{2.10}$$

It should be noted that in Ref. [10] 21 operators are listed, but three of them (tT, τ_z and $\sigma\tau_z$) are almost equal zero in practical calculations [10], [90] and have been skipped in the final version of the OPE-Gaussian potential. The free parameter a, which determines the width of the functions $F_{i,n}(r)$, together with the operator coefficients $V_{i,n}$ were fixed from the data NN collected in the Granada-2013 database [54].

The construction of this database was done in the following steps:

1. The Granada group collected 8124 available np- and pp-scattering data taken between 1950 and 2013 in the laboratory energy range $E_{\rm lab}$ up to 350 MeV. They removed data with unknown or unclear statistical and systematic uncertainties.

Operator	$V_{1,n}$	$V_{2,n}$	$V_{3,n}$	$V_{4,n}$
$\mathbb{1}$	-19.28330126	126.28715008	-648.61345585	694.49367435
$\vec{\tau}_1 \cdot \vec{\tau}_2$	2.36233395	-25.47505195	130.03224633	-284.71844492
$\vec{\sigma}_1 \cdot \vec{\sigma}_2$	6.05581487	-75.18832503	372.41961972	-530.80008401
$\tau\sigma$	7.36008330	-48.55160272	273.71591816	-349.00547346
$(\vec{\sigma}_1 \cdot \vec{\sigma}_2)(\vec{\tau}_1 \cdot \vec{\tau}_2)$	1.99828652	-22.12164190	70.84584496	-50.72248959
$S_{12}, S_{12}(\vec{\tau}_1 \cdot \vec{\tau}_2)$	15.02271531	-38.34776035	183.80564790	-160.48060286
$\vec{L} \cdot \vec{S}$	-2.61725312	39.43014573	-217.03270342	-109.64162556
$\vec{L} \cdot \vec{S}(\vec{\tau}_1 \cdot \vec{\tau}_2)$	0.01009424	2.59116238	-26.57555840	-77.56809604
$\vec{L}^2$,$\vec{L}^2(\vec{\tau}_1 \cdot \vec{\tau}_2)$	1.43519736	-23.58906341	67.86552330	144.11773134
$\vec{L}^2(\vec{\sigma}_1 \cdot \vec{\sigma}_2)$	-0.41138176	8.33346137	-82.98819447	175.09618737
$\vec{L}^2(\vec{\sigma}_1 \cdot \vec{\sigma}_2)(\vec{\tau}_1 \cdot \vec{\tau}_2)$	-0.09972181	2.25339230	-51.87819771	175.08890636
$(\vec{L} \cdot \vec{S})^2$	-0.26615545	6.63257735	-55.34306118	100.71528331
$(\vec{L} \cdot \vec{S})^2(\vec{\tau}_1 \cdot \vec{\tau}_2)$	0.46072934	-11.65544792	150.58275714	-302.07573779
$ls2\tau$	0.71538487	-18.88652666	141.73160452	-182.73368764
T_{12}	0.63788724	-7.90421846	24.23180376	-19.73899169
$(\vec{\sigma}_1 \cdot \vec{\sigma}_2)$	-0.63788724	7.90421846	-24.23180376	19.73899169
$\vec{L}^2 T_{12}$	-0.10631454	1.31736974	-4.03863396	3.28983195
$\vec{L}^2(\vec{\sigma}_1 \cdot \vec{\sigma}_2)T_{12}$	0.10631454	-1.31736974	4.03863396	-3.28983195

Table 2.1: The central values of operator coefficients $V_{i,n}$ (in MeV) of the OPE-Gaussian potential. The parameter a is 2.30347728 [fm]. Numbers from Ref. [90].

2. They performed the least-squares fitting procedure to this database and the deuteron binding energy by the coarse-grained potential and delta-shell representation for the short and intermediate part of the NN interaction in terms of partial-wave decomposition at given scattering energy and angle [54, 91].

3. Some sets of data were incompatible with each other. To remove them, R. Navarro Pérez and collaborators applied the 3σ-criterion introduced by the Nijmegen group in the PWA93. Namely, for the Gaussian statistical data uncertainties ΔO_i^{data}, the residuals for observables O_i, $\left(O_i^{data} - O_i^{theory}\right)/\Delta O_i^{data}$ should be normal-distributed within a 3σ-confidence level. Unfortunately, this criterion has disadvantages. One of them is that when non-normal outliers data is rejected, it leads to a significantly improved fitting of compatible data (overestimation) [54]. Therefore, they applied the improved 3σ-criterion [54] to the complete database based on the idea of 3σ self-consistent rejection given by Gross and Stadler [92] and again refitted the parameters. As a result, they obtained a new database (the 3σ self-consistent Granada-2013 database), that incorporates 6713 *pp* and *np* data points and confirmed the good statistical properties of their χ^2 fit with the value of χ^2/datum = 1.05. Having the database and emerging phase shifts it was possible to fix 42 free partial-wave parameters of the OPE-Gaussian potential which are linear functions of operator coefficients $V_{i,n}$ [10]. The final values of $V_{i,n}$, used also in this thesis, are presented in Table 2.1. The resulting χ^2/datum for the OPE-Gaussian force amounts to 1.06 when fitted to data listed in Ref. [54]. The performed extensive statistical analysis of data and careful fitting procedures allowed authors of Ref. [93] to

provide not only the values of free parameters but also their covariance matrix [93].

The knowledge of the covariance matrix of parameters allowed authors of Ref. [93] to sample, from the multivariate normal distribution other sets of potentials parameters. They provided us with a sample of 50 sets of parameters $\{V_{i,n}, a\}$ and their central values. Finally, we would like to note, that the OPE-Gaussian potential has a similar structure to the AV18 force and thus it can be regarded as a remastered version of the standard AV18 model.

2.2 The chiral SMS potential

Choosing nucleons and pions as the only particles in the theory, the chiral NN potential can be written as

$$V_{2N} = V_{\text{cont}} + V_{\pi} \tag{2.11}$$

where V_{cont} is the contact interaction between nucleons and V_{π} represents the pion contributions to the two-nucleon potential. The long-range part of nuclear forces is completely determined by the chiral symmetry of QCD and experimental information on pion-nucleon (πN) scattering. Moreover, the pion exchange contributions can be separated by the number of exchanged pions at each chiral order of the chiral expansion, i.e. $V_{\pi} = V_{1\pi} + V_{2\pi} + \dots$ with

$$\begin{aligned} V_{1\pi} &= V_{1\pi}^{(0)} + V_{1\pi}^{(2)} + V_{1\pi}^{(3)} + V_{1\pi}^{(4)} + V_{1\pi}^{(5)} + \dots \ , \\ V_{2\pi} &= V_{1\pi}^{(2)} + V_{1\pi}^{(3)} + V_{1\pi}^{(4)} + V_{1\pi}^{(5)} + \dots \ . \end{aligned} \tag{2.12}$$

For example, the OPE potential at order Q^0 (LO) given directly in momentum space reads

$$V_{1\pi}^{(0)}(\vec{q}) = -\left(\frac{g_A}{2F_{\pi}}\right) \vec{\tau}_1 \cdot \vec{\tau}_2 \frac{\vec{\sigma}_1 \cdot \vec{q}\ \vec{\sigma}_2 \cdot \vec{q}}{q^2 + m_{\pi}^2} \ . \tag{2.13}$$

Here $\vec{q}$ is the relative momentum transfer of the exchanged pion $\vec{q} = \vec{p}\,' - \vec{p}$, $\vec{p}$ and $\vec{p}\,'$ are the initial and final relative momenta of the two nucleons in the c.m.s, $\vec{\tau}_1$, $\vec{\tau}_2$ denote isospin matrices of nucleons 1 and 2, respectively. $g_A = 1.29$ is the pion-nucleon axial coupling constant and $F_{\pi} = 92.4$ MeV is the pion decay constant.

Similarly, the contact interaction between nucleons, which plays the role of the short-range part of the NN force takes the form

$$V_{\text{cont}} = V_{\text{cont}}^{(0)} + V_{\text{cont}}^{(2)} + V_{\text{cont}}^{(4)} \dots \ . \tag{2.14}$$

The chiral potential with semilocal regularization in momentum space (the SMS potential) has been derived completely up to the fifth-order (N^{4}LO) of the chiral expansion by the Bochum-Bonn group [9]. Comparing to the previous chiral forces, the authors fixed the πN low-energy constants (LECs) using the Roy-Steiner analysis [94], skipped redundant contact terms in the higher order of the chiral expansion (starting at order Q^4, i.e. N^{3}LO), and, using the Granada-2013 database, determined adjustable parameters of the potential from *np* and *pp* scattering data and the deuteron binding energy. They also added the four leading contact terms acting in the N^{5}LO (Q^6 order) F-waves from Ref. [59] to their N^{4}LO, potential obtaining so-called N^{4}LO$^+$ interaction.

The general structure of the contact interactions of the chiral SMS force up to fourth-

order (N^3LO) Q^4 is

$$
\begin{aligned}
V_{\rm cont}^{(0)} &= C_S + C_T \vec{\sigma}_1 \cdot \vec{\sigma}_2 \ , \\
V_{\rm cont}^{(2)} &= C_1 q^2 + C_2 k^2 + \left(C_3 q^2 + C_4 k^2\right) \left(\vec{\sigma}_1 \cdot \vec{\sigma}_2\right) + \frac{i}{2} C_5 \left(\vec{\sigma}_1 \cdot \vec{\sigma}_2\right) \cdot \left(\vec{k} \times \vec{q}\right) \\
&\quad + C_6 \left(\vec{q} \cdot \vec{\sigma}_1\right) \left(\vec{q} \cdot \vec{\sigma}_2\right) + C_7 \left(\vec{k} \cdot \vec{\sigma}_1\right) \left(\vec{k} \cdot \vec{\sigma}_2\right) \ , \\
V_{\rm cont}^{(4)} &= D_1 q^4 + D_2 k^4 + D^3 q^2 k^2 + D_4 \left(\vec{q} \times \vec{k}\right)^2 \\
&\quad + \left(D_5 q^4 + D_6 k^4 + D_7 q^2 k^2 + D_8 \left(\vec{q} \times \vec{k}\right)^2\right) \left(\vec{\sigma}_1 \cdot \vec{\sigma}_2\right) \\
&\quad + \frac{i}{2} \left(D_9 q^2 + D_{10} k^2\right) \left(\vec{\sigma}_1 + \vec{\sigma}_2\right) \cdot \left(\vec{k} \times \vec{q}\right) + \left(D_{11} q^2 + D_{12} k^2\right) \left(\vec{\sigma}_1 \cdot \vec{q}\right) \left(\vec{\sigma}_2 \cdot \vec{q}\right) \\
&\quad + \left(D_{13} q^2 + D_{14} k^2\right) \left(\vec{\sigma}_1 \cdot \vec{q}\right) \left(\vec{\sigma}_2 \cdot \vec{q}\right) + D_{15} \vec{\sigma}_1 \cdot \left(\vec{q} \times \vec{k}\right) \vec{\sigma}_2 \cdot \left(\vec{q} \times \vec{k}\right) \ ,
\end{aligned}
\tag{2.15}
$$

where $\vec{k} = (\vec{p} + \vec{p}\,')/2$ and C_S, C_T $C_{1,\ldots,7}$ and $D_{1,\ldots,15}$ are the LECs which determine the strength of short-range interaction and should be find from data.

Application of nuclear forces derived from χEFT in few- and many-body problems requires regularization for the pion exchange contributions to reduce the amount of finite-cutoff terms and to avoid divergences after substituting, e.g., into the Lippmann-Schwinger equation. In Ref. [58], the Bochum-Bonn group implemented the local regularization of the long-range potential in coordinate space, see Eq. 1.5. Although such a regulator made it possible to significantly reduce the long-range cutoff terms, its application turned out to be difficult for the regularization of 3NFs and currents at higher orders of the chiral expansion. Therefore, the Bochum group introduced a local regularization scheme of long-range forces in momentum space by emplyoing a regularization of the static one-pion exchange propagator [9] in form of regulator

$$
f(p', p) \propto \exp\left(-\frac{\left(m_\pi^2 - \vec{q}^{\,2}\right)^2}{\Lambda^2}\right) \ , \tag{2.16}
$$

with the cutoff values of $\Lambda = 400, 450, 550$, and 550 MeV. Such an regulator, according to authors of Ref. [9], contributes only to the short-range terms and does not influence the long-range pion exchange potentials.

Implementing local regularization to the long-range potential and multiplying the contact terms with a non-local Gaussian regulator $\exp\left(-\frac{p'^2+p^2}{\Lambda^2}\right)$ in combination with the very detailed fitting procedure of the NN contact LECs leads to a high-quality potential. Additionally, for the chiral SMS potentials of Ref. [9] obtained with the Granada-2013 database [10] the covariance matrices of its free parameters (LECs) at all chiral orders (LO – N^4LO^+) have been obtained. The number of free parameters (LECs) is 2, 9, 9, 22, 23, 27 at LO, NLO, N^2LO, N^3LO, N^4LO and N^4LO^+, respectively. A sample visualization of correlations among the various LECs is given in Figure 10 of Ref. [9] for the chiral N^4LO^+ SMS potential with $\Lambda = 450$ MeV.

Currently, the chiral SMS NN potential delivers the best description of NN data. For example, the SMS N^4LO^+ with regularization parameter $\Lambda = 450$ MeV gives χ^2/datum = 1.06 (*np* scattering data) and χ^2/datum = 1.00 (*pp* scattering data), see Table 4 of Ref. [9]

up to 300 MeV. In addition, the availability of covariance matrices of LECs for all chiral cutoffs and orders allows us to study, for the first time for a chiral force, the propagation of uncertainties of NN interaction parameters to 3N continuum observables, see Chapter 3 and Chapter 5.

Chapter 3

Application of a covariance matrix

In Chapter 1, I have outlined the advantages of using the covariance matrix of NN potential parameters and briefly mentioned the types of errors relevant to the Nd scattering observables. In Section 3.1 I discuss the various sources of theoretical uncertainties in the *ab initio* type calculations based on the chiral SMS model at various orders, neglecting the 3N force present in describing the 3N processes. The main results of such a study are already shown in our papers (Refs. [11, 12]). Studies of correlations among all calculated 2N and 3N observables, as well as between observables and specific potential parameters, are discussed in Section 3.2.

3.1 Uncertainty quantification in 3N studies

3.1.1 Determination of statistical uncertainty in a 3N system

As defined in Chapter 1, the statistical uncertainty refers to an error arising from uncertainties of parameters of a given NN interaction. In our method of estimation, computation of the statistical uncertainties requires a big sample of predictions obtained with different sets of parameters within one model of interaction.

The algorithm for determining the statistical uncertainty is as follows, its further use for the chiral SMS force can be divided into the following steps:

1. Preparation of sets of the potential parameters.

   Having at our disposal the covariance matrix for the potential parameters, as well as the central values of the parameters, I sample 50 sets of the potential parameters from the multivariate normal distribution. This number of sets guarantees a statistically significant probe, as will be shown in Chapter 5. The multivariate sampling was done using the Mathematica® [95] computing system (see Appendix A).

2. Computing observables for each set of potential parameters

   For each set S_i $(i = 0, 1, \ldots, 50)$ I computed the deuteron wave-function by solving the Schrödinger equation and the t-matrix elements from the Lippmann-Schwinger equation and solved the Faddeev equation to construct the transition amplitude from which the 3N observables can be obtained for all investigated models of NN interaction. From solutions of the Lippmann-Schwinger equation 2N observables can be also computed. More details about these calculations will be given in Chapter 4. As a result, an angular dependence of various 3N scattering observables is known for each set of parameters S_i. The obtained predictions can be used to study:

(a) for a given observable X at an energy E and at a scattering angle θ, the empirical probability density function of the observable $X(E,\theta)$ resulting when various sets S_i, $(i = 1, \ldots, 50)$ are used;

(b) for a given observable X, both the angular and energy dependencies of results based on various sets S_i.

This, in turn, allows one to find the magnitude of statistical uncertainty of a given 3N observable X and to analyze correlations among all observables.

3. Quantification of the statistical uncertainty

Various estimators can be used to quantify the statistical uncertainty of the observable $X(E,\theta)$. For example, by assuming there are 50 sets of potential parameters:

(a) The sample standard deviation $\sigma(X) = \sqrt{\frac{1}{50-1}\sum_{i=1}^{50}\left(X_i(E,\theta) - \bar{X}(E,\theta)\right)^2}$, where $\bar{X}(E,\theta)$ is the mean value of predictions and $X_i(E,\theta)$ is the value of the i-th point in the dataset for each computed observable.

(b) $\frac{1}{2}\Delta_{100\%} \equiv \frac{1}{2}\left(\max\{X_i(E,\theta)\} - \min\{X_i(E,\theta)\}\right)$, where the minimum and maximum are taken over all predictions $\{X_i(E,\theta)\}$ based on 50 sets of LECs $S_i, i = 1, 2, \ldots, 50$.

(c) $\frac{1}{2}\Delta_{68\%} \equiv \frac{1}{2}\left(\max\{X_i(E,\theta)\} - \min\{X_i(E,\theta)\}\right)$, where the minimum and maximum are taken over 34 (68% of 50) predictions based on different sets of LECs. The set of 34 observables is constructed by discarding the 8 lowest and the 8 highest predictions for a given observable and at a specific scattering angle and energy.

(d) $\frac{1}{2}$IQR: half of the standard estimator of the interquartile range being the difference between the third and the first quartile IQR $= Q_3 - Q_1$. For the sample of size 50, this corresponds to taking half of the difference between the predictions on 37th and 13th positions in a sample sorted in ascending order.

The estimators $\frac{1}{2}\Delta_{100\%}$ and $\sigma(X)$ are sensitive to possible outliers in the sample, and thus accepting them as estimators of dispersion can lead to overestimation of the statistical uncertainty. On the other hand, due to the fact that the IQR is calculated using only half of the elements in the sample can leads to an underestimation of the theoretical uncertainty. In addition, $\sigma(x)$ is derived under the assumption of normality of sample, which is not necessarily fulfilled in the case of 3N observables [11]. Therefore, we chose $\frac{1}{2}\Delta_{68\%}$ as an optimal measure for dispersion of predictions and consequently as an estimator of the statistical uncertainty [11].

3.1.2 Determination of truncation errors with the EKM method

In addition to the statistical uncertainties also the truncation errors, which play the role of systematic uncertainty, can be evaluated. As was outlined in Chapter 1, the truncation errors are uncertainties arising from restriction to a given order of the chiral expansion. One way to evaluate truncation errors is using the EKM approach [58]. Namely, any 3N scattering observable X can be expanded up to the k-th order of the chiral expansion Q^k

$(k = 0, 2, 3, \ldots)$ in the form

$$X = X^{(0)} + \Delta X^{(0)} + \Delta X^{(2)} + \Delta X^{(3)} + \ldots + \Delta X^{(k)} \,, \tag{3.1}$$

where $\Delta X^{(2)} := X^{(2)} - X^{(0)}$, $\Delta X^{(k)} := X^{(k)} - X^{(k-1)}$ with $k > 2$, and $X^{(k)}$ is a prediction obtained at k-th order.

The truncation error $\delta(X)^{(k)}$ of an observable X at k-th order of the chiral expansion with $k = 0, 2, \ldots$ is given as

$$\begin{aligned} \delta(X)^{(0)} &\geq \max\left(Q^2|X^{(0)}|\right) \,, \\ \delta(X)^{(2)} &\geq \max\left(Q^3|X^{(0)}|, Q|X^{(2)} - X^{(0)}|\right) \,, \\ \delta(X)^{(k)} &\geq \max_{2\leq j\leq k}\left(Q^{k+1}|X^{(0)}|, Q^{k+1-j}|\Delta^{(j)}|\right) \text{ for } j \geq 2 \,, \end{aligned} \tag{3.2}$$

with the additional constraints $\delta(X)^{(2)} \geq Q\delta(X)^{(0)}$ and $\delta(X)^{(k)} \geq Q\delta(X)^{(k-1)}$ for $k \geq 3$ imposed on the truncation errors. The chiral expansion parameter Q is defined as

$$Q = \max\left(\frac{p}{\Lambda_b}, \frac{m_\pi}{\Lambda_b}\right) \,. \tag{3.3}$$

In my calculations the breakdown scale of the chiral expansion Λ_b was chosen as $\Lambda_b = 600$ MeV based on the results from Refs [13, 14] with the physical pion mass m_π and the c.m.s. momentum p corresponding to the considered incoming nucleon laboratory energy E_{lab}.

3.1.3 The truncation errors with a given Bayesian model

The EKM approach does not provide a statistical interpretation of the alleged uncertainties, thus we apply also the Bayesian approach to estimate the truncation error. The authors of Refs. [60, 15] developed the Bayesian method to calculate the posterior probability distribution of truncation errors in χEFT for the np total cross section at selected energies by applying the chiral NN potentials from Ref. [58]. Within the LENPIC project the Bayesian model of Ref. [15] was slightly modified to study truncation errors not only in NN but also in 3N scattering, [61]. The same Bayesian procedure was already used in Ref. [12].

This Bayesian procedure of determining the truncation errors bases on rewriting Eq. (3.1) in terms of dimensionless expansion coefficients c_k in the form

$$\begin{aligned} X &= X^{(0)} + \Delta X^{(2)} + \Delta X^{(3)} + \Delta X^{(4)} + \ldots + \Delta X^{(k)} + \ldots \\ &= X_{\text{ref}}\left(c_0 + c_2 Q^2 + c_3 Q^3 + c_4 Q^4 + \ldots\right) \,, \end{aligned} \tag{3.4}$$

where $\Delta X^{(k)}$ are the same as in Eq. (3.2) and the dimensionless expansion coefficients c_k are

$$c_k = \frac{X^{(k)} - X^{(k-1)}}{X_{\text{ref}} Q^k} \,. \tag{3.5}$$

The overall scale X_{ref} is

$$X_{\text{ref}} = \begin{cases} \max\left(|X^{(0)}|, Q^{-2}|\Delta X^{(2)}|\right) & \text{for } k = 2 \,, \\ \max\left(|X^{(0)}|, Q^{-2}|\Delta X^{(2)}|, Q^{-3}|\Delta X^{(3)}|\right) & \text{for } k \geq 3 \,, \end{cases} \tag{3.6}$$

assuming that $\Delta X^{(i)}$ are known explicitly up to the $k = 3$. One can estimate the size of the truncation error at the k-th order of chiral expansion as $\delta X^{(k)}_{Bayes} \equiv X_{ref}\Delta$ where $\Delta \equiv \sum_{i=k+1}^{\infty} c_i Q^i \approx \sum_{i=k+1}^{k+h} c_i Q^i$ is distributed, given the knowledge of $\{c_{i\leq k}\}$, with a posterior probability density function [15]

$$\mathrm{pr}_h\left(\Delta \mid \{c_{i\leq k}\}\right) = \frac{\int_0^\infty d\bar{c}\ \mathrm{pr}_h\left(\Delta \mid \bar{c}\right)\mathrm{pr}(\bar{c})\prod_{i\in\tilde{A}}\mathrm{pr}(c_i \mid \bar{c})}{\int_0^\infty d\bar{c}\ \mathrm{pr}(\bar{c})\prod_{i\in A}\mathrm{pr}(c_i \mid \bar{c})}\ . \tag{3.7}$$

Here the prior probability density function $\mathrm{pr}(c_i \mid \bar{c})$ is taken in form of a Gaussian $\mathrm{N}(0,\bar{c}^2)$ function and $\mathrm{pr}(\bar{c})$ is a log-uniform distribution in range $(\bar{c}_<, \bar{c}_>)$. Set $\tilde{A}$ is defined as $\tilde{A} = \{n \in \mathrm{N}_0 \mid \mathrm{n} \leq \mathrm{k}\ \wedge\ \mathrm{n} \neq 1 \wedge \mathrm{n} \neq \mathrm{m}\}$, $m \in \{0, 2, 3\}$ and

$$\mathrm{pr}_h(\Delta \mid \bar{c}) \equiv \left[\prod_{i=k+1}^{k+h}\int_\infty^\infty dc_i \mathrm{pr}(c_i \mid \bar{c})\right]\delta\left[\Delta - \sum_{j=k+1}^{k+h} c_j Q^j\right]\ , \tag{3.8}$$

with h being the number of the chiral orders above k which contributes to the truncation error. The resulting $\mathrm{pr}_h(\Delta \mid \{c_{i\leq k}\})$ is symmetric about $\Delta = 0$ thus one can find the degree-of-belief (DoB) interval $(-d_k^{(p)}, d_k^{(p)})$ at the DoB level p, as an inversion problem from the numerical integration

$$p = \int_{-d_k^{(p)}}^{d_k^{(p)}} \mathrm{pr}_h(\Delta \mid \{c_{i\leq k}\})d\Delta \tag{3.9}$$

and get the truncation error $\delta X^{(k)}_{Bayes} = X_{ref} d_k^{(p)}$.

In following we use $h = 10$, $\bar{c}_< = 0.5$, $\bar{c}_> = 10$, $\Lambda_b = 650$ MeV and $M_\pi^{\mathrm{eff}} = 200$ MeV which corresponds to the model $\bar{C}^{650}_{0.5-10}$ from Ref. [61]. The two latter quantities enter the expansion parameter $Q = max\left(\frac{p}{\Lambda_b}, \frac{M_\pi^{\mathrm{eff}}}{\Lambda_b}\right)$ with the momentum scale p defined in Eq. (17) of Ref. [61]

$$p = \sqrt{\frac{A}{A+1} m E_{\mathrm{lab}}}\ , \tag{3.10}$$

where $A = 2$ for the deuteron, m is the nucleon mass $m = 2m_p m_n/(m_p + m_n) = 938.918$ MeV/c^2 and E_{lab} is incoming-nucleon laboratory energy.

The detailed expression for $\mathrm{pr}_h\left(\Delta \mid \{c_{i\leq k}\}\right)$ at assumed priors[1] which were shown in Appendix A[2] of Ref. [61] takes the form

$$\begin{aligned}\mathrm{pr}_h\left(\Delta \mid \{c_{i\leq k}\}\right) = {} & \frac{1}{\sqrt{\pi\bar{q}^2\boldsymbol{c_k^2}}}\left(\frac{\boldsymbol{c_k^2}}{\boldsymbol{c_k^2} + \Delta^2/\bar{q}^2}\right)^{k/2} \\ & \times \frac{\Gamma\left[\frac{k}{2}, \frac{1}{2c_>^2}\right]\left(\boldsymbol{c_k^2} + \frac{\Delta^2}{\bar{q}^2}\right) - \Gamma\left[\frac{k}{2}, \frac{1}{2c_<^2}\right]\left(\boldsymbol{c_k^2} + \frac{\Delta^2}{\bar{q}^2}\right)}{\Gamma\left[\frac{k-1}{2}, \frac{\boldsymbol{c_k^2}}{2c_>^2}\right] - \Gamma\left[\frac{k-1}{2}, \frac{\boldsymbol{c_k^2}}{2c_<^2}\right]}\end{aligned} \tag{3.11}$$

[1]Since, in general, the coefficients c_k are unknown *a priori*, they can be obtained from various initial probability distribution (priors) with a characteristic size.

[2]The expression was first given in Appendix A of Ref. [15]

where $\bar{q}^2 \equiv \sum_{i=k+1}^{k+h} Q^{2i}$, $\boldsymbol{c_k^2} \equiv \sum_{i\in A} c_i^2$ and the incomplete gamma function is

$$\Gamma(s,x) = \int_x^\infty t^{s-1}e^{-t}\mathrm{dt}\ . \tag{3.12}$$

3.2 Correlations among observables in 2N and 3N systems

In the second part of this thesis (Chapter 6) I focus on looking for a set of observables which due to their uncorrelation can serve as database to precise fixing the free parameters of the nuclear interaction. This is especially important in the context of fixing parameters of three-nucleon interaction. In general, to fix free parameters of the 3NF various observables can be used. In the older models (like the Tucson-Melbourne [77, 78, 79] or the UrbanaIX [80]) the ^{3}H binding energy and the density of nuclear matter have been used. In the case of chiral interaction, a three-nucleon force occurs at the N^{2}LO for the first time. Its two free parameters have been fixed from the ^{3}H binding energy and the nucleon-deuteron doublet scattering length $^2a_{nd}$ in Ref. [96]. More recently the differential cross section at medium energies has been used instead of $^2a_{nd}$ [86]. Thirteen new free parameters for 3NF are expected at N^{4}LO order. Fixing them will be a tremendous computational effort, and therefore the set of observables used for this must be carefully selected. Specifically, to minimize uncertainties of fixed parameters, the selected observables should be uncorrelated.

As mentioned above, in the case of the chiral models, besides the ^{3}H binding energy, the differential cross section for Nd elastic scattering at $E_{\mathrm{lab}} = 60$ MeV around its minimum has been used to fix free parameters of 3NF. However, the question of a possible correlation between the binding energy ^{3}H and the scattering cross section is still open. The study presented in this thesis allows me to answer this question and, in a systematic way, to point out the correlated observables in the 3N system. However, a study of correlations in the two-nucleon system is also interesting and can impact future procedures used to fix free parameters of the two-body force interaction. A systematic study of the correlations between the parameters of the NN potential and two-nucleon observables can be valuable, too. While there exist many experimental data at low energies most of them are the unpolarized cross sections or polarization observables with only one particle polarized in the initial state. Knowledge if one of these observables is strongly correlated to given potential parameter would allow ones to use it to fix this specific parameter. This, in turn, reduces the number of remaining free parameters what simplifies the fitting procedure. Existence of such a correlated observable-potential parameter pair could also motivate experimental groups to perform precise measurement of such an observable, especially if a suitable experiment has not been performed yet. My work is a first step in this direction.

In the past, a study of correlations has not been possible, at a statistically significant level, due to the lack of a sufficiently large number of the existing potentials and data. Currently, this situation is changed. Using the OPE-Gaussian or the chiral SMS forces allows us to prepare many sets of the potential parameters and thus, after a procedure described in subsection 3.1.1, obtain a number of predictions big enough to analyze correlations and to draw a plausible conclusion. Some attempts to study correlations in

The magnitude of r	Interpetation
$0 < \|r\| \leq 0.3$	very weak (no correlation)
$0.3 < \|r\| \leq 0.5$	weak
$0.5 < \|r\| \leq 0.7$	moderate
$0.7 < \|r\| \leq 0.9$	strong
$0.9 < \|r\| \leq 1$	very strong

Table 3.1: Interpretation of correlation coefficient. "No correlation" in the second row should be understood as no linear dependencies between observables.

few-nucleon sectors are given in papers [97], [98] and [99]. In Ref. [97] authors study, using the Monte-Carlo bootstrap analysis as a method to randomize *pp* and *np* scattering predictions, correlations between the ground states of the ^{2}H, ^{3}H and ^{4}He binding energies, focusing mainly on the Tjon line [100] (correlation between ^{3}H and ^{4}He binding energies), but do not study the scattering observables. In Ref. [98] the correlations between three- and four-nucleon observables have been studied within the pionless Effective Field Theory with the Resonating Group Method. Because this approach can be applied only to processes at very low energies authors focus on the study of bound-state properties and the ^{3}H-neutron S-wave scattering length, finding the latter correlated with the ^{3}He binding energy. A.Kievsky *et al.*, [99] studied some correlations between low-energy bound state observables in the two- and three-nucleon system, the triton binding energy, and extending this to study some features of the light nuclei and beyond up to nuclear matter and neutron star properties. Using a simple model of "Leading-order Effective Field Theory inspired potential" they found evidence of the connection between few- and many observables. Note, none of these works focuses on the study of correlations in the context of three-nucleon observables.

To find a correlation coefficient between two variables, e.g. observables, first, I need to collect pairs of predictions obtained with various sets of potential. I use the same sets of parameters as in Chapter 5, supplementing them, if needed, by additional sets. Having predictions I calculate the standard sample correlation coefficients $r(X, Y)$

$$r(X,Y) = \frac{\sum_{i=1}^{n} \left(x_i - \bar{X}\right)\left(y_i - \bar{Y}\right)}{\sqrt{\sum_{i=1}^{n} \left(x_i - \bar{X}\right)^2 \sum_{i=1} \left(y_i - \bar{Y}\right)^2}} , \tag{3.13}$$

where X and Y stand for chosen observables or parameters and index "i" runs over the sets of $n = 50$ versions of potentials. $\bar{X}$ and $\bar{Y}$ are means $\bar{X} = \sum_{i=1}^{n} x_i$ and $\bar{Y} = \sum_{i=1}^{n} y_i$, respectively.

Interpretation of correlation coefficient is arbitrary in many respects, and we can not be too strict with it. The correlation coefficient takes values from -1 to 1. A value of $r = +1$ shows increasing linear dependence between X and Y while $r = -1$ means decreasing linear dependence between X and Y. If the correlation coefficient equals 0, then there is no linear correlation between the variables, however, variables can still be nonlinearly dependent. Table 3.1 provides the qualitative interpretation of the correlation coefficient that we use in this thesis. In our studies, determining the correlation coefficient for a given pair of observables, we have in practice only one 50-element sample

at our disposal. Thus estimation of uncertainty of computed sample correlation coefficients is not straightforward. To find this uncertainty I apply three methods. Firstly, I make use of additional samples, see Chapter 6.1. Secondly, I use the well-known Fisher transformation [101, 102]. To construct a confidence interval by Fisher's method, it is assumed that X and Y have a bivariate normal distribution, which is only approximately satisfied by observables [11]. The variable $Z = \frac{1}{2}\ln\left(\frac{1-\mathrm{r(X,Y)}}{1+\mathrm{r(X,Y)}}\right)$, which has the standard normal distribution is used to construct a confidence interval at a given confidence level γ. After inverse transformation of confidence limits one gets the confidence interval for $r(X,Y)$. Applying this method to various pairs (X,Y), I found that the obtained half confidence interval at $\gamma = 0.9$ is usually ≈ 0.05 for $r \approx 0.9$ and ≈ 0.25 for $r \approx 0.25$. This shows that determined values of correlation coefficients should be treated qualitatively. Thus, in following, I will restrict myself to rather qualitative discussion of correlation coefficients. Since I am interested is determining whether given observables are or not are correlated, such qualitative conclusions are sufficient at this stage of the research. Finally, I used also the bootstrap resampling method [103, 104, 105] to estimate uncertainties of $r(X,Y)$. The advantage of the bootstrap method is in working directly with sample elements without assumption on normalness of distribution of X and Y. Resampling (up to 1000 (X,Y)-elements) allows me to find the properties (e.g. distribution or standard derivation) of bootstrap estimator for the correlation coefficient and thus estimate uncertainty of original received $r(X,Y)$ again as half of bootstrap confidence interval. Typically, the half of bootstrap confidence interval at $\gamma = 0.9$ is ≈ 0.05 for $r \approx 0.9$ (≈ 0.23 for $r \approx 0.25$). In most cases, the Fisher method gives a much larger uncertainty than the others. However since we interpretate the correlation coefficient qualitatively the different values of uncertainties of $r(X,Y)$ do not change our conclusions.

My results for sample correlation coefficients and resulting conclusions are presented in Chapter 6.

Chapter 4

Theoretical formalism and numerical realization

All results in this work have been obtained in momentum space by resorting to partial-wave decomposition (PWD) what is convenient for calculations in the framework of the Faddeev equations. We use the non-relativistic formalism, neglect the Coulomb force and the 3N interaction.

4.1 2N bound state

The Hamiltonian of two-nucleon systems can be written in general form

$$H^{(2)} = H_0^{(2)} + V_{\mathrm{2N}} \ , \tag{4.1}$$

where $H_0^{(2)}$ is the kinetic energy of two nucleons and $V_{\mathrm{2N}}^{(2)}$ is the NN potential. The kinetic energy of the two-particle system is

$$H_0^{(2)} = \frac{\vec{p}_1^{\,2}}{2m_1} + \frac{\vec{p}_2^{\,2}}{2m_2} = \frac{\vec{p}^{\,2}}{2\mu} + \frac{\vec{\mathcal{P}}^{\,2}}{2M} \ , \tag{4.2}$$

where $\mu = \frac{m_1 m_2}{m_1+m_2}$ is the reduced nucleon mass and $M = m_1 + m_2$. Using the average nucleon mass $m_1 = m_2 = m = \frac{2m_p m_n}{m_p+m_n}$ and individual momenta $\vec{p}_1$, $\vec{p}_2$, the relative momentum $\vec{p} = \frac{m_1\vec{p}_2 - m_2\vec{p}_1}{m_1+m_2} = \frac{1}{2}\left(\vec{p}_2 - \vec{p}_1\right)$ and the total momentum for two nucleons is $\vec{\mathcal{P}} = \vec{p}_1 + \vec{p}_2$.

The deuteron bound wave function $|\Psi_d\rangle$ is a solution of the time-independent Schrödinger equation

$$\left(H_0^{(2)} + V_{\mathrm{2N}}\right)|\Psi_{\mathrm{d}}\rangle = E_d\,|\Psi_{\mathrm{d}}\rangle \ , \tag{4.3}$$

where $E_d < 0$. Using Eq. (4.2) and assuming that V_{2N} depends only on the relative degrees of freedom leads to two separated equations

$$\frac{\vec{p}^{\,2}}{m}\,\langle\vec{p}|\Psi_d\rangle + \int_0^\infty \mathrm{d}\vec{p}\,'\,\langle\vec{p}|V_{\mathrm{2N}}|\vec{p}\,'\rangle\,\langle\vec{p}\,'|\Psi_d\rangle = (E_d - E_{\mathrm{c.m.}})\,\langle\vec{p}|\Psi_d\rangle \ , \tag{4.4}$$

and

$$\frac{\vec{\mathcal{P}}^2}{2m}\left\langle\vec{\mathcal{P}}|\Psi_d\right\rangle = E_{\text{c.m.}}\left\langle\vec{\mathcal{P}}|\Psi_d\right\rangle \ . \tag{4.5}$$

Since the total momentum of the system is conserved, the relative energy of the center-of-mass (c.m.) between two nucleons, $E_{\text{c.m.}}$, equals zero (deuteron is at rest) and equation (4.5), which describes the free motion of a particle with mass M, is omitted.

We use the momentum partial-wave representation

$$|p\alpha_2\rangle \equiv |p(ls)jm_j\rangle\,|tm_t\rangle \ , \tag{4.6}$$

where $p \equiv |\vec{p}|$ is the magnitude of the relative momentum, and α_2 is a set of discrete quantum numbers describing 2N system $|\alpha_2\rangle \equiv |(ls)jm_j\rangle\,|tm_t\rangle$, where l, s, j, and t denote the orbital angular momentum, total spin, total angular momentum, and total isospin of 2N system, respectively. Further m_j (m_t) are the projections of j (t) onto the quantization axis. The coupling of the above-mentioned quantum numbers is given by

$$\begin{aligned}
|p(ls)jm_j\rangle &= \sum_{m_l} c(lsj; m_l, m_j - m_l, m_j)\,|plm_l\rangle\,|sm_j - m_l\rangle \ , \\
|sm_s\rangle &= \sum_{m_1=-1/2}^{1/2} C\left(\frac{1}{2},\frac{1}{2},s; m_1, m_s - m_1, m_s\right)\left|\frac{1}{2}m_1\right\rangle\left|\frac{1}{2}m_s - m_1\right\rangle \ , \\
|tm_t\rangle &= \sum_{\nu=-1/2}^{1/2} C\left(\frac{1}{2},\frac{1}{2},t; \nu, m_s - \nu, m_t\right)\left|\frac{1}{2}\nu\right\rangle\left|\frac{1}{2}m_t - \nu\right\rangle \ ,
\end{aligned} \tag{4.7}$$

where m_l is the projection of the orbital angular momentum. Further, spin states $|sm_s\rangle$ correspond to 2N spin states with the total spin 0 or 1; $C(j_1, j_2, j; m_1, m_2, m)$ denote the Clebsch-Gordan coefficients. Similarly, $|tm_t\rangle$ is the ispospin state. We assume for individual particles the isospin projection $\nu = \frac{1}{2}$ for proton and $\nu = -\frac{1}{2}$ for neutron.

The 2N states are antisymmetric as for a system of two identical fermions, which leads to additional constraint on quantum numbers l, s and t:

$$(-1)^{l+s+t} = -1 \ . \tag{4.8}$$

The partial-wave states (4.6) fulfills

$$\left\langle\vec{p}'|plm_l\right\rangle = \frac{\delta(p-p')}{pp'}Y_{lm_l}(\theta,\phi) \ , \tag{4.9}$$

where $Y_{lm_l}(\theta,\phi)$ denotes the spherical harmonic function with angles θ, ϕ pointing direction of momentum $\vec{p}$ [106]. The completeness relation for $|p\alpha_2\rangle$ states is expressed as

$$\sum_{\alpha_2}\int_0^\infty \mathrm{d}pp^2\,|p\alpha_2\rangle\,\langle p\alpha_2| = \mathbb{1} \ . \tag{4.10}$$

The only two deuteron components that contribute to the bound state, $^3S_1$- and $^3D_1$, correspond to $l = 0$ and $l = 2$, respectively, (we use the standard notation $^{2s+1}l_j$) with

	N^{2}LO	N^{3}LO	N^{4}LO	N^{4}LO$^+$	OPEG	Exp. [107]
E_d [MeV]	-2.1999 $\pm$0.0041	-2.2233 $\pm$0.0024	-2.2233 $\pm$0.00099	-2.2233 $\pm$0.0012	-2.2225 $\pm$0.00001	-2.2246 $\pm$0.0092
$P(^3S_1)$ [%]	95.3665 $\pm$0.0041	95.3034 $\pm$0.0024	95.4633 $\pm$0.00099	95.4114 $\pm$0.0012	94.6987 $\pm$0.0412	—

Table 4.1: The deuteron binding energy E_d with the statistical uncertainty (see text in Chapter 3.1.1) obtained with various NN interactions.

$s = j = 1$ and $t = m_t = 0$. This leads to two coupled equations

$$\frac{p^2}{m}\psi_l(p) + \sum_{l'=0}^{2} \int_0^\infty dp' p'^2 \, \langle pl|V_{\rm 2N}|p'l'\rangle \, \psi_{l'}(p') = E_d \psi_l(p) \; , \tag{4.11}$$

for the partial-wave components of the deuteron wave function $\psi_l(p) = \langle pl|\psi_d\rangle = \\ = \langle p(l1)1m_d| \, \langle 00|\psi_d\rangle$.

In numerical realization the integral (4.11) can be discretized using the Gaussian quadrature. We use Gaussian points and weights (p_j, w_j) with $j = 1, 2, \ldots, N_p$ distributed in the finite interval $(0, \bar{p})$, where the upper limit of the integration, $\bar{p}$ has to be adjusted to the used NN potential $V_{\rm 2N}$. Using this Eq. (4.11) can be expressed as

$$\frac{p_i^2}{m}\psi_l(p_i) + \sum_{l'=0}^{2} \sum_{j=1}^{N_p} w_j p_j^2 \, \langle p_i l|V_{\rm 2N}|p_j l'\rangle \, \psi_{l'}(p_j) = E_d \psi_l(p_i) \; . \tag{4.12}$$

We solve the resulting eigenvalue problem using FORTRAN code together with the LAPACK library [108] and compute the deuteron wave function and the deuteron binding energy, E_d. The deuteron binding energy computed with the chiral SMS potentials at various chiral orders with cutoff $\Lambda = 450$ MeV and with the OPE-Gaussian force is given in Table 4.1.

In the final step the deuteron wave functions $\psi_0(p)$ and $\psi_2(p)$ require normalization via

$$\int_0^\infty dp p^2 \left(\psi_0^2(p) + \psi_2^2(p)\right) = 1 \; . \tag{4.13}$$

In Figure 4.1 I show the $^3S_1$- and $^3D_1$-states obtained by using the chiral N^{2}LO, N^{3}LO, N^{4}LO, N^{4}LO$^+$ SMS forces and the OPE-Gaussian potential. It can be seen that all predictions almost coincide with each other. The magnitude of $^3S_1$-state is nearly 70 times bigger than in $^3D_1$-state. The corresponding $^3S_1$-component probability is given in the bottom row of Table 4.1.

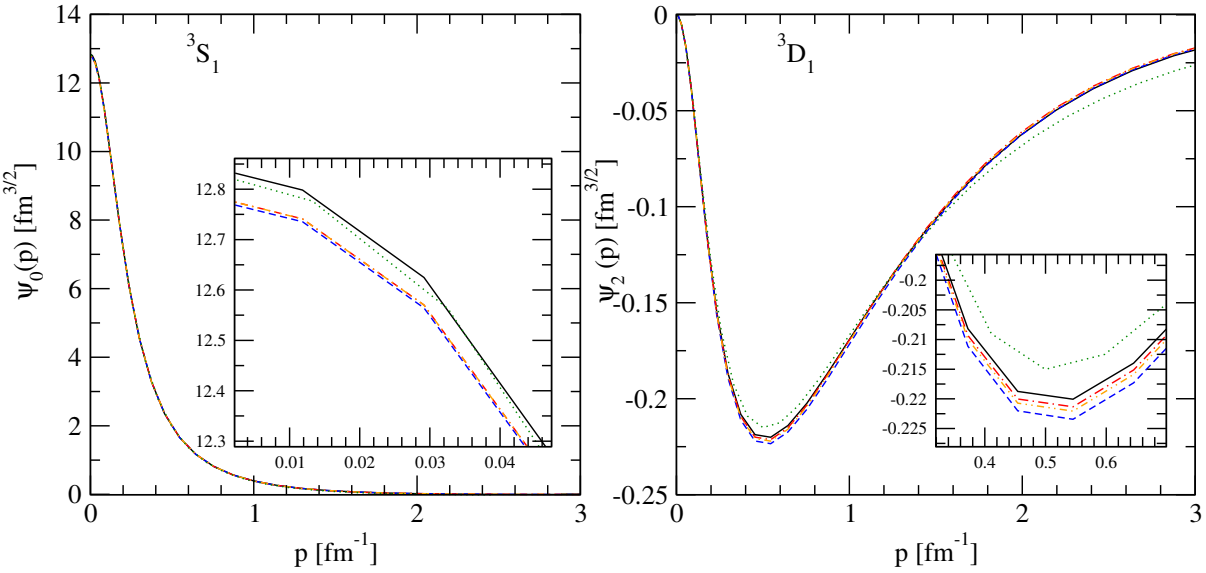

Figure 4.1: The deuteron wave functions in momentum $\Psi_l(p)$ space. The $^3S_1$ and the $^3D_1$ components are shown in the left and right columns, respectively. The black solid, blue dashed, red dashed-dotted, orange dashed-dot-dotted and green dotted curves are for the chiral N^{2}LO, N^{3}LO, N^{4}LO, N^{4}LO$^+$ and the OPEG potentials, respectively.

4.2 2N scattering

In this chapter, I introduce the essential components of 2N scattering calculations. I start with a discussion of the Lippmann-Schwinger equation for the scattering state in momentum space. This equation can be solved for the transition matrix (t-matrix) via PWD. Next, I obtain K-matrix, which in turn, is related to the scattering matrix S-matrix. S-matrix can be further expressed in terms of a linear combination of Wolfenstein parameters [109] that allowed us to compute observables, e.g. the cross section and various polarization observables.

4.2.1 The Lippmann-Schwinger equation

The scattering state $|\Psi_{\vec{p}}\rangle$ of two particles in momentum space, fulfils the time-independent Schrödinger equation

$$(H_0 + V_{2\mathrm{N}})\,|\Psi_{\vec{p}}\rangle = E\,|\Psi_{\vec{p}}\rangle \ , \tag{4.14}$$

with $E > 0$. Its solution fulfils the Lippmann-Schwinger equation

$$|\Psi_{\vec{p}}\rangle = |\Psi_0\rangle + \frac{1}{E - H_0 \pm i\varepsilon} V_{2\mathrm{N}}\,|\Psi_{\vec{p}}\rangle \ , \tag{4.15}$$

with $\varepsilon \to 0^+$. If we write down (4.15) in coordinate representation, we will get two parts of the solution — a spherical outgoing wave ($+i\varepsilon$) or a plane incoming wave ($-i\varepsilon$) [1], see Refs. [110, 111] for more details. The state $|\Psi_0\rangle$ is momentum eigenstate

$$|\Psi_0\rangle \equiv |\vec{p}\rangle \ \text{ with } \frac{\vec{p}^{\,2}}{2\mu} = E \ , \tag{4.16}$$

[1] "$-i\varepsilon$"-states appear, for example, in the photodisintegration process ($\gamma + {}^2\mathrm{H} \to n + p$).

where $\vec{p}$ is the relative momentum of the two nucleons and E depends on the incoming nucleon energy in the laboratory reference frame [2]. The solution of Eq. (4.15) can be denoted as $|\Psi_{\vec{p}}\rangle = |\vec{p}\rangle^+$.

Eq. (4.15) can be rewritten as

$$|\vec{p}\rangle^+ = |\vec{p}\rangle + \tilde{G}_0(E+i\varepsilon)V\,|\vec{p}\rangle^+ \ , \tag{4.17}$$

where $V \equiv V_{2\mathrm{N}}$ and the free propagator

$$\tilde{G}_0(E) \equiv \frac{1}{E - H_0} \ . \tag{4.18}$$

Using the definition of the transition operator (t-matrix)

$$V\,|\vec{p}\rangle^+ = t^+\,|\vec{p}\rangle \ , \tag{4.19}$$

and substituting it into Eq. (4.17) we find

$$V\,|\vec{p}\rangle^+ = V\,|\vec{p}\rangle + V\tilde{G}_0(E+i\varepsilon)V\,|\vec{p}\rangle^+ \ , \tag{4.20}$$

and thus

$$t^+\,|\vec{p}\rangle = V\,|\vec{p}\rangle + V\tilde{G}_0(E+i\varepsilon)t^+\,|\vec{p}\rangle \ . \tag{4.21}$$

The latter equation is the form of the Lippmann-Schwinger equation for the operator t^+

$$t^+ = V + V\tilde{G}_0(E+i\varepsilon)t^+ \ . \tag{4.22}$$

Note that in general case Eq. (4.22) can be iterated for scattering on V

$$t = V + V\tilde{G}_0V + V\tilde{G}_0V\tilde{G}_0V + V\tilde{G}_0V\tilde{G}_0V\tilde{G}_0V + \dots \ , \tag{4.23}$$

this is the so-called von Neumann series. Finally, one can express $|\vec{p}\rangle^+$ through the t-matrix

$$|\vec{p}\rangle^+ = |\vec{p}\rangle + \tilde{G}_0(E+i\varepsilon)t(E+i\varepsilon)\,|\vec{p}\rangle \ . \tag{4.24}$$

Considering the t-matrix for general states $\left|\vec{p}\,'\right\rangle$, $|\vec{p}\rangle$, which obeys the Lippmann-Schwinger equation (4.15), we get the off-the-energy-shell amplitude [110]

$$\begin{aligned}\left\langle \vec{p}\,'\right|t(E+i\varepsilon)\left|\vec{p}\right\rangle &= \left\langle \vec{p}\,'\right|V(E+i\varepsilon)\left|\vec{p}\right\rangle \\ &+ \lim_{\varepsilon\to 0^+}\int_0^\infty \mathrm{d}\vec{p}\,''\left\langle \vec{p}\,'\right|V(E+i\varepsilon)\left|\vec{p}\,''\right\rangle \frac{\left\langle \vec{p}\,''\right|t\left|\vec{p}\right\rangle}{E_{p'}+i\varepsilon-E_{p''}} \ ,\end{aligned} \tag{4.25}$$

where $E_{p'} = \frac{|\vec{p}\,'|^2}{m}$ and $E_{p''} = \frac{|\vec{p}\,''|^2}{m}$. In a similar manner as has been done for the deuteron, PWD projection of Eq. (4.25) onto the same complete set of basis state (4.6) and using

[2] Given E_{lab} and assuming that $m_p = m_n = m$, each nucleon in the c.m.s. has a relative momentum which refers to an unknown $E \equiv E_{\mathrm{cm}} = \frac{\vec{p}^{\,2}}{m}$. In turn, $E = E_{\mathrm{lab}} - \frac{\vec{p}^{\,2}}{2(2m)} = \frac{1}{2}E_{\mathrm{lab}}$.

the upper limit for the p'' integration, $\bar{p}$, results in

$$\langle p'\alpha_2'|t|p\alpha_2\rangle = \langle p'\alpha_2'|V|p\alpha_2\rangle + \sum_{l''} \lim_{\varepsilon\to 0^+} \int_0^{\bar{p}} \mathrm{d}p'' \frac{p''^2 \langle p'\alpha_2'|V|p'\alpha_2''\rangle \langle p''\alpha_2''|t|p\alpha_2\rangle}{E_{p'} - E_{p''} + i\varepsilon} \ . \tag{4.26}$$

The t-matrix at $E = \frac{p^2}{m}$ is related to the K-matrix [110] and to the S-matrix via

$$t = (1 + 2i\pi\mu p K)^{-1} K \ , \tag{4.27}$$

and

$$S = (1 + 2i\pi\mu p K)^{-1}(1 - 2i\pi\mu p K)^{-1} \ , \tag{4.28}$$

which is used to get phase shifts.

4.2.2 2N scattering observables

Studying the elastic scattering of particles with spin 1/2 allows one to carry out much more diverse measurements than only cross sections. Experiments can be made for different polarization of the beam, target and/or outgoing particles, polarized individually or simultaneously. As a result, there are $16 \times 16 = 256$ of various experiments, but due to the parity conservation and the time- reversal symmetry, the number of independent experiments is reduced up to 11 *np*- and 9 *pp*-measurements [110]. The general scattering amplitude can be expressed in terms of the M-matrix and its representation is

$$\begin{aligned} M = a + c\,(\vec{\sigma}_1 + \vec{\sigma}_2)\,\hat{N} + m\left(\vec{\sigma}_1\hat{N}\right)\left(\vec{\sigma}_2\hat{N}\right) + (g+h)\left(\vec{\sigma}_1\hat{P}\right)\left(\vec{\sigma}_2\hat{P}\right) \\ + (g-h)\left(\vec{\sigma}_1\hat{K}\right)\left(\vec{\sigma}_2\hat{K}\right) \ , \end{aligned} \tag{4.29}$$

where a, m, c, g and h are the Wolfenstein parameters [109, 110] (see also [112] for an exact determination from scattering observables) and

$$\hat{K} \equiv \frac{\vec{p}' - \vec{p}}{|\vec{p}' - \vec{p}|} \ , \ \hat{P} \equiv \frac{\vec{p}' + \vec{p}}{|\vec{p}' + \vec{p}|} \ , \ \hat{N} \equiv \frac{\vec{p}' \times \vec{p}}{|\vec{p} \times \vec{p}'|} \ . \tag{4.30}$$

Since the S -matrix contains full dynamic information, then decomposing it on the partial-waves basis to obtain $S^{js}_{l'l}$-matrix elements and taking them on-the-energy-shell allows to calculate the partial-wave elements of M, see Ref. [110],

$$\begin{aligned} M^{st}_{m_s' m_s} = \frac{1}{ip} \sum_{jl'l} C\,(l', s, j; m_s - m_s', m_s', m_s)\, Y_{l'(m_s'-m_s)}(\theta, \phi) \\ \times\, i^{l-l'} \left(S^{js}_{l'l} - \delta_{l'l}\right) C\,(l, s, j; 0, m_s, m_s) \sqrt{\pi(2l+1)} \left[1 - (-1)^{l+s+t}\right] \ . \end{aligned} \tag{4.31}$$

The partial-wave $S^{js}_{l'l}$-matrix element is nothing else but $S^{js}_{l'l} \equiv \langle l' s j|S|l s j\rangle$.

In the uncoupled case ($l = l'$) and for a given j, s the S-matrix can be parameterized by one phase shift

$$S^{js}_{ll} = e^{2i\delta_l} \ . \tag{4.32}$$

For the coupled channels (for which the nuclear force allows for changes of angular momentum) the S-matrix is 2×2 unitary and symmetric. According to the Stapp parameterization [113] it can be written as

$$S = \begin{pmatrix} S^{j1}_{j-1j-1} & S^{j1}_{j-1j+1} \\ S^{j1}_{j+1j-1} & S^{j1}_{j+1j+1} \end{pmatrix} = \begin{pmatrix} \cos(2\varepsilon)\exp(2i\delta_1) & i\sin(2\varepsilon)\exp(i(\delta_1+\delta_2)) \\ i\sin(2\varepsilon)\exp(i(\delta_1+\delta_2)) & \cos(2\varepsilon)\exp(2i\delta_2) \end{pmatrix} , \quad (4.33)$$

where δ_1, δ_2 are phase shifts and ε is a mixing parameter.

Using the M-matrix [110], the resulting spin averaged differential cross section is given by

$$\frac{d\sigma}{d\Omega} = \frac{1}{4}\mathrm{Tr}\{MM^\dagger\} . \quad (4.34)$$

The polarization of one of the two particles is defined as

$$P = \frac{\mathrm{Tr}\{MM^\dagger\vec{\sigma}\}}{\mathrm{Tr}\{MM^\dagger\}} = \frac{8\mathrm{Re}\{c^*(a+m)\}}{\mathrm{Tr}\{MM^\dagger\}}\hat{N} , \quad (4.35)$$

where $\vec{\sigma}$ can be either $\vec{\sigma}_1$ or $\vec{\sigma}_2$.

The remaining 2N scattering spin observables expresses as

$$\begin{aligned} D &= \frac{\mathrm{Tr}\{M(\vec{\sigma}\cdot\hat{N})M^\dagger(\vec{\sigma}\cdot\hat{N})\}}{\mathrm{Tr}\{MM^\dagger\}} , \\ R &= \frac{\mathrm{Tr}\{M(\vec{\sigma}\hat{N}\times\hat{p})M^\dagger(\vec{\sigma}\cdot\hat{K})\}}{\mathrm{Tr}\{MM^\dagger\}} , \\ R' &= \frac{\mathrm{Tr}\{M(\vec{\sigma}\hat{N}\times\hat{p})M^\dagger(\vec{\sigma}\cdot\hat{P})\}}{\mathrm{Tr}\{MM^\dagger\}} , \\ A &= \frac{\mathrm{Tr}\{M(\vec{\sigma}\cdot\hat{p})M^\dagger(\vec{\sigma}\cdot\hat{K})\}}{\mathrm{Tr}\{MM^\dagger\}} , \\ A' &= \frac{\mathrm{Tr}\{M(\vec{\sigma}\cdot\hat{p})M^\dagger(\vec{\sigma}\cdot\hat{P})\}}{\mathrm{Tr}\{MM^\dagger\}} , \end{aligned} \quad (4.36)$$

where $\hat{p} = (\sin\theta\cos\phi, \sin\theta\sin\phi, \cos\theta)$. The observable D determines the change of polarization with respect to normal direction, the depolarisation observables R, R', A, and A' determine the four possible linear combinations referring to beam and target spin polarization in scattering plane.

In the case of two polarised particles we find the spin correlation coefficients, e.g.

$$C_{NN} = \frac{\mathrm{Tr}\{MM^\dagger\vec{\sigma}_1\cdot\hat{N}\vec{\sigma}_2\cdot\hat{N}\}}{\mathrm{Tr}\{MM^\dagger\}} . \quad (4.37)$$

More detailed information about the 2N scattering observables and the partial-wave decomposition can be found in Ref. [110].

4.3 3N scattering

In this chapter, I outline the foundations of the formalism of the Faddeev equations for 3N scattering calculations. I start with a discussion of the Faddeev framework. This

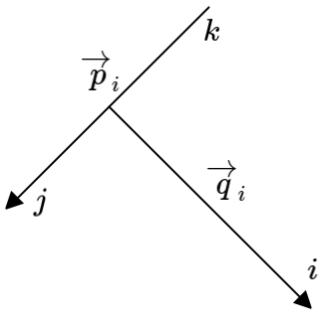

Figure 4.2: Jacobi momenta $\vec{p}_i$ and $\vec{q}_i$ for system of i, j, k particles.

leads me to discussion how to calculate the elastic Nd and the neutron induced deuteron breakup scattering observables.

4.3.1 The Faddeev equation

Theoretical investigations of Nd scattering can be performed within the Faddeev formalism [2]. This is one of the standard techniques to investigate 3N reactions and has been described in detail many times, see, e.g. Refs. [1, 2, 110]. In the following I will just briefly describe the key points of the formalism and its practical implementation.

In case of the 3N system it is convenient to use the relative ($\vec{p}$ and $\vec{q}$) momenta and the total 3N momentum, $\vec{\mathcal{P}}$ expressed in terms of individual nucleon momenta $\vec{k}_i$, $i \in \{1, 2, 3\}$

$$\begin{aligned} \vec{p}_1 \equiv \vec{p} &= \frac{1}{2}\left(\vec{k}_2 - \vec{k}_3\right) \ , \\ \vec{q}_1 \equiv \vec{q} &= \frac{2}{3}\left(\vec{k}_1 - \frac{1}{2}\left(\vec{k}_2 + \vec{k}_3\right)\right) \ , \\ \vec{\mathcal{P}} &= \vec{k}_1 + \vec{k}_2 + \vec{k}_3 \ . \end{aligned} \tag{4.38}$$

The Jacobi momentum $\vec{p}$ is a relative momentum of nucleons 2 and 3 and the Jacobi momentum $\vec{q}$ is the momentum of nucleon 1 with respect to the center-of-mass of the 2-3 subsystem. The definition 4.38 can be extended to other permutations where the Jacobi momenta $\vec{p}_i, \vec{q}_i$ are used, see Figure 4.2. We are working in the center-of-mass of the 3N system ($\vec{\mathcal{P}} = \vec{0}$) which allows us to deal with two instead of three independent momenta.

Assuming that the neutron and proton masses are the same and equal to m, the full 3N Hamiltonian reads

$$H = H_0 + V_{23} + V_{13} + V_{12} + V_{123} \ , \tag{4.39}$$

where $H_0 = \frac{\vec{p}^2}{m} + \frac{3}{4}\frac{\vec{q}^2}{m}$ is the free 3N Hamiltonian in the c.m. frame written in terms of the Jacobi momenta, V_{ij} denotes the NN potential acting between nucleons i and j, and V_{123} is the 3N potential, which can be splitted into a sum:

$$V_{123} = V_4^{(1)} + V_4^{(2)} + V_4^{(3)} \ , \tag{4.40}$$

where $V_4^{(i)}$ is symmetric under the exchange of nucleons j and k such that $i \neq j \neq k$. In the case of three identical particles the totally antisymmetric state $|\Psi\rangle$ of three nucleons

is given by

$$|\Psi\rangle = |\psi_1\rangle + |\psi_2\rangle + |\psi_3\rangle = (1+P)\,|\psi_1\rangle \ , \tag{4.41}$$

where the permutation operator $P \equiv P_{12}P_{23} + P_{13}P_{23}$ is built from single particle permutations P_{ij}, which exchange particles i and j and $|\psi_1\rangle$ is the Faddeev component of $|\Psi\rangle$. The Faddeev-component of three-nucleon bound state $|\Psi_1\rangle$ fulfills [71]

$$|\psi_1\rangle = G_0 t P\,|\psi_1\rangle \ , \tag{4.42}$$

where the two-nucleon t-operator obtaining by Eq. (4.22) acts now in the 3N space and G_0 is the free 3N propagator. For the 3N bound states, the energy argument of G_0 plays the role of the binding energy.

The transition amplitude U for the elastic Nd scattering is calculated prior to computing 3N scattering observables. Its matrix elements between the initial Nd $|\phi\rangle$ and final Nd $|\phi'\rangle$ scattering states, neglecting 3NF, are given by [2]

$$\langle\phi'|U|\phi\rangle = \left\langle\phi'|PG_0^{-1}|\phi\right\rangle + \langle\phi'|PT|\phi\rangle \ . \tag{4.43}$$

For the deuteron breakup reaction the transition amplitude U_0 fulfils

$$\langle\phi_0'|U_0|\phi\rangle = \langle\phi_0'|(1+P)T|\phi\rangle \ , \tag{4.44}$$

where $|\phi_0'\rangle$ carries the information about the final free three-nucleon breakup channel.

The Faddeev equation for the auxiliary state $T\,|\phi\rangle$ with nucleons interacting via a NN interaction V entering a t-matrix and a 3NF V_{123} expresses as [2]

$$\begin{aligned} T\,|\phi\rangle = {} & tP\,|\phi\rangle + tPG_0T\,|\phi\rangle + (1+tG_0)V_4^{(1)}(1+P)\,|\phi\rangle \\ & + (1+tG_0)V_4^{(1)}(1+P)T\,|\phi\rangle \ , \end{aligned} \tag{4.45}$$

where the initial state $|\phi\rangle = |\varphi_d m_d\rangle\,|\vec{q}_0 m_N\rangle$ is composed of the deuteron wave function $|\varphi_d\rangle$ and a relative momentum eigenstate of the projectile nucleon, $|\vec{q}_0\rangle$, with corresponding the spin quantum numbers m_d and m_N, respectively. This is the key equation for the nucleon-deuteron scattering and also the basis of predictions shown in this thesis. Neglecting the 3NF, Eq. (4.45) reduces to

$$T\,|\phi\rangle = tP\,|\phi\rangle + tPG_0T\,|\phi\rangle \ . \tag{4.46}$$

Now we introduce momentum basis states for the 3N systems. We perform PWD of three-nucleons operators in $|pq\alpha\rangle$ basis

$$\begin{aligned} |pq\alpha\rangle \equiv {} & \left|pq\,(ls)\,j\left(\lambda\frac{1}{2}\right)I\,(jI)\,JM_J\right\rangle \left|\left(t\frac{1}{2}\right)TM_T\right\rangle = \\ & \sum_{m_j} C(jIJ; m_j, M_J - m_j, M_J)\,|p(ls)JM_J\rangle \left|q\left(\lambda\frac{1}{2}\right)IM_J - m_j\right\rangle \\ & \sum_{m_t} C(t\frac{1}{2}T; m_t, M_T - m_t, M_T)\,|tm_t\rangle \left|\frac{1}{2}M_T - m_t\right\rangle \ . \end{aligned} \tag{4.47}$$

Here, l, s, j, and t denotes the orbital angular momentum, total spin, total angular momentum, and total isospin of the 2-3 c.m.s. subsystem, respectively, with $p = |\vec{p}|$ and $q = |\vec{q}|$ being the magnitudes of the Jacobi momenta. Next, the motion of nucleon 1 with respect to 2–3 c.m.s. subsystem is given in terms of the orbital momentum λ coupled with its spin $\frac{1}{2}$ to give the total angular momentum of nucleon 1, I. Further, j is coupled with I to give the total angular momentum of the 3N system, J, with its projection M_J on the quantization axis $\hat{z}$. Finally, T and M_T are the total 3N isospin and its projection. T arises from coupling of 2N isospin t (= 0, 1) and the isospin $\frac{1}{2}$ of the nucleon 1. The $|pq\alpha\rangle$ basis is orthonormalized as

$$\langle p'q'\alpha'|pq\alpha\rangle = \frac{\delta(q'-q)}{qq'}\frac{\delta(p'-p)}{pp'}\delta_{\alpha\alpha'} \ , \tag{4.48}$$

and satisfies conditions of antisymmetrization of 2-3 subsystem by constraint $(-1)^{l+s+t} = -1$. Finally, its normalization is

$$\sum_{\alpha}\int_0^\infty dpp^2\int_0^\infty dqq^2\,|pq\alpha\rangle\,\langle pq\alpha| = \mathbb{1} \ . \tag{4.49}$$

Our first step in solving the Faddeev equation (4.46) is projecting it onto the partial-wave states (4.55) [2, 110]

$$\begin{aligned}\langle pq\alpha|T|\phi\rangle = \langle pq\alpha|tP|\phi\rangle + \sum_{\alpha'}\int_0^\infty dp'p'^2\int_0^\infty dq'q'^2\sum_{\alpha''}\int_0^\infty dp''p''^2\int_0^\infty dq''q''^2 \\ \langle pq\alpha|t|p'q'\alpha'\rangle\,\langle p'q'\alpha'|P|p''q''\alpha''\rangle\,\langle p''q''\alpha''|G_0T|\phi\rangle \ .\end{aligned} \tag{4.50}$$

The t-matrix is diagonal in the quantum numbers of the nucleon 1

$$\begin{aligned}\langle pq\alpha|t(E)|p'q'\alpha'\rangle =& \frac{\delta(q-q')}{qq'}\delta_{\lambda\lambda'}\delta_{ss'}\delta_{tt'}\delta_{jj'}\delta_{II'}\delta_{JJ'}\delta_{m_Jm_{J'}}\delta_{TT'}\delta_{m_Tm_{T'}} \\ & \tilde{t}_{\tilde{\alpha}_2\tilde{\alpha}_2'}\left(p,p',E-\frac{3}{4}\frac{\vec{q}^{\,2}}{m}\right) \ ,\end{aligned} \tag{4.51}$$

where $\tilde{t}$ denotes the NN t-matrix and $\tilde{\alpha}_2$ contains the information about $lsjt$ components.

Assuming that $T = T' = 1/2$, the two-nucleon t-matrix in the two-nucleon subsystem takes the form [114, 115]

$$\left\langle\left(t\frac{1}{2}\right)T|t|\left(t'\frac{1}{2}\right)T'\right\rangle = \delta_{tt'}\delta_{TT'}\delta_{T1/2}\left[\delta_{t0}t_{np}^{t=0}+\delta_{t1}\left(\frac{2}{3}t_{nn}^{t=1}+\frac{1}{3}t_{np}^{t=1}\right)\right] \ . \tag{4.52}$$

For the elastic scattering the isospin $T = \frac{3}{2}$ components are negligible.

Among various expressions for $\langle p'q'\alpha'|P|pq\alpha\rangle$ we use [2]

$$\langle p'q'\alpha'|P|pq\alpha\rangle = \int_{-1}^{1}dx\frac{\delta(p'-\pi_1)}{p'^{l'+2}}\frac{\delta(p-\pi_2)}{p'^{l+2}}G_{\alpha'\alpha}(q'qx) \ , \tag{4.53}$$

where

$$\pi_1 = \sqrt{q^2 + \frac{1}{4}q'^2 qq'x}\ ,\ \pi_2 = \sqrt{q'^2 + \frac{1}{4}q'^2 qq'x}\ , \tag{4.54}$$

and $G_{\alpha'\alpha}(q'qx)$ is a purely geometrical quantity (given explicitly in [2]).

The three-nucleon propagator in partial-wave basis is

$$\langle pq\alpha|G_0|p'q'\alpha'\rangle = \frac{1}{E - \frac{p^2}{m} - \frac{3}{4m}q^2}\frac{\delta(q-q')}{qq'}\frac{\delta(p-p')}{pp'}\delta_{\alpha\alpha'}\ . \tag{4.55}$$

Inserting decompositions (4.50), (4.51), (4.53), and (4.55) and reducing momenta integrations with the help of δ-functions one gets

$$\begin{aligned}\langle pq\alpha|T|\phi\rangle = &\sum_{\alpha'}\int_{-1}^{1} dx \frac{\tilde{t}_{\tilde{\alpha}_2\tilde{\alpha}'_2}(p,\pi_1,E-(3/4)q^2)}{\pi_1^{l'}}\sum_{\alpha''}\delta_{\alpha''\alpha_d}G_{\alpha'\alpha''}(q,q_0,x)\frac{\varphi_{l''}(\pi_2)}{\pi_2^{l''}}C_{\alpha''}^{m_d m_N}\\ &+\sum_{\alpha'}\sum_{\alpha''}\int_0^\infty dq'q'^2\int_{-1}^{1}dx\frac{\tilde{t}_{\tilde{\alpha}_2\tilde{\alpha}'_2}(p,\pi_1,E-(3/4)q^2)}{\pi_1^{l'}}\\ &\times G_{\alpha'\alpha''}(qq'x)\frac{1}{E+i\varepsilon-q^2/m-q'^2/m-qq'x/m}\frac{\langle\pi_2 q'\alpha''|T|\phi\rangle}{\pi_2^{l''}}\ ,\end{aligned} \tag{4.56}$$

where

$$C_{\alpha''}^{m_d m_N} = \sqrt{\frac{2\lambda+1}{4\pi}}C\left(\lambda\frac{1}{2}I,0m_N\right)C\left(1IJ,m_d m_N\right)\ , \tag{4.57}$$

and α_d denotes the set of discrete quantum numbers for the 2N subsystem containing the deuteron quantum numbers $l=0,2$, $s=1$, $j=1$, and $t=0$.

In all my numerical 3N calculations, Eq. (4.46) is solved numerically by generating its Neumann series which is next summed up using the Padè method [2, 110]. The partial wave basis comprising 3N states includes all states with the two-body subsystem total angular momentum $j \leq 5$ and the total 3N angular momentum $J \leq \frac{25}{2}$. This guarantees the convergence of predictions with respect to the total angular momenta. The total number of three-nucleon channels states $|\alpha\rangle$ for given J amounts up to 142. The range and size of grid points representing momenta p and q are adjusted separately for each of the potential models. I use grids of 32 p points in the range 0-40 fm^{-1} and 37 q points in the range 0-25 fm^{-1} both for the chiral SMS force and the OPE-Gaussian potential.

4.3.2 3N scattering observables

Here we give a very brief overview of 3N scattering observables, for more details see Ref. [2]. The 3N scattering processes are characterized by a large set of spin-observables. In addition to the polarized differential cross section and the vector analyzing powers of nucleons, there are also vector and tensor analyzing powers of the deuteron. Further information on the dynamics can be found in the spin transfer and the spin correlation coefficients. In total, there are 55 different observables for elastic scattering. By solving Eqs. (4.56) and (4.43) one find the elastic transition amplitude U. It is directly related to

the physical elastic scattering amplitude taking into account various polarization states

$$M_{ij} \equiv -\frac{2}{3} m (2\pi)^2 \left\langle \phi' | U | \phi \right\rangle = -\frac{2}{3} m (2\pi)^2 \left\langle \phi'_j | U | \phi_i \right\rangle \ , \tag{4.58}$$

where i, j denote the initial and final spin states, respectively. From M_{ij} any elastic 3N observable can be computed.

For example, the polarized differential cross section for the elastic Nd scattering in the c.m.s. equals

$$\frac{d\sigma}{d\Omega} = |M_{m'_d m'_N m_d m_N}(\vec{q}', \vec{q}_0)|^2 \ , \tag{4.59}$$

where $\vec{q}_0$ is the relative momentum of the incident nucleon with respect to the deuteron, and $\vec{q}'$ describes the same momentum in the final state. A more general representation for the spin-averaged (unpolarized) differential cross section is given by

$$\frac{d\sigma}{d\Omega} \equiv I_0 = \frac{1}{6} \mathrm{Tr}(M M^\dagger) \ , \tag{4.60}$$

with the trace taken over spin states.

In case of the deuteron breakup, the five-fold differential cross section in the c.m.s. is given as

$$\frac{d^5\sigma}{d\hat{p} d\hat{q} dq} = \frac{(2\pi)^4 m^2}{3 q_0} p q^2 | \left\langle \phi_0 | U_0 | \phi \right\rangle |^2 \ . \tag{4.61}$$

In practice, $\frac{d^5\sigma}{d\hat{p} d\hat{q} dq}$ is expressed as a function of laboratory scattering angles of two nucleons and energy of one of the nucleons, $\frac{d^5\sigma}{d\Omega_1 d\Omega_2 dE}$, or the arc-length of the S-curve, $\frac{d^5\sigma}{d\Omega_1 d\Omega_2 dS}$, see Ref. [2]. In principle, this is also valid for 3N breakup polarization observables.

The same representation allows to define the spin observables [2]. The initial state polarization of the nucleon leads to the definition of the nucleon analyzing powers

$$A_k(N) \equiv \frac{\mathrm{Tr}(M \sigma_k M^\dagger)}{\mathrm{Tr}(M M^\dagger)} \ . \tag{4.62}$$

Using the common convention to choose the scattering plane as the $x - z$ plane and the y axis pointing to the direction $\vec{k}_{in} \times \vec{k}_{out}$, where $\vec{k}_{in}$ and $\vec{k}_{out}$ are the momenta of the incoming and outgoing nucleons, respectively, results in a non-zero nucleon vector analyzing power $A_y(N)$, while $A_x(N) = A_z(N) = 0$.

The deuteron vector and the tensor polarizations of the deuteron in the initial state lead to the vector A_i and the tensor A_{jk} deuteron analyzing powers, respectively,

$$A_i = \frac{\mathrm{Tr}(M \mathcal{P}_i M^\dagger)}{M M^\dagger} \ , \ A_{jk} = \frac{\mathrm{Tr}(M \mathcal{P}_{jk} M^\dagger)}{M M^\dagger} \ , \tag{4.63}$$

where $\mathcal{P}_i$ is the initial polarization vector and $\mathcal{P}_{jk}$ is the initial polarization tensor. Parity conservation reduces the number of observables. Conventionally, one introduces analyzing powers iT_{11} and T_{ij} defined as

$$\mathrm{iT}_{11} = \frac{\sqrt{3}}{2} \mathrm{A_y} \ , \ \mathrm{T}_{20} = \frac{1}{\sqrt{2}} \mathrm{A_{zz}} \ , \ \mathrm{T}_{21} = -\frac{1}{\sqrt{3}} \mathrm{A_{xz}} \ , \ \mathrm{T}_{22} = \frac{1}{2\sqrt{3}} (\mathrm{A_{xx}} - \mathrm{A_{yy}}) \ . \tag{4.64}$$

When, both the incident nucleon and the deuteron are polarized in the initial state

various spin correlation coefficients $C_{j,k}$ and $C_{jk,i}$ can be defined. In the case when one particle is polarized in the initial state and one in the final state we deal with the spin transfer coefficients $K_k^{l'}$ and $K_k^{li'}$.

All those above-mentioned quantities depend on the scattering angle and reaction energy. Extending the above definitions one can define the spin observables in the deuteron breakup process for which the number of 3N observables is greater than for the elastic scattering.

Chapter 5

Theoretical uncertainties for the elastic and inelastic Nd scattering observables

In this Chapter I present predictions obtained with the chiral SMS interaction employing the regulator $\Lambda = 450$ MeV at different orders of the chiral expansion and with the OPE-Gaussian potential for observables in the elastic neutron-deuteron (nd) scattering at incoming neutron laboratory energies $E_{\rm lab} = 13, 65, 135$ and 200 MeV. In order to draw reliable conclusions based on the comparison of theoretical predictions and data, an estimation of theoretical uncertainties is necessary. One type of such uncertainties are statistical errors. I compare them with others, such as truncation errors based on the EKM approach or on the Bayesian approach. In some of the following figures, theoretical predictions are also compared with the proton-deuteron cross section data. In these configurations small effects of the Coulomb force can be neglected. Significant effects of the Coulomb force are visible only at lower energies and at forward and backward scattering angles for the differential cross section [116].

5.1 Results for the elastic Nd scattering

I start presenting my results with the differential cross section $d\sigma/d\Omega$ obtained with the central values of the chiral N^{2}LO, N^{4}LO and N^{4}LO$^+$ ($\Lambda = 450$ MeV) SMS potential parameters [9]. For the sake of comparison I also show in Figure 5.1 predictions obtained using the OPE-Gaussian [10] and the AV18 potentials [52]. At $E_{\rm lab} = 13$ MeV, the predictions based on the chiral SMS potentials practically do not differ from each other and difference between them remains below 1% at all scattering angles. At $E_{\rm lab} = 65$ MeV, the difference in predictions based on the chiral potentials N^{4}LO and N^{2}LO SMS forces reaches 5.3%, but between N^{4}LO SMS and OPE-Gaussian potentials is slightly above 10% in the region around the minimum of the cross section. At $E_{\rm lab} = 135$ MeV the difference in predictions between N^{4}LO SMS and OPE-Gaussian potentials in the same region of angles reaches approximately 26%, between N^{4}LO and N^{2}LO SMS potentials is approximately 15.4% at scattering angles $\theta_{c.m.} \in [60^\circ, 100^\circ]$. At $E_{\rm lab} = 200$ MeV the difference in predictions between N^{4}LO and N^{2}LO SMS potentials is 11.5%, but between N^{4}LO SMS and OPE-Gaussian potential amounts $\approx 24\%$ at the minimum of differential cross section for both pairs of potentials. The predictions based on the OPE-Gaussian force are in agreement with the predictions based on the AV18 potential. Only small ($\approx 3.9\%$ at $E_{\rm lab} = 13$ MeV and $\approx 3.5\%$ at $E_{\rm lab} = 200$ MeV) differences are seen in the minimum of the cross section. The discrepancy with data around the minimum of the

cross section is due to neglecting 3N forces contributions at all presented here energies.

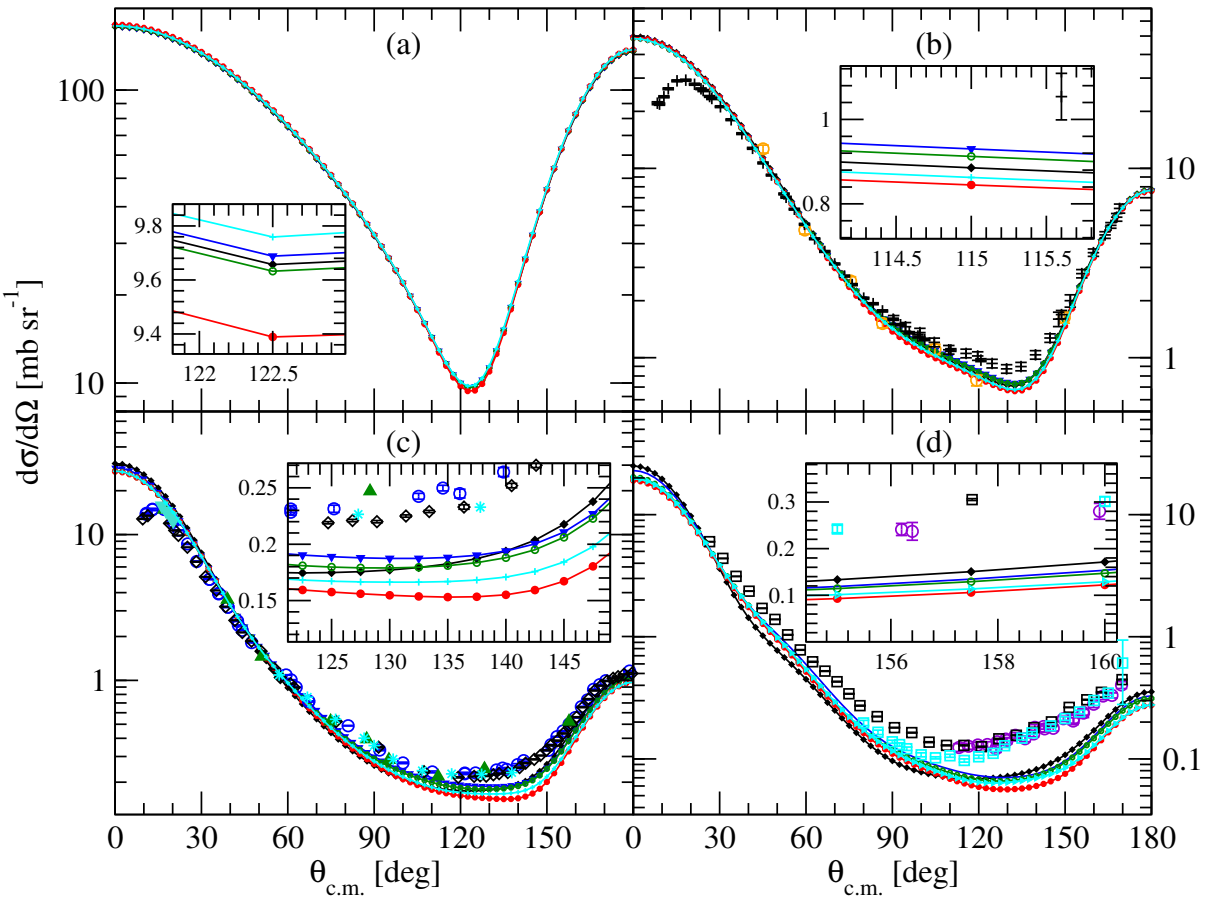

Figure 5.1: The differential cross section $d\sigma/d\Omega$ for the elastic nd scattering process at the incoming neutron laboratory energy (a) $E_{\rm lab}$ = 13 MeV, (b) $E_{\rm lab}$ = 65 MeV, (c) $E_{\rm lab}$ = 135 MeV and (d) $E_{\rm lab}$ = 200 MeV as a function of the c.m. scattering angle $\theta_{c.m.}$. The solid black line with diamonds, the solid blue line with triangles down, the solid green line with open circles and the solid red line correspond to the central values of the chiral N^{2}LO, N^{4}LO, N^{4}LO$^+$ (Λ = 450 MeV) SMS, and the OPE-Gaussian potential parameters, respectively, and the cyan line with open squares represents predictions based on the AV18 force. The experimental data are in: (b) from Ref. [117] (*pd* black pluses) and [118] (*nd* open orange circles), (c) from Ref. [119] (*dp* blue open circles), Ref. [120] (*dp* black open diamonds), Ref. [85] (*dp* cyan stars) and Ref. [121] (*pd* green triangles up) and in (d) from Ref. [122] (*pd* black open squares, $E_{\rm lab}$ = 190 MeV), Ref. [123] (*pd* cyan open squares, $E_{\rm lab}$ = 198 MeV) and Ref. [124] (*dp* violet open circles, $E_{\rm lab}$ = 181 MeV).

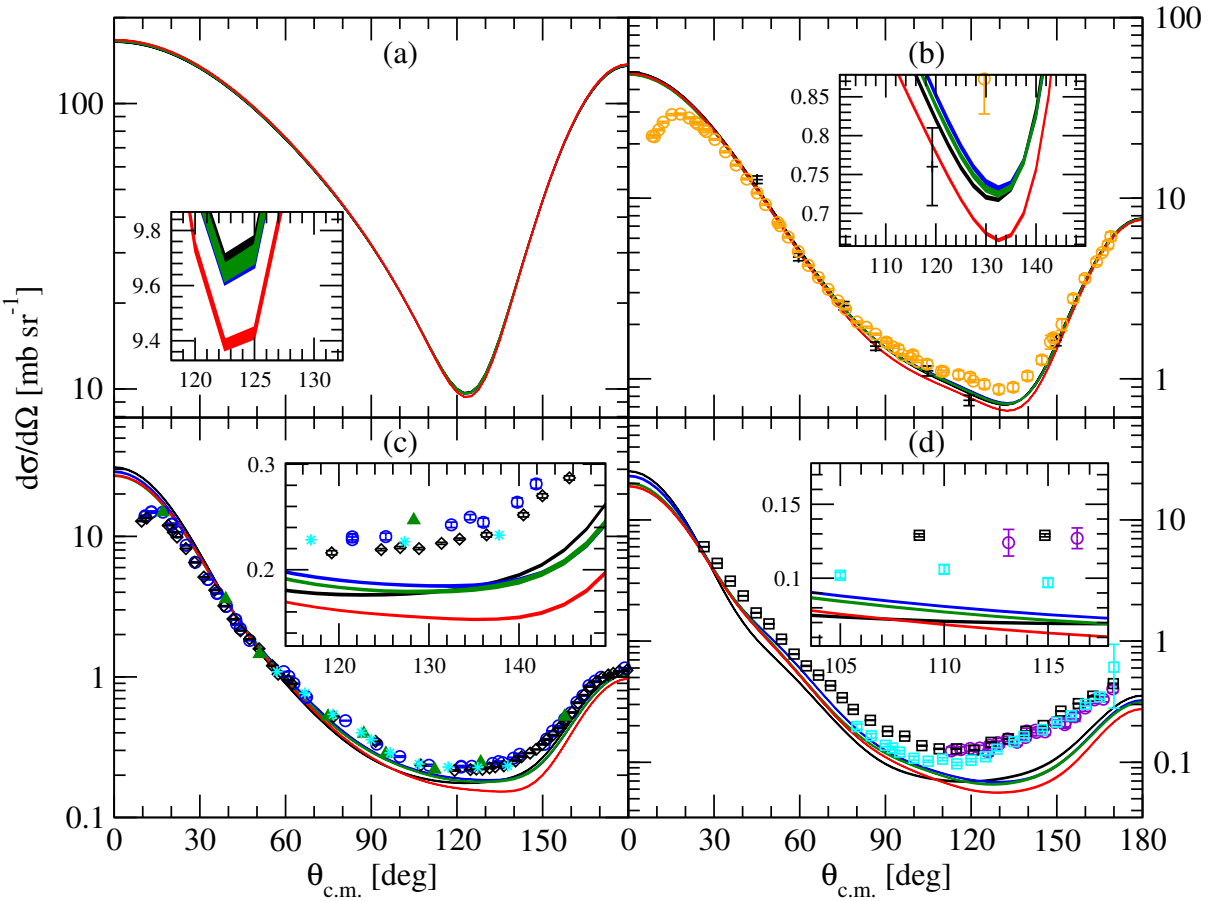

Figure 5.2: The differential cross section $d\sigma/d\Omega$ for the elastic nd scattering process at the incoming neutron laboratory energy (a) $E_{\rm lab}$ = 13 MeV, (b) $E_{\rm lab}$ = 65 MeV, (c) $E_{\rm lab}$ = 135 MeV and (d) $E_{\rm lab}$ = 200 MeV as a function of the c.m. scattering angle $\theta_{c.m.}$. The black, blue, green and red bands represent statistical uncertainties based on the chiral N^{2}LO, N^{4}LO, N^{4}LO$^+$ (Λ = 450 MeV) SMS forces and the OPE-Gaussian potential, respectively. The experimental data are in: (b) from Ref. [117] (*pd* black pluses) and [118] (*nd* open orange circles), (c) from Ref. [119] (*dp* blue open circles), Ref. [120] (*dp* black open diamonds), Ref. [85] (*dp* cyan stars) and Ref. [121] (*pd* green triangles up) and in (d) from Ref. [122] (*pd* black open squares, $E_{\rm lab}$ = 190 MeV), Ref. [123] (*pd* cyan open squares, $E_{\rm lab}$ = 198 MeV) and Ref. [124] (*dp* violet open circles, $E_{\rm lab}$ = 181 MeV). Note that the statistical uncertainties are so small that the width of the bands cannot be seen at the scale of the figure.

In Figure 5.2 I show estimation of statistical uncertainties for the elastic scattering differential cross section data description obtained with the aforementioned chiral SMS forces and the OPE-Gaussian potential. Those predictions are represented by bands which cover a range of $\Delta_{68\%}$ estimator of the statistical uncertainty. At the lowest energy, $E_{\rm lab}$ = 13 MeV, the maximum of the relative difference [1] among predictions obtained with the chiral potentials is small ($\approx$ 1.2% around the minimum of the cross section between the chiral N^{2}LO and N^{4}LO SMS results) and even smaller for other pairs of chiral orders. The maximum of relative difference between the widths of the N^{4}LO SMS and the OPE-Gaussian bands of predictions at $E_{\rm lab}$ = 13 MeV reaches 3.2% at scattering

[1] $\left|\frac{1}{2}\Delta^i_{68\%} - \frac{1}{2}\Delta^j_{68\%}\right| / (\frac{1}{2}(\left|\frac{1}{2}\Delta^i_{68\%}\right| + \left|\frac{1}{2}\Delta^j_{68\%}\right|))$, where the indices i and j correspond to the selected potentials the predictions of which are compared.

angle $\theta_{c.m.} = 127.5°$, while the statistical error of the N^{4}LO results is $\approx 2.5\%$. The narrowness of bands clearly shows that at this energy the uncertainty of the nd elastic cross section arising from the uncertainty of the NN potential parameters is very small for all scattering angles. With increasing energy spreads of the different order of chiral NN potential results become larger, however, the values of statistical uncertainties remain small. At $E_{\rm lab} = 200$ MeV there is a significant increase of distance between the N^{4}LO SMS predictions with respect to the OPE-Gaussian results up to 24% at $\theta_{c.m.} = 155°$, but statistical errors remain below 1% for both potentials at the same scattering angle. The difference between the N^{2}LO and the N^{4}LO SMS predictions is 16% at the same angle, but for example at $\theta_{c.m.} = 80°$ it amounts 25%.

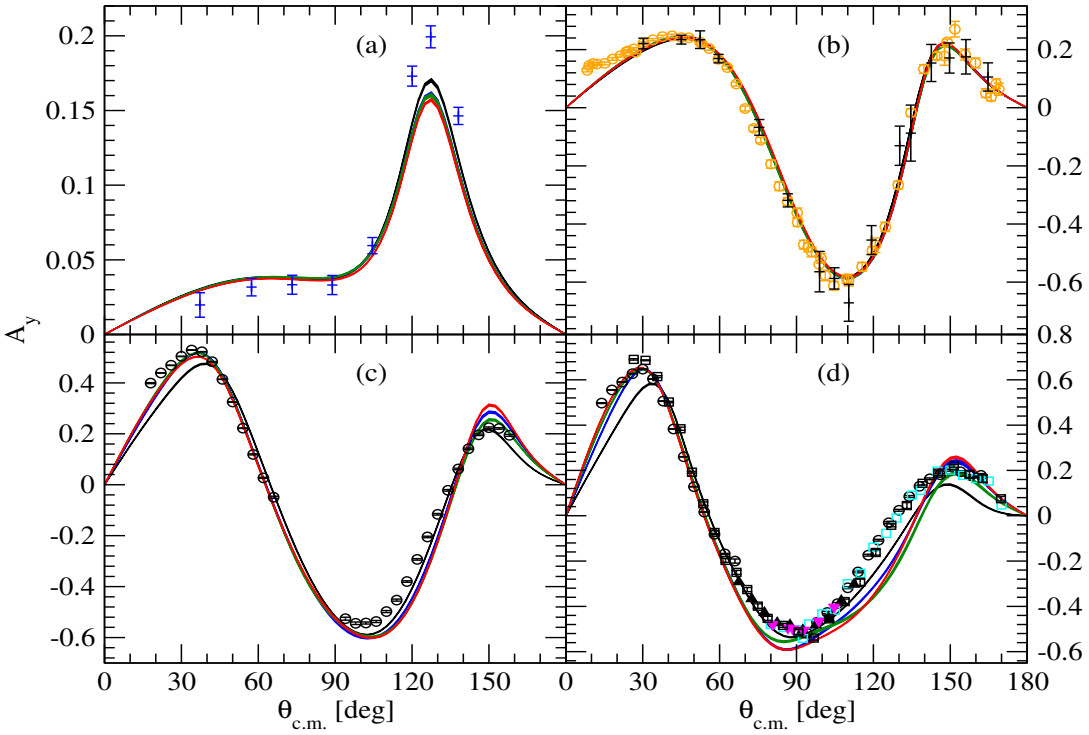

Figure 5.3: The nucleon vector analyzing power A_y for the elastic nd scattering process at the same energies as used in Figure 5.2 shown as a function of the c.m. scattering angle $\theta_{c.m.}$. For description of curves and bands see Figure 5.2. The data are in: (a) from Ref. [125] (nd blue pluses), (b) from Ref. [118] (nd black pluses), Ref. [117] (pd orange open circles), (c) from Ref. [126] (pd black open circles) and (d) Ref. [126] (pd black open circles, $E_{\rm lab} = 200$ MeV), Ref. [122] (pd black open squares, $E_{\rm lab} = 190$ MeV), Ref. [123] (pd cyan open squares, $E_{\rm lab} = 198$ MeV), Ref. [127] (pd black triangles up, $E_{\rm lab} = 197$ MeV) and Ref. [128] (pd magenta triangles down, $E_{\rm lab} = 200$ MeV).

In Figure 5.3 the neutron vector analyzing power A_y is shown. Although the magnitudes of the statistical uncertainties grow slightly with increasing scattering energy, they remain small enough to conclude that they are negligible compared to the spread of the predictions obtained using the different potentials. At $E_{\rm lab} = 13$ MeV the maximum of relative difference between predictions based on the chiral N^{4}LO SMS force (the maximum of $\frac{1}{2}\Delta_{68\%} \lesssim 0.08\%$) and the ones obtained with the OPE-Gaussian potential (the maximum of $\frac{1}{2}\Delta_{68\%} \lesssim 0.06\%$) reaches a maximum of 7.56% and between the N^{2}LO and the N^{4}LO is approximately 8% around the maximum of A_y. The comparison of the theoretical predictions with data reveals a big gap. Thus, the nature of the A_y-puzzle

remains unsolved at this energy. In the case of $E_{\rm lab} = 200$ MeV the maximum spread between the N^{4}LO and the OPE-Gaussian predictions is 21% at $\theta_{c.m.} = 137.5°$, while the statistical error of the N^{4}LO (OPE-Gaussian) is 0.52% (0.32%) at the same angle. It has also to be noted that the dispersion between N^{4}LO and N^{4}LO$^+$ is approximately 2% (≈ 2.6 at backward angles) at $E_{\rm lab} = 13$ MeV near the maximum magnitude of A_y, but at $E = 200$ MeV is quite big difference around 5.5% in the minimum of A_y (at $\theta_{c.m.} = 137.5$).

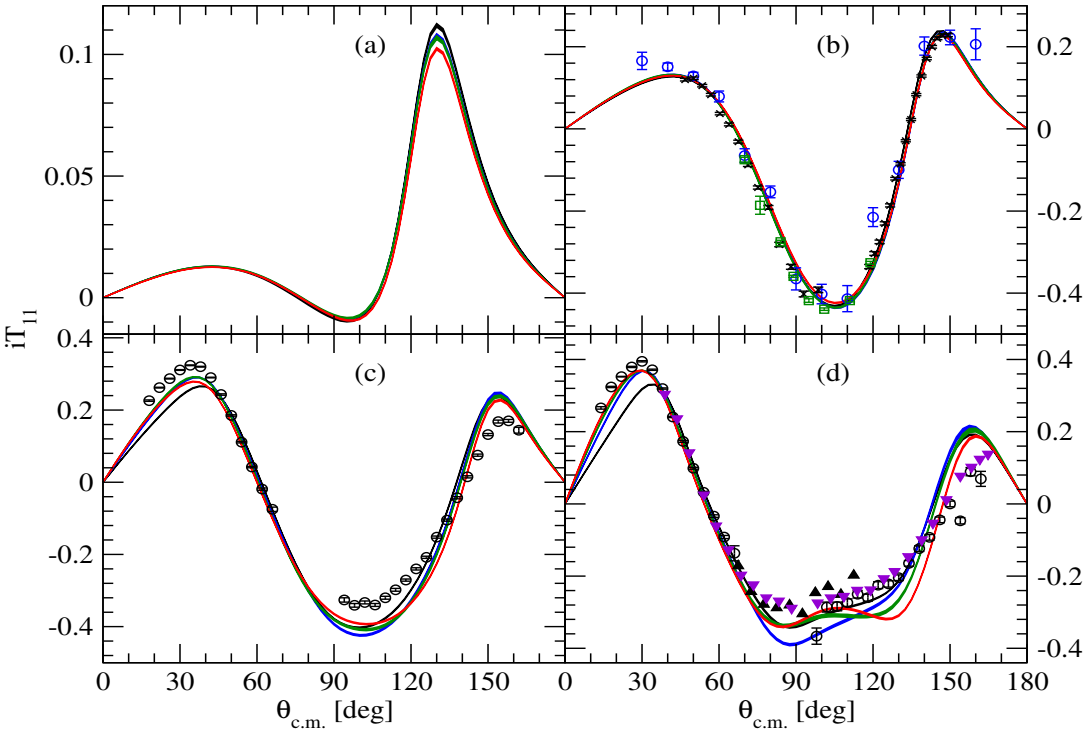

Figure 5.4: The deuteron vector analyzing power iT$_{11}$ for the elastic nd scattering process at the same energies as used in Figure 5.2 as a function of the c.m. scattering angle $\theta_{\rm c.m.}$. Description of curves and bands is as in Figure 5.2. The data are in: (b) Ref. [129] (pd blue open circles), Ref. [130] (dp black $\times$'s, $E_{\rm lab} = 130$ MeV) and Ref. [131] (dp green open squares, $E_{\rm lab} = 130$ MeV), (c) from Ref. [126] (pd black open circles) and (d) Ref. [126] (pd black open circles, $E_{\rm lab} = 200$ MeV), Ref. [127] (pd black triangles up, $E_{\rm lab} = 197$ MeV) and Ref. [7] (dp violet triangles up, $E_{\rm lab} = 186.6$ MeV).

The behavior of statistical uncertainties for the deuteron vector analyzing power iT$_{11}$, presented in Figure 5.4, is very similar to that for A_y. It is clearly seen that all potentials give practically the same predictions, but small diverges from each other are observed around the maximum at $E_{\rm lab} = 13$ MeV. For example, the relative difference between the N^{4}LO and the OPE-Gaussian predictions reaches $\approx 6.7\%$ at the maximum of iT$_{11}$. At $E = 200$ MeV there is a huge spread between all results, for example the N^{4}LO band differs from the OPE-Gaussian ones by factor two at $\theta_{c.m.} = 55°$ and at $\theta_{c.m.} = 145°$, while the corresponding static errors are not exceed even 0.5% for both potentials. The same behavior is for relative differences between the N^{4}LO and the N^{4}LO$^+$ results.

The deuteron analyzing powers T$_{20}$, T$_{21}$ and T$_{22}$ are presented in Figures 5.5, 5.6 and 5.7, respectively. At $E_{\rm lab} = 135$ and 200 MeV for T$_{20}$ and T$_{22}$ it is clearly seen that predictions based on the OPE-Gaussian potential strongly deviate from results obtained with the chiral SMS forces. As for T$_{21}$ the chiral N^{2}LO SMS predictions differ from

remaining results. The resulting statistical uncertainties of the tensor analyzing powers do not exceed even 1% and this is true for all energies and potentials.

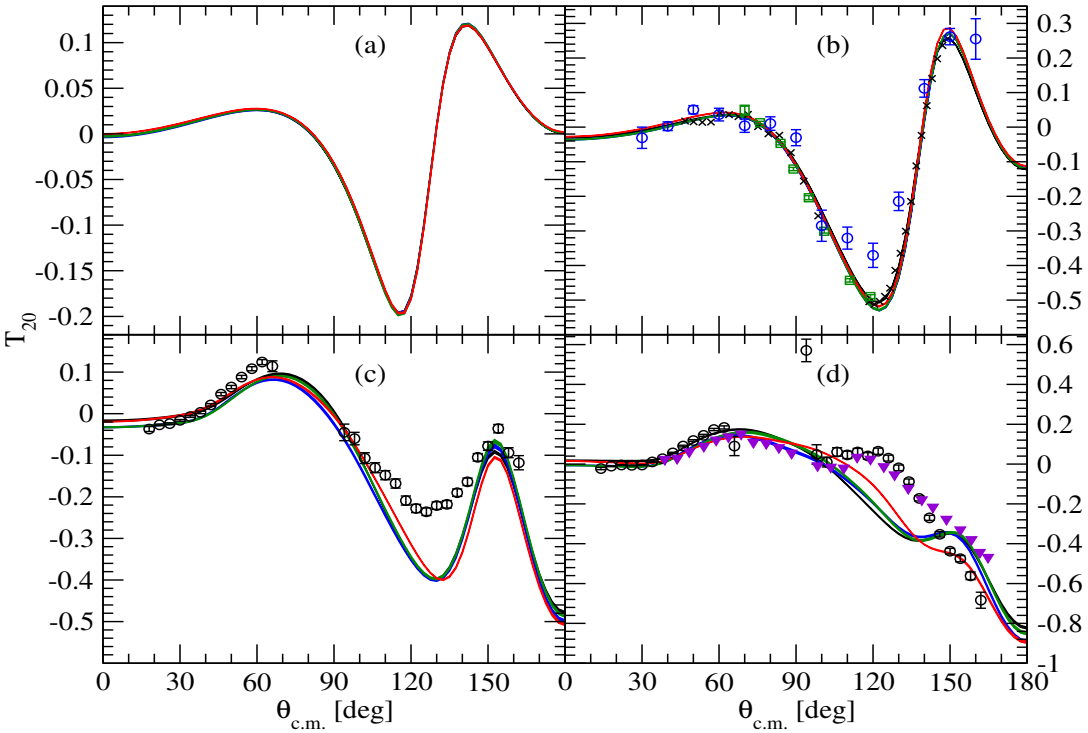

Figure 5.5: The deuteron tensor analyzing power T_{20} for the elastic nd scattering process at the same energies as used in Figure 5.2 as a function of the c.m. scattering angle $\theta_{\text{c.m.}}$. Description of curves and bands is as in Figure 5.2. The data are in: (b) Ref. [130] (dp black $\times$'s, $E_{\text{lab}} = 130$ MeV), Ref. [129] (dp blue open circles, $E_{\text{lab}} = 131$ MeV), and Ref. [131] (green open squares, $E_{\text{lab}} = 130$ MeV), (c) from Ref. [126] (pd black open circles) and (d) Ref. [126] (pd black open circles, $E_{\text{lab}} = 200$ MeV) and Ref. [7] (dp violet triangles up, $E_{\text{lab}} = 186.6$ MeV).

Now we turn to the description of the spin correlation coefficients. I have chosen a several spin correlation coefficients to demonstrate that predictions based on various potentials differ strongly between each other, especially for high energies, see Figures 5.8 – 5.17. For some observables there are differences in predictions even for lower energies. It should be noted that the spreads of the resulting statistical uncertainties for each potential are still smaller than uncertainties of experimental results. This is similar to results for the differential cross section and polarization observables discussed above.

In Figure 5.12 the spin correlation coefficient C_{zz} is shown as an example for the case when resulting statistical error is smaller than the dependence on interaction models both at medium and high energies. All predictions are almost converged at $E_{\text{lab}} = 13$ MeV. At $E_{\text{lab}} = 65$ MeV the OPE-Gaussian band deviates from remaining predictions, for example, its maximum difference with the N^{4}LO SMS predictions is 13% at $\theta_{c.m.} = 145°$. At higher energies, the N^{2}LO order is not sufficient, the spread of its predictions is too large when comparing the results obtained using other potentials, especially at $\theta_{c.m.} < 60°$ for $E_{\text{lab}} = 135$ MeV and $\theta_{c.m.} < 45°$ for $E_{\text{lab}} = 200$ MeV. The relative spread of the N^{4}LO and the N^{4}LO$^+$ SMS results grows with energy, and while at lowest energy $E_{\text{lab}} = 13$ MeV it is negligible, at $E_{\text{lab}} = 200$ MeV its size is noticeable. The statistical uncertainties $\frac{1}{2}\Delta_{68\%} < 0.5\%$ for all potentials.

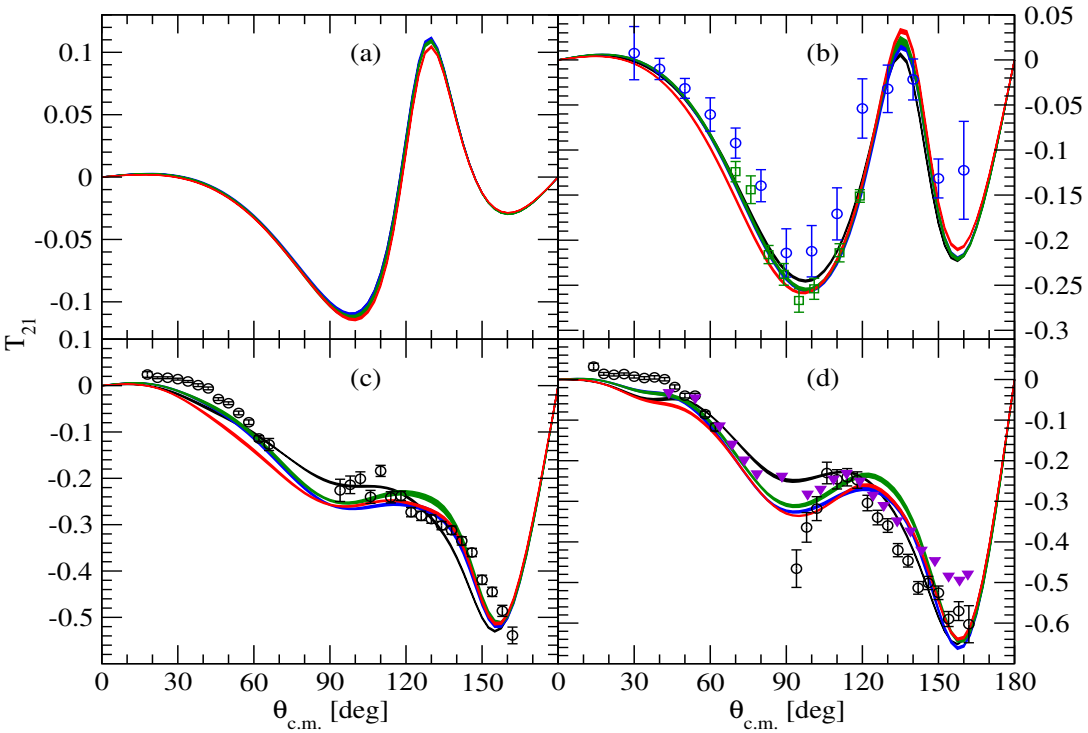

Figure 5.6: The deuteron tensor analyzing power T_{21} for the elastic nd scattering process at the same energies as used in Figure 5.2 as a function of the c.m. scattering angle $\theta_{\text{c.m.}}$. Description of curves and bands is as in Figure 5.2. The data are in: (b) Ref. [129] (dp blue open circles, $E_{\text{lab}} = 131$ MeV) and Ref. [131] (green open squares, $E_{\text{lab}} = 130$ MeV), (c) from Ref. [126] (pd black open circles) and (d) Ref. [126] (pd black open circles, $E_{\text{lab}} = 200$ MeV) and Ref. [7] (dp violet triangles up, $E_{\text{lab}} = 186.6$ MeV).

Next, I would like to give a brief description of predictions for spin transfer coefficients. Four nucleon to nucleon spin transfer coefficients $K_x^{x'}(n)$, $K_y^{y'}(n)$, $K_z^{z'}(n)$ and $K_z^{x}(n)$ are shown in Figures 5.18 – 5.22, respectively. Predictions for $K_y^{y'}(n)$, presented in Figure 5.19, are more interesting than others. It is clearly seen how the OPE-Gaussian results do not coincidence with the chiral SMS predictions at $E_{\text{lab}} = 135$ (200) MeV. The relative differences between the two predictions, the OPE-Gaussian and the N^{4}LO SMS, amount approximately 8.3% (16%) at $\theta_{c.m.} = 137.5°$, but at the same time the statistical errors of the OPE-Gaussian and the N^{4}LO SMS are 0.24% and 0.27% (0.32% and 0.26%), respectively.

Figures 5.23 – 5.25 demonstrate the neutron-deuteron vector spin transfer coefficients $K_x^{x'}(d), K_z^{x'}(d)$, and $K_y^{y'}(d)$. Again, let us consider in detail one example, namely the $K_z^{x'}(d)$. As in all previous examples there are the overall agreements between all bands at $E_{\text{lab}} = 13$ and 65 MeV. At $E_{\text{lab}} = 135$ (200) MeV a spread of the OPE-Gaussian predictions with respect to N^{4}LO SMS band increases to 14% (21%) around the minimum and 35% (18%) at the maximum of $K_z^{x'}(d)$. The statistical uncertainties of theoretical predictions remain smaller than 0.5%. Using the N^{2}LO SMS potential leads to predictions not consistent with others results when describing the dependence of $K_y^{y'}(d)$ at higher energies.

Finally, the neutron-deuteron tensor spin transfer coefficients: $K_z^{y'z'}(d)$, $K_z^{x'y'}(d)$, $K_x^{x'y'}(d)$, $K_x^{y'z'}(d)$, and $K_y^{x'x'} - K_y^{y'y'}(d)$ are presented in Figures 5.26 – 5.30. Here the uncertainties remain negligible at all energies. For example, the statistical errors of the

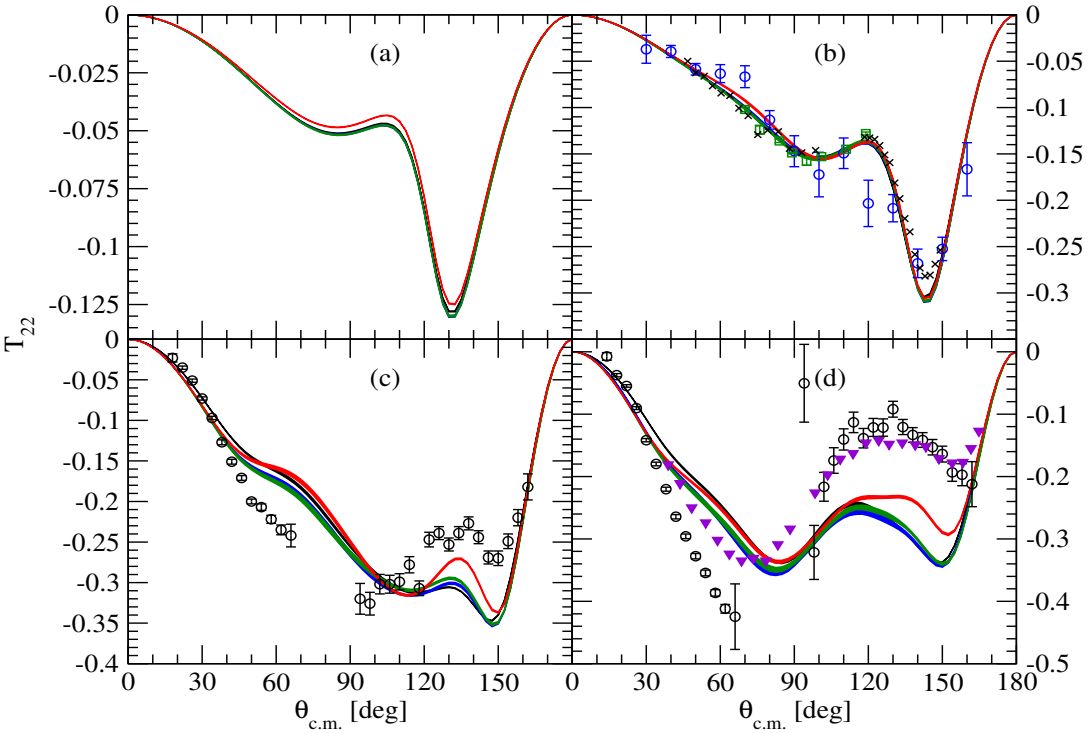

Figure 5.7: The deuteron tensor analyzing power T_{22} for the elastic nd scattering process at the same energies as used in Figure 5.2 as a function of the c.m. scattering angle $\theta_{\rm c.m.}$. Description of curves and bands is as in Figure 5.2. The data are in: (b) Ref. [130] (dp black $\times$'s, $E_{\rm lab} = 130$ MeV), Ref. [129] (dp blue open circles, $E_{\rm lab} = 131$ MeV), and Ref. [131] (green open squares, $E_{\rm lab} = 130$ MeV), (c) from Ref. [126] (pd black open circles) and (d) Ref. [126] (pd black open circles, $E_{\rm lab} = 200$ MeV) and Ref. [7] (dp violet triangles up, $E_{\rm lab} = 186.6$ MeV).

magnitude of these observables do not exceed 0.5% (0.7% in the case of $K_y^{x'x'} - K_y^{y'y'}(d)$). But on the other hand, there are rather strong discrepancies in the results between predictions based on the OPE-Gaussian potential and the chiral SMS forces predictions, especially at high energies. For instance, at $E_{\rm lab} = 135$ MeV (200 MeV) and $\theta_{c.m.} = 135°$ the relative difference for $K_x^{x'y'}(d)$ between the two predictions (the OPE-Gaussian and the N^{4}LO) reaches 70% (93%). Similarly, for $K_x^{y'z'}(d)$ the relative difference between predictions amounts $\approx 64\%$ (52%) at $E_{\rm lab} = 135$ MeV ($E_{\rm lab} = 200$ MeV) and $\theta_{c.m.} = 135°$. There is also a large relative difference between the N^{2}LO SMS and the remaining chiral predictions. Such discrepancies in the results for all 3N observables may be due to the fact that chiral potentials use different LEC values and at higher energies observables become sensitive to new structures in potential arising in higher orders.

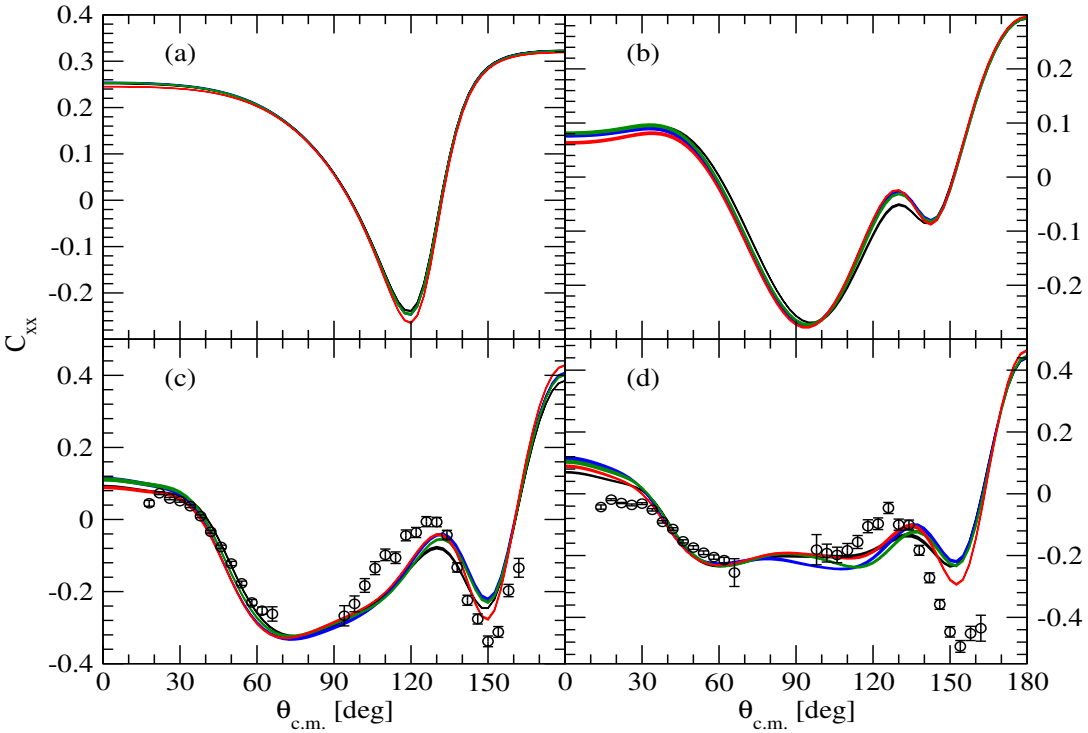

Figure 5.8: The spin correlation coefficient C_{xx} for the elastic nd scattering process at the same energies as used in Figure 5.2 for the elastic nd scattering process as a function of the c.m. scattering angle $\theta_{\rm c.m.}$. Description of curves and bands is as in Figure 5.2. The data are in: (c) from Ref. [126] (pd black open circles) and (d) Ref. [126] (pd black open circles).

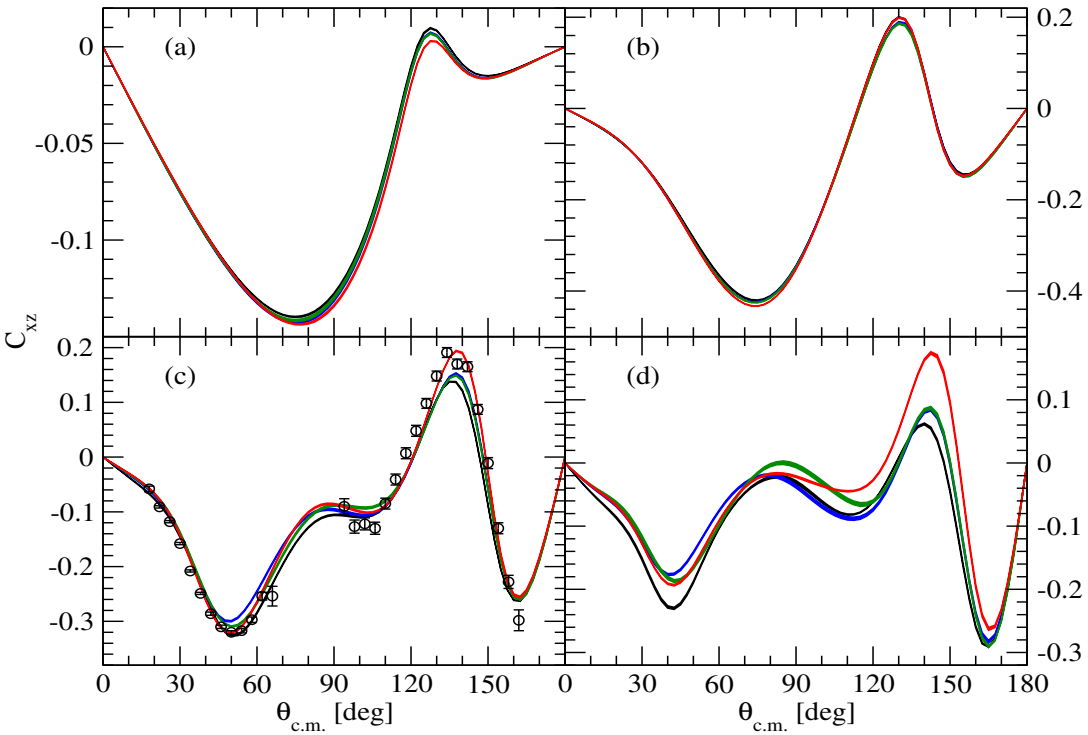

Figure 5.9: The spin correlation coefficient C_{xz} for the elastic nd scattering process at the same energies as used in Figure 5.2 for the elastic nd scattering process as a function of the c.m. scattering angle $\theta_{\rm c.m.}$. Description of curves and bands is as in Figure 5.2. The data are in: (c) from Ref. [126] (pd black open circles).

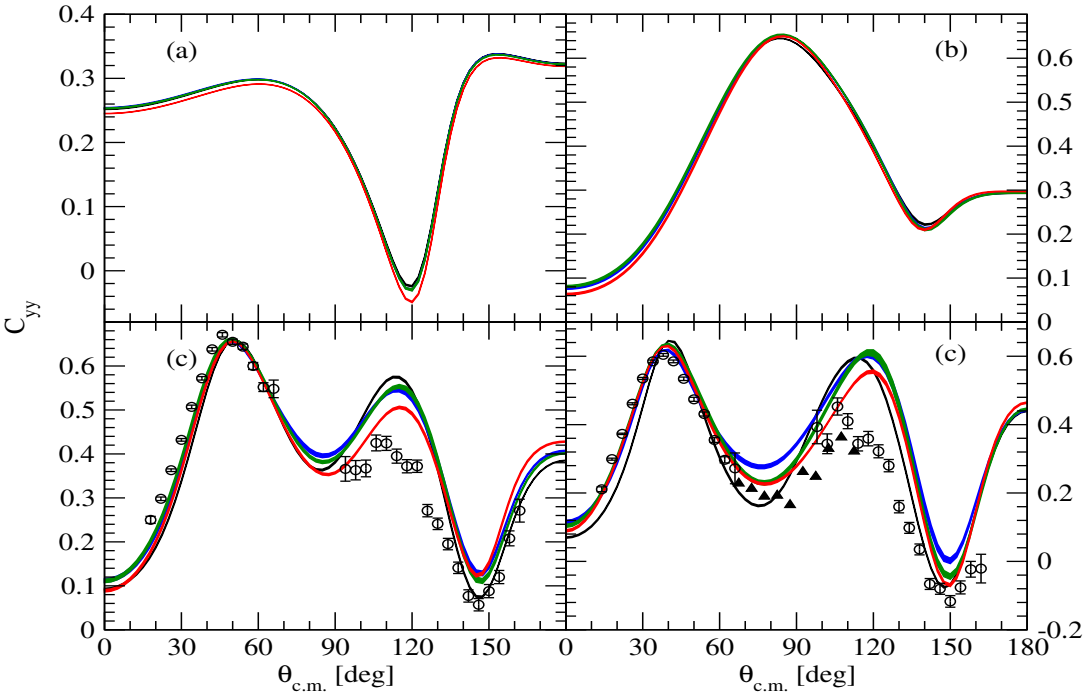

Figure 5.10: The spin correlation coefficient C_{yy} for the elastic nd scattering process at the same energies as used in Figure 5.2 as a function of the c.m. scattering angle $\theta_{\text{c.m.}}$. Description of curves and bands is as in Figure 5.2. The data are in: (c) from Ref. [126] (pd black open circles), and Ref. [127] (pd black triangle up, $E_{\text{lab}} = 197$ MeV) and (d) Ref. [126] (pd black open circles).

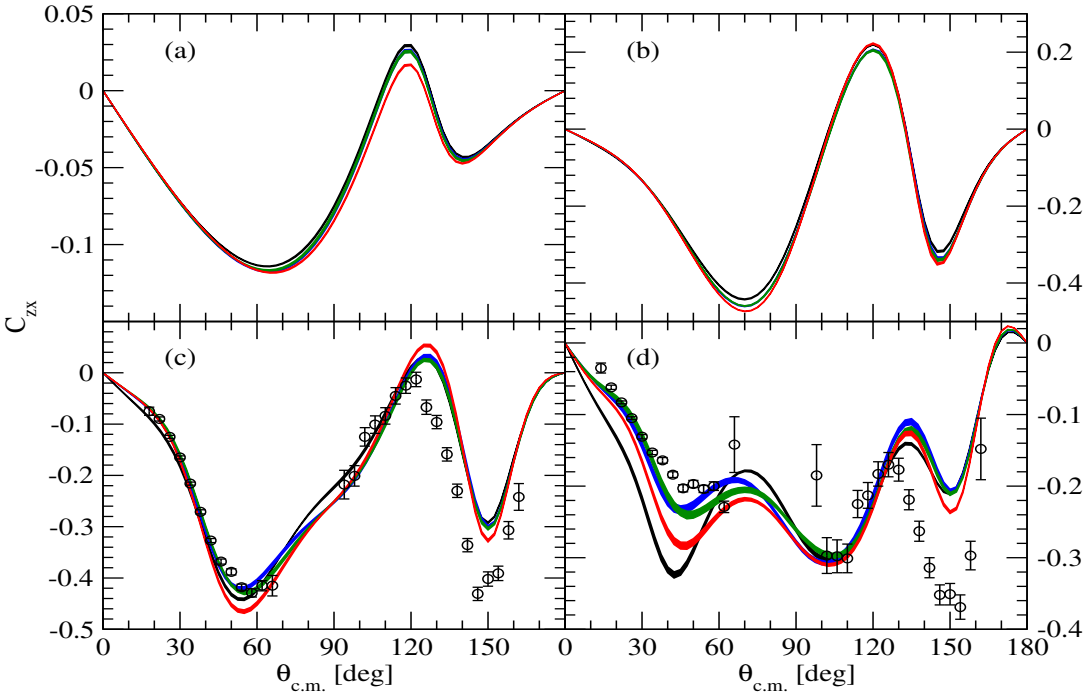

Figure 5.11: The spin correlation coefficient C_{zx} for the elastic nd scattering process at the same energies as used in Figure 5.2 as a function of the c.m. scattering angle $\theta_{\text{c.m.}}$. Description of curves and bands is as in Figure 5.2. The data are in: (c) from Ref. [126] (pd black open circles) and (d) Ref. [126] (pd black open circles).

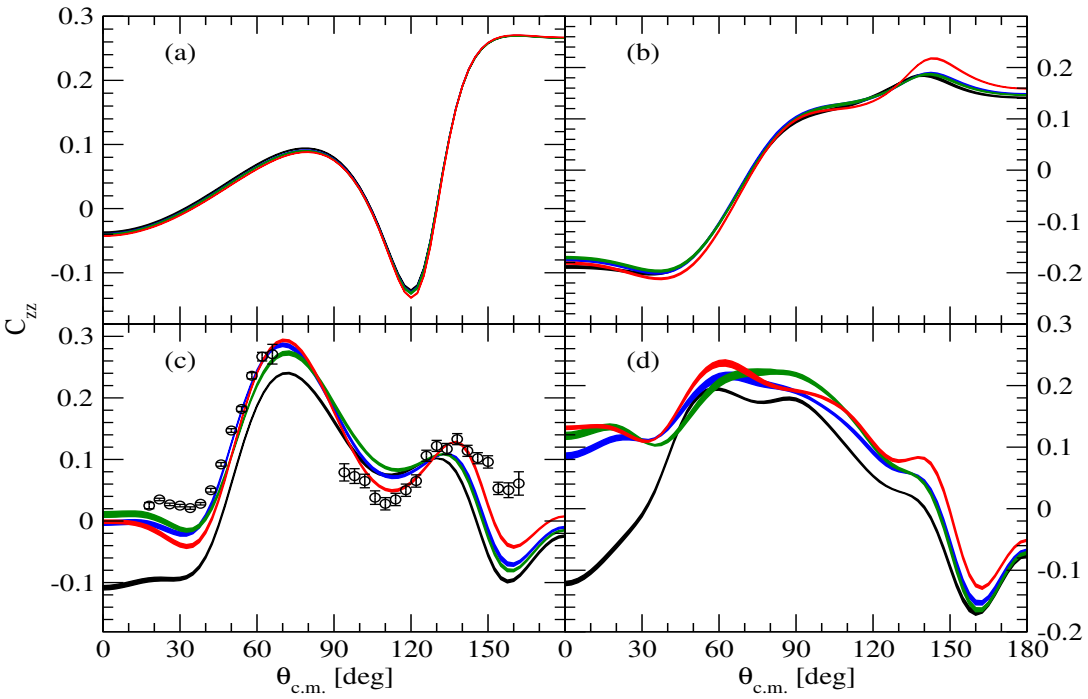

Figure 5.12: The spin correlation coefficient C_{zz} for the elastic nd scattering process at the same energies as used in Figure 5.2 as a function of the c.m. scattering angle $\theta_{\text{c.m.}}$. Description of curves and bands is as in Figure 5.2. The data are in: (c) from Ref. [126] (pd black open circles).

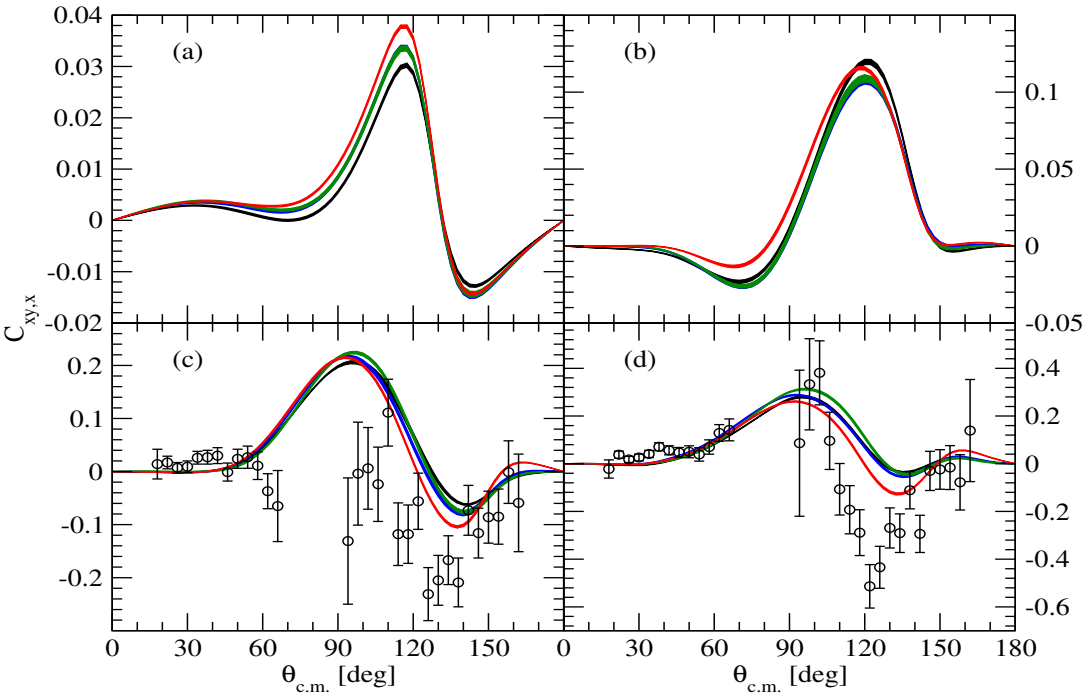

Figure 5.13: The spin correlation coefficient $C_{xy,x}$ for the elastic nd scattering process at the same energies as used in Figure 5.2 as a function of the c.m. scattering angle $\theta_{\text{c.m.}}$. Description of curves and bands is as in Figure 5.2. The data are in: (c) from Ref. [126] (pd black open circles) and (d) Ref. [126] (pd black open circles).

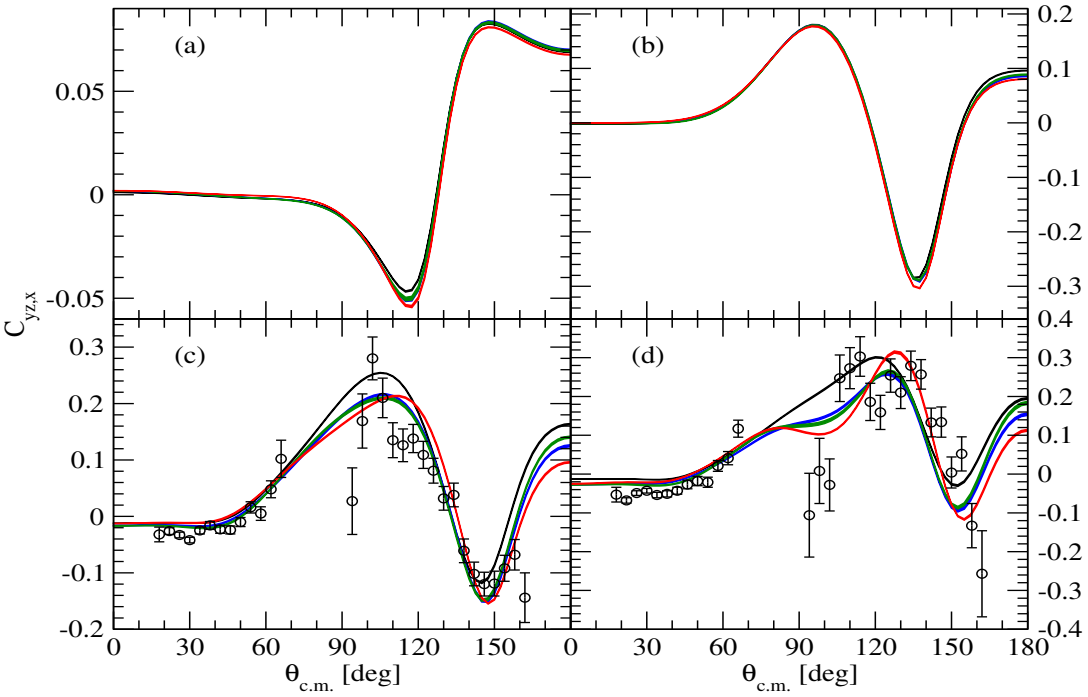

Figure 5.14: The spin correlation coefficient $C_{yz,x}$ for the elastic nd scattering process at the same energies as used in Figure 5.2 as a function of the c.m. scattering angle $\theta_{\text{c.m.}}$. Description of curves and bands is as in Figure 5.2. The data are in: (c) from Ref. [126] (pd black open circles) and (d) Ref. [126] (pd black open circles).

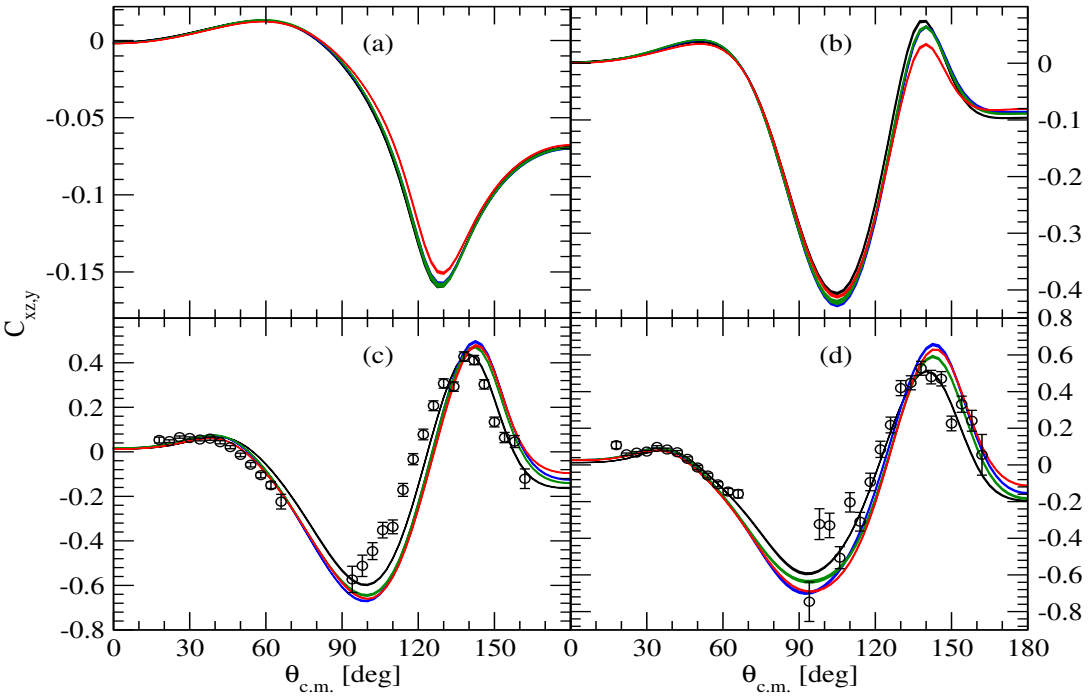

Figure 5.15: The spin correlation coefficient $C_{xz,y}$ for the elastic nd scattering process at the same energies as used in Figure 5.2 as a function of the c.m. scattering angle $\theta_{\text{c.m.}}$. Description of curves and bands is as in Figure 5.2. The data are in: (c) from Ref. [126] (pd black open circles) and (d) Ref. [126] (pd black open circles).

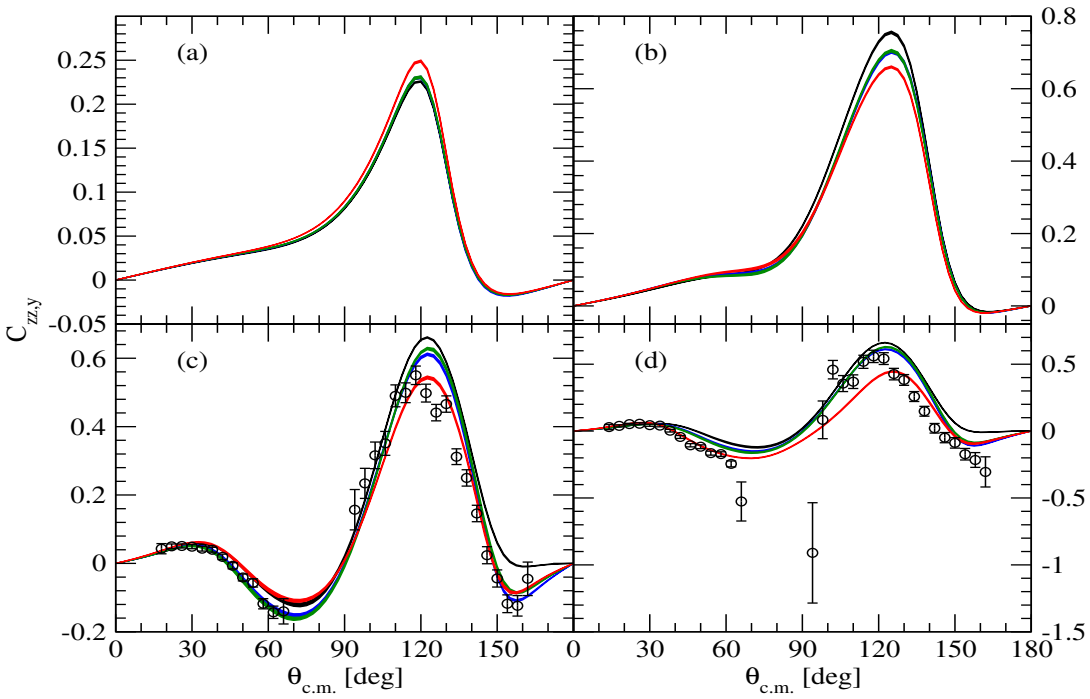

Figure 5.16: The spin correlation coefficient $C_{zz,y}$ for the elastic nd scattering process at the same energies as used in Figure 5.2 as a function of the c.m. scattering angle $\theta_{\text{c.m.}}$. Description of curves and bands is as in Figure 5.2. The data are in: (c) from Ref. [126] (pd black open circles) and (d) Ref. [126] (pd black open circles).

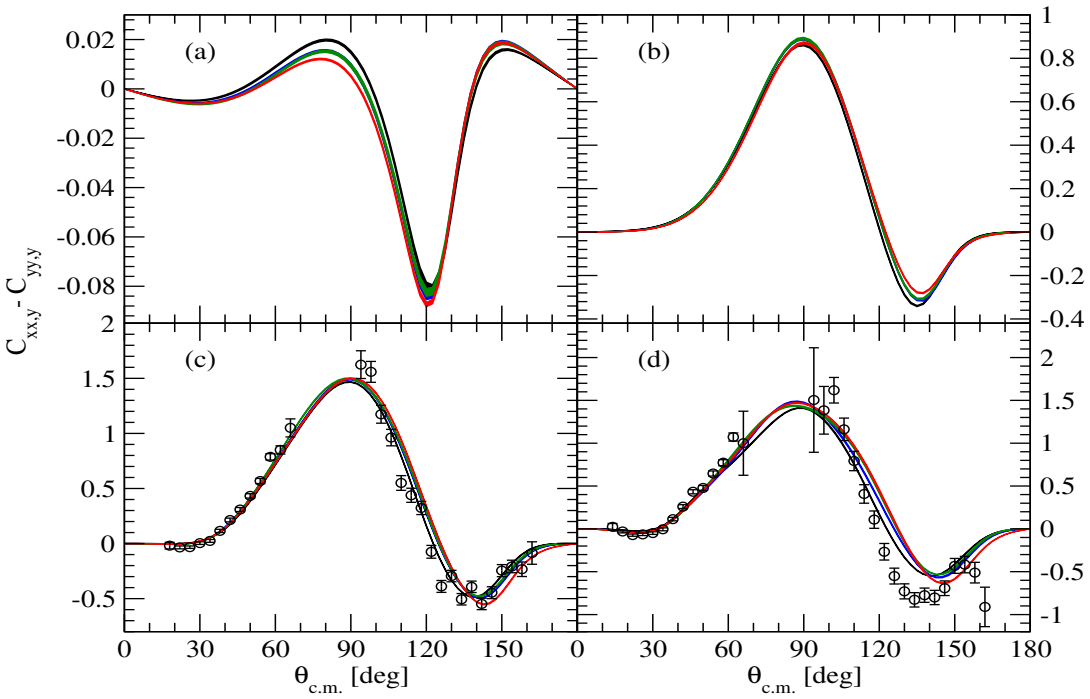

Figure 5.17: The spin correlation coefficient $C_{xx,y} - C_{yy,y}$ for the elastic nd scattering process at the same energies as used in Figure 5.2 as a function of the c.m. scattering angle $\theta_{\text{c.m.}}$. Description of curves and bands is as in Figure 5.2. The data are in: (c) from Ref. [126] (pd black open circles) and (d) Ref. [126] (pd black open circles).

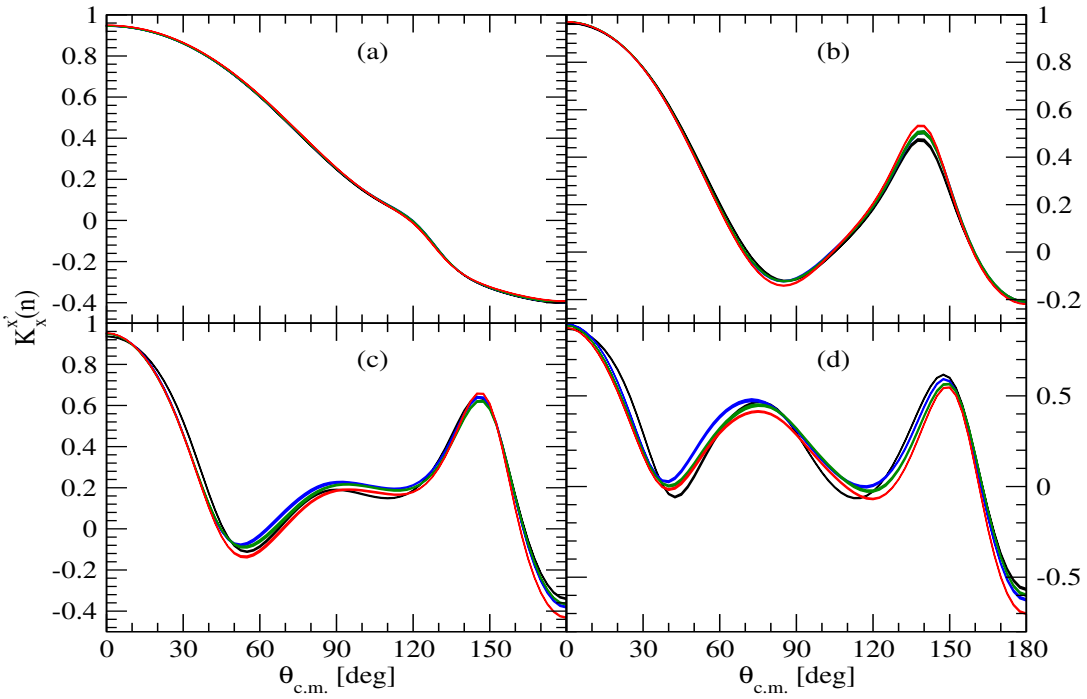

Figure 5.18: The nucleon to nucleon spin transfer coefficient $K_x^{x'}(n)$ for the elastic nd scattering process at the same energies as used in Figure 5.2 as a function of the c.m. scattering angle $\theta_{\text{c.m.}}$. Description of curves and bands is as in Figure 5.2.

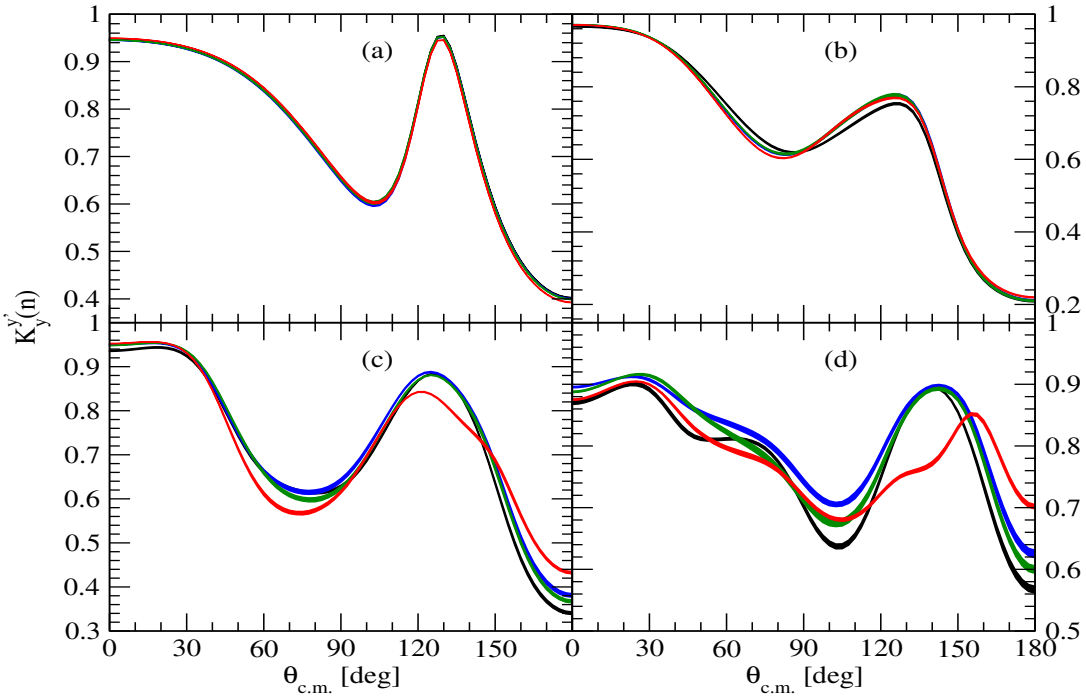

Figure 5.19: The nucleon to nucleon spin transfer coefficient $K_y^{y'}(n)$ for the elastic nd scattering process at the same energies as used in Figure 5.2 as a function of the c.m. scattering angle $\theta_{\text{c.m.}}$. Description of curves and bands is as in Figure 5.2.

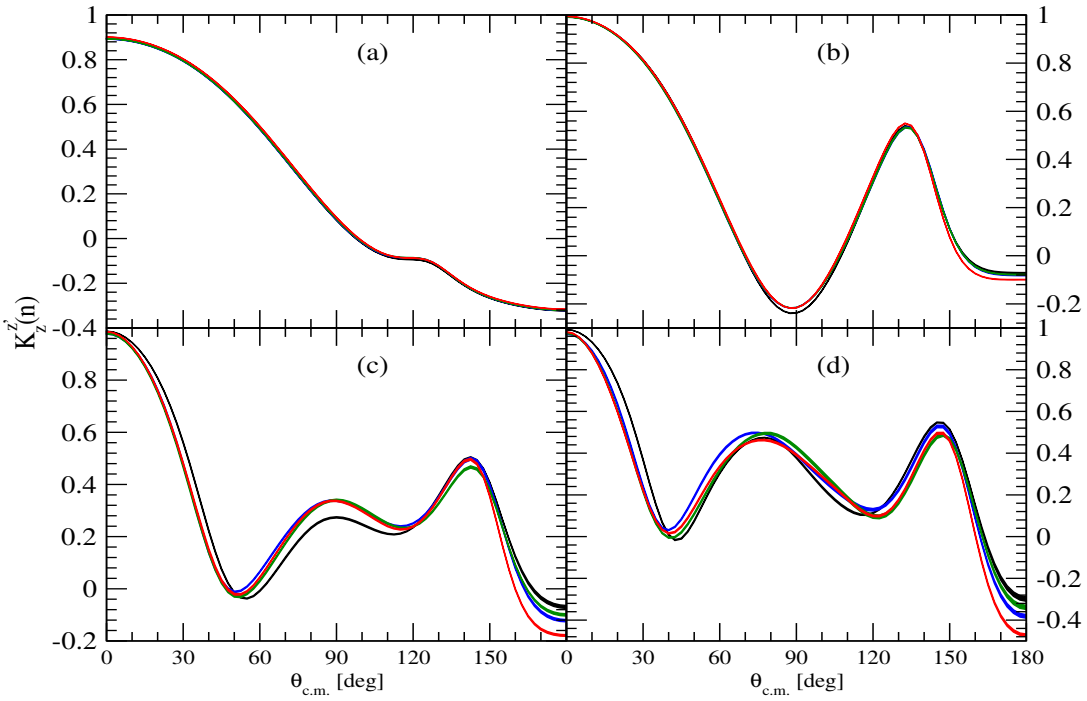

Figure 5.20: The nucleon to nucleon spin transfer coefficient $K_z^{z'}(n)$ for the elastic nd scattering process at the same energies as used in Figure 5.2 as a function of the c.m. scattering angle $\theta_{\text{c.m.}}$. Description of curves and bands is as in Figure 5.2.

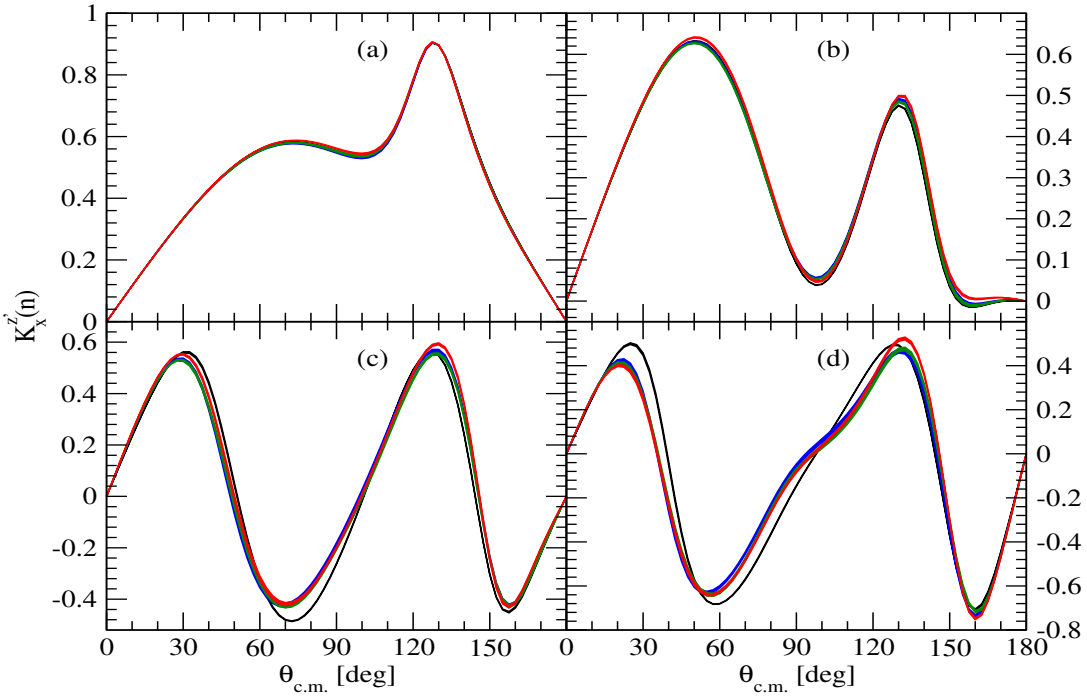

Figure 5.21: The nucleon to nucleon spin transfer coefficient $K_x^{z'}(n)$ for the elastic nd scattering process at the same energies as used in Figure 5.2 as a function of the c.m. scattering angle $\theta_{\text{c.m.}}$. Description of curves and bands is as in Figure 5.2.

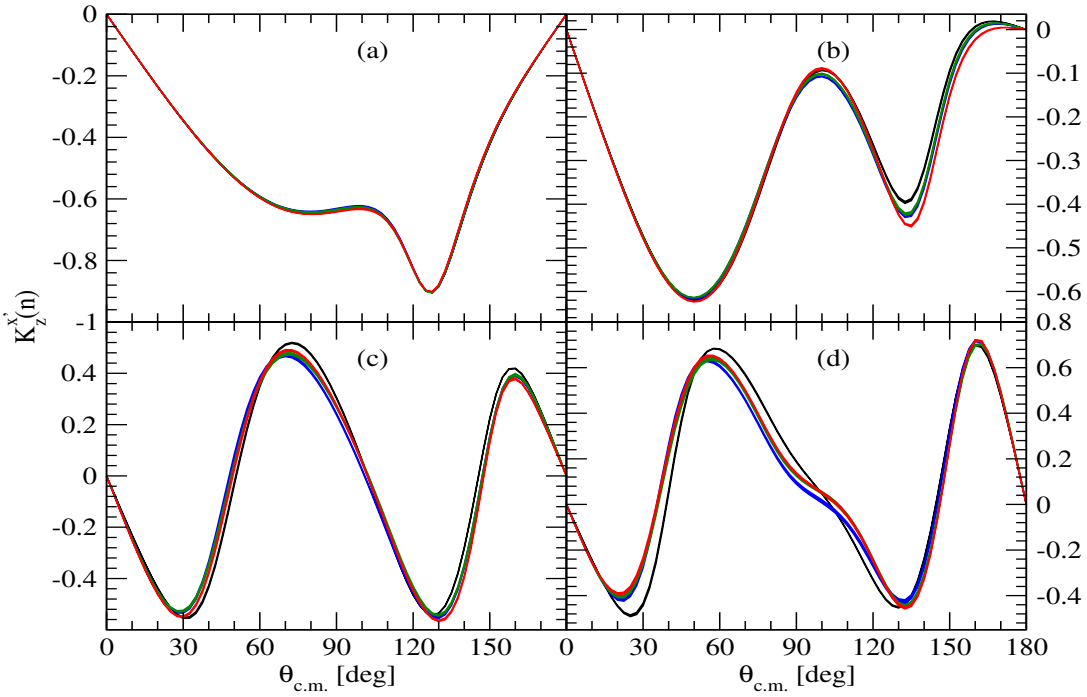

Figure 5.22: The nucleon to nucleon spin transfer coefficient $K_z^{x'}(n)$ for the elastic nd scattering process at the same energies as used in Figure 5.2 as a function of the c.m. scattering angle $\theta_{\text{c.m.}}$. Description of curves and bands is as in Figure 5.2.

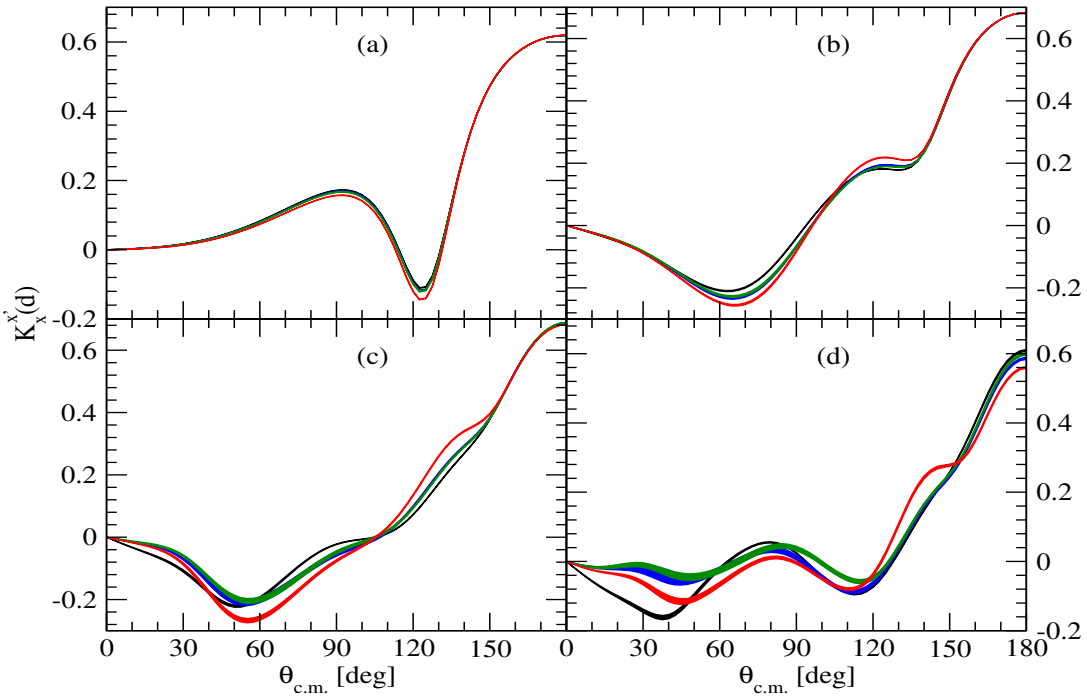

Figure 5.23: The neutron-deuteron vector spin transfer coefficient $K_x^{x'}(d)$ for the elastic nd scattering process at the same energies as used in Figure 5.2 as a function of the c.m. scattering angle $\theta_{\text{c.m.}}$. Description of curves and bands is as in Figure 5.2.

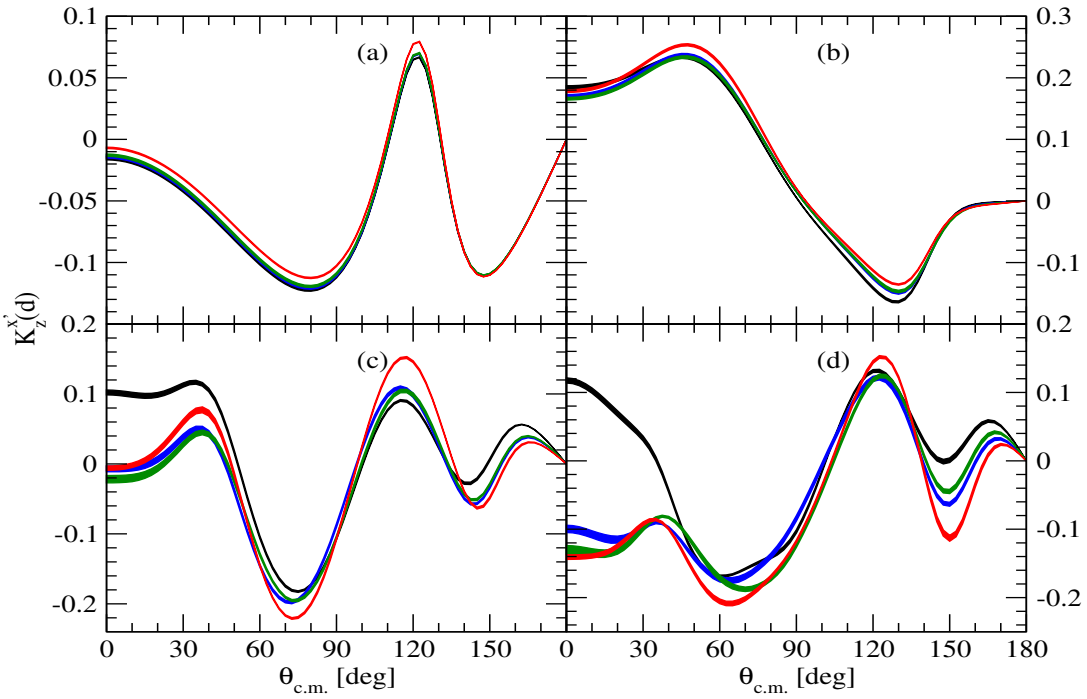

Figure 5.24: The neutron-deuteron vector spin transfer coefficient $K_z^{x'}(d)$ for the elastic nd scattering process at the same energies as used in Figure 5.2 as a function of the c.m. scattering angle $\theta_{\text{c.m.}}$. Description of curves and bands is as in Figure 5.2.

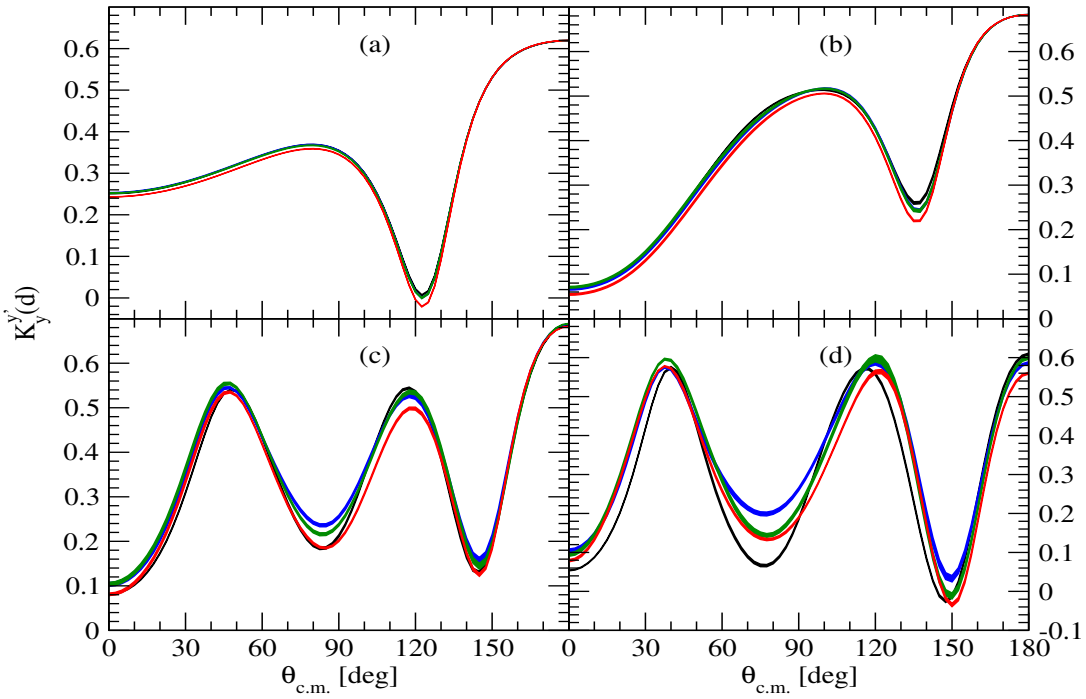

Figure 5.25: The neutron-deuteron vector spin transfer coefficient $K_y^{y'}(d)$ for the elastic nd scattering process at the same energies as used in Figure 5.2 as a function of the c.m. scattering angle $\theta_{\text{c.m.}}$. Description of curves and bands is as in Figure 5.2.

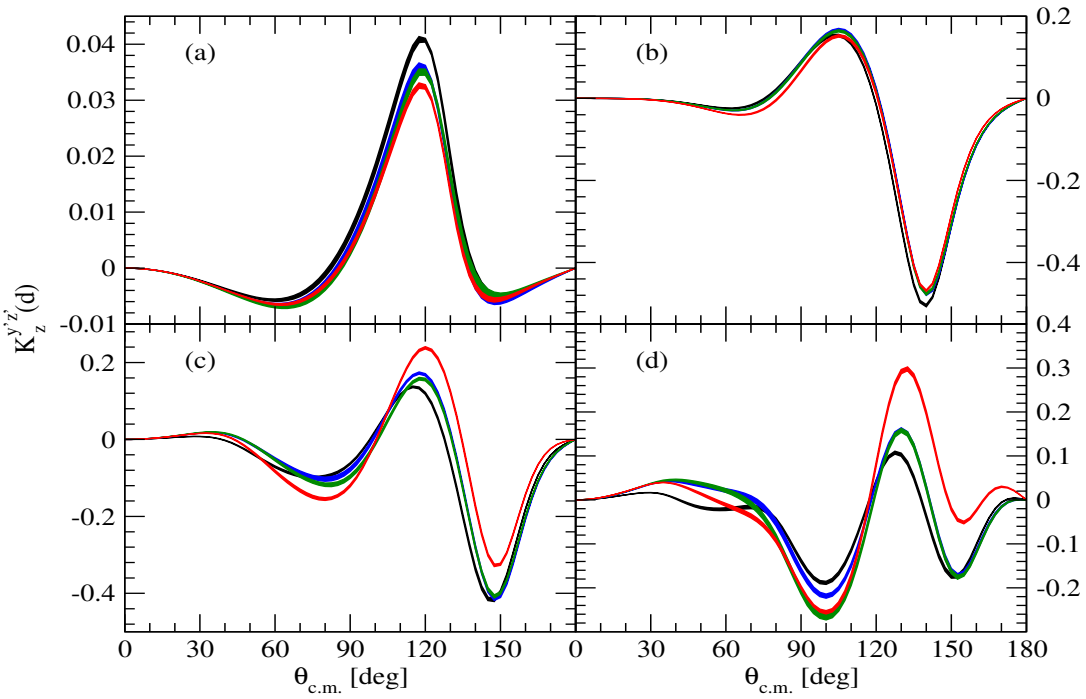

Figure 5.26: The neutron-deuteron tensor spin transfer coefficient $K_z^{y'z'}(d)$ for the elastic *nd* scattering process at the same energies as used in Figure 5.2 as a function of the c.m. scattering angle $\theta_{\rm c.m.}$. Description of curves and bands is as in Figure 5.2.

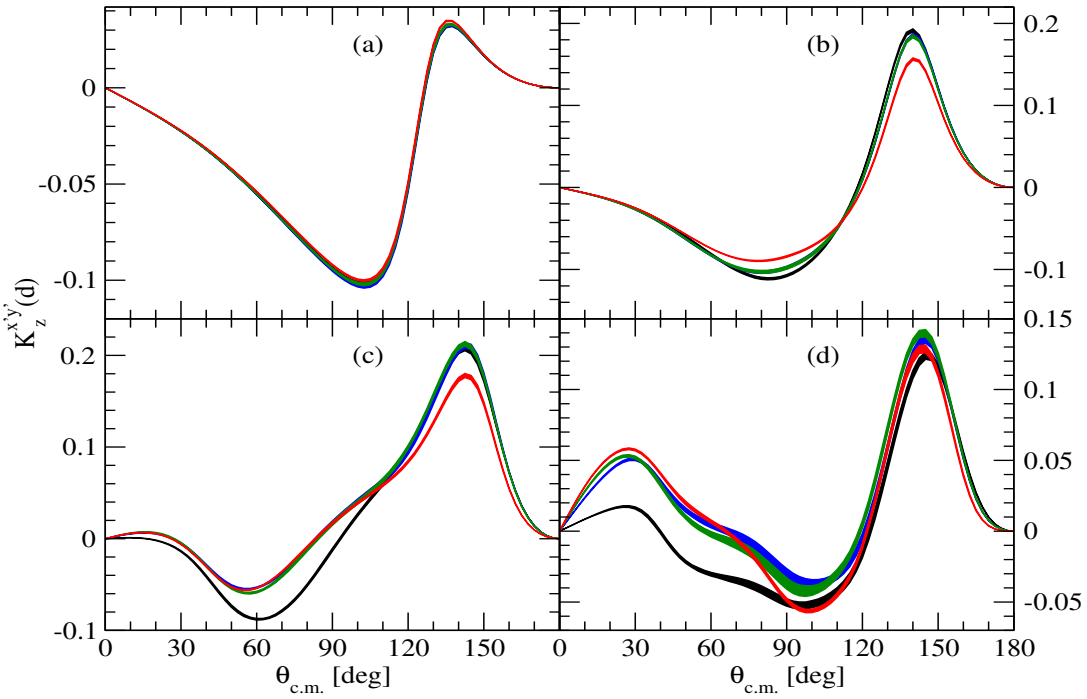

Figure 5.27: The neutron-deuteron tensor spin transfer coefficient $K_z^{x'y'}(d)$ for the elastic *nd* scattering process as a function of the c.m. scattering angle $\theta_{\rm c.m.}$. Description of curves and bands is as in Figure 5.2.

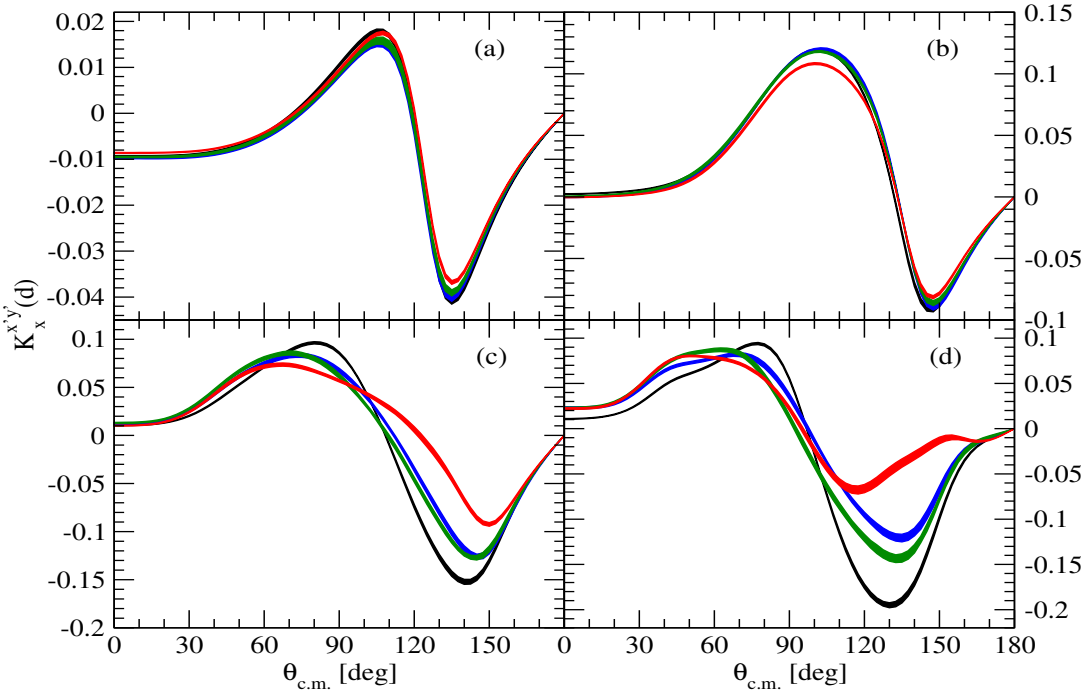

Figure 5.28: The neutron-deuteron tensor spin transfer coefficient $K_x^{x'y'}(d)$ for the elastic *nd* scattering process at the same energies as used in Figure 5.2 as a function of the c.m. scattering angle $\theta_{\text{c.m.}}$. Description of curves and bands is as in Figure 5.2.

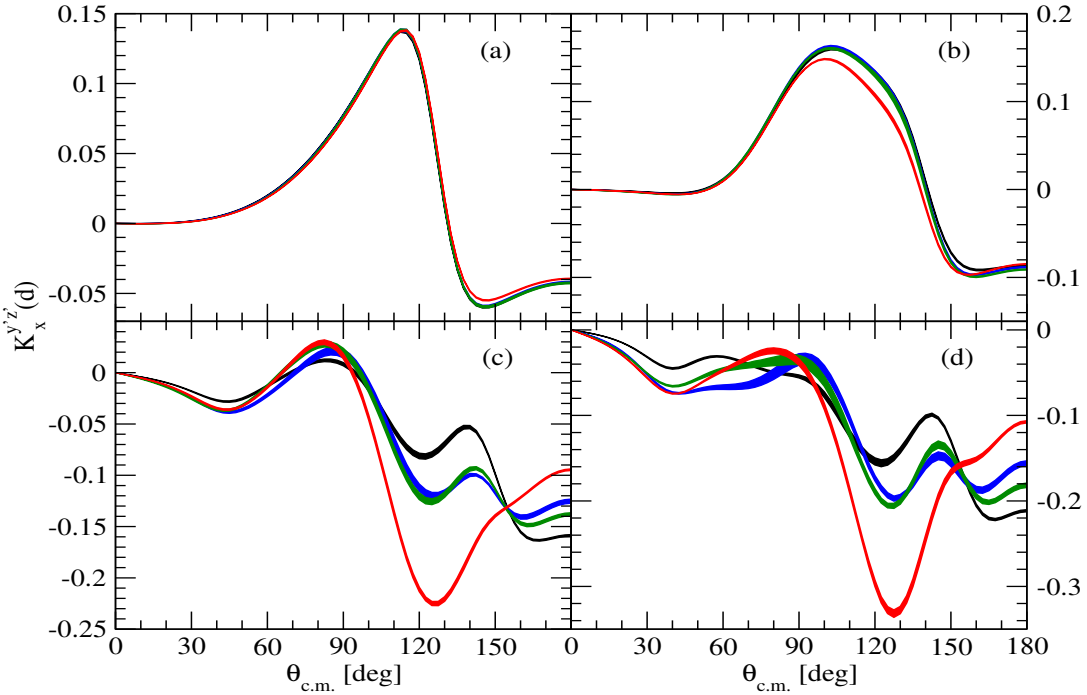

Figure 5.29: The neutron-deuteron tensor spin transfer coefficient $K_x^{y'z'}(d)$ for the elastic *nd* scattering process at the same energies as used in Figure 5.2 as a function of the c.m. scattering angle $\theta_{\text{c.m.}}$. Description of curves and bands is as in Figure 5.2.

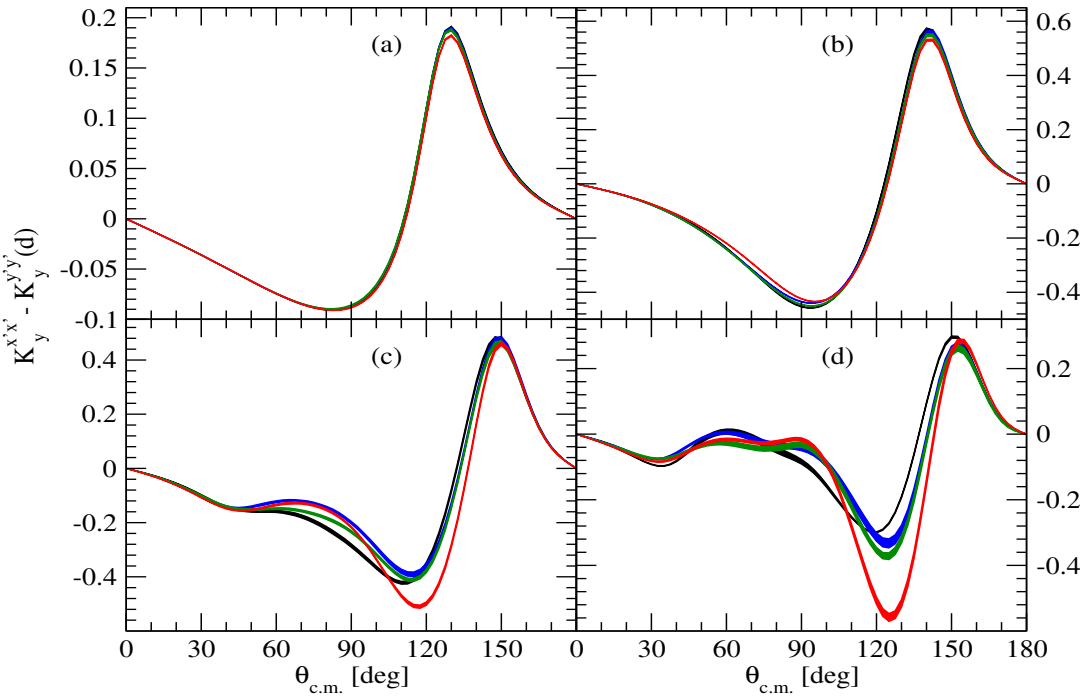

Figure 5.30: The neutron-deuteron tensor spin transfer coefficient $K_y^{x'x'} - K_y^{y'y'}(d)$ for the elastic nd scattering process at the same energies as used in Figure 5.2 as a function of the c.m. scattering angle $\theta_{\text{c.m.}}$. Description of curves and bands is as in Figure 5.2.

It is interesting to compare the statistical errors with other kinds of theoretical uncertainties. Firstly, I would like to show one example which demonstrate the truncation errors obtained by using the method from reference [13]. In Figure 5.31 a comparison of the statistical and truncation errors for the deuteron vector analyzing power iT_{11} is shown. The N^{4}LO SMS force with $\Lambda = 450$ MeV is used. For the sake of clarity, for the truncation errors we show only, with the cyan curves, borders of the corresponding band. The relative difference between the widths of two bands at $E_{\text{lab}} = 65$ MeV reaches a few percent at scattering angle $\theta_{c.m.} = 90°$. However, with increasing energy there is a significant increase in the magnitude of the truncation error which leads to an increase of the relative difference between the widths of two bands. For instance, at $E_{\text{lab}} = 135$ MeV and $\theta_{c.m.} = 90°$, that difference approaches about 84% (with $\delta^{(5)}(\text{iT}_{11}) > \frac{1}{2}\Delta_{68\%}$), but already at $E_{\text{lab}} = 200$ MeV it amounts up to 92%. Last but not least, I have to note that the ratios of the magnitude of the statistical uncertainties to the magnitude of the truncation error, that is $\frac{1}{2}\Delta_{68\%}/\delta(X)^{(5)}$, for the polarization observables are for most of the scattering angles much bigger than the same ratios but for the cross section. This is due to a bigger sensitivity of polarization observables to the specific potential parameters of the chiral interaction used.

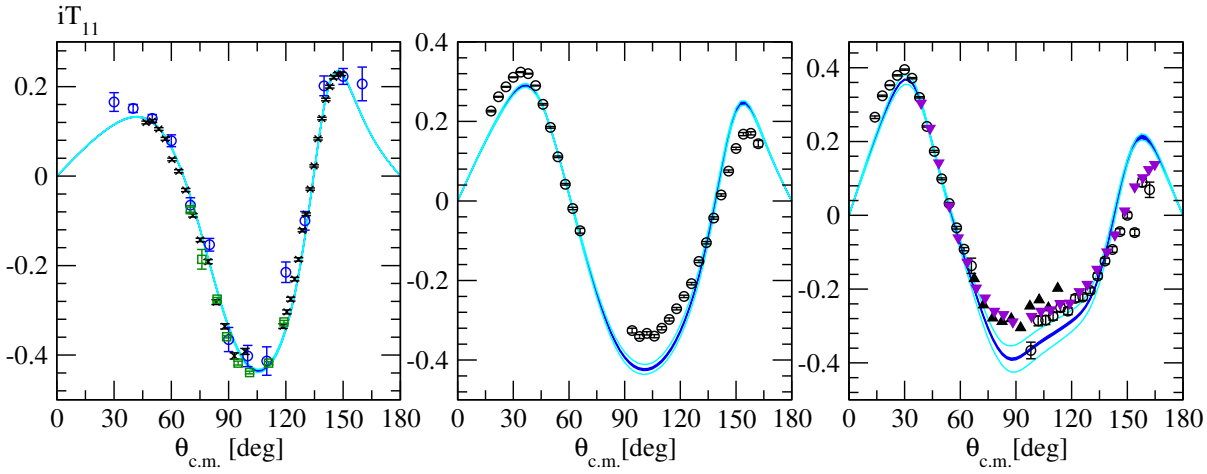

Figure 5.31: The deuteron vector analyzing power iT_{11} for the elastic nd scattering at the incoming neutron laboratory energy (a) $E_{\rm lab}$ = 65 MeV, (b) $E_{\rm lab}$ = 135 MeV and (c) $E_{\rm lab}$ = 200 MeV as a function of the c.m. scattering angle $\theta_{c.m.}$. The blue solid band represents the statistical uncertainties based on the chiral N^{4}LO (Λ = 450 MeV) potential and the cyan lines represent the borders of the band for the truncation error for the same potential estimated using Eq. (3.2). The experimental data are the same as in Figure 5.4.

E [MeV]	$\theta_{c.m.}$ [deg]	$iT_{11}(S_0)$	$\mid iT_{11}(S_0)$ - $iT_{11}^{min}\mid$	$\mid iT_{11}^{max}$ - $iT_{11}(S_0)\mid$	$\frac{1}{2}\Delta_{68\%}$	$\delta(iT_{11})^{(5)}$
65	30	0.115234	0.000644	0.000493	0.000569	0.000425
	75	-0.117815	0.000820	0.000577	0.000699	0.001685
	120	-0.342291	0.002194	0.001620	0.001911	0.002680
	165	-0.089323	0.000486	0.000313	0.000399	0.000599
135	30	0.270409	0.001503	0.001204	0.001354	0.004570
	75	-0.233802	0.001052	0.001486	0.001269	0.009550
	120	-0.326824	0.003196	0.001554	0.002375	0.015205
	165	0.155717	0.001594	0.001174	0.001385	0.003405
200	30	0.367730	0.000706	0.001307	0.001007	0.012490
	75	-0.307313	0.002202	0.003750	0.002976	0.026585
	120	-0.286319	0.003595	0.002643	0.003119	0.028870
	165	0.175372	0.003484	0.002954	0.003219	0.007540

Table 5.1: The deuteron analyzing power iT_{11}obtained, for the given energy of incoming neutron $E_{\rm lab}$, and at given scattering angle $\theta_{c.m.}$, for the expectation values of the chiral SMS N^{4}LO potential parameters (denoted as set S_0), and its statistical $\frac{1}{2}\Delta_{68\%}$ and truncation $\delta^{(5)}$ errors. In addition the borders of iT_{11} for 34 sets ($iT_{11}^{\rm min}$ and $iT_{11}^{\rm max}$) are shown. $\Delta_{68\%}$ = $iT_{11}^{\rm max}$ - $iT_{11}^{\rm min}$.

Table 5.1 provides more details on the statistical errors and truncation uncertainties for the deuteron vector analyzing power iT_{11} shown in Figure 5.31. Here, in addition to the predictions for iT_{11} obtained using the SMS N^{4}LO potential, the statistical ($\frac{1}{2}\Delta_{68\%}$) and truncation ($\delta(X)^{(5)}$) errors are presented. Again, one can observe a rapid decrease of the $\frac{\Delta_{68\%}}{\delta(X)^{(5)}}$ with energy change. The predictions, based on the genuine set of the potential parameters S_0, shown in the third column of Table 5.1 does not need to be in the centre of predictions obtained with various sets of the potential parameters. Hence, in the 4th and the 5th columns of Table 5.1 there are the distances between the predictions from the 3rd column and minimal and maximal predictions among predictions based on 34 sets

of potential parameters taking into account when calculating $\Delta_{68\%}$. Indeed the different magnitudes of these distances, at given energy and scattering angle, points to a nonlinear behaviour of 3N observables with the potential parameters.

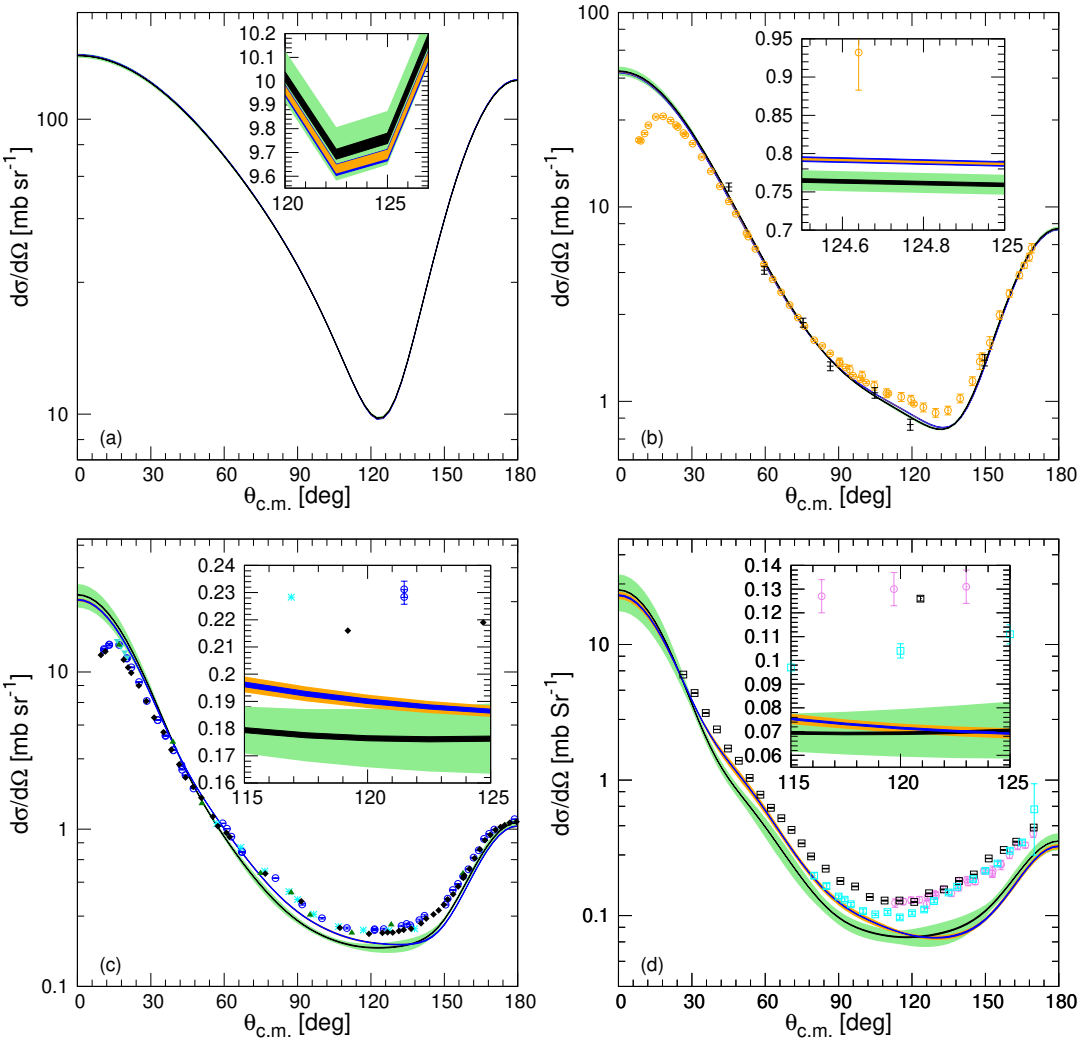

Figure 5.32: The differential cross section $\mathrm{d}\sigma/\mathrm{d}\Omega$ for the elastic *nd* scattering process at the incoming neutron laboratory energy (a) $E_{\mathrm{lab}} = 13$ MeV, (b) $E_{\mathrm{lab}} = 65$ MeV, (c) $E_{\mathrm{lab}} = 135$ MeV and (d) $E_{\mathrm{lab}} = 200$ MeV as a function of the c.m. scattering angle $\theta_{c.m.}$. The black and blue bands represent the statistical uncertainty obtained with the chiral N^{2}LO and N^{4}LO ($\Lambda = 450$ MeV) SMS potentials, respectively. The light-green and orange bands show 68% DoB intervals from the Bayesian model $\bar{C}^{650}_{0.5-10}$ based on the chiral N^{2}LO and N^{4}LO ($\Lambda = 450$ MeV) SMS potentials, respectively. The experimental data are the same as in Figure 5.2.

The Bayesian approach is a more sophisticated method which allows one to draw more reliable conclusions about the convergence and to quantify truncation errors in perturbative calculations. I would like to compare now the statistical uncertainties with the truncation errors estimated within the Bayesian procedure already described in Section 3.1.3 to study truncation errors in 3N scattering.

In the following I compare, for several selected observables, predictions based on the chiral N^{2}LO and N^{4}LO SMS potentials along with the truncation error (more precisely

the 68% DoB intervals) and the statistical uncertainty obtained with the same forces. For example, in Figures 5.32 – 5.33 the differential cross section, the neutron vector, A_y, and the deuteron vector, iT_{11}, analyzing powers in elastic neutron-deuteron scattering at the laboratory energies $E_{\rm lab} = 13, 65, 135$ and 200 MeV are shown. For the differential cross section the magnitude of the statistical uncertainty is bigger or comparable to the magnitude of the truncation errors at $E_{\rm lab} = 13$ MeV, but with increasing energy the width of 68% DoB interval at N^{2}LO from the $\bar{C}^{650}_{0.5-10}$ Bayesian model exceeds the statistical uncertainty at small and big scattering angles and at the minimum of the cross section. At higher energies the statistical uncertainties are smaller compared to the truncation ones. Thus we observe that at those energies the truncation errors become a dominant source of the theoretical uncertainty. The situation changes extremely with increasing chiral order when the width of trunction error drops to the size of statistical uncertainty even at higher energies. The relative difference between 68% DoB interval and the statistical error for N^{4}LO SMS predictions reaches no more than 1% at $E_{\rm lab} =$ 200 MeV.

For A_y the truncation error at N^{2}LO appears much bigger than statistical uncertainty at all energies. This domination appears just at specific ranges of scattering angles for two lower energies and at higher energies the truncation errors exceed the statistical ones for all scattering angles. The magnitude of the truncation errors is, as expected, much smaller at N^{4}LO than at N^{2}LO and the magnitude of the statistical uncertainties remains similar at these two orders of the chiral NN potential and at the same reaction energies. The magnitude of the relative difference between the statistical uncertainty and 68% DoB interval for A_y is $\lesssim 3\%$ for the SMS N^{4}LO force at higher energies. Examples of other observables are shown in Figures 5.34 – 5.37. The general picture arising from comparison of the statistical error and 68 % DoB interval does not change dramatically. We observe that at N^{4}LO the truncation errors are significantly bigger compared to the statistical uncertainty. This situation will likely change after applying higher orders contributions to the chiral force what should decrease the truncation error. The magnitude of the truncation errors is, as it should be, much smaller at N^{4}LO than at N^{2}LO and the magnitude of the statistical uncertainties remains similar at the both orders of the chiral expansion and at the same reaction energy.

In Figure 5.38, I show one example of estimated DoB intervals for truncation errors of the elastic differential cross section for more orders of chiral expansion. Clearly, at all energies truncation error obtained with the Bayesian approach becomes smaller with increasing order of the chiral expansion. Only at low energies and at N^{4}LO truncation errors is smaller than statistical uncertainty. The same picture is also valid for other investigated 3N observables presented in Appendix B.

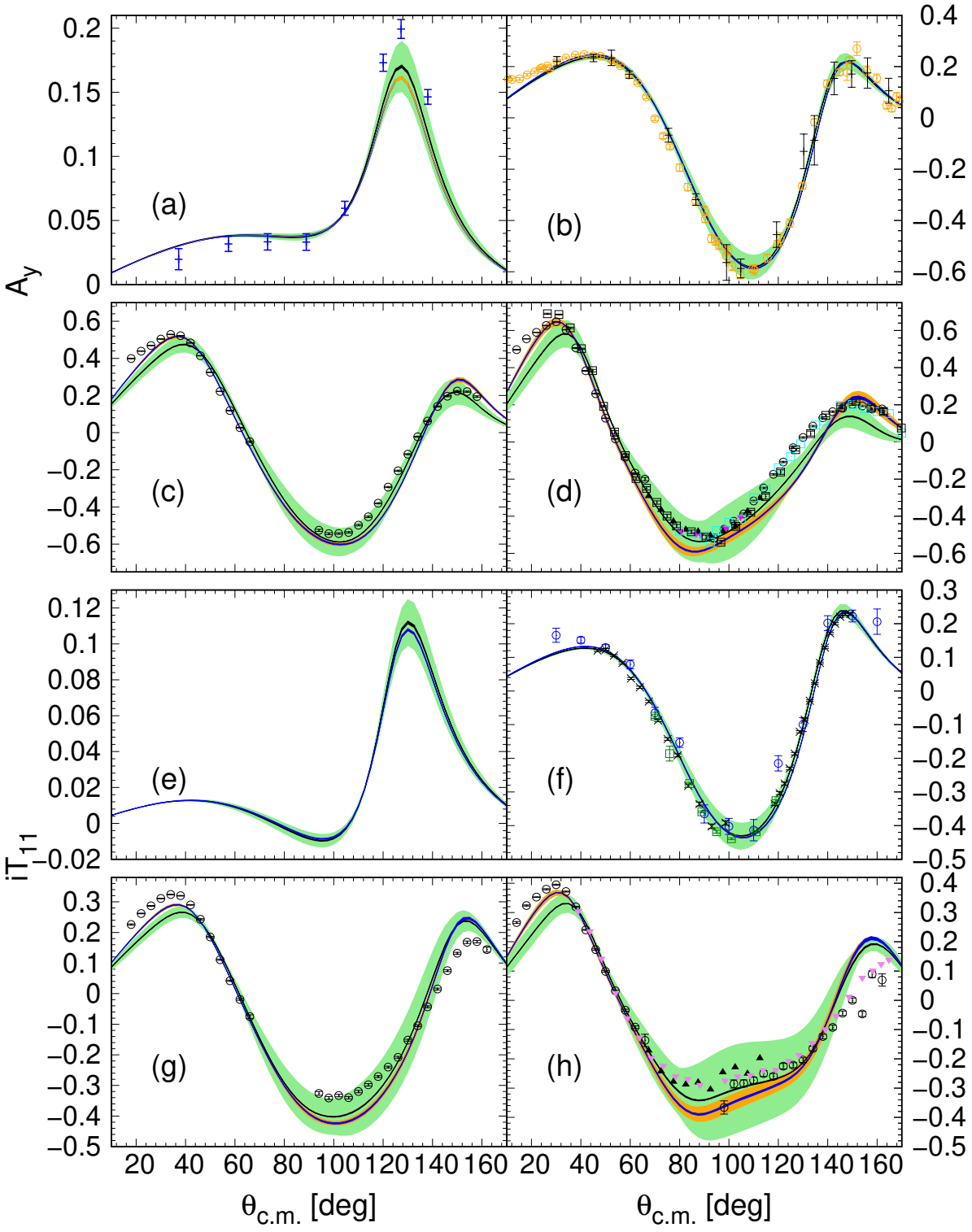

Figure 5.33: The neutron vector analyzing power A_y and the deuteron vector analyzing power iT_{11} for the elastic nd scattering process at the incoming neutron laboratory energy (a, e) $E_{\rm lab}$ = 13 MeV, (b, f) $E_{\rm lab}$ = 65 MeV, (c, g) $E_{\rm lab}$ = 135 MeV and (d, h) $E_{\rm lab}$ = 200 MeV as a function of the c.m. scattering angle $\theta_{c.m.}$. Bands are as in Figure 5.32. The experimental data are the same as in Figures 5.3 and 5.4, respectively.

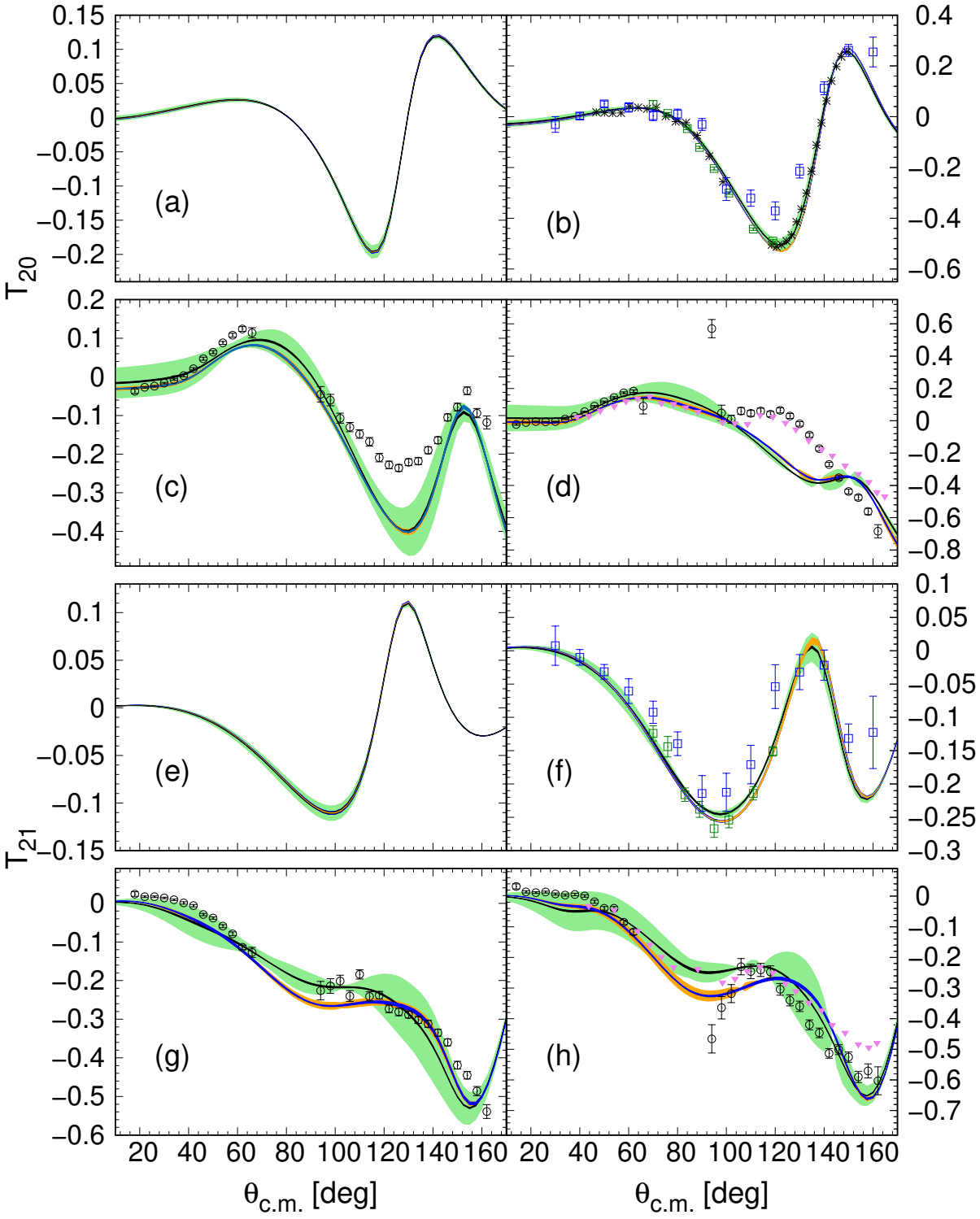

Figure 5.34: The deuteron tensor analyzing powers T_{20} and T_{21} for the elastic *nd* scattering process at the incoming neutron laboratory energy (a, e) $E_{\rm lab} = 13$ MeV, (b, f) $E_{\rm lab} = 65$ MeV, (c, g) $E_{\rm lab} = 135$ MeV and (d, h) $E_{\rm lab} = 200$ MeV as a function of the c.m. scattering angle $\theta_{c.m.}$. Bands are as in Figure 5.32. The experimental data are the same as in Figures 5.5 and 5.6, respectively.

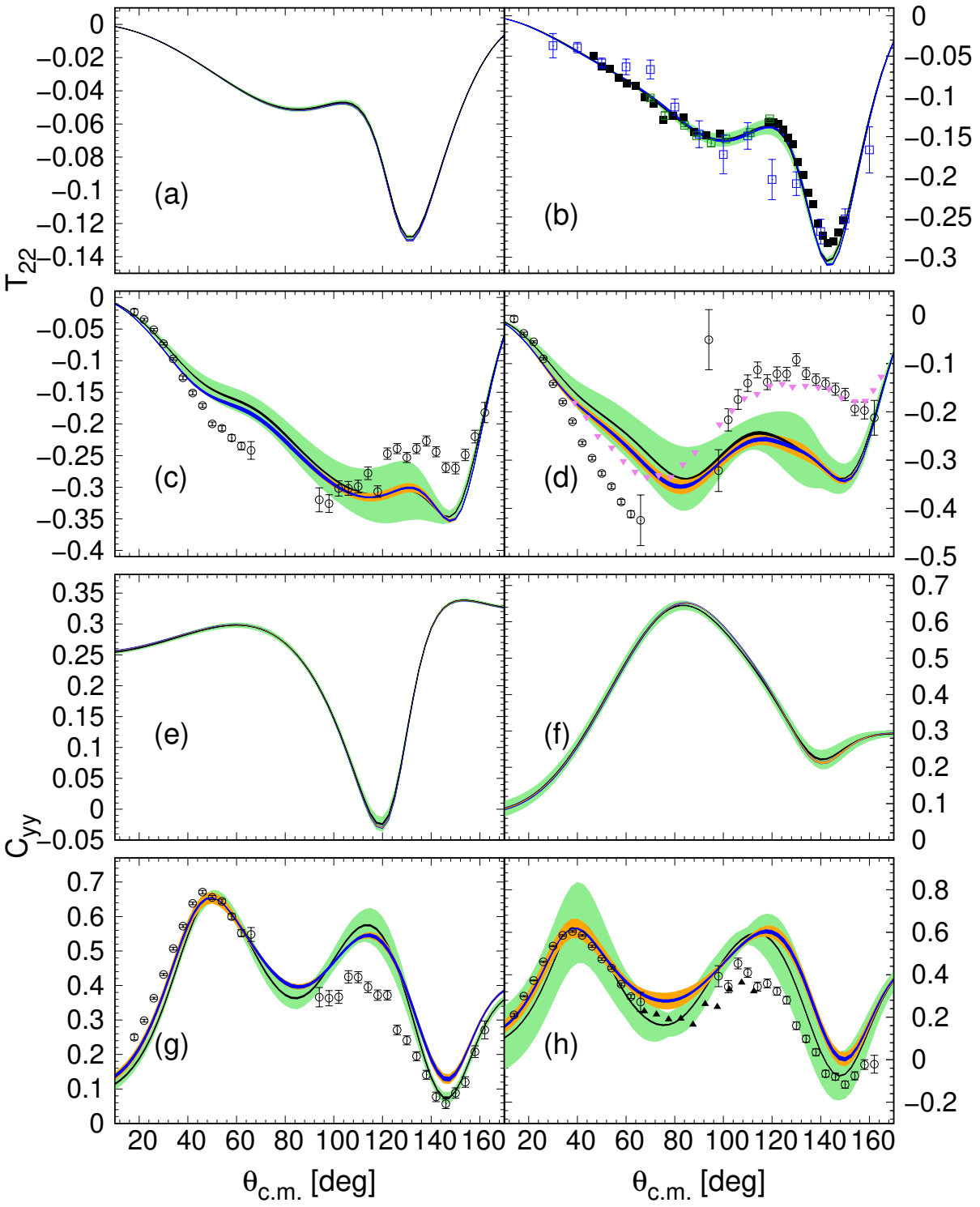

Figure 5.35: The deuteron tensor analyzing powers T_{22} and the spin correlation coefficient C_{yy} for the elastic nd scattering process at the incoming neutron laboratory energy (a, e) $E_{\rm lab} = 13$ MeV, (b, f) $E_{\rm lab} = 65$ MeV, (c, g) $E_{\rm lab} = 135$ MeV and (d, h) $E_{\rm lab} = 200$ MeV as a function of the c.m. scattering angle $\theta_{c.m.}$. Bands are as in Figure 5.32. The experimental data are the same as in Figures 5.7 and 5.10, respectively.

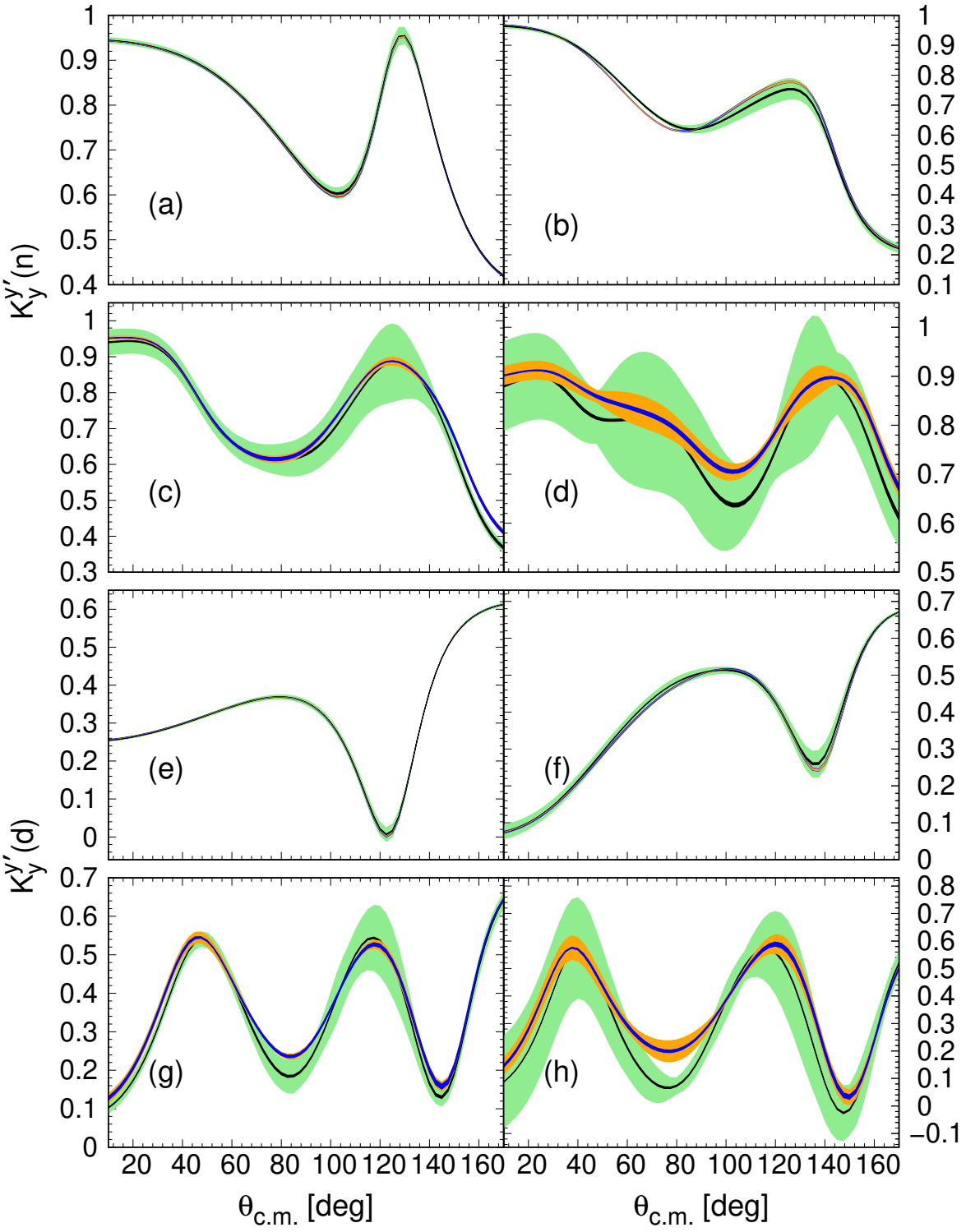

Figure 5.36: The nucleon to nucleon spin $K_y^{y'}(n)$ and the neutron-deuteron vector spin $K_y^{y'}(d)$ transfer coefficients for the elastic nd scattering process at the incoming neutron laboratory energy (a, e) $E_{\rm lab} = 13$ MeV, (b, f) $E_{\rm lab} = 65$ MeV, (c, g) $E_{\rm lab} = 135$ MeV and (d, h) $E_{\rm lab} = 200$ MeV as a function of the c.m. scattering angle $\theta_{c.m.}$. Bands are as in Figure 5.32.

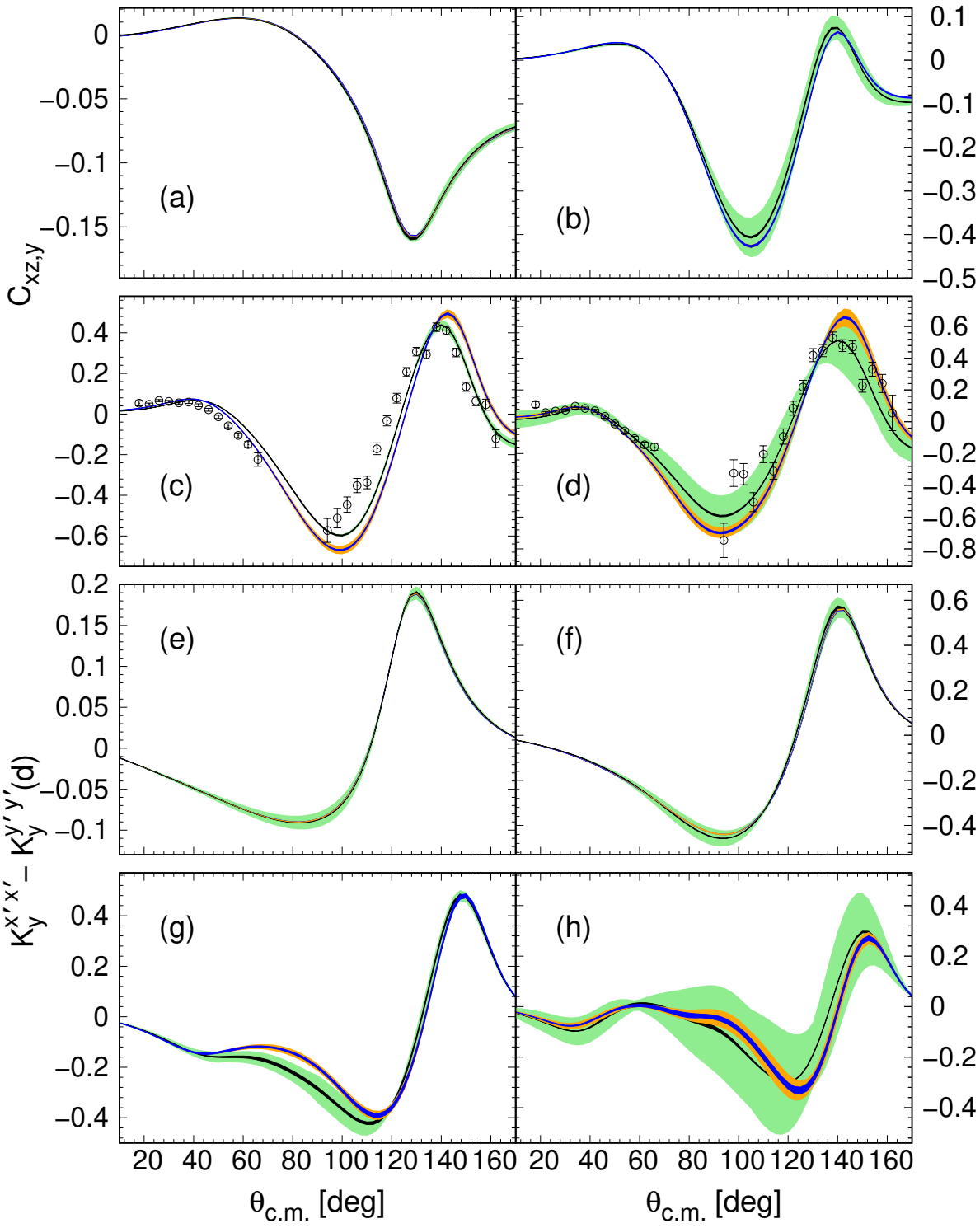

Figure 5.37: The spin correlation coefficient $C_{xz,y}$ and the neutron-deuteron tensor spin transfer coefficient $K_y^{x'x'} - K_y^{y'y'}(d)$ for the elastic nd scattering process at the incoming neutron laboratory energy (a, e) $E_{\rm lab}$ = 13 MeV, (b, f) $E_{\rm lab}$ = 65 MeV, (c, g) $E_{\rm lab}$ = 135 MeV and (d, h) $E_{\rm lab}$ = 200 MeV as a function of the c.m. scattering angle $\theta_{c.m.}$. Bands are as in Figure 5.32. The experimental data are the same as in Figure 5.15.

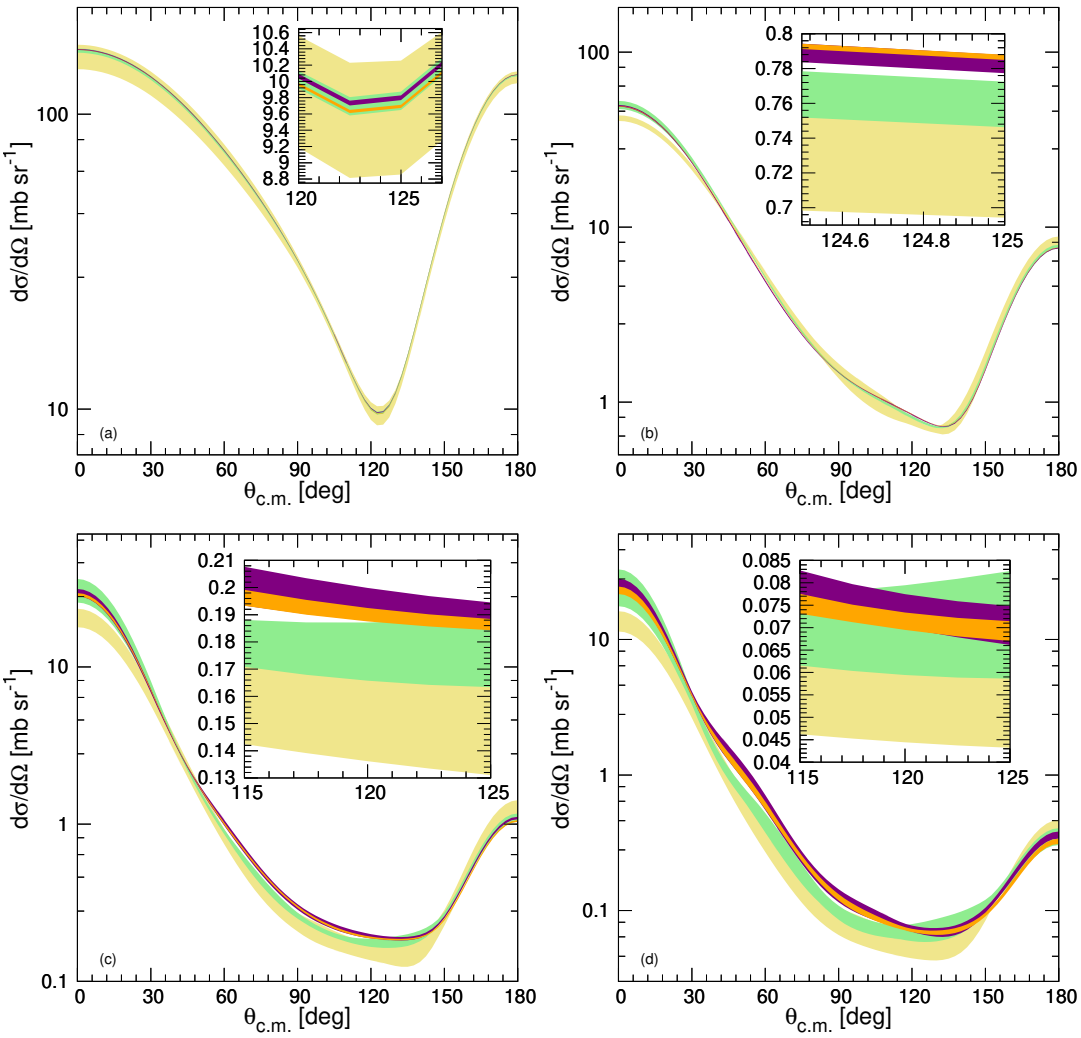

Figure 5.38: The differential cross section $\mathrm{d}\sigma/\mathrm{d}\Omega$ for the elastic nd scattering process at the incoming neutron laboratory energy (a) $E_{\rm lab} = 13$ MeV, (b) $E_{\rm lab} = 65$ MeV, (c) $E_{\rm lab} = 135$ MeV and (d) $E_{\rm lab} = 200$ MeV as a function of the c.m. scattering angle $\theta_{c.m.}$. The light-shaded brown and green, purple and orange bands depict 68% DoB intervals from the Bayesian model $\bar{C}^{650}_{0.5-10}$ based on the chiral NLO, N^{2}LO, N^{3}LO and N^{4}LO ($\Lambda = 450$ MeV) SMS potentials, respectively.

Last but not least, it is also interesting to consider the residual cutoff dependence of 3N observables. In Figures 5.39 – 5.41, I present predictions for a few observables obtained with the central values of parameters of the N^{4}LO$^+$ SMS force for four values of the regulator $\Lambda = 400$, 450, 500, and 550 MeV. As shown in Figure 5.39, the differential cross section $d\sigma/d\Omega$ is very stable with respect to the cutoff Λ, i.e., the resulting spread of predictions is barely visible for all energies. In the case of the deuteron vector analyzing power iT$_{11}$ (see Figure 5.40) the picture is similar, but some sensitivity to cutoff at higher energies and medium angles is seen. Even bigger regulator dependence is seen for the spin correlation coefficient C_{zz} in Figure 5.41. It increases with energy, and in particular the predictions for $\Lambda = 400$ MeV separates at most scattering angles. These three figures reveal typical pattern: the cross section predictions are practically independent on used value of the regulator parameter, but the role of the regulator grows with the complexity of spin observable. Of course, it is interesting to compare magnitudes of uncertainty

related to the regulator with the statistical uncertainty. Thus, for the N^{4}LO$^+$ SMS force, I computed the ratios of the magnitude of the cutoff dependences and the statistical uncertainties (at $\Lambda = 450$ MeV) to the magnitude of predictions at $\Lambda = 450$ MeV defined as $E_{\rm reg} \equiv \frac{1}{2}\left|\frac{\max\{X_i\}-\min\{X_i\}}{X_2}\right|$ and $E_{\rm stat} \equiv \frac{1}{2}\left|\frac{\Delta_{68\%}}{X_2}\right|$, respectively. The predictions X_i, with $i \in \{1,2,3,4\}$, are results obtained with the cutoff parameter $\Lambda = 400, 450, 500$ and 550 MeV, respectively. In the case of the differential cross section ratios $E_{\rm reg}$ ($E_{\rm stat}$) are at $E_{\rm lab} = 65$ MeV 0.009 (0.004) at $\theta_{c.m.} = 60°$, and 0.02 (0.005) at $\theta_{c.m.} = 130°$. For $E_{\rm lab} = 200$ MeV they amount 0.01 (0.008) at $\theta_{c.m.} = 60°$, and 0.02 (0.01) at $\theta_{c.m.} = 130°$. The same ratios for iT$_{11}$ are 0.05 (0.33) at $\theta_{c.m.} = 60°$, and 0.03 (0.07) at $\theta_{c.m.} = 105°$ for $E_{\rm lab} = 65$ MeV and 0.07 (0.002) at $\theta_{c.m.} = 105°$, and 0.07 (0.009) at $\theta_{c.m.} = 155°$ for $E_{\rm lab} = 200$ MeV. In the case of C_{zz} the ratios are 0.02 (0.28) at $\theta_{c.m.} = 40°$, 0.06 (0.02) at $\theta_{c.m.} = 145°$ for $E_{\rm lab} = 65$ MeV, and 0.08 (0.02) at $\theta_{c.m.} = 40°$, and 0.16 (0.01) at $\theta_{c.m.} = 160°$ for $E_{\rm lab} = 200$ MeV. Analyzing the obtained values, we come to the conclusion that in most cases the statistical uncertainty obtained with the chiral N^{4}LO$^+$ SMS force is smaller than the error related to cutoff dependence. However, the numbers above are biased by the choice of scattering angles, which has been chosen partly as angles for which the cutoff dependence is especially big. For many other angles, and not shown here observables, regulator dependence remains small and comparable in size to statistical errors.

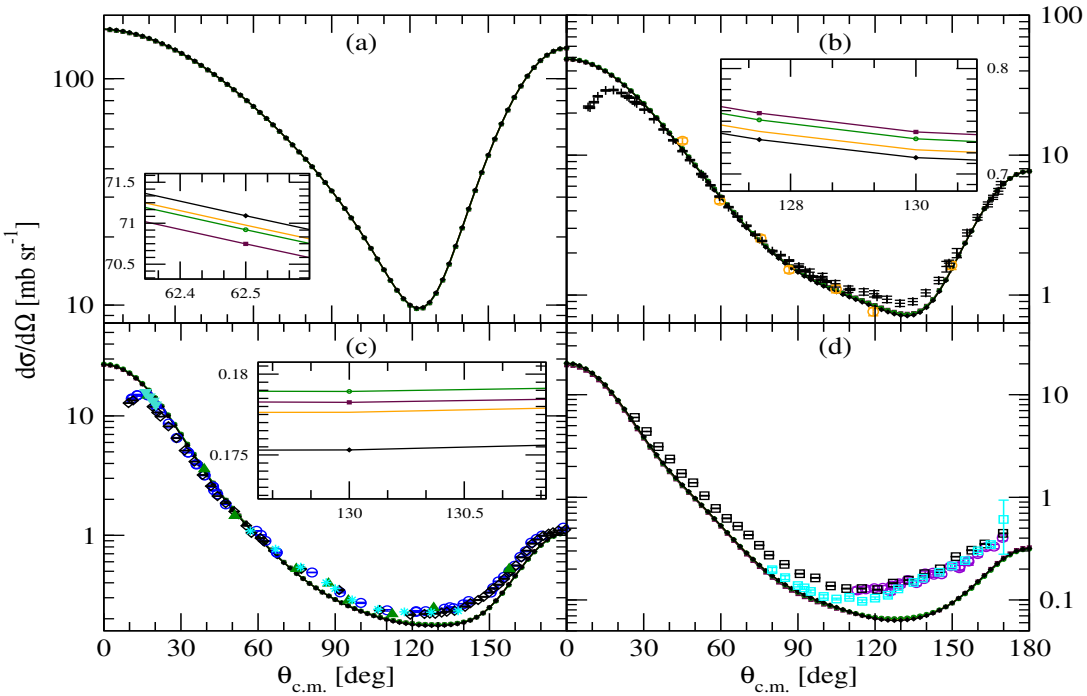

Figure 5.39: The differential cross section dσ/dΩ for the elastic *nd* scattering process at the same energies as used in Figure 5.38 as a function of the c.m. scattering angle $\theta_{\rm c.m.}$. The solid maroon line with squares, the solid green line with open circles, the solid orange line and the solid black line with diamonds show predictions of the chiral N^{4}LO$^+$ SMS force using the cutoff parameters $\Lambda = 400$, 450, 500, and 550 MeV, respectively. The experimental data are the same as in Figure 5.2.

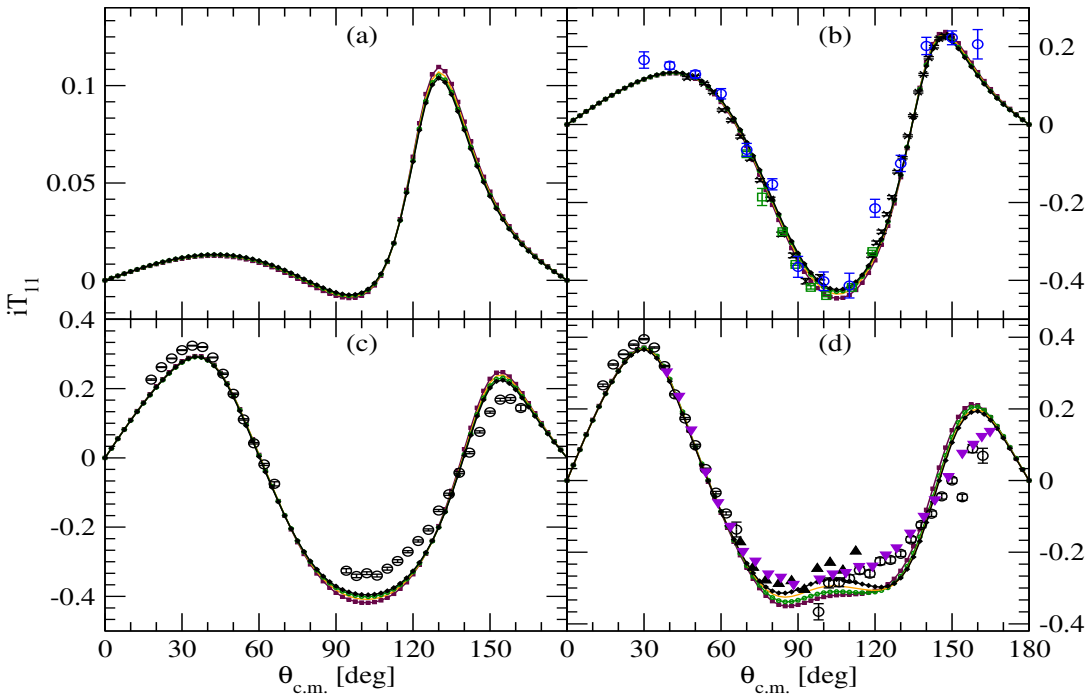

Figure 5.40: Same as in Figure 5.39, but for the deuteron vector analyzing power iT_{11}. The experimental data are the same as in Figure 5.4.

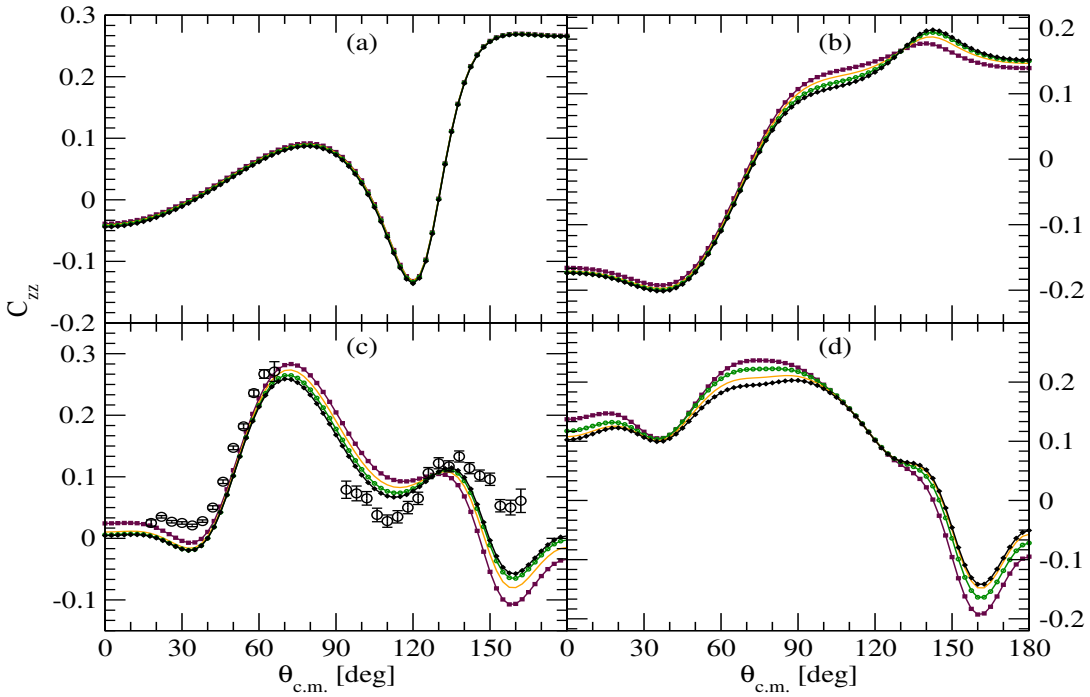

Figure 5.41: Same as in Figure 5.39, but for the spin correlation coefficient C_{zz}. The experimental data are the same as in Figure 5.12.

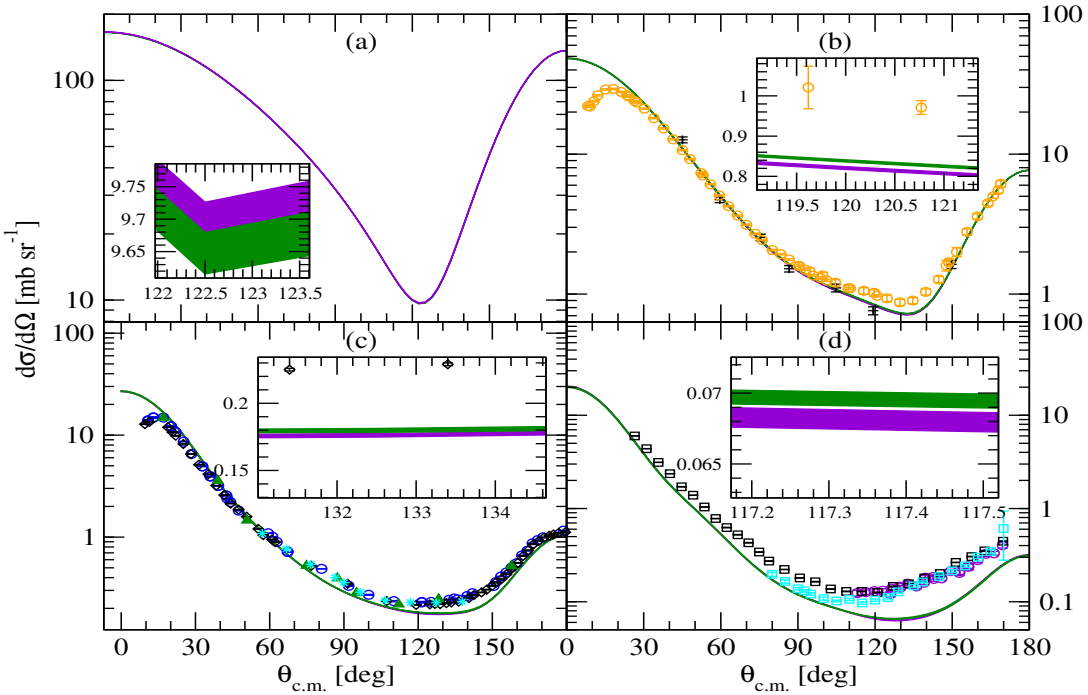

Figure 5.42: The differential cross section $d\sigma/d\Omega$ for the elastic *nd* scattering process at the same energies as used in Figure 5.38 as a function of the c.m. scattering angle $\theta_{\text{c.m.}}$. The green and violet bands represent statistical uncertainties based on the chiral N^{4}LO$^+$ SMS force using the cutoff parameters $\Lambda = 450$ and 550 MeV, respectively. The experimental data are the same as in Figure 5.2.

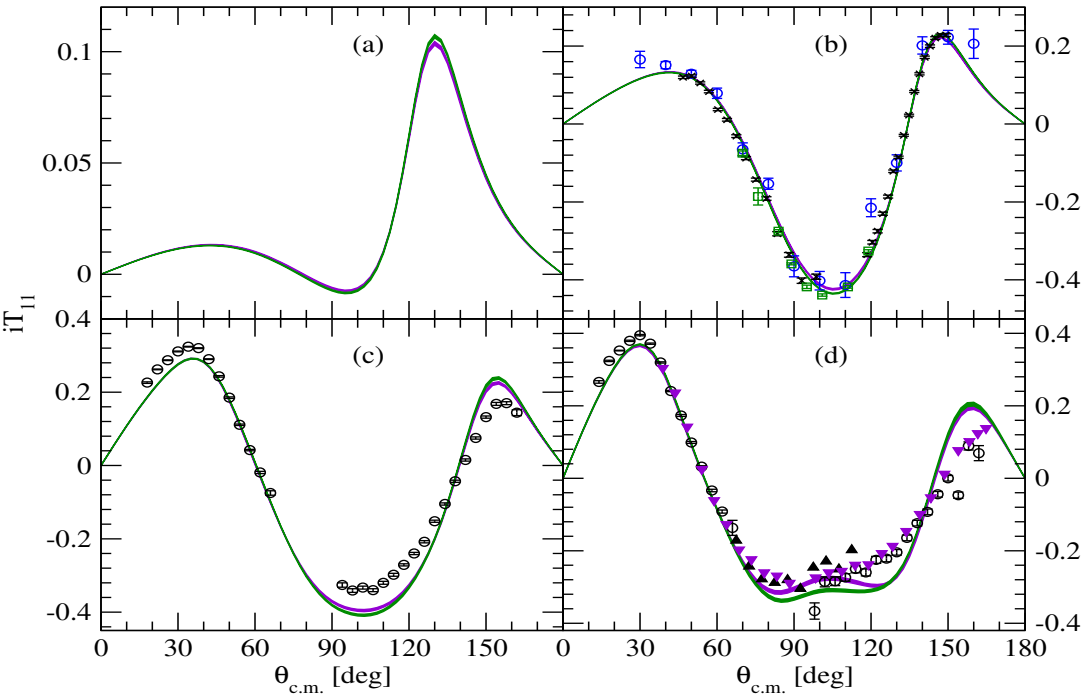

Figure 5.43: Same as in Figure 5.42, but for the deuteron vector analyzing power iT_{11}. The experimental data are the same as in Figure 5.4.

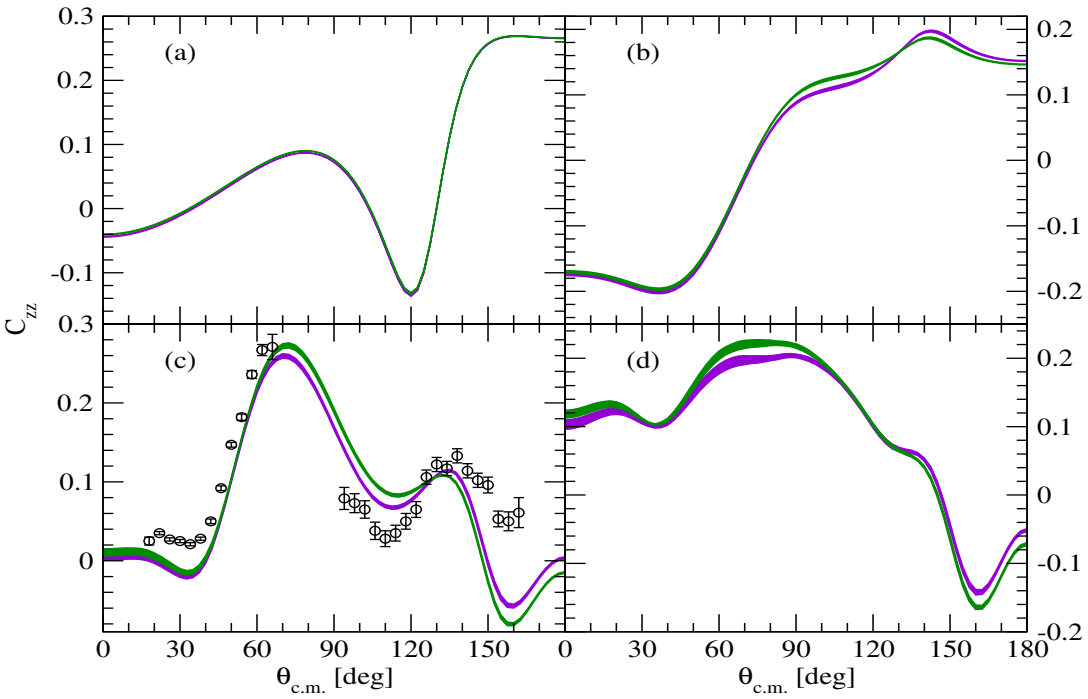

Figure 5.44: Same as in Figure 5.42, but for the spin correlation coefficient C_{zz}. The experimental data are the same as in Figure 5.12.

Finally, in Figures 5.42 – 5.44 I compare the statistical errors computed using the chiral N4LO+ SMS force with two values $\Lambda = 450$ MeV and $\Lambda = 550$ MeV, again for the differential cross section $d\sigma/d\Omega$, the deuteron vector analyzing power iT_{11} and the spin correlation coefficient C_{zz}. As can be seen, in all cases the two bands corresponding to the statistical uncertainty have similar widths at given scattering angle. We may conclude, that used regulator value has no significant effect to the magnitude of statistical uncertainty, however, the uncertainty obtained with $\Lambda = 450$ MeV is usually slightly smaller than this for $\Lambda = 550$ MeV.

To summarize shortly this part of my thesis, I conclude that:

- All theoretical errors for higher orders of chiral force and the OPE-Gaussian potential are small (very small below about 100 MeV) and, in general, remain smaller than experimental ones.
- The statistical uncertainty is usually smaller than the truncation errors.
- The magnitudes of statistical uncertainties obtained with the chiral N^{4}LO SMS force and the OPE-Gaussian potential are found to be similar.
- The magnitude of statistical uncertainty is smaller than the uncertainty of predictions induced by different values of the cutoff parameter.
- We observe the same picture for the differential cross section and for the polarization observables.

5.2 Results for the deuteron breakup reaction

In the case of the neutron induced deuteron breakup reaction a few kinematical configurations were selected to exemplify only the statistical uncertainties for observables in this process.

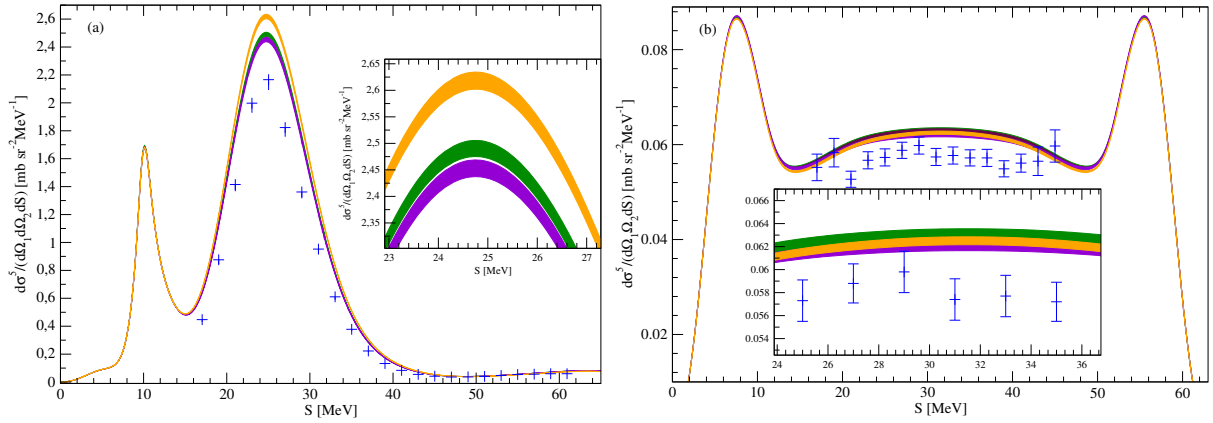

Figure 5.45: The five-fold cross section $\frac{d^5\sigma}{d\Omega_1 d\Omega_2 dS}$ for the $d(n, n_1 n_2)p$ breakup reaction at the incoming nucleon laboratory kinetic energy $E_{\rm lab}$= 65 MeV for the following directions of momenta of outgoing neutrons: (a) $\theta_1 = 30.5°, \theta_2 = 59.5°, \phi_{12} = 180°$ (QFS configuration) and (b) $\theta_1 = \theta_2 = 54.0°, \phi_{12} = 120°$ (SST configuration). The orange, green and violet bands represent statistical uncertainties obtained with the OPE-Gaussian force, the chiral N^{4}LO and N^{4}LO+ (Λ = 450 MeV), respectively. The experimental data are from Ref. [132] for (a) and from Ref. [133] for (b).

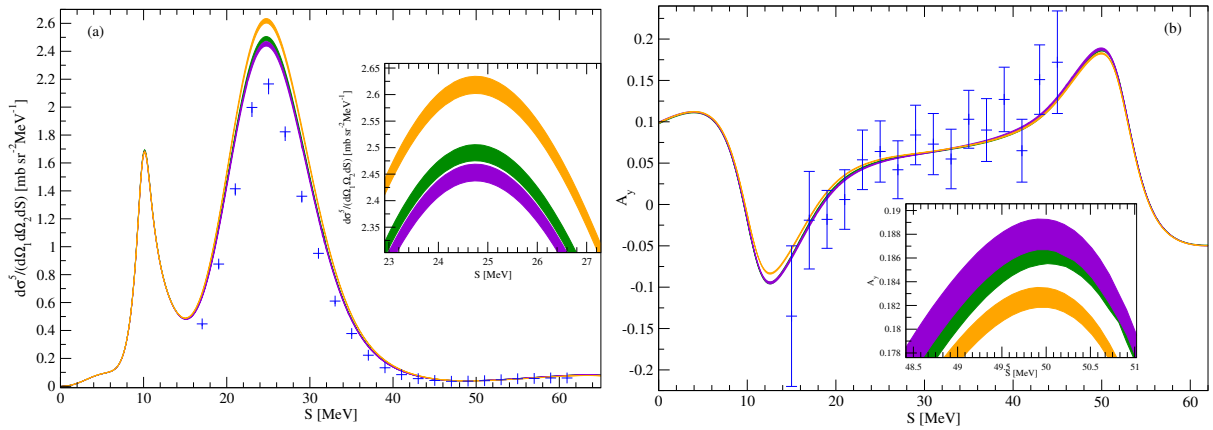

Figure 5.46: The neutron vector analyzing power A_y(n) for the $d(n, n_1 n_2)p$ breakup reaction at the incoming nucleon laboratory kinetic energy $E_{\rm lab}$= 65 MeV for the following directions of momenta of outgoing neutrons: (a) $\theta_1 = 30.5°, \theta_2 = 59.5°, \phi_{12} = 180°$ and (b) $\theta_1 = \theta_2 = 54.0°, \phi_{12} = 120°$. Curves and bands are as in Figure 5.45. Data are from Ref. [132].

Acting in the same way as for elastic nd scattering, the theoretical statistical uncertainties of 3N observables due to the uncertainty of the parameters of the SMS NN potential are estimated. Figure 5.45 shows these uncertainties for the nd breakup cross section, obtained using the chiral SMS potential with Λ = 450 MeV at two orders of

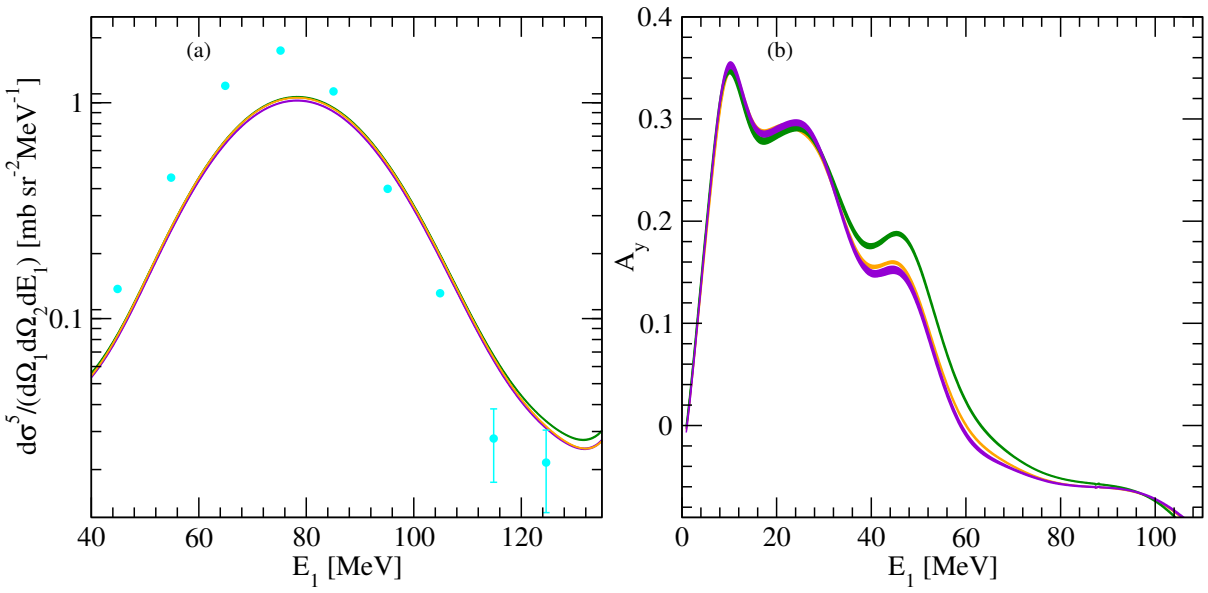

Figure 5.47: (color online) (a) The five-fold differential cross section $\frac{d^5\sigma}{d\Omega_1 d\Omega_2 dE_1}$ for the directions of momenta of outgoing neutrons $\theta_1 = 45.0°, \theta_2 = 35.0°, \phi_{12} = 180°$ and (b) the neutron vector analyzing power for the $d(n, n_1 n_2)p$ breakup reaction for $\theta_1 = 52.0°, \theta_2 = 45.0°, \phi_{12} = 180°$ at the incoming nucleon laboratory kinetic energy $E_{\rm lab} = 200$ MeV. Curves and bands are as in Figure 5.45. The experimental data are for (a) from Ref. [134].

chiral expansion, N^{4}LO and N^{4}LO$^+$, and compares them with the results from the OPE-Gaussian interaction. The magnitudes of statistical uncertainties for the cross section reach their maximum approximately at $S =$ 25 MeV for the quasi-free scattering (QFS) configuration in Figure 5.45(a). Predictions obtained with the chiral N^{4}LO and N^{4}LO$^+$ potentials (at $\Lambda =$ 450 MeV) slightly differ one each other but the OPE-Gaussian force based results are clearly separated from the chiral predictions. For the SSI configuration (Figure 5.45(b)) the predictions obtained by the same potentials overlap each other.

In Figures 5.46(a) and 5.46(b) I show examples of the neutron vector analyzing power for the QFS and SST configurations at $E_{\rm lab} = 65$ MeV, respectively. Here the statistical uncertainties remain negligible for both configurations. The differences between predictions based on the OPE-Gaussian force and the chiral potentials at N^{4}LO and N^{4}LO$^+$ amounts up to 7% as seen in the maximum of the A_y(n) for the SST configuration. Figure 5.47 exemplifies that at higher energy, $E_{\rm lab} = 200$ MeV the statistical uncertainties remain small. It is also interesting to note, that for the breakup process there exist kinematical configurations for which a clear difference between chiral predictions at N^{4}LO and N^{4}LO$^+$ is observed. It is shown in Figure 5.47(b), where the calculations of the nucleon analyzing power around $S = 100$ MeV leads to nearly 14% difference between predictions at these two orders of the chiral expansion. Such configurations and observables are interesting in context of studying higher order contributions to the chiral forces. Thus, concluding my findings for inelastic Nd scattering I find that statistical errors remain still small in the deuteron breakup process at the considered kinematical configurations independently from the employed NN force model.

Chapter 6

Correlations among 2N and 3N observables and potential parameters

6.1 Correlations among two-nucleon observables

Before proceeding to the results on the systematic analysis of the correlation coefficients in 2N and 3N systems, I would like to point the reader's attention to a few points. When fixing potential parameters, an appropriate set of experimental results should be used. Traditionally, all available 2N data (the deuteron binding energy, the np scattering cross section and numerous polarization observables) are taken into account. Such a choice yields precise values of free parameters but, in turn, models fixed in that way have only a moderate predictive power in the two-body system restricted to other observables, energies and angular ranges. In addition, if correlated observables are used during the fixing procedure, the obtained values of parameters can be biased. The sensitivity of a given observable to the potential parameters is another important question. Clearly using the observables which are not sensitive to the given potential parameter does not allow one to precisely fix the value of that parameter. Such a doubtful fixing procedure leads to questionable predictions of the considered potential model.

The JISP16 potential [142] serves as a good example. This potential was fitted to some bound and excited states of light nuclei up to ^{16}O. It delivers a reasonable description of the nuclear states [143] and has been even used to predict for the first time the existence of ^{19}F nucleus [144]. However, our application of this force to Nd elastic scattering at low energies [145] revealed that parameters responsible for p-waves in this interaction are wrong as the JIPS16 is not able to describe the nucleon analyzing power A_y in the Nd elastic scattering process. This observable is known to be very sensitive to the p-wave components of the NN interaction. The reason why the JISP16 treats the p-waves incorrectly is the fact that the observables taken into account during the fitting procedure for this force are not sensitive enough to the NN interaction in this partial wave. Thus the JISP16 model requires refitting to other observables, more sensitive to the interaction in the p-waves. This example shows that knowledge of the sensitivity of specific observables to potential parameters acting in given partial waves can bring valuable information for setting the potential parameters. Of course, one has to be aware that the sensitivity of various observables to the same potential parameter makes these observables correlated. Having separate, complete information about the correlations among the observables themselves and between observables and potential parameters will allow us to better understand the nature of the (potentially) observed correlation. It is also well known

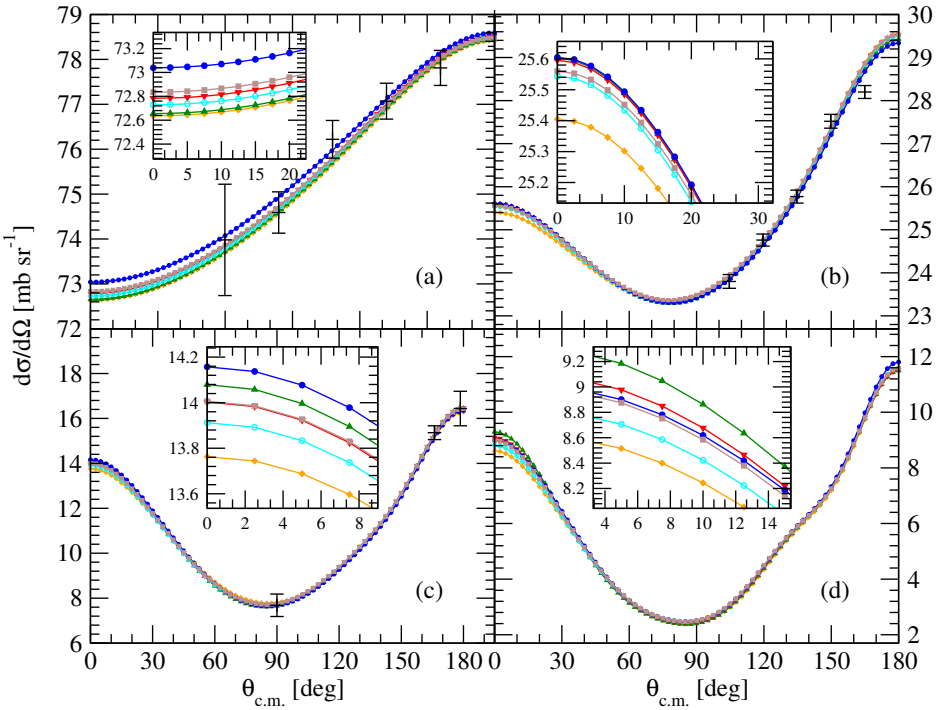

Figure 6.1: The differential np elastic scattering cross section $\mathrm{d}\sigma/\mathrm{d}\Omega\,[\mathrm{mb\ sr}^{-1}]$ at the incoming neutron laboratory energy (a) $E_{\mathrm{lab}} = 10$ MeV, (b) $E_{\mathrm{lab}} = 30$ MeV, (c) $E_{\mathrm{lab}} = 65$ MeV and (d) $E_{\mathrm{lab}} = 135$ MeV as a function of the c.m. scattering angle $\theta_{c.m.}$. The orange diamonds, green triangles up, red triangles down, open cyan circles, and blue circles represent results obtained with the central values of the chiral N^{2}LO, N^{3}LO, N^{4}LO, N^{4}LO$^+$ ($\Lambda = 450$ MeV) SMS and OPE-Gaussian potential parameters, respectively, and the brown squares show predictions based on the CD-Bonn potential [53]. The experimental data are in: (a) from Ref. [135] (np black pluses), (b) from Ref. [136] (np black pluses, $E_{\mathrm{lab}} = 29.90$ MeV) and in (c) from Ref. [137] (np black pluses).

that some observables are trivially correlated by fundamental symmetries, such as time reversal symmetry, for example, nucleon-nucleon analyzing power is related to the induced polarization of nucleons observed in the final state [146].

In Subsection 4.2.2, a brief description of our method to calculate the elastic 2N scattering observables is presented. The computation of the 2N scattering observables requires calculation of the transition amplitude between initial and final 2N states. To this end the Lippmann-Schwinger equation is solved for each of the investigated models of NN interaction and all sets of parameter values.

Before turning to correlation coefficients, in Figures 6.1 – 6.8 I demonstrate our results for the set of eight np observables as a function of the c.m. scattering angle at four representative incident neutron energies: $E_{\mathrm{lab}} = 10, 30, 65$ and 135 MeV. These results base on the central values of potential parameters of the chiral N^{2}LO, N^{4}LO, N^{4}LO$^+$ SMS (with the regulator parameter $\Lambda = 450$ MeV), the OPE-Gaussian and the CD-Bonn potentials. In general, various potentials lead to similar predictions, and only for a few observables, there is a visible spread of predictions at lower and higher energies. This agreement is not surprising as all potentials deliver a very good description of the np phase shifts.

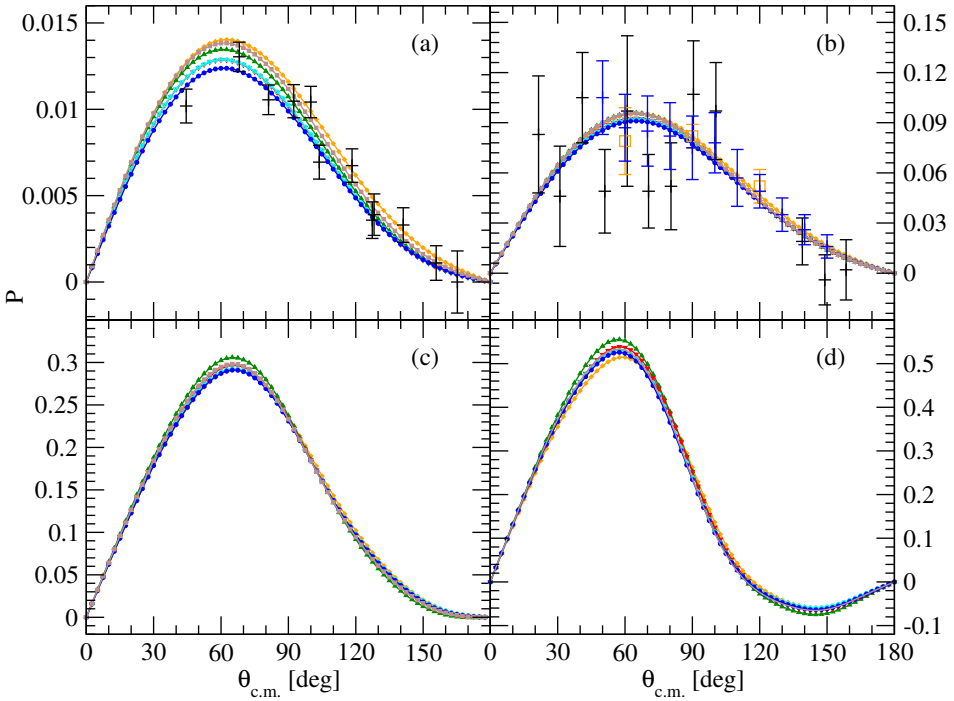

Figure 6.2: The polarization P in np scattering at the incoming neutron laboratory energy (a) $E_{\rm lab} = 10$ MeV, (b) $E_{\rm lab} = 30$ MeV, (c) $E_{\rm lab} = 65$ MeV and (d) $E_{\rm lab} = 135$ MeV as a function of the c.m. scattering angle $\theta_{c.m.}$. Curves are as in Figure 6.1. The experimental data are in: (a) from Ref. [138] (np black pluses, $E_{\rm lab} = 10.03$ MeV), (b) from Ref. [139] (open np orange squares, $E = 29.60$ MeV), Ref. [140] (np blue pluses, $E_{\rm lab} = 29.60$ MeV) and Ref. [141] (np black pluses).

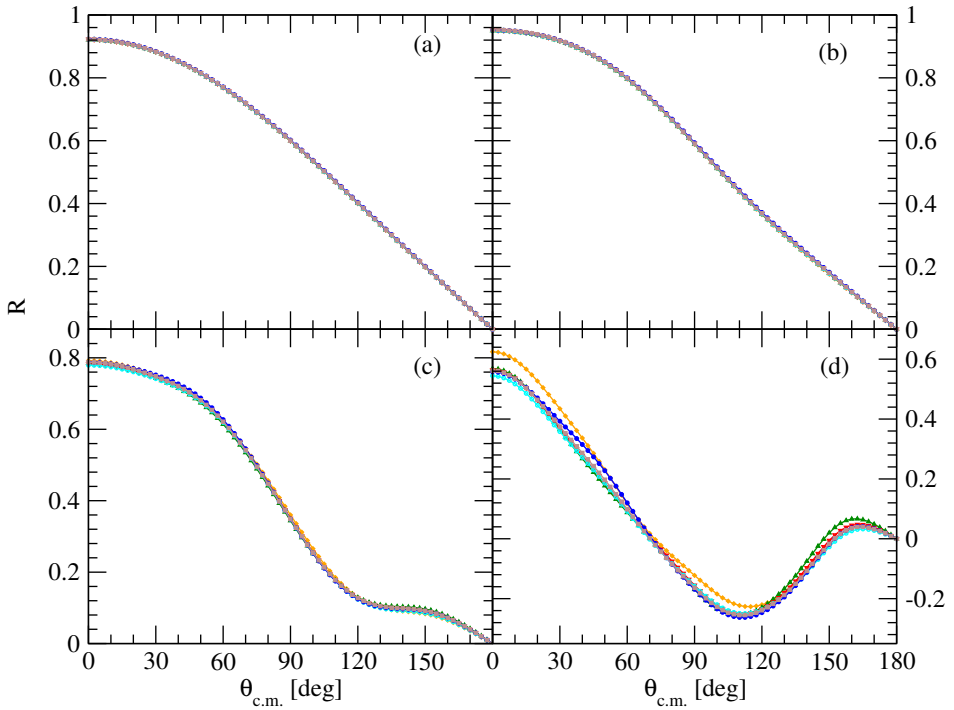

Figure 6.3: The depolarization R in np scattering at the incoming neutron laboratory energy (a) $E_{\rm lab} = 10$ MeV, (b) $E_{\rm lab} = 30$ MeV, (c) $E_{\rm lab} = 65$ MeV and (d) $E_{\rm lab} = 135$ MeV as a function of the c.m. scattering angle $\theta_{c.m.}$. Curves are as in Figure 6.1.

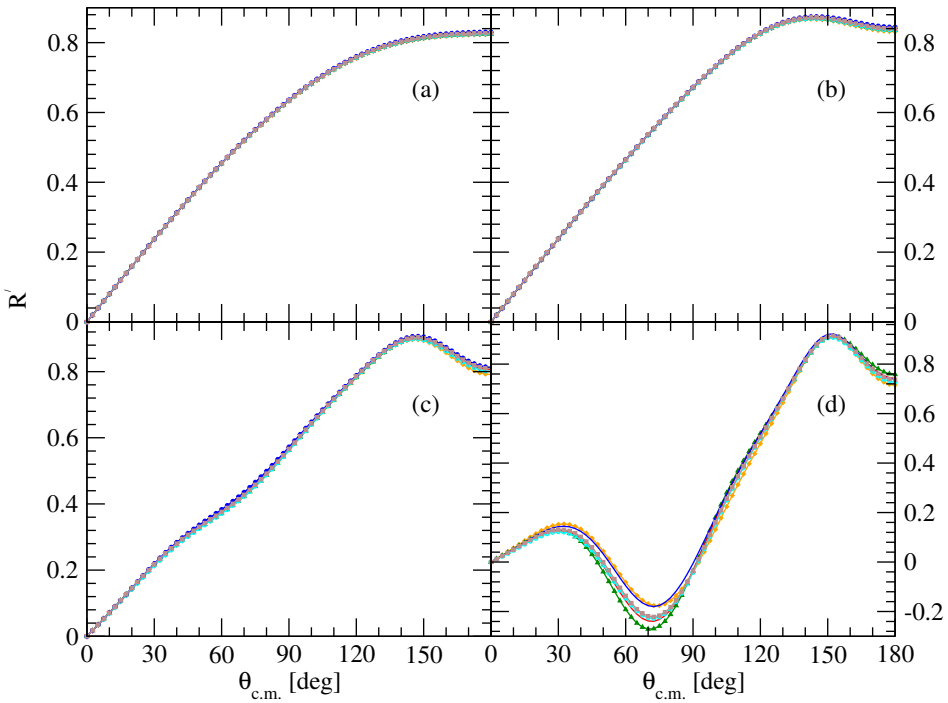

Figure 6.4: The depolarization R' in np scattering at the incoming neutron laboratory energy (a) $E_{\rm lab} = 10$ MeV, (b) $E_{\rm lab} = 30$ MeV, (c) $E_{\rm lab} = 65$ MeV and (d) $E_{\rm lab} = 135$ MeV as a function of the c.m. scattering angle $\theta_{c.m.}$. Curves are as in Figure 6.1.

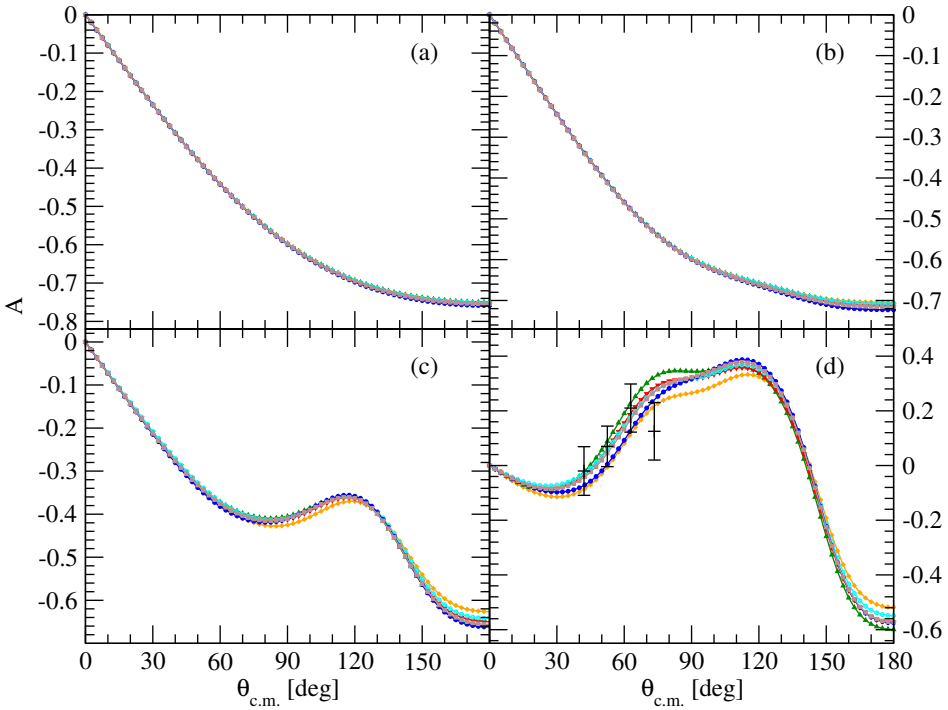

Figure 6.5: The asymmetry A in np scattering at the incoming neutron laboratory energy (a) $E_{\rm lab} = 10$ MeV, (b) $E_{\rm lab} = 30$ MeV, (c) $E_{\rm lab} = 65$ MeV and (d) $E_{\rm lab} = 135$ MeV as a function of the c.m. scattering angle $\theta_{c.m.}$. Curves are as in Figure 6.1. Data in (d) are from [147].

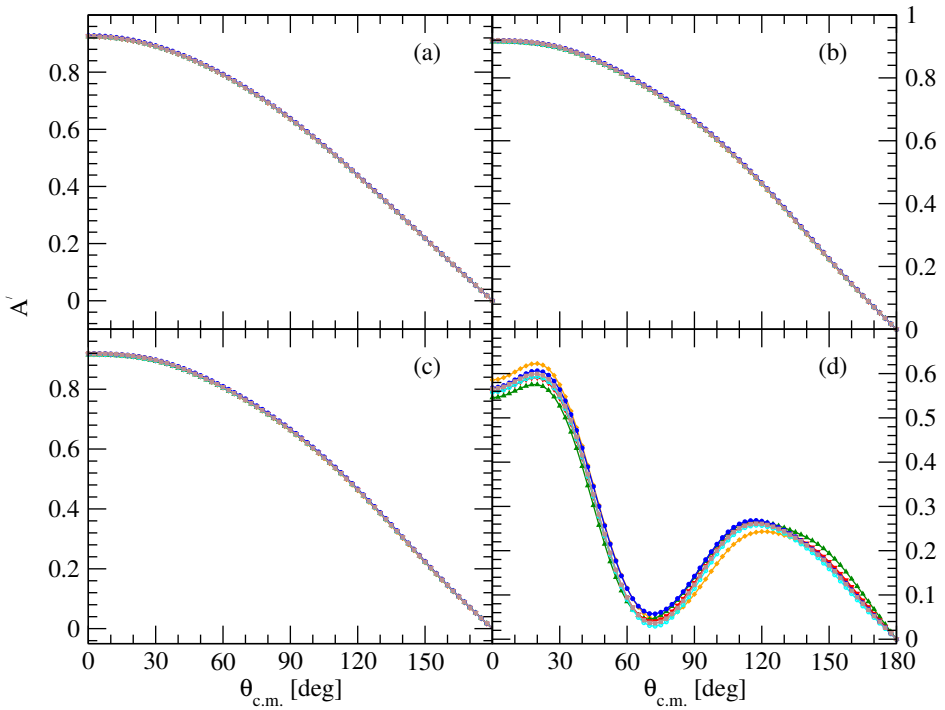

Figure 6.6: The asymmetry A' in np scattering at the incoming neutron laboratory energy (a) $E_{\rm lab} = 10$ MeV, (b) $E_{\rm lab} = 30$ MeV, (c) $E_{\rm lab} = 65$ MeV and (d) $E_{\rm lab} = 135$ MeV as a function of the c.m. scattering angle $\theta_{c.m.}$. Curves are as in Figure 6.1.

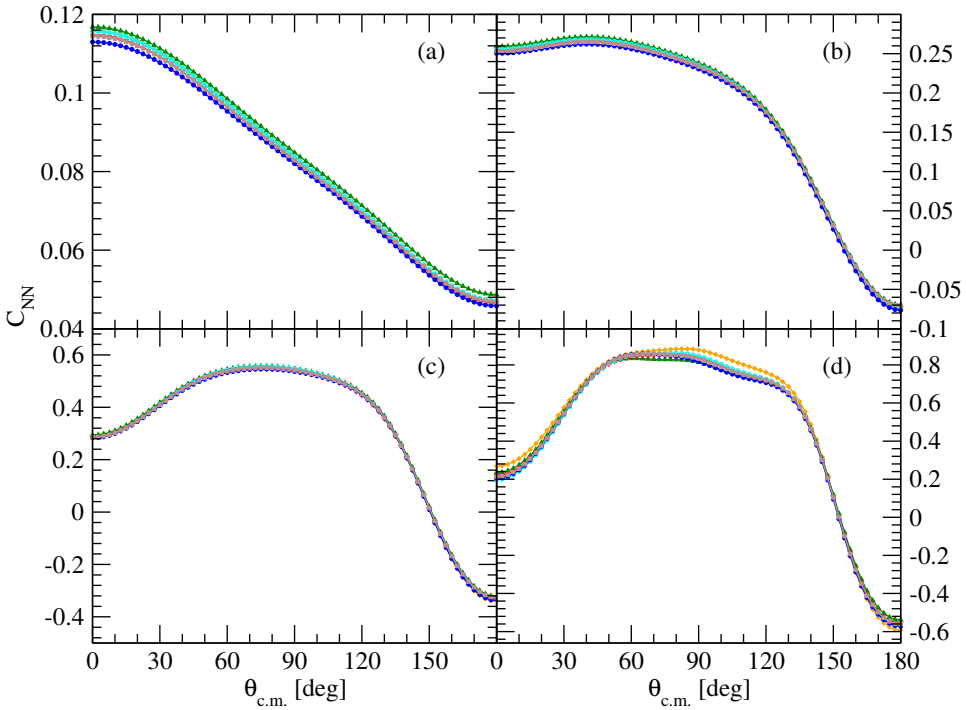

Figure 6.7: The spin correlation parameter C_{NN} in np scattering at the incoming neutron laboratory energy (a) $E_{\rm lab} = 10$ MeV, (b) $E_{\rm lab} = 30$ MeV, (c) $E_{\rm lab} = 65$ MeV and (d) $E_{\rm lab} = 135$ MeV as a function of the c.m. scattering angle $\theta_{c.m.}$. Curves are as in Figure 6.1.

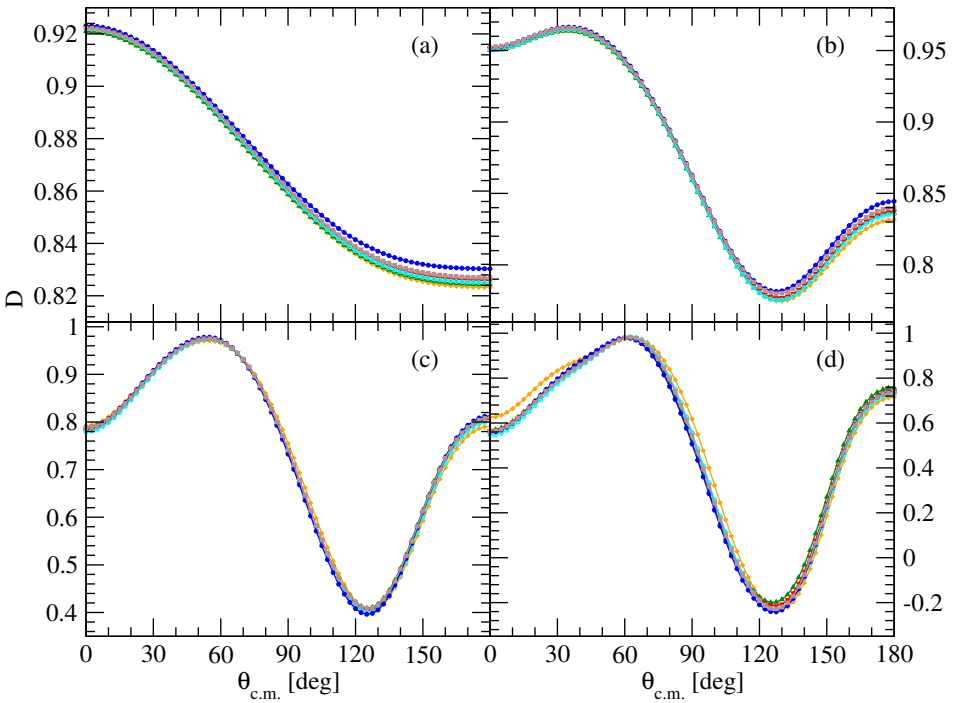

Figure 6.8: The spin transfer coefficient D in np scattering at the incoming neutron laboratory energy (a) $E_{\rm lab} = 10$ MeV, (b) $E_{\rm lab} = 30$ MeV, (c) $E_{\rm lab} = 65$ MeV and (d) $E_{\rm lab} = 135$ MeV as a function of the c.m. scattering angle $\theta_{c.m.}$. Curves are as in Figure 6.1.

In the cases of the OPE-Gaussian and the chiral potentials, we are able to estimate a correlation coefficients between observables (see Chapter 3.2). This is demonstrated in Figures 6.9 – 6.14. We use the same 50 sets of potential parameters as in Chapter 5, but we also add 50 more new sets of parameters for testing proposes. In following the corresponding correlation coefficients are denoted by r_{50}, r'_{50} (new), and their association r_{100}, respectively.

Figure 6.9 demonstrates the scatter plots for pairs of observables: the differential cross section $d\sigma/d\Omega$ and the depolarization R and for $d\sigma/d\Omega$ and the asymmetry A', at two nucleon laboratory energies $E_{\rm lab} = 10$ and 135 MeV, and at the c.m. scattering angles $\theta_{c.m.} = 50°$ and 150°. One can see strong positive correlation at $E_{\rm lab} = 10$ MeV for both scattering angles, and both pairs of observables, i.e., for $(d\sigma/d\Omega, R)$ $r_{50} = 0.95$ and $r_{100} = 0.93$ at $\theta_{c.m.} = 50°$, $r_{50} = 0.82$ and $r_{100} = 0.80$ at $\theta_{c.m.} = 150°$, and for $(d\sigma/d\Omega, A')$ $r_{50} = 0.88$ and $r_{100} = 0.87$ at $\theta_{c.m.} = 50°$, $r_{50} = 0.83$ and $r_{100} = 0.78$ at $\theta_{c.m.} = 150°$. At the highest of considered energies $E_{\rm lab} = 135$ MeV, the correlation coefficients are much smaller $r_{50} = 0.29$ and $r_{100} = 0.37$ at $\theta_{c.m.} = 50°$, and at $\theta_{c.m.} = 150°$ a weak anticorrelation is visible, e.g. $r_{50} = -0.40$ and $r_{100} = -0.44$ for $(d\sigma/d\Omega, R)$ pair, and $r_{50} = 0.24$ and $r_{100} = 0.27$ at $\theta_{c.m.} = 50°$, $r_{50} = -0.35$ and $r_{100} = -0.41$ at $\theta_{c.m.} = 150°$ for $(d\sigma/d\Omega, A')$ pair. While a small (around 5%) difference between r_{50} and r_{100} is seen, the qualitative picture (also seen in figures) remains unchanged with the increasing size of a sample.

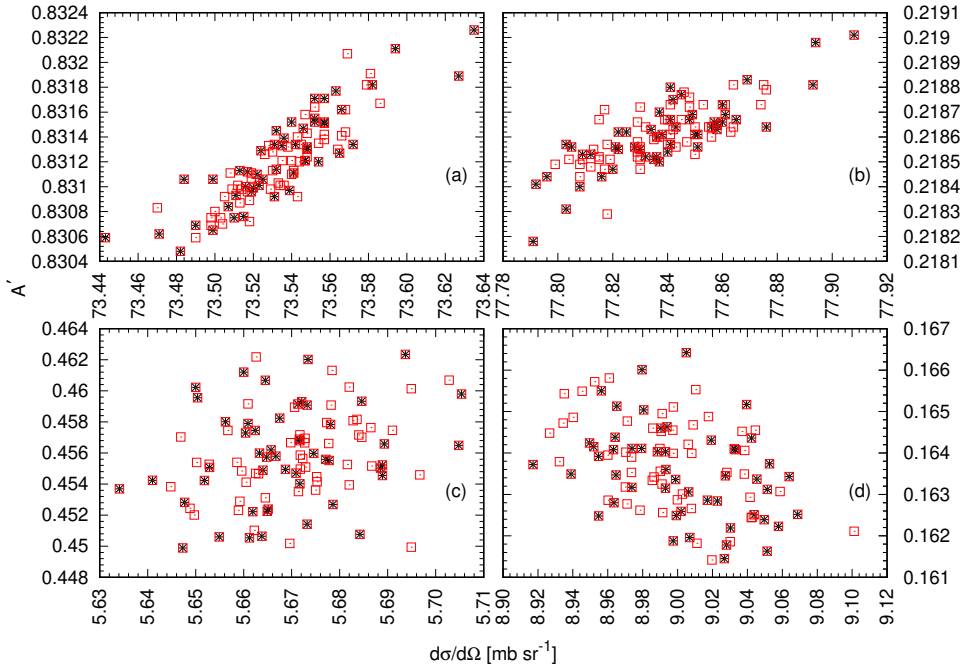

Figure 6.9: The scatter plots for $(d\sigma/d\Omega, A')$ in np scattering at the c.m. scattering angle $\theta_{c.m.} = 50°$ (left) and $\theta_{c.m.} = 150°$ (right) and at the incoming neutron laboratory energy $E_{\rm lab} = 10$ MeV (a, b) and 135 MeV (c, d) based on 50 sets (the black stars) and 100 sets (old 50 + new 50) (the open red squares) of potential parameters of the chiral N^{4}LO SMS ($\Lambda = 450$ MeV) potential.

As one more test of my method, in Figures 6.10 – 6.11, I show again the scatter plots for $(d\sigma/d\Omega, R)$ and (P, A) calculated with two 50 sampled sets of potential parameters of the chiral SMS force at N^{4}LO chiral order. As is seen from Figure 6.10, there are no any unexpected gaps in results for the $(d\sigma/d\Omega,\, R)$ pair at the aforementioned scattering energies and angles. At $E_{\rm lab} = 10$ MeV the correlation coefficients reach $r_{50} = 0.95$ and $r'_{50} = 0.90$ at $\theta_{c.m.} = 50°$, $r_{50} = 0.82$ and $r'_{50} = 0.75$ at $\theta_{c.m.} = 150°$; at $E_{\rm lab} = 135$ MeV the correlation coefficients are $r_{50} = 0.29$ and $r'_{50} = 0.47$ at $\theta_{c.m.} = 50°$, and $r_{50} = -0.40$ and $r'_{50} = -0.46$ at $\theta_{c.m.} = 150°$. For two differently sampled 50 sets of potential parameters, predictions are mixed and resulting correlation coefficients are in qualitative agreement.

The relationship between polarization P and asymmetry A demonstrates case of uncorrelated observables (Figure 6.11). Here, at $E_{\rm lab} = 10$ MeV the correlation coefficients are $r_{50} = 0.09$ and $r'_{50} = 0.16$ at $\theta_{c.m.} = 50°$, $r_{50} = -0.06$ and $r'_{50} = -0.31$ at $\theta_{c.m.} = 150°$. At $E_{\rm lab} = 135$ MeV we get $r_{50} = -0.15$ and $r'_{50} = -0.30$ at $\theta_{c.m.} = 50°$, but at $\theta_{c.m.} = 150°$ we obtain $r_{50} = 0.43$ and $r'_{50} = 0.58$. We observe significant differences for correlation coefficients between P and A (Figure 6.11) for two probes of 50 sets of parameters, r_{50} and r'_{50}. However, since they remain small, our conclusion on the lack of correlation between P and A is valid for both samples.

Basing on these observations we can conclude that 50 sampled sets of potential parameters, in principle, are sufficient to perform correlation analysis among 2N scattering observables. This encourages us to stay with a 50-element sample in the following.

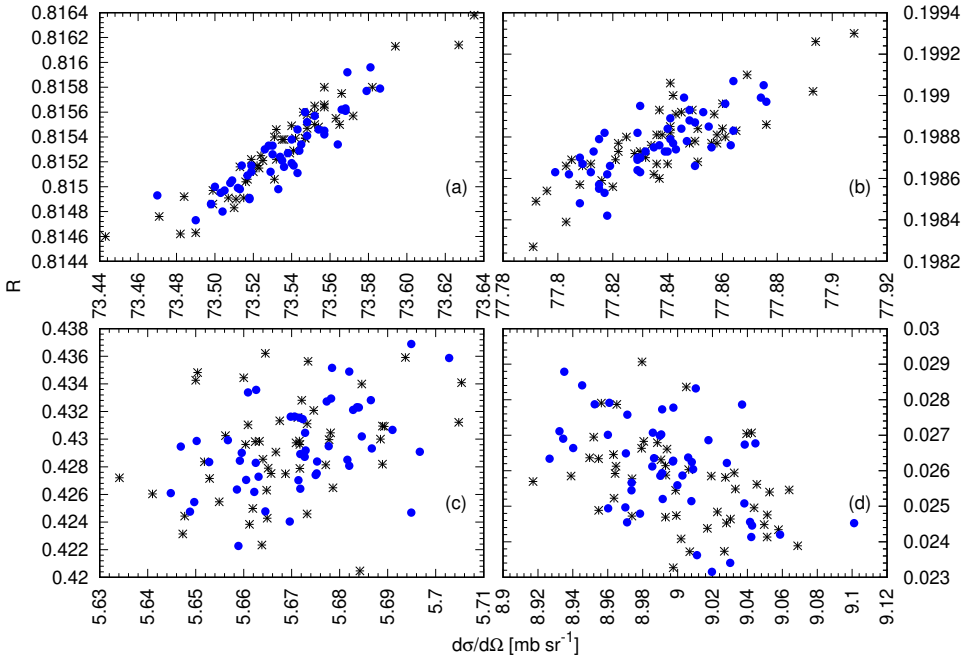

Figure 6.10: The scatter plots for the differential cross section $d\sigma/d\Omega$ and the depolarization R in np scattering at the c.m. scattering angle $\theta_{c.m.} = 50°$ (left) and $\theta_{c.m.} = 150°$ (right) and at the incoming neutron laboratory energy $E_{\rm lab} = 10$ MeV (top) and 135 MeV (bottom) based on the previously used 50 sets (the black stars) and the new generated 50 sets (the blue dots) of potential parameters of the chiral N^{4}LO SMS potential.

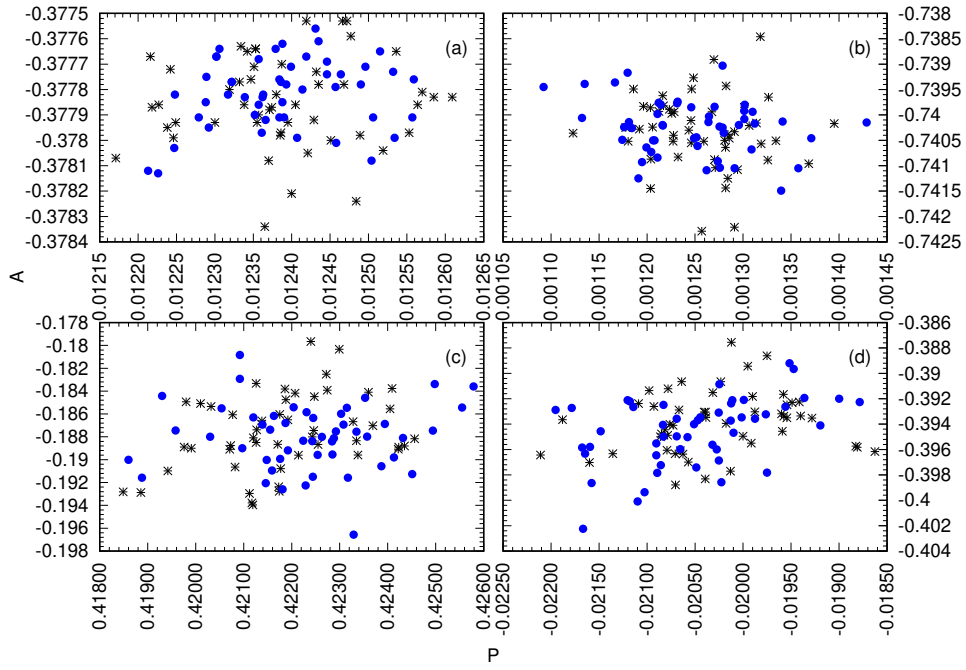

Figure 6.11: The scatters plot for P and A in np scattering at the c.m. scattering angle $\theta_{c.m.} = 50°$ (left) and $\theta_{c.m.} = 150°$ (right) and at the incoming neutron laboratory energy $E_{\rm lab} = 10$ MeV (top) and 135 MeV (bottom). Symbols are the same as in Figure 6.10.

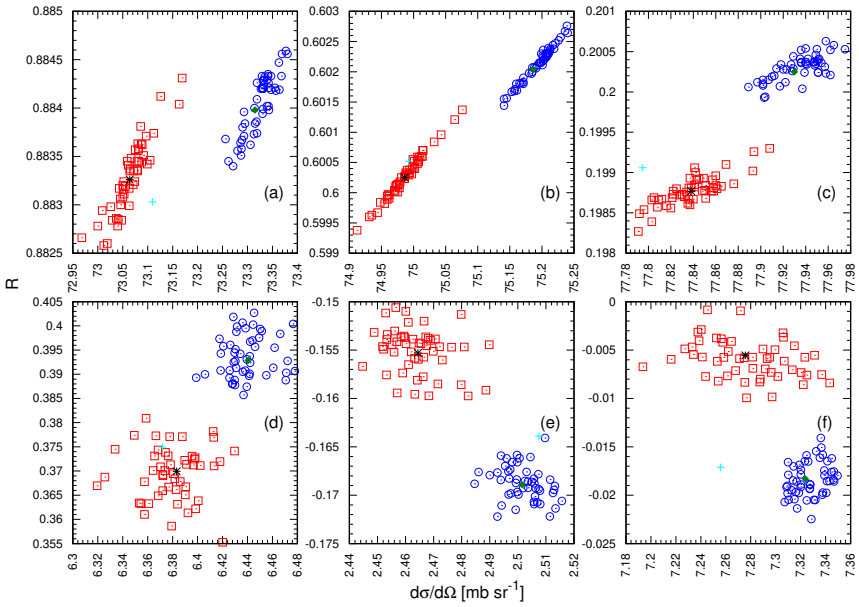

Figure 6.12: The scatter plots for the np differential cross section $d\sigma/d\Omega$ and the depolarization R at the c.m. scattering angle $\theta_{c.m.} = 30°$ (left), $\theta_{c.m.} = 90°$ (middle), and $\theta_{c.m.} = 150°$ (right) and at the incoming neutron laboratory energy $E_{\rm lab} = 10$ MeV (top) and $E_{\rm lab} = 135$ MeV (bottom). The open blue circles and red squares represent 50 sets of potential parameters of the chiral N^{4}LO ($\Lambda = 450$ MeV) SMS force and the OPE-Gaussian potential, respectively; the single black star and the single green diamond show predictions obtained with the central values of the chiral N^{4}LO ($\Lambda = 450$ MeV) SMS and OPE-Gaussian potential parameters, respectively, and the single cyan plus represent predictions based on the CD-Bonn potential [53].

In Figures 6.12 – 6.14 I summarize my results on dependences between 2N scattering observables based on the two models (the OPE-Gaussian and the chiral N^{4}LO SMS potentials) using the first 50 sets of potential parameters. I also compare those results with predictions of the CD-Bonn force. The top panel in Figure 6.12 visualizes a strong positive correlation between the differential cross section $d\sigma/d\Omega$ and the depolarization observable R at $E_{\rm lab} = 10$ MeV and at three scattering angles $\theta_{c.m.} = 30°$, $90°$, $150°$ with the corresponding magnitudes of the correlation coefficients $r(\theta_{c.m.} = 30°) = 0.91$, $r(\theta_{c.m.} = 90°) = 0.99$, $r(\theta_{c.m.} = 150°) = 0.82$ for the chiral N^{4}LO SMS force ($r(\theta_{c.m.} = 30°) = 0.88$, $r(\theta_{c.m.} = 90°) = 0.989$, $r(\theta_{c.m.} = 150°) = 0.72$ for the OPE-Gaussian potential). For $E_{\rm lab} = 135$ MeV and the three scattering angles, the scatter plots in the bottom row of Figure 6.12, indicate a weak correlation between the pair $(d\sigma/d\Omega, R)$ for both potentials. An analysis of Figure 6.13 leads to conclusion that the $d\sigma/d\Omega$ is weakly correlated with P independently of the mentioned NN potentials, scattering energy, and angle (in fact, that is true for the entire interval of $\theta_{c.m.}$). Another behavior of correlation for the (R, D) pair is shown in Figure 6.14. While at $E_{\rm lab} = 10$ MeV a strong positive correlation occures for three scattering angles, at $E_{\rm lab} = 135$ MeV correlation changes from strong positive to almost negligible, depending on scattering angle. As was expected the symbols (the black star and the green diamond) associated with values of an individual observable obtained with the central values of potential parameters are disposed within the corresponding cloud of 50 values. In addition, comparing all the predictions, we see that in most cases CD-Bonn results lie within the spread of 50 values obtained from the OPE-Gaussian potential, sometimes CD-Bonn results are inside the N^{4}LO cloud.

However, there are also cases, like the $(d\sigma/d\Omega, P)$ pair (top row of Figure 6.13) when the predictions for these observables, especially for P, based on the CD-Bonn potential differs significantly from the predictions obtained with the central values of the chiral N^{4}LO SMS and OPE-Gaussian potential parameters.

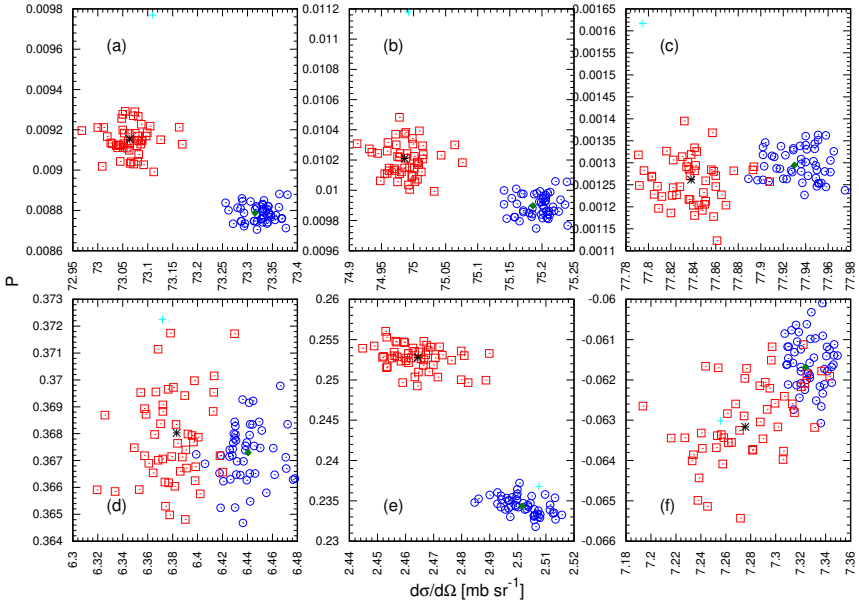

Figure 6.13: The scatter plots for the np differential cross section $d\sigma/d\Omega$ and the polarization P at the c.m. scattering angle $\theta_{c.m.} = 30°$ (left), $\theta_{c.m.} = 90°$ (middle), and $\theta_{c.m.} = 150°$ (right) and at the incoming neutron laboratory energy $E_{\rm lab} = 10$ MeV (top) and $E_{\rm lab} = 135$ MeV (bottom). Symbols are the same as in Figure 6.12.

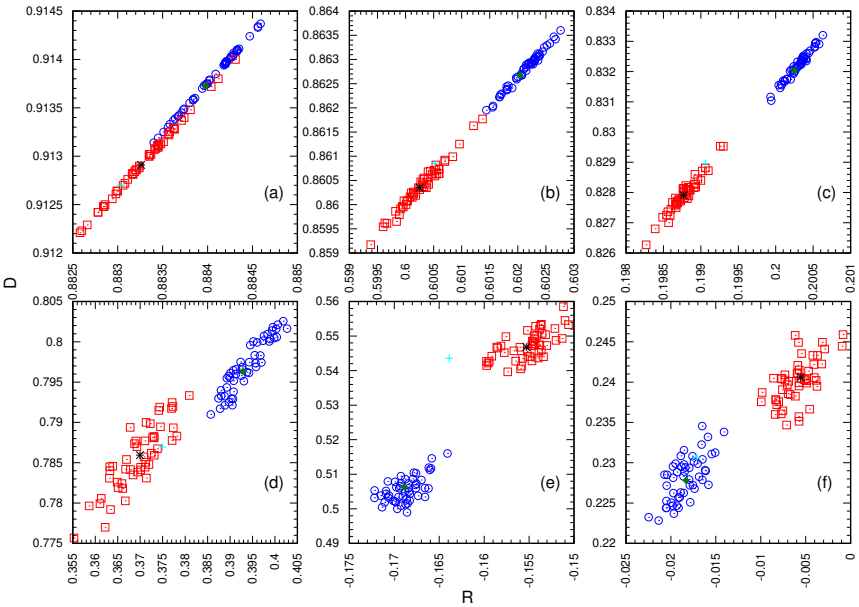

Figure 6.14: The scatter plots for the np depolarization R and the spin transfer coefficient D at the c.m. scattering angle $\theta_{c.m.} = 30°$ (left), $\theta_{c.m.} = 90°$ (middle), and $\theta_{c.m.} = 150°$ (right) and at the incoming neutron laboratory energy $E_{\rm lab} = 10$ MeV (top) and $E_{\rm lab} = 135$ MeV (bottom). Symbols are the same as in Figure 6.12.

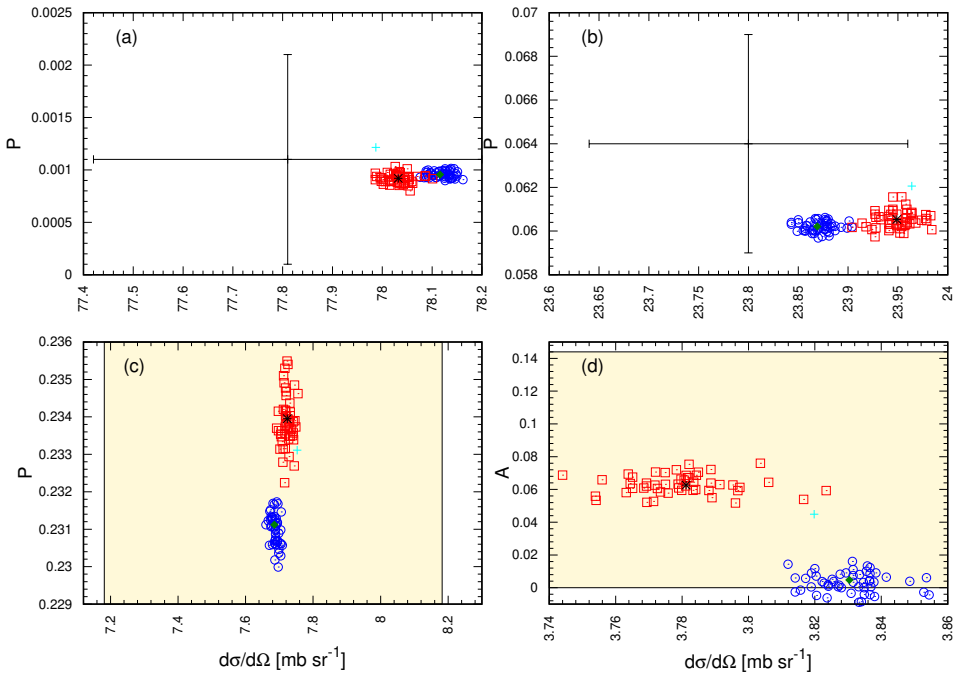

Figure 6.15: The scatter plots for selected np scattering observables: (a, b, c) $d\sigma/d\Omega$ and P, and (d) $d\sigma/d\Omega$ and A at the incoming neutron laboratory energy and at c.m. scattering angle (a) $E_{\rm lab} = 10$ MeV, $\theta_{c.m.} = 155°$, (b) $E_{\rm lab} = 30$ MeV, $\theta_{c.m.} = 105°$, (c) $E_{\rm lab} = 65$ MeV, $\theta_{c.m.} = 90°$, and (d) $E_{\rm lab} = 135$ MeV, $\theta_{c.m.} = 52.5°$. The open blue circles and red squares represent 50 sets of potential parameters of the chiral N^{4}LO SMS force and the OPE-Gaussian potential, respectively; the black star and the green diamond show predictions obtained with the central values of the chiral N^{4}LO ($\Lambda = 450$ MeV) SMS and OPE-Gaussian potential parameters, respectively, and the cyan plus represent predictions based on the CD-Bonn potential. The experimental data (np black plus and light-golden band) are in: (a) from Ref. [135] ($E_{\rm lab} = 10$ MeV and $\theta_{c.m.} = 155.94°$), (b) from Ref. [136] ($E_{\rm lab} = 29.90$ MeV and $\theta_{c.m.} = 104.6°$), (c) from Ref. [137] ($E_{\rm lab} = 65$ MeV and $\theta_{c.m.} = 90°$), and (d) from Ref. [147] ($E_{\rm lab} = 135$ MeV and $\theta_{c.m.} = 52.5°$).

Last but not least, in addition to displaying the scatter plots for theoretical results, it is interesting to compare predictions with the available experimental data. Figure 6.15 shows such examples for $(d\sigma/d\Omega, P)$ and $(d\sigma/d\Omega, A)$ pairs. As seen from the top panel all theoretical predictions are in the range of experimental data point (the black plus). At the bottom panel, due to the lack of data for P at $E_{\rm lab} = 65$ MeV and $d\sigma/d\Omega$ at $E_{\rm lab} = 135$ MeV we represent only a vertical band or horizontal band, reflecting available data. Summing up, we conclude that for presented pairs of 2N observables very good agreement between predictions and data is observed.

While scatter plots illustrate predictions at a given scattering angle, it is also interesting to study the dependence of correlation coefficients on the scattering angle. Thus, let us consider now the angular dependence of selected correlation coefficients for pairs of 2N observables as functions of the c.m. scattering angle in the range of $\theta_{c.m.} \in [12.5°, 167.6°]$ [1], shown in Figures 6.16 – 6.21.

[1]This interval was chosen to avoid, divergences occurring due to division by a very small value or by zero for $\theta_{c.m.} = 0°$ or $\theta_{c.m.} = 180°$ when the variance of observable tends to zero

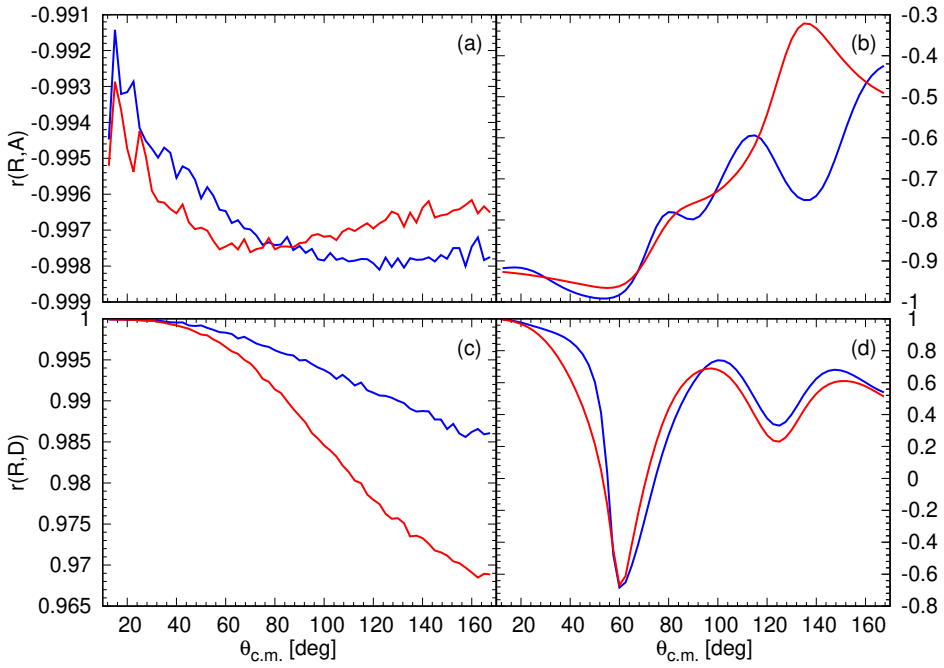

Figure 6.16: The angular dependence of correlations coefficients between np scattering observables: (R, A) (top) and (R, D) (bottom) at the incoming neutron laboratory energy $E_{\rm lab} = 10$ MeV ((a) and (c)), and $E_{\rm lab} = 135$ MeV ((b) and (d)). The solid red curve represents predictions of the chiral N^{4}LO SMS force and the blue curve shows predictions based on the OPE-Gaussian potential.

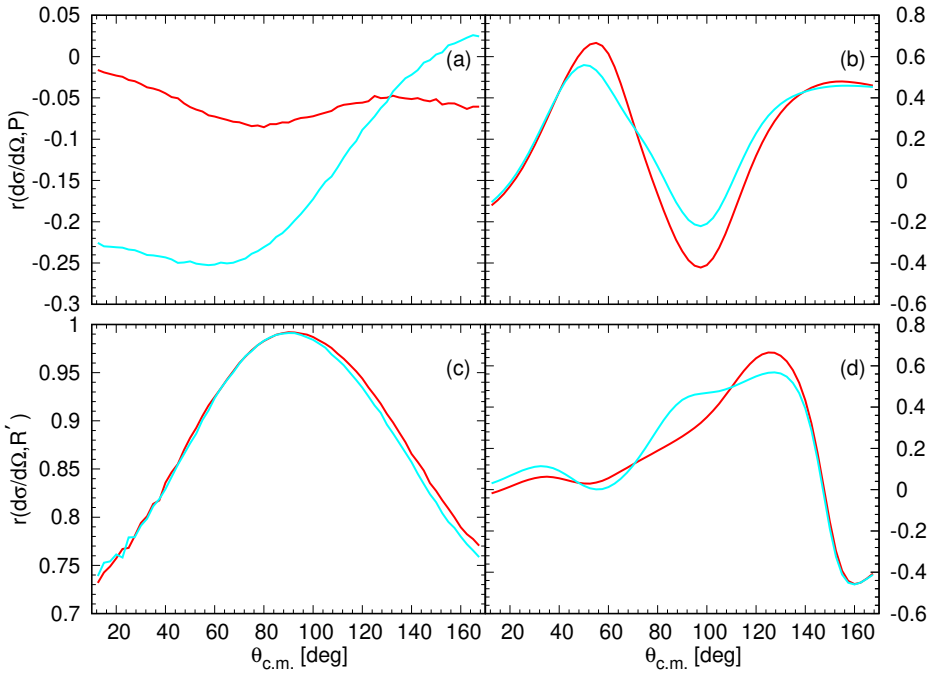

Figure 6.17: The angular dependence of correlations coefficients between np scattering observables: $(d\sigma/d\Omega, P)$ and $(d\sigma/d\Omega, R')$ at the incoming neutron laboratory energy $E_{\rm lab} = 10$ MeV ((a) and (c)), and $E_{\rm lab} = 135$ MeV ((b) and (d)). The solid red and cyan curves represent predictions of the chiral N^{4}LO and N^{4}LO$^+$ SMS forces, respectively.

Firstly, I would like to spotlight a couple of examples of the obtained correlation coefficients, focusing on the comparison of the predictions based on the chiral N^{4}LO SMS force and on the OPE-Gaussian potential (Figure 6.16), and on comparison of the chiral SMS forces at N^{4}LO and N^{4}LO$^+$ (Figure 6.17). As can be seen from Figure 6.16 typically the OPE-Gaussian predictions are in a nice agreement with the chiral N^{4}LO SMS ones [2]. However, I have found also a clear difference between predictions of these potentials at $E_{\rm lab} = 135$ MeV for correlation coefficients for (R, A) pair at backward scattering angles around $\theta_{c.m.} \approx 135^\circ$, see Figure 6.16 (b). Here the OPE-Gaussian potential leads to moderate r while the chiral N^{4}LO SMS force suggests uncorrelated observables.

For the chiral interactions at N^{4}LO and N^{4}LO$^+$, the $(d\sigma/d\Omega, P)$ pair (Figure 6.17 (a)) is especially interesting. Here we observe a disagreement in values of correlation coefficients at low energy. However, this does not change the finding of a weak correlation between $d\sigma/d\Omega$ and the polarization P. The observed difference can be caused by different numbers and values of LECs, and at each chiral order, see Table C1 in Appendix C.

As seen from Figures 6.18 – 6.19, the np differential cross section $d\sigma/d\Omega$ is, in general, strongly correlated with R, A', and D over a wide range of scattering angle at the incoming neutron laboratory energies $E_{\rm lab} = 10$ and 30 MeV. A magnitude of the correlation coefficient between the observables reaches more than 0.8, what means a strong correlation in our interpretations. With increasing energies ($E_{\rm lab} = 65$ and 135 MeV) the correlation decreases, but still at some regions correlation is moderate. This is especially clearly seen for the chiral N^{4}LO and N^{4}LO$^+$ SMS, and the OPE-Gaussian predictions. There is a weak correlation for the ($d\sigma/d\Omega$, P) pair for chiral N^{4}LO and N^{4}LO$^+$ SMS, and OPE-Gaussian potentials regardless of scattering energy. It is clearly seen that in the case of chiral interaction, the variations of correlation coefficient depend on the chiral order, however, moving to higher orders of chiral expansion doesn't change qualitative conclusions on the correlation between observables.

[2] Note a small range of y-axis in subfigures (a) and (c).

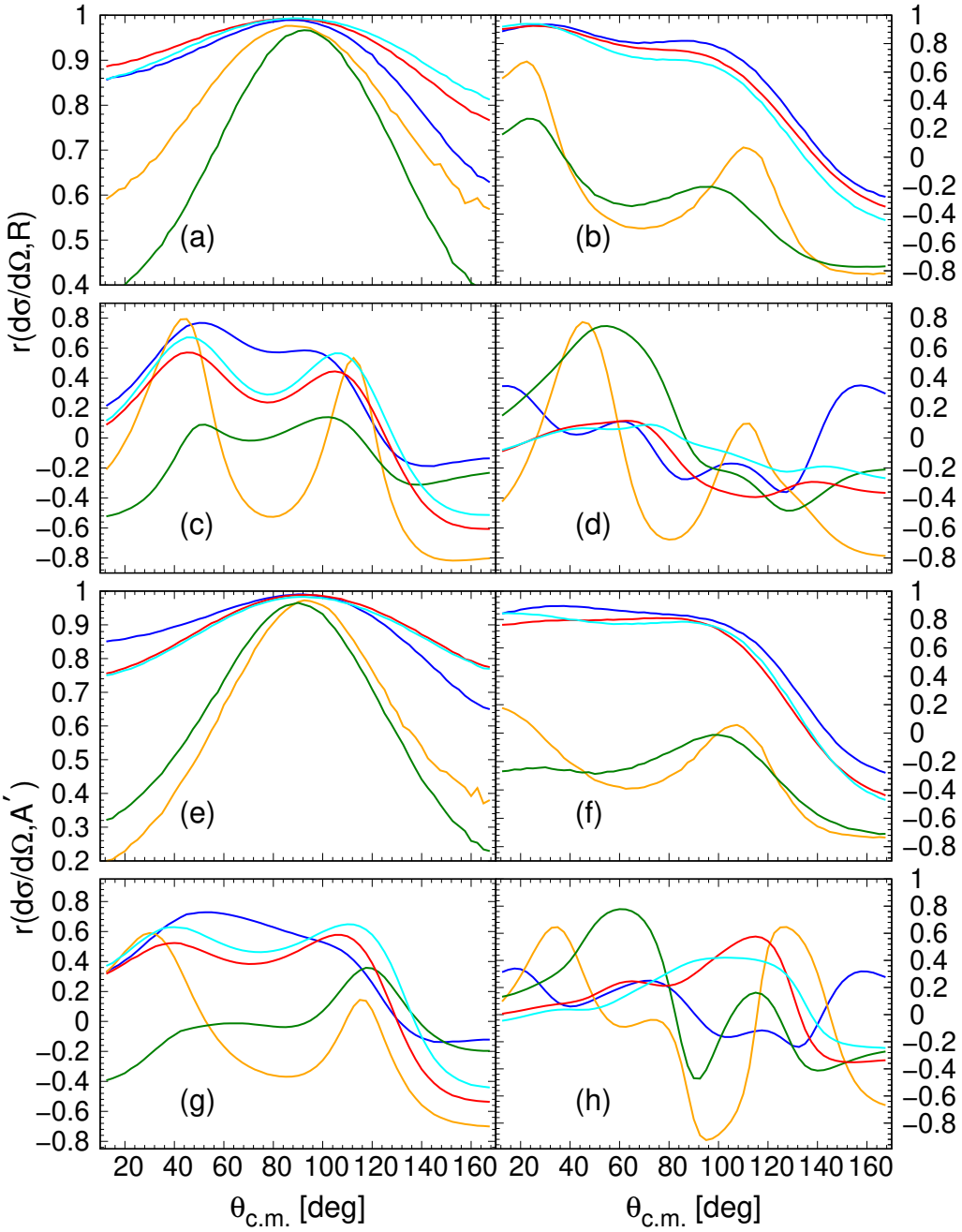

Figure 6.18: The angular dependence of correlation coefficients between $(d\sigma/d\Omega, R)$ and $(d\sigma/d\Omega, A')$ in np scattering at the incoming neutron laboratory energy (a, e) $E_{\rm lab}$ = 10 MeV, (b, f) $E_{\rm lab}$ = 30 MeV, (c, g) $E_{\rm lab}$ = 65 MeV, and (d, h) $E_{\rm lab}$ = 135 MeV. The solid orange, green, red, cyan curves represent predictions of the chiral N^{2}LO, N^{3}LO, N^{4}LO and N^{4}LO$^+$ SMS forces, respectively, and the blue line represents predictions based on the OPE-Gaussian potential.

Figure 6.20 shows the correlation coefficients for (R, A') and (R', A) pairs which are strongly correlated for the chiral N^{4}LO, N^{4}LO$^+$ SMS and the OPE-Gaussian potentials at $E_{\rm lab}$ = 10 and 30 MeV. At $E_{\rm lab}$ = 65 MeV, the magnitude of correlation coefficient for (R, A') still takes big values, but in the interval $\theta_{c.m.} \in (100°, 150°)$ reaches its minimum of $r \approx 0.65$ for the chiral N^{4}LO SMS potential ($r \approx 0.75$ for N^{4}LO$^+$). At $E_{\rm lab}$ = 135 MeV, a strong correlation is observed at $\theta_{c.m.} \in (50°, 70°)$ and only negative moderate correlation

at $\theta_{c.m.} \in (110°, 130°)$. For the (R', A) pair, we observe that at $E_{\rm lab} = 65$ MeV the magnitude of correlation is still strong, and for the interval of $\theta_{c.m.} \in (100°, 150°)$ it becomes moderate, but strong enough not to be ignored. At much higher energy, $E_{\rm lab} = 135$ MeV, the absolute value of correlation coefficient gradually decreases starting out from $\theta_{c.m.} = 70°$ and reaches its minimum, for example, about $r \approx 0.05$ for $\mathrm{N^4LO^+}$ potential, but from $\theta_{c.m} \approx 145°$ it increases again and anti-correlation becomes strong at large backward scattering angles.

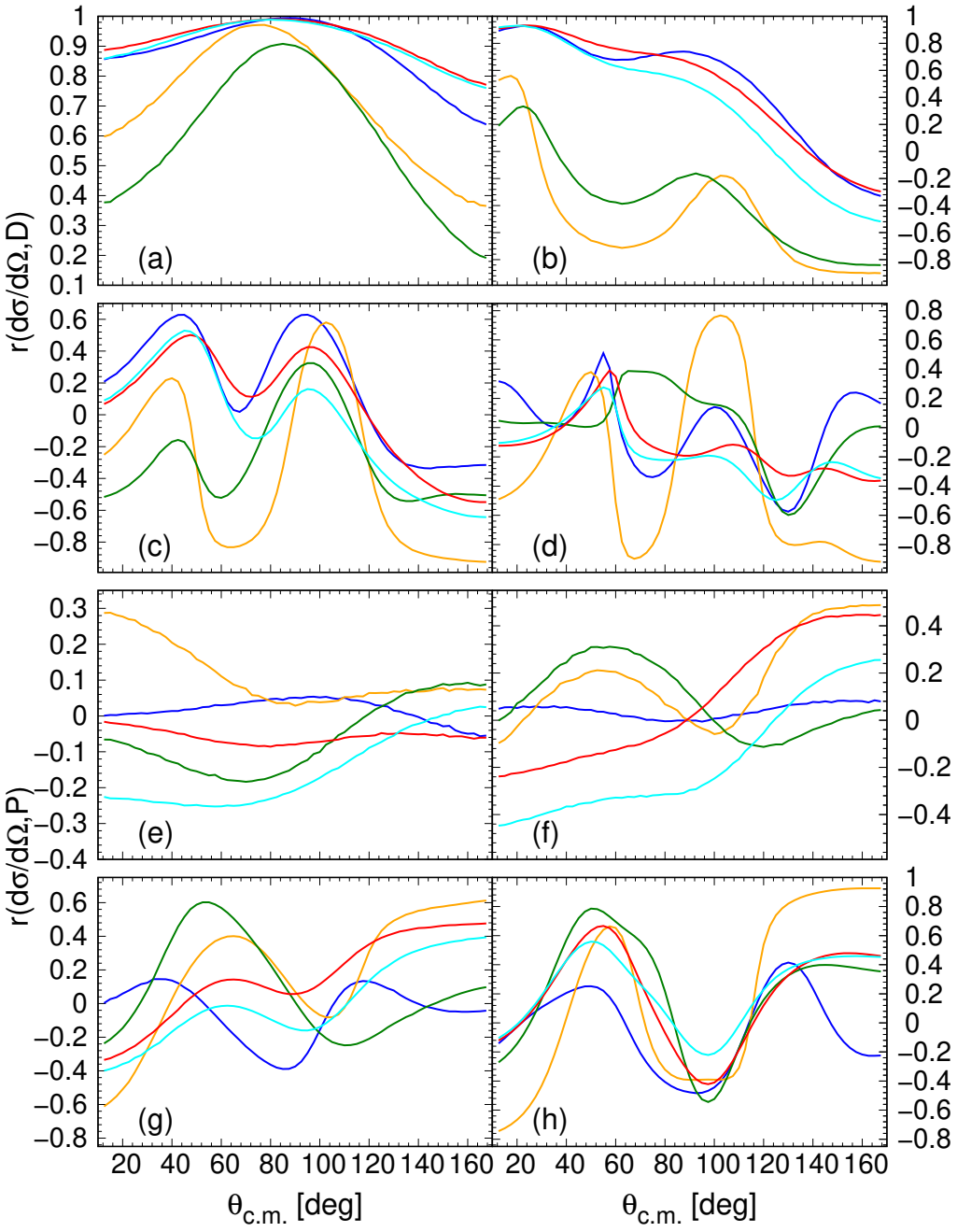

Figure 6.19: The angular dependence of correlation coefficients between $(d\sigma/d\Omega, D)$ and $(d\sigma/d\Omega, P)$ in np scattering at the incoming neutron laboratory energy (a, e) $E_{\rm lab} = 10$ MeV, (b, f) $E_{\rm lab} = 30$ MeV, (c, g) $E_{\rm lab} = 65$ MeV, and (d, h) $E_{\rm lab} = 135$ MeV. Curves are the same as in Figure 6.18.

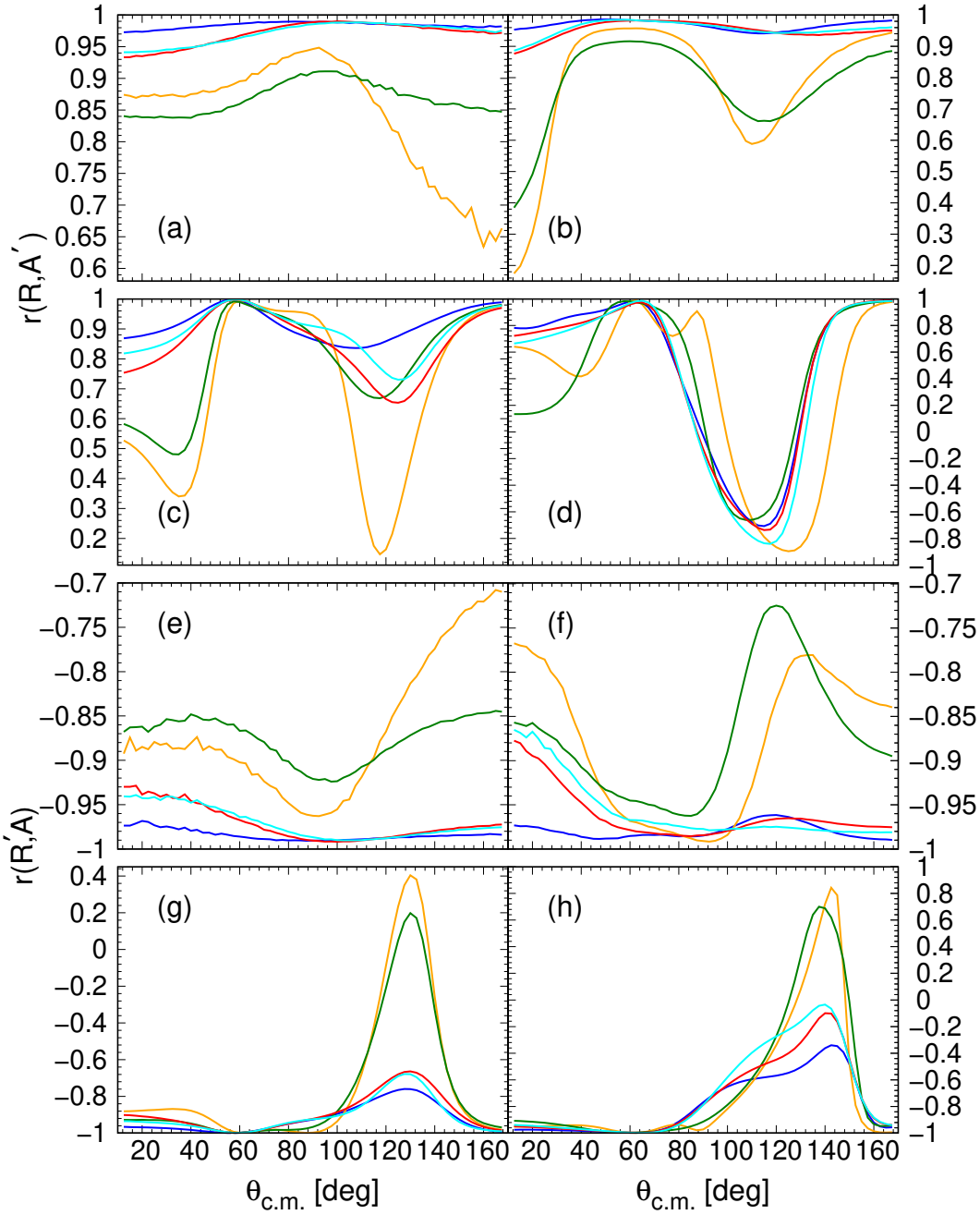

Figure 6.20: The angular dependence of correlation coefficients between (R, A') and (R', A) in np scattering at the incoming neutron laboratory energy (a, e) $E_{\rm lab} = 10$ MeV, (b, f) $E_{\rm lab} = 30$ MeV, (c, g) $E_{\rm lab} = 65$ MeV, and (d, h) $E_{\rm lab} = 135$ MeV. Curves are the same as in Figure 6.18.

In the case of P and A, see Figure 6.21, one gets a weak correlation for each of N^{4}LO, N^{4}LO$^+$ SMS and the OPE-Gaussian potentials for most of scattering angles and at all energies. The exceptional, maxima of r are observed with $r \approx 0.65$ for N^{4}LO force ($r \approx 0.6$ for N^{4}LO$^+$) in $\theta_{c.m.} \in (60°, 80°)$ for $E_{\rm lab} = 65$ MeV. At $E_{\rm lab} = 135$ MeV the correlation coefficient can reach 0.8 at large backward scattering angles for the chiral force at N^{4}LO$^+$ order.

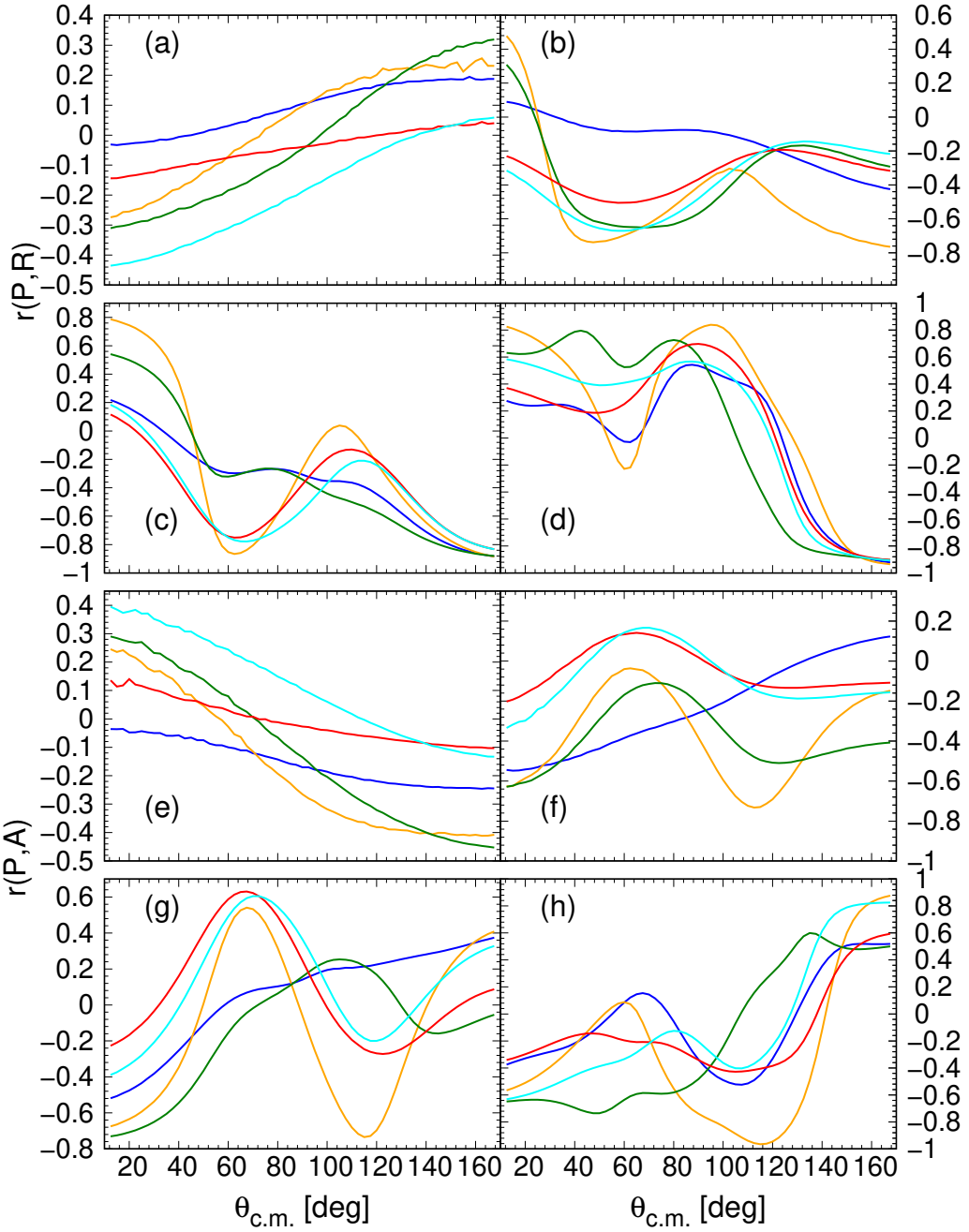

Figure 6.21: The angular dependence of correlation coefficients between (P, R) and (P, A) in np scattering at the incoming neutron laboratory energy (a, e) $E_{\rm lab} = 10$ MeV, (b, f) $E_{\rm lab} = 30$ MeV, (c, g) $E_{\rm lab} = 65$ MeV, and (d, h) $E_{\rm lab} = 135$ MeV. Curves are the same as in Figure 6.18.

The correlation coefficients for most pairs of 2N observables, also not shown in figures, at N^{4}LO and N^{4}LO$^+$ are close ones to another. This reflects the similarity of predictions for these forces. But for some cases, the predictions of correlation coefficients for N^{4}LO are slightly shifted with respect to the ones at N^{4}LO$^+$. This is especially often observed at energies above 30 MeV. The observed behavior of correlation coefficients is presumably influenced by different numbers and values of LECs present at various orders of the chiral expansion.

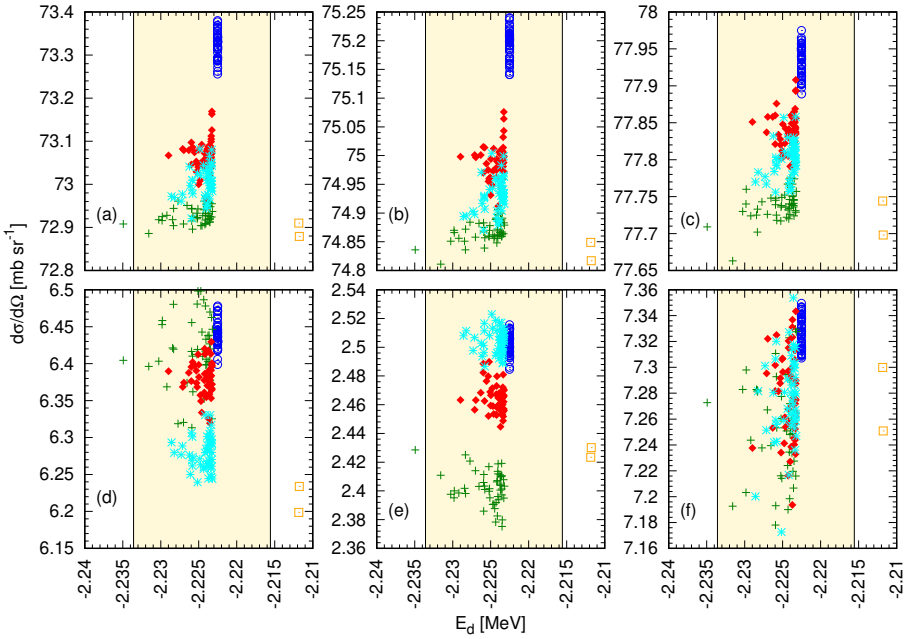

Figure 6.22: The scatter plot for the np differential cross section $d\sigma/d\Omega$ and the deuteron binding energy E_d at the c.m. scattering angle $\theta_{c.m.} = 30°$ (left), $\theta_{c.m.} = 90°$ (middle), and $\theta_{c.m.} = 150°$ (right) and at the incoming neutron laboratory energy $E_{\rm lab} = 10$ MeV (top) and $E_{\rm lab} = 135$ MeV (bottom). The open orange squares, green pluses, red diamonds, cyan stars, and the open blue circles represent results obtained using 50 sets of potential parameters of the chiral N^{2}LO, N^{3}LO, N^{4}LO, and N^{4}LO$^+$ SMS forces and the OPE-Gaussian potential, respectively. The experimental binding energy is from Ref. [107] (light-golden band).

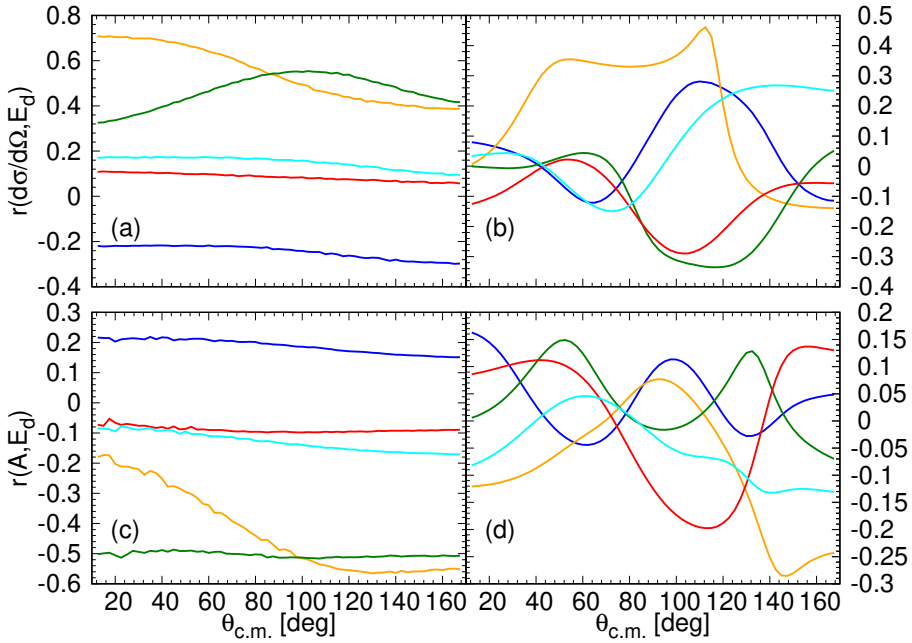

Figure 6.23: The angular dependence of correlations coefficients between the deuteron binding energy E_d and the np differential cross section $d\sigma/d\Omega$ (top) or asymmetry A (bottom) at the incoming neutron laboratory energy $E_{\rm lab} = 10$ MeV (left) and $E_{\rm lab} = 30$ MeV (right). Curves are the same as in Figure 6.18.

Our next point in study correlations in 2N systems is the identification of correlation between the differential cross section (taken at $E_{\rm lab} = 10$ and 135 MeV, and at three scattering angles $\theta_{c.m.} = 30°$, 90°, and 150°) and the deuteron binding energy, see Figure 6.22. The scatter plots clearly show the chiral N^2LO SMS predictions (only partly visible in Figure 6.22) are outlier points with respect to the remaining results which are within the interval of experimental uncertainty. At $E_{\rm lab} = 10$ MeV the chiral SMS N^4LO points are mixed with the chiral N^4LO^+ SMS ones at all angles, and at $E_{\rm lab} = 135$ MeV overlapping with the OPE-Gaussian predictions is also seen. Figure 6.23 shows that the ($d\sigma/d\Omega$, E_d) and (A, E_d) pairs, regardless of the potentials and scattering energy are weakly correlated at all scattering angles. This gives us a reason to point the deuteron binding energy, in addition to mutually uncorrelated 2N scattering observables, as independent observable suitable for usage during fixing parameters of the NN potential. A gap between N^4LO and N^4LO^+ is clear as at higher energy contributions from 6th order to the cross section are nonzero.

Summarizing all above observation for 2N scattering observables we conclude:

- We observe complex behavior of correlation coefficients with scattering angle and energy.
- The polarisation P is characterized by a weak correlation with the remaining 2N scattering observables. This is true for all NN potentials (in the case of the chiral SMS forces starting from N^3LO), the scattering energies and scattering angles.
- The differential cross section $d\sigma/d\Omega$ is strongly correlated with all 2N scattering observables, except P, at energies up to $E_{\rm lab} = 30$ MeV, in specific intervals of $\theta_{c.m.}$. In the case of the chiral SMS interaction the magnitude of r increases at specific a scattering angles with increasing chiral order. The predictions of the OPE-Gaussian potential are in good agreement with the chiral N^4LO SMS ones.
- The remaining 2N observables, such as R, R', A, A', and D are strongly correlated/uncorrelated between each other at investigated here energies up to $E_{\rm lab} =$ 30 MeV. For some pairs of observables it is true at 60 MeV, but not over the entire interval of $\theta_{c.m.}$.
- Correlation between R, R', A, A', D, and C_{NN} is moderate or weak.

Now I turn to analyze correlations between selected neutron-proton scattering observables and potential parameters (LECs) for the case of the N^4LO potential with $\Lambda = 450$ MeV. This potential involves 23 NN LECs. I restrict here myself to the only example of potential analysis as study the dependencies between given observable and a specific potential parameter requires investigations beyond this thesis. In general, each observable depends on a whole set of correlated parameters, and studying only a correlation coefficient between given observable and single parameter brings no information if variation of observable is due to specific parameter. The dependence on the parameter would be obvious if we could vary only one parameter and keep the others unchanged, but in such a case we spoil correlated sampling from a joint probability density function.

As seen in Figure C1 (Appendix C) showing correlations between different LECs for the case of the chiral N^4LO ($\Lambda = 450$ MeV) SMS potential or in similar Figure 10 from reference [9] in the case of chiral N^4LO^+ potential ($\Lambda = 450$ MeV), the strongest correlations and/or anticorrelations are observed between the LECs in the channels with

the largest number of potential parameters, especially $^1S_0$ and in $^3S_1$-$^3D_1$, see Appendix A of Ref. [9]. In particular, according to the authors of Ref. [9], this explains the fact that the statistical uncertainties of the respective LECs are greater than those for LECs in other channels. Another important aspect is that we do not fulfill the condition of linear dependence of 2N observables on potential parameters, which is usually assumed for regression methods. The Lippmann-Schwinger equation, introduces rather polynomial dependence of observables on potential parameters. Thus, in Figure 6.24 I give only a few examples for correlation between observables and potential parameters and postpone the analysis of multiple nonlinear regression with correlated predictors to future works.

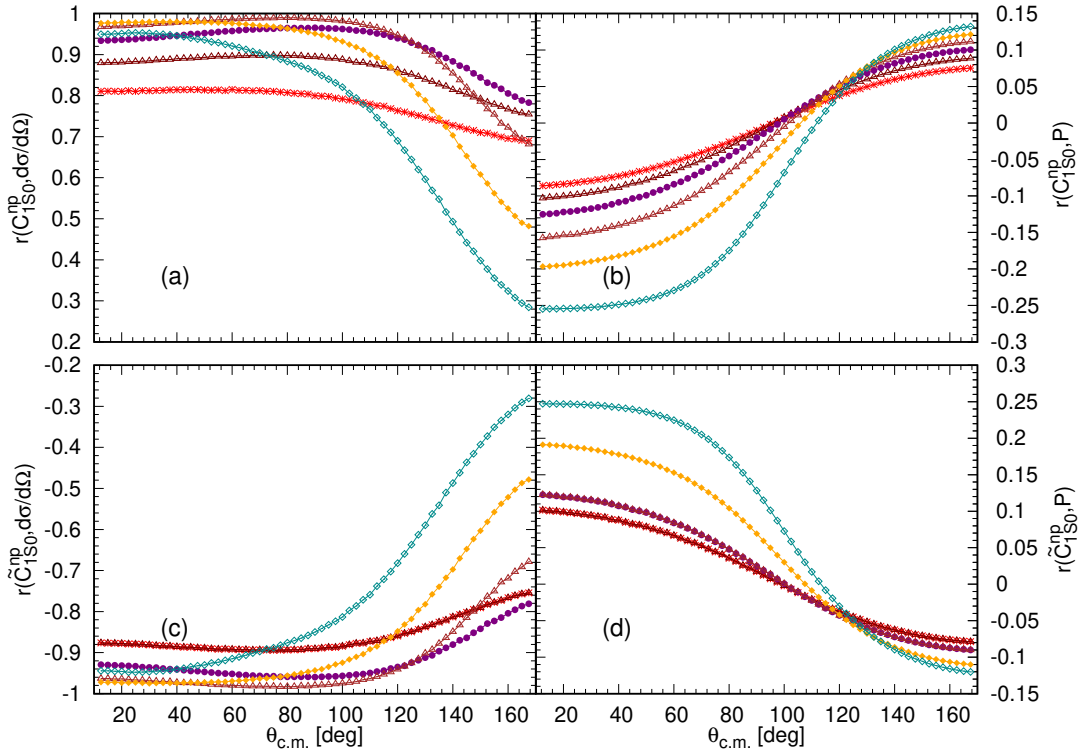

Figure 6.24: The angular dependence of correlation coefficients between $(C^{np}_{1S0}, d\sigma/d\Omega)$ and (C^{np}_{1S0}, P) (top), and $(\tilde{C}^{np}_{1S0}, d\sigma/d\Omega)$ and $(\tilde{C}^{np}_{1S0}, P)$ (bottom) obtained using the chiral N^{4}LO SMS force $\Lambda = 450$ MeV for np scattering at the incoming neutron laboratory energy from $E_{\rm lab} = 7.6$ MeV up to 30 MeV. The red solid line with stars, the maroon solid line with up triangles, the purple solid with circles, the brown solid with up triangles, the orange solid with diamonds, and the dark cyan solid with diamonds curves correspond to $E_{\rm lab} = 7.6, 10, 13, 17,$ 22, and 30 MeV, respectively.

In Figure 6.24 I present correlation coefficients between the potential parameters $C^{np}_{1S0}, \tilde{C}^{np}_{1S0}$ and the observables $d\sigma/d\Omega, P$ at few incoming neutron energies, in the range 7.6 – 30 MeV. The differential cross section appears strongly correlated (anti-correlated) with C^{np}_{1S0}, $(\tilde{C}^{np}_{1S0})$, for most of the scattering energies and angles. For the polarization observable P there is no correlation between these LECs again regardless of energy and angle. As can be observed, the behavior of the angular dependence of the coefficient between two observables with C^{np}_{1S0} is opposite to the correlation between observables and $\tilde{C}^{np}_{1S0}$. The reason is that C^{np}_{1S0} is strongly anti-correlated with $\tilde{C}^{np}_{1S0}$ with $r(C^{np}_{1S0}, \tilde{C}^{np}_{1S0}) = -0.998$. Once again, while obtained result suggests independence of polarization P on these specific parameters, this observation should be confirmed in future.

6.2 Correlations among three-nucleon observables

Let us now turn to an analysis of the correlation coefficients among 3N elastic scattering observables. I analyze various pairs of 3N observables computing correlation coefficients at three laboratory energies of the incident neutron $E_{\rm lab} = 13, 65$ and 135 MeV and in the range $\theta_{c.m.} \in [12.5°, 167.5°]$ of the c.m. scattering angle [3]. Correlations between selected 3N observables are investigated with the chiral N^{2}LO, N^{4}LO and N^{4}LO$^+$ SMS potentials ($\Lambda = 450$ MeV) and with the OPE-Gaussian potential. For one energy we have $\frac{55\times54}{2}$ pairs of 3N observables for which I calculate correlation coefficients at a given scattering angle. I repeat the path already done for 2N observables, but due to much larger numerical requirements for 3N scattering I skip tests comprising results from various 50 or 100 samples-element samples. Thus, in following I give a few examples of scatter plot for 3N observables, (Figures 6.25 – 6.32), and show representative examples of the angular dependences of correlation coefficients, in Figures 6.33 – 6.42.

Correlations between two selected 3N observables, i.e. the differential cross section $d\sigma/d\Omega$ and the spin correlation coefficient C_{xx}, were investigated with the chiral N^{4}LO and N^{4}LO$^+$ SMS potentials $\Lambda = 450$ MeV. To make a better visualization of this correlation, the scatter plot is shown at three scattering angles $\theta_{c.m.} = 30°, 90°$ and 150°. As shown in Figure 6.25, $d\sigma/d\Omega$ appears strongly correlated with C_{xx} at $\theta_{c.m.} = 90°$ and $\theta_{c.m.} = 150°$ for $E_{\rm lab} = 13$ MeV, as well at $\theta_{c.m.} = 30°$ and $\theta_{c.m.} = 150°$ for $E_{\rm lab} = 135$ MeV for the two employed potentials. However, it is observed that for other scattering angles only a weak correlation for this pair of 3N observables exists.

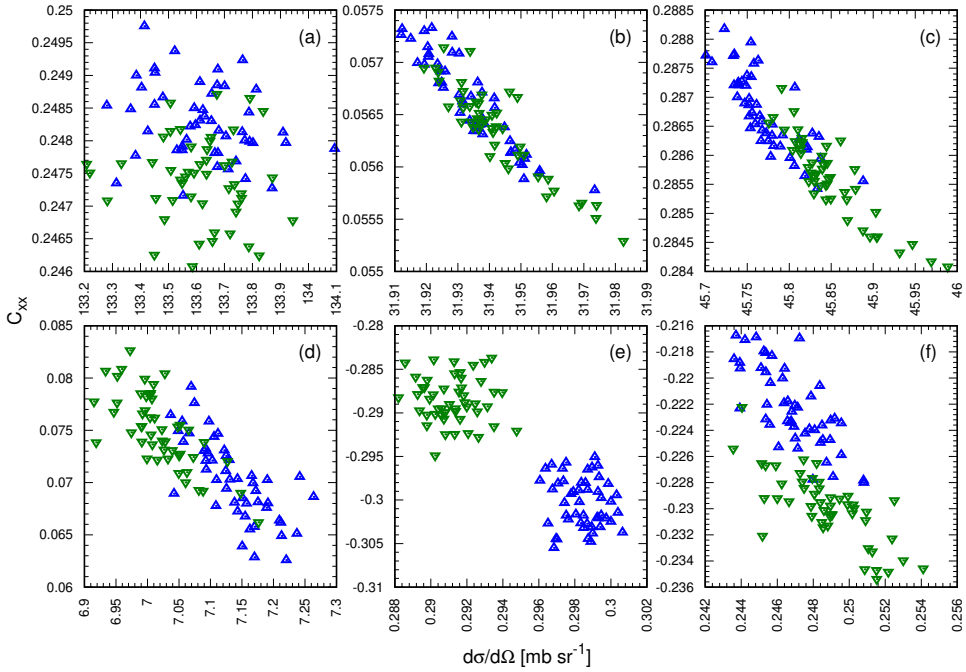

Figure 6.25: The scatter plot between $(d\sigma/d\Omega, C_{xx})$ in the elastic nd scattering at the c.m. scattering angle $\theta_{c.m.} = 30°$ (left), $\theta_{c.m.} = 90°$ (middle), and $\theta_{c.m.} = 150°$ (right) and at the incoming neutron laboratory energy $E_{\rm lab} = 13$ MeV (top) and $E_{\rm lab} = 135$ MeV (bottom). The blue and the green triangle represent results with N^{4}LO and N^{4}LO$^+$ SMS potentials, respectively.

[3] As in the 2N case, we want to avoid correlations associated with the behavior of observables at $\theta_{c.m.} \approx 0°$ or $\theta_{c.m.} \approx 180°$.

Another picture occures for A_y and iT_{11} which are strongly or moderately correlated, depending on scattering angle and energy, see Figure 6.26. In the top row, we see that $\mathrm{N^4LO^+}$ SMS predicts much smaller the magnitude of r in contrast to $\mathrm{N^4LO}$ at $\theta_{c.m.} = 90°$. Specifically, the $\mathrm{N^4LO}$ ($\mathrm{N^4LO^+}$) potential yields for $E_{\mathrm{lab}} = 13$ MeV: at $\theta_{c.m.} = 30°$ $r = 0.95$ ($r = 0.94$), at $\theta_{c.m.} = 90°$ $r = 0.90$ ($r = 0.63$), and at $\theta_{c.m.} = 150°$ $r = 0.99$ ($r = 0.99$). In the bottom row ($E_{\mathrm{lab}} = 135$ MeV), the relationship between the observables looks more linearly at $\theta_{c.m.} = 30°$ and indeed the magnitudes of r are: $\theta_{c.m.} = 30°$ $r = 0.99$ ($r = 0.98$), $\theta_{c.m.} = 90°$ $r = 0.60$ ($r = 0.33$), and $\theta_{c.m.} = 150°$ $r = 0.71$ ($r = 0.77$) with $\mathrm{N^4LO}$ ($\mathrm{N^4LO^+}$).

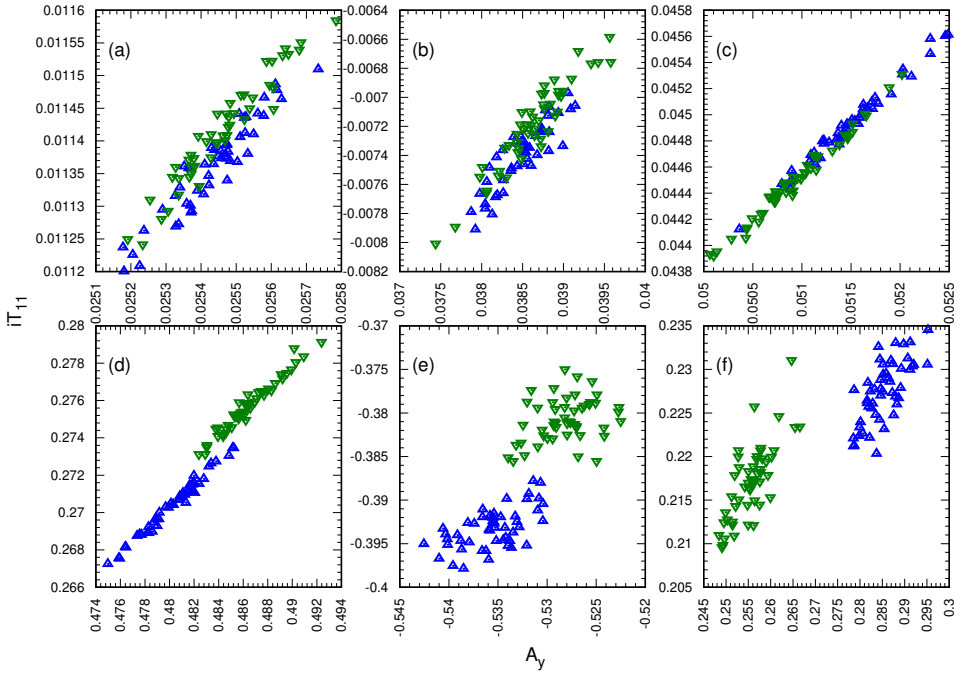

Figure 6.26: Same as in Figure 6.25, but for (A_y, iT_{11}) pair.

For other scatter plots shown in Figures 6.27 – 6.32, it can be generally concluded that for the vast majority of selected angles at $E_{\mathrm{lab}} = 13$ MeV there is often a strong correlation, or rarely observed moderate correlation. For the higher energy, $E_{\mathrm{lab}} = 135$ MeV, we often observe a weak correlation at almost all scattering angles, but there are exceptions that indicate a moderate correlation.

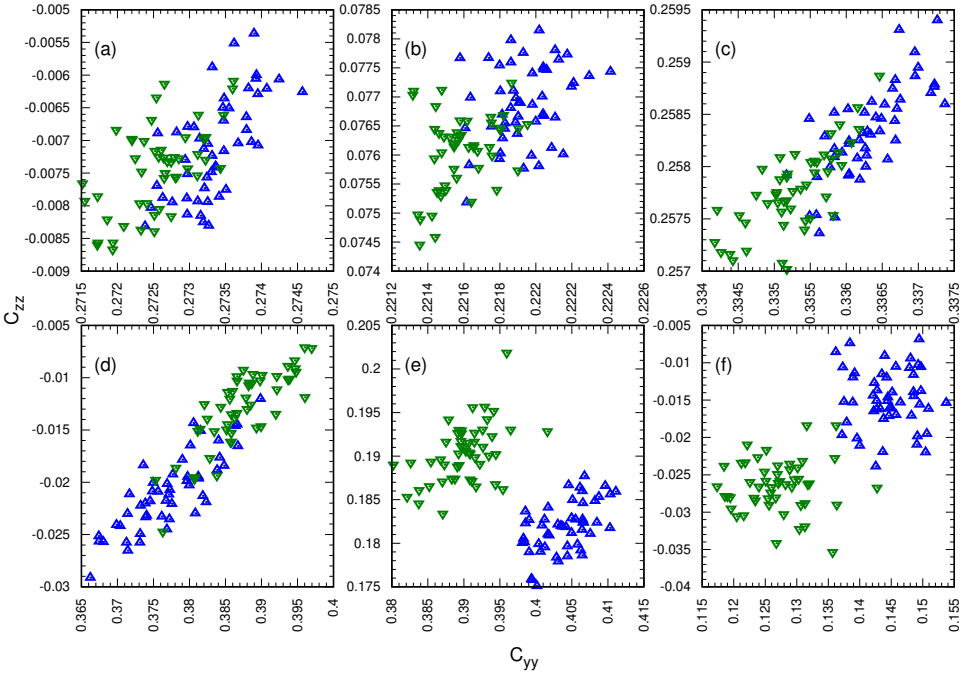

Figure 6.27: Same as in Figure 6.25, but for (C_{yy}, C_{zz}) pair.

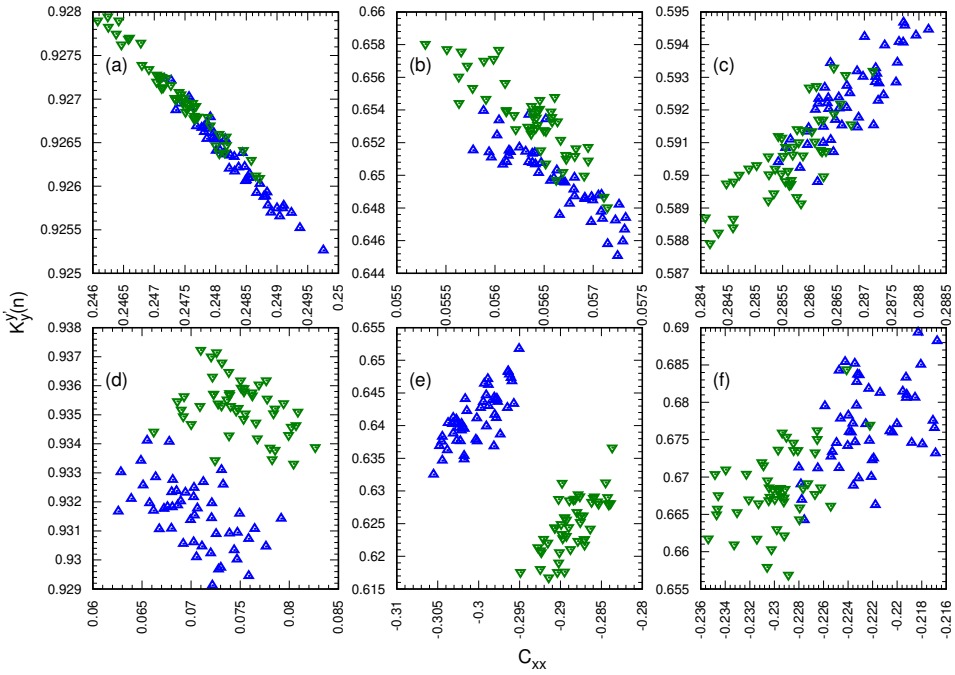

Figure 6.28: Same as in Figure 6.25, but for $(C_{xx}, K_y^{y'}(n))$ pair.

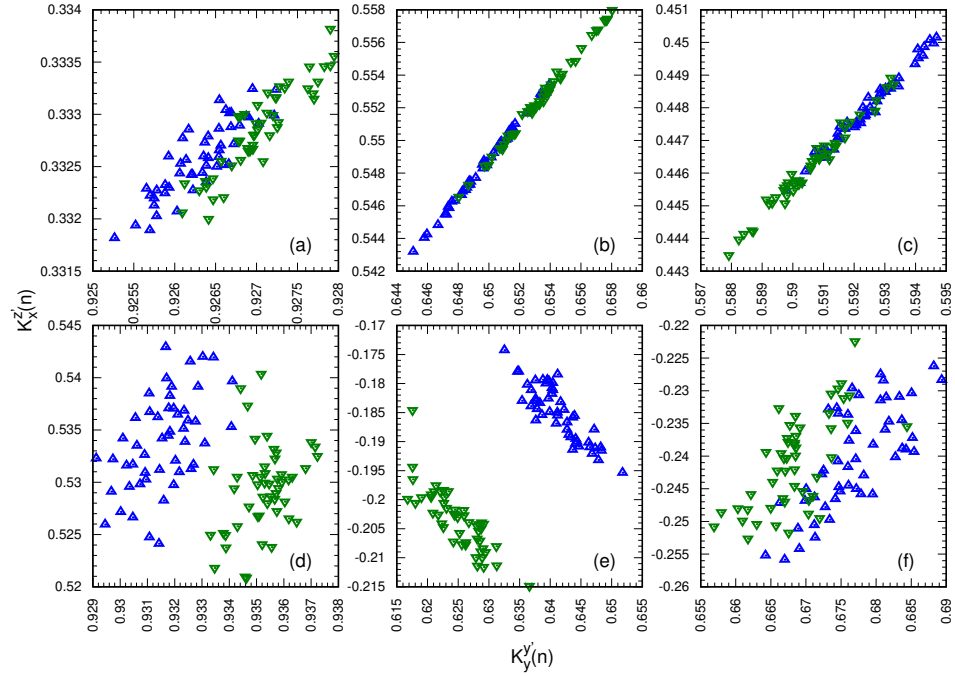

Figure 6.29: Same as in Figure 6.25, but for $(K_y^{y'}(n), K_x^{z'}(n))$ pair.

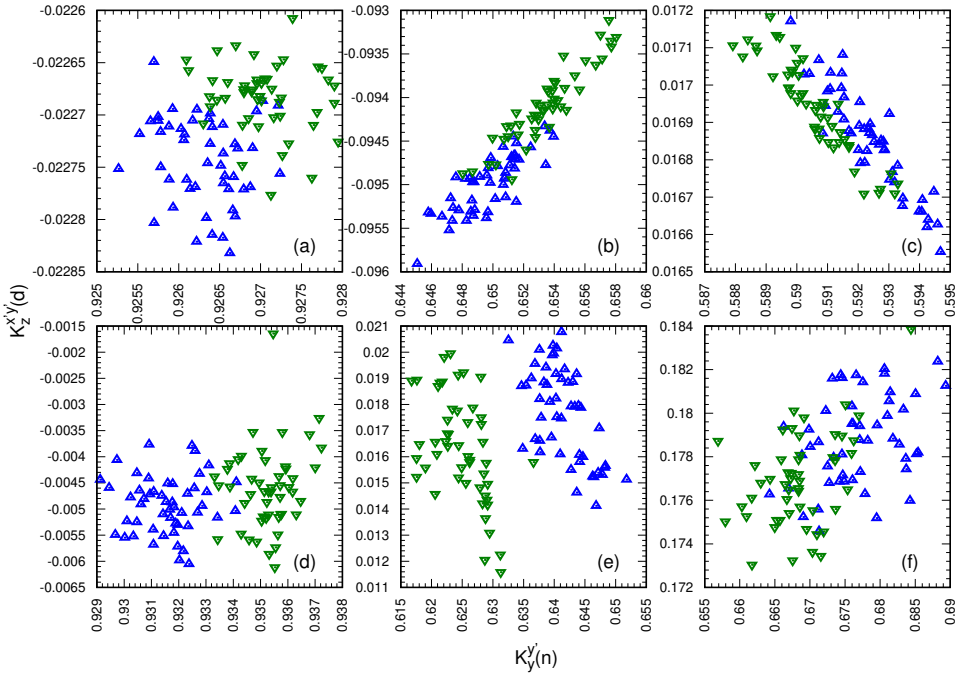

Figure 6.30: Same as in Figure 6.25, but for $(K_y^{y'}(n), K_z^{x'y'}(d))$ pair.

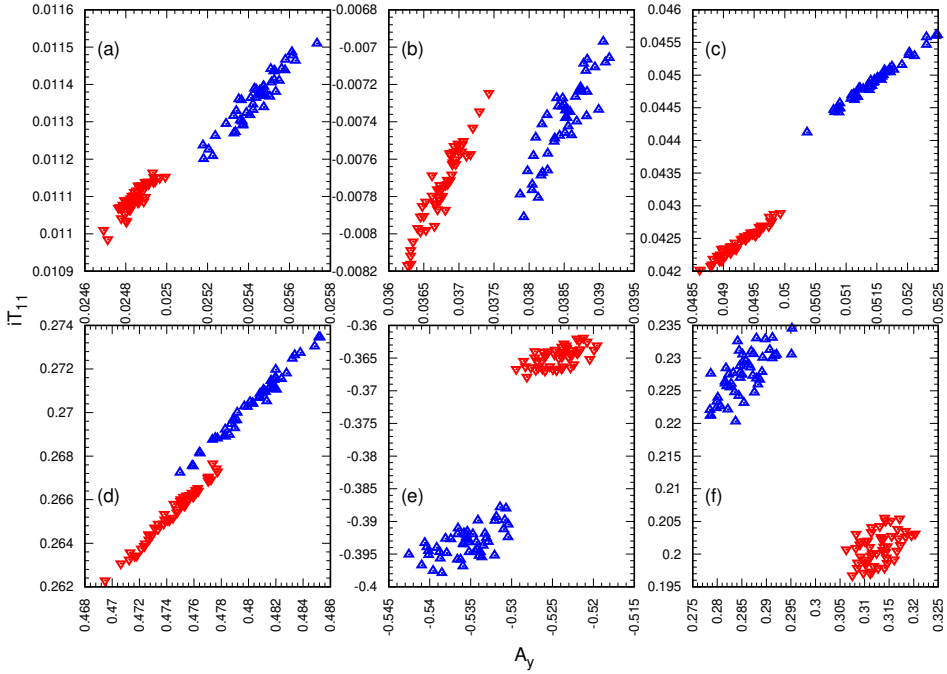

Figure 6.31: The scatter plot between (A_y, iT_{11}) in the elastic nd scattering at the c.m. scattering angle $\theta_{c.m.} = 30°$ (left), $\theta_{c.m.} = 90°$ (middle), and $\theta_{c.m.} = 150°$ (right) and at the incoming neutron laboratory energy $E_{\mathrm{lab}} = 13$ MeV (top) and $E_{\mathrm{lab}} = 135$ MeV (bottom). The red and the blue triangle represent results with the chiral N^{4}LO SMS force and the OPE-Gaussian potential, respectively.

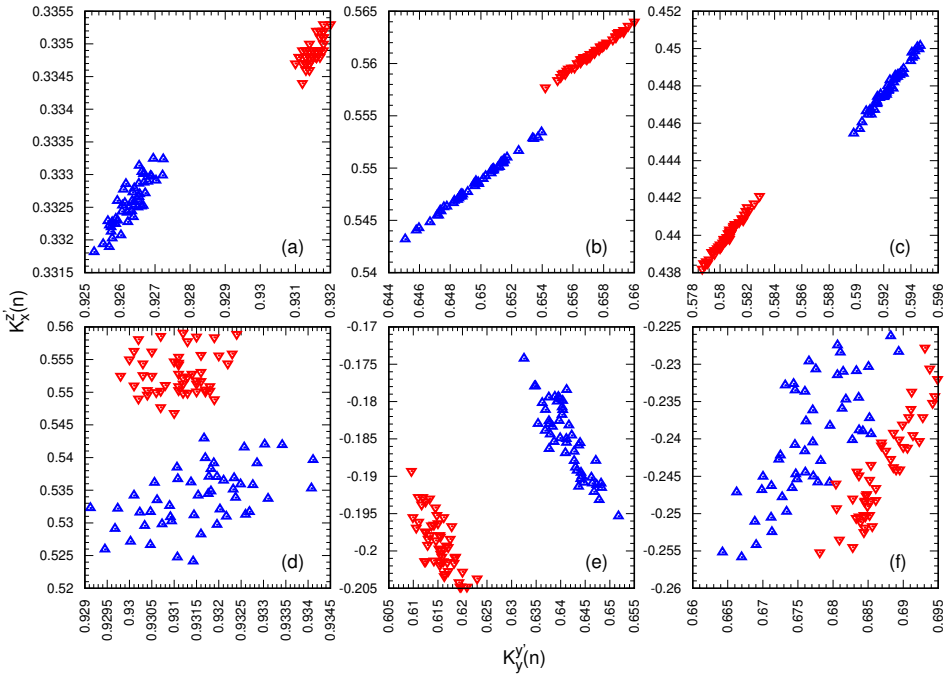

Figure 6.32: Same as in Figure 6.31, but for $(K_y^{y'}(n), K_x^z(n))$ pair.

Figures 6.31 and 6.32 show a comparison of predictions based on the chiral N^{4}LO SMS force and on the OPE-Gaussian potential, similarly to results shown in Figures 6.26 – 6.29. One can see that on both figures the OPE-Gaussian results are almost similar

to the N^{4}LO predictions. As an example, see Figure 6.31, the OPE-Gaussian potential predicts that the correlation coefficients for the pair (A_y, iT_{11}) takes the values: $r = 0.89$ at $\theta_{c.m.} = 30°$, $r = 0.95$ at $\theta_{c.m.} = 90°$, and $r = 0.98$ at $\theta_{c.m.} = 150°$ for $E_{\rm lab} = 13$ MeV ($r = 0.99$ at $\theta_{c.m.} = 30°$, $r = 0.61$ at $\theta_{c.m.} = 90°$, and $r = 0.45$ at $\theta_{c.m.} = 150°$ for $E_{\rm lab} = 135$ MeV). The correlation coefficients for the pair $(K_y^{y'}(n), K_x^z(n))$ calculated with the OPE-Gaussian potential are: $r = 0.72$ at $\theta_{c.m.} = 30°$, $r = 0.997$ at $\theta_{c.m.} = 90°$, and $r = 0.992$ at $\theta_{c.m.} = 150°$ for $E_{\rm lab} = 13$ MeV ($r = 0.12$ at $\theta_{c.m.} = 30°$, $r = -0.74$ at $\theta_{c.m.} = 90°$, and $r = 0.88$ at $\theta_{c.m.} = 150°$ for $E_{\rm lab} = 135$ MeV). At the same time, the results with the N^{4}LO SMS force for this pair are given: $r = 0.86$ at $\theta_{c.m.} = 30°$, $r = 0.999$ at $\theta_{c.m.} = 90°$, and $r = 0.991$ at $\theta_{c.m.} = 150°$ for $E_{\rm lab} = 13$ MeV ($r = 0.53$ at $\theta_{c.m.} = 30°$, $r = -0.86$ at $\theta_{c.m.} = 90°$, and $r = 0.74$ at $\theta_{c.m.} = 150°$ for $E_{\rm lab} = 135$ MeV). In conclusion, one can say that the correlation coefficient for these observables between the OPE-Gaussian, N^{4}LO, and N^{4}LO$^+$ are close one to another, this reflects the similarity of predictions, and the difference between them strongly depends on the scattering angle.

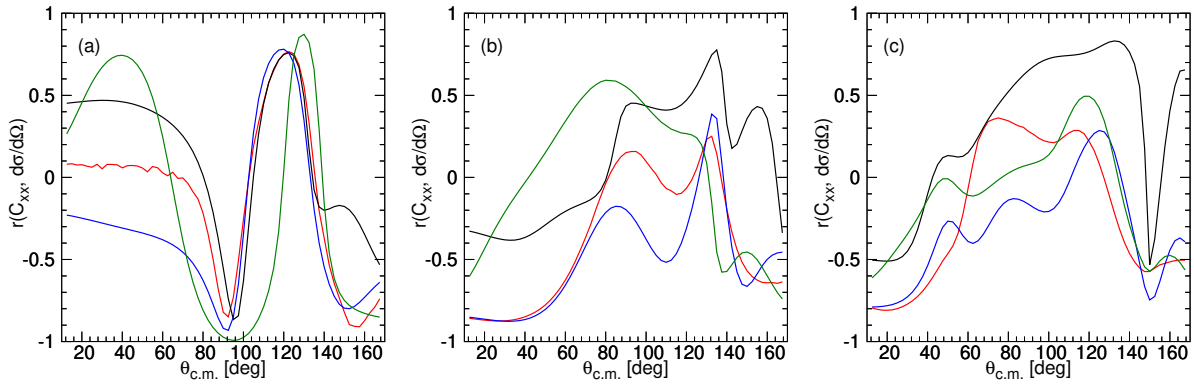

Figure 6.33: The angular dependence of the correlations coefficients between the spin correlation coefficients C_{xx} and $d\sigma/d\Omega$ for the incoming neutron laboratory energies $E_{\rm lab} = 13$ MeV (a), $E_{\rm lab} = 65$ MeV (b) and $E_{\rm lab} = 135$ MeV (c) in the elastic neutron-deuteron scattering. The black, blue, green and red solid curves represent predictions of the SMS chiral N^{2}LO, N^{4}LO and N^{4}LO$^+$ forces with $\Lambda = 450$ MeV and the OPE-Gaussian potential, respectively.

As in the 2N case, I would like to present now the angular dependence of the correlation coefficient among the various observables. As first example, in Figure 6.33, as addition to Figure 6.25, I show the correlation coefficient for the $(d\sigma/d\Omega, C_{xx})$ pair at three scatering energies $E_{\rm lab} = 13, 65$, and 135 MeV. The differential cross section $d\sigma/d\Omega$ is, in general, moderately correlated with C_{xx} for the chiral SMS force at N^{4}LO and N^{4}LO$^+$ orders, and for the OPE-Gaussian potential at all energies. However, we can also observe a weak or, conversely, a strong correlation at certain intervals of the scattering angle. Characteristically, a weak correlation for this pair is observed at forward or backward scattering angles at $E_{\rm lab} = 13$ MeV, between $70° < \theta_{c.m.} < 150°$ for $E_{\rm lab} = 65$ MeV, and between $45° < \theta_{c.m.} < 140°$ at $E_{\rm lab} = 135$ MeV. A strong correlation is detected, in the case of N^{4}LO$^+$ SMS, between $75° < \theta_{c.m.} < 115°$ and at $120° < \theta_{c.m.} < 140°$ for $E_{\rm lab} = 13$ MeV. Increasing energy a strong correlation appears at forward/backward scattering angles. Interesting that the N^{4}LO SMS and OPE-Gaussian predictions are much qualitatively similar than with the N^{4}LO$^+$ SMS results. This is true for all energies. However, for our qualitative interpretation of the correlation coefficient, this does not greatly affect on general conclusion about the relationship between these 3N

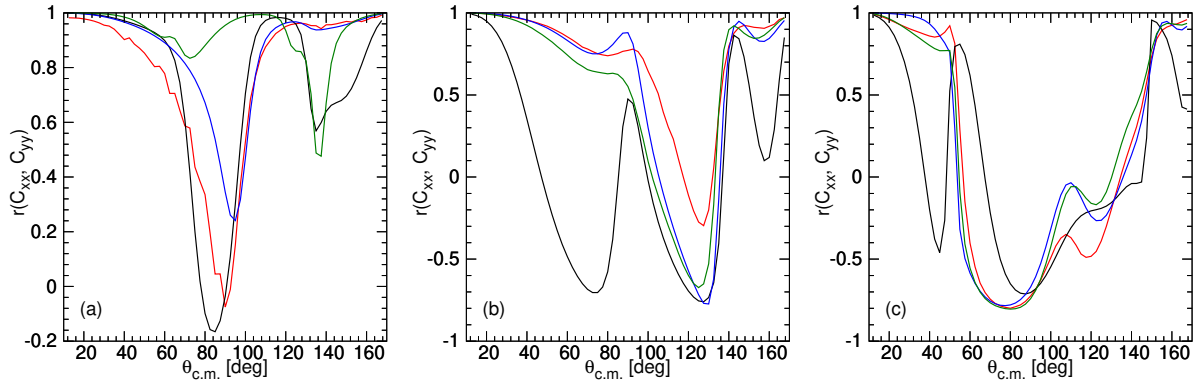

Figure 6.34: The angular dependence of the correlations coefficients between the spin correlation coefficients C_{xx} and C_{yy} for the incoming neutron laboratory energies $E_{\rm lab}$ = 13 MeV (a), $E_{\rm lab} = 65$ MeV (b) and $E_{\rm lab} = 135$ MeV (c) in the elastic neutron-deuteron scattering. Curves are as in Figure 6.33.

observables.

Figure 6.34 shows correlation coefficient between two spin correlation coefficients (C_{xx}, C_{yy}). At $E_{\rm lab} = 13$ MeV starting from a strong correlation for small angles, all potentials, except N^{4}LO$^+$ predict a sharp minimum at $\theta_{c.m.} = 85°$. With increasing values of $\theta_{c.m.}$ r based on the OPE-Gaussian and N^{4}LO SMS potentials grows which leads to a strong correlation above $\theta_{c.m.} \approx 100°$. N^{2}LO SMS potential deliveries similar prediction but additionally r decreases again for $130° \leq \theta_{c.m.} < 155°$ revealing a moderate correlation. For the chiral N^{4}LO$^+$ SMS force, there is a strong correlation between the observables up to $\theta_{c.m.} \approx 120°$ and for $\theta_{c.m.} \geq 150°$, but again it becomes weaker at $130° < \theta_{c.m.} < 145°$. With increasing energy, we observe a strong/moderate/weak correlation for specific intervals of $\theta_{c.m.}$. The curves of correlation coefficients for the (C_{xx}, C_{yy}) pair at the N^{4}LO, N^{4}LO$^+$ SMS, and the OPE-Gaussian potential are practically identical to each other at a qualitative level, but N^{2}LO results clearly separate from others at $E_{\rm lab} = 65$ MeV and $20° < \theta_{c.m.} < 90°$ and $\theta > 150°$. Also at $E_{\rm lab} = 135$ MeV N^{2}LO yields correlation coefficients different from other predictions, especially at $\theta_{c.m.} < 50°$.

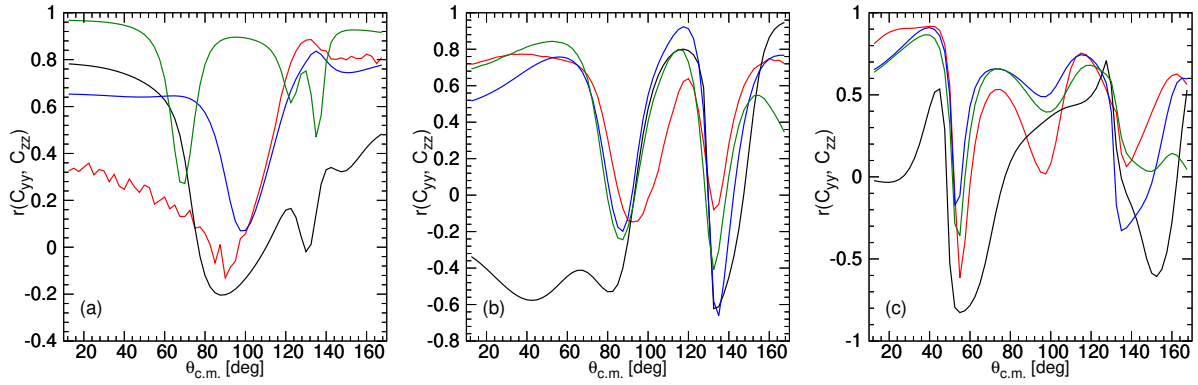

Figure 6.35: The angular dependence of the correlations coefficients between the spin correlation coefficients C_{yy} and C_{zz} for the incoming neutron laboratory energies $E_{\rm lab}$ = 13 MeV (a), $E_{\rm lab} = 65$ MeV (b) and $E_{\rm lab} = 135$ MeV (c) in the elastic neutron-deuteron scattering. Curves are as in Figure 6.33.

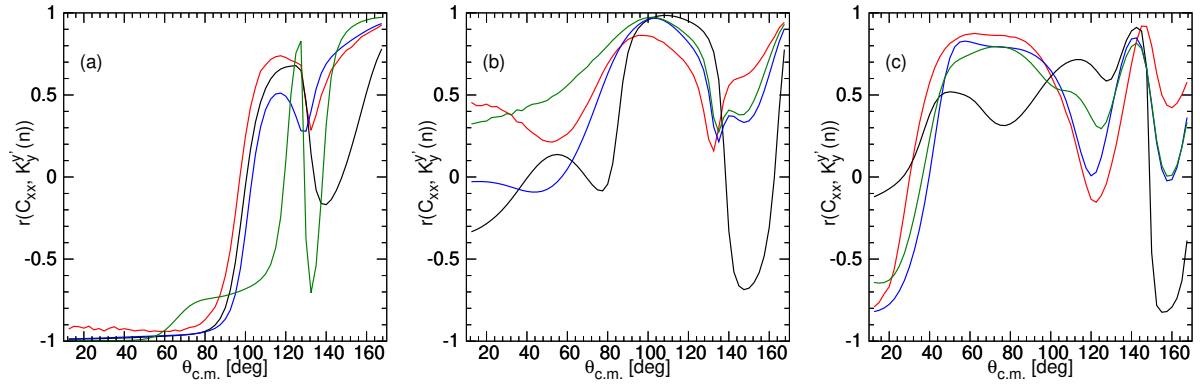

Figure 6.36: The angular dependence of the correlations coefficients between the spin correlation coefficient C_{xx} and the nucleon to nucleon spin transfer coefficient $K_y^{y'}(n)$ for the incoming neutron laboratory energies $E_{\rm lab}$ = 13 MeV (a), $E_{\rm lab}$ = 65 MeV (b) and $E_{\rm lab}$ = 135 MeV (c) in the elastic neutron-deuteron scattering. Curves are as in Figure 6.33.

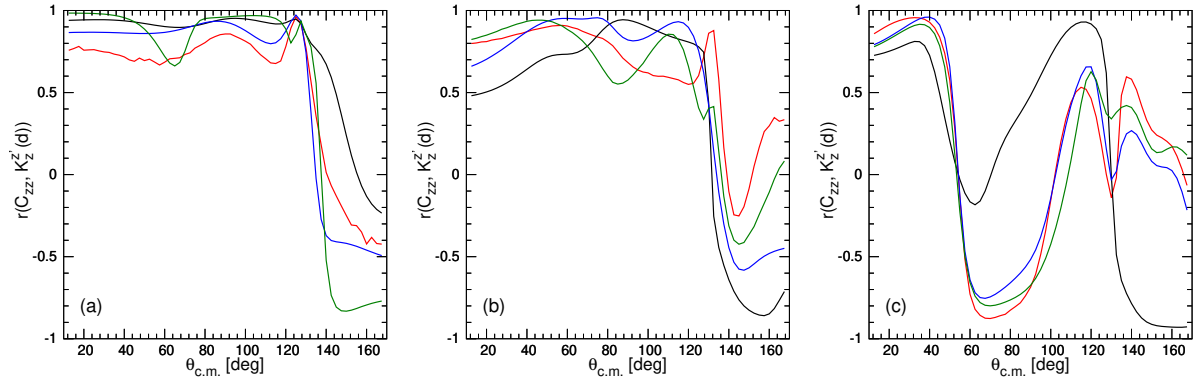

Figure 6.37: The angular dependence of the correlations coefficients between the spin correlation coefficient C_{zz} and the nucleon to deuteron vector spin transfer coefficient $K_z^{z'}(d)$ for the incoming neutron laboratory energies $E_{\rm lab}$ = 13 MeV (a), $E_{\rm lab}$ = 65 MeV (b) and $E_{\rm lab}$ = 135 MeV (c) in the elastic neutron-deuteron scattering. Curves are as in Figure 6.33.

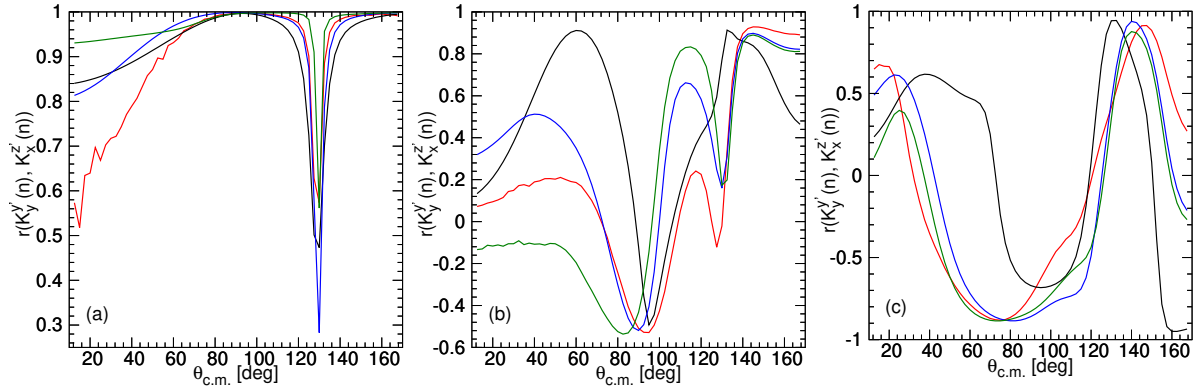

Figure 6.38: The angular dependence of the correlations coefficients between the nucleon to nucleon spin transfer coefficients $K_y^{y'}(n)$ and $K_x^{z'}(n)$ for the incoming neutron laboratory energies $E_{\rm lab}$ = 13 MeV (a), $E_{\rm lab}$ = 65 MeV (b) and $E_{\rm lab}$ = 135 MeV (c) in the elastic neutron-deuteron scattering. Curves are as in Figure 6.33.

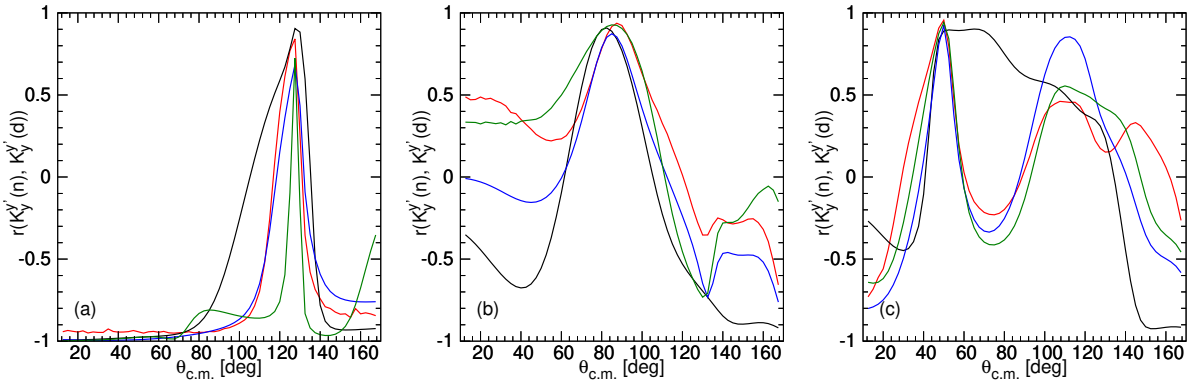

Figure 6.39: The angular dependence of the correlations coefficients between the nucleon to nucleon spin transfer coefficient $K_y^{y'}(n)$ and the nucleon to deuteron vector spin transfer coefficient $K_y^{y'}(d)$ for the incoming neutron laboratory energies $E_{\rm lab} = 13$ MeV (a), $E_{\rm lab} = 65$ MeV (b) and $E_{\rm lab} = 135$ MeV (c) in the elastic neutron-deuteron scattering. Curves are as in Figure 6.33.

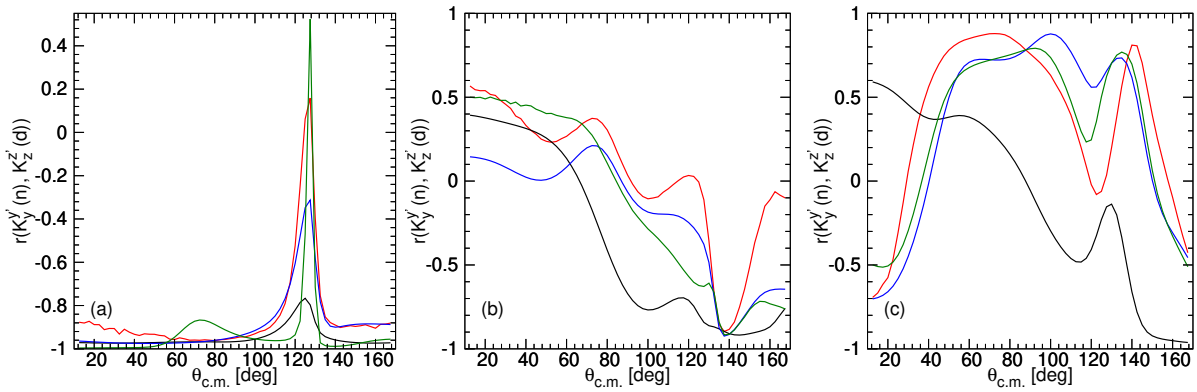

Figure 6.40: The angular dependence of the correlations coefficients between the nucleon to nucleon spin transfer coefficient $K_y^{y'}(n)$ and the nucleon to deuteron vector spin transfer coefficient $K_z^{z'}(d)$ for the incoming neutron laboratory energies $E_{\rm lab} = 13$ MeV (a), $E_{\rm lab} = 65$ MeV (b) and $E_{\rm lab} = 135$ MeV (c) in the elastic neutron-deuteron scattering. Curves are as in Figure 6.33.

In Figures 6.35 – 6.42, we observe more examples of angular dependence of correlation coefficients between 3N observables. Analyzing these figures, I can conclude that the change in the value of the correlation coefficient with scattering angle for some pairs of 3N observables (e.g $(C_{zz}, K_z^{z'}(d)$ or $(K_y^{y'}(n), K_y^{y'}(d)))$ does not depend on the model, but for others (like $(C_{xx}, d\sigma/d\Omega)$, (C_{yy}, C_{zz})), there is a strong dependence on the order of chiral expansion, and the correlation coefficient depends strongly on the scattering energy in all cases. The predictions for correlation coefficients for N^{4}LO$^+$ are usually slightly shifted with respect to ones at N^{4}LO. For the phenomenological OPE-Gaussian potential, we see that the behavior of predictions is similar to the one for results based on the SMS N^{4}LO force for all energies.

General conclusions I get from analysis of Figures 6.33 – 6.42 and not shown here figures for other pairs of observables are following:

- The angular dependence of the correlation coefficients reveals complex structures for all pairs of observables and energies. These structures are the result of the non-

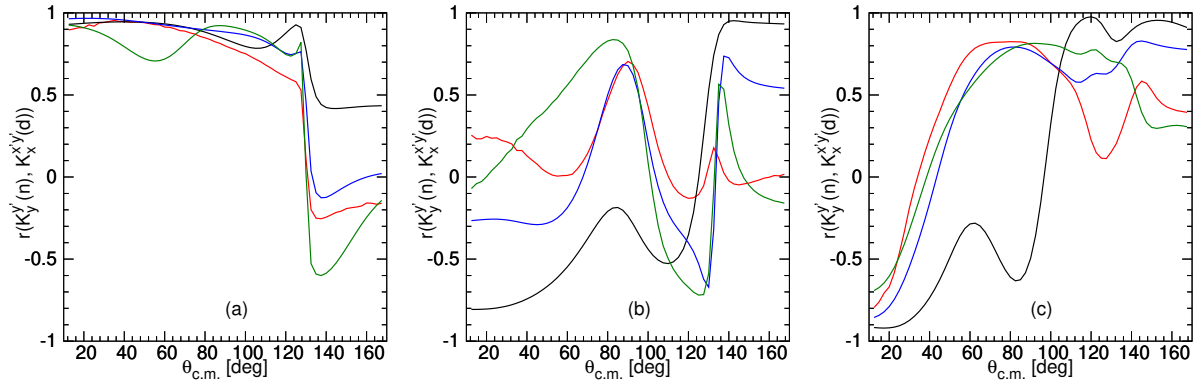

Figure 6.41: The angular dependence of the correlations coefficients between the nucleon to nucleon spin transfer coefficient $K_y^{y'}(n)$ and the nucleon to deuteron tensor spin transfer coefficient $K_x^{x'y'}(d)$ for the incoming neutron laboratory energies $E_{\rm lab} = 13$ MeV (a), $E_{\rm lab} = 65$ MeV (b) and $E_{\rm lab} = 135$ MeV (c) in the elastic neutron-deuteron scattering. Curves are as in Figure 6.34.

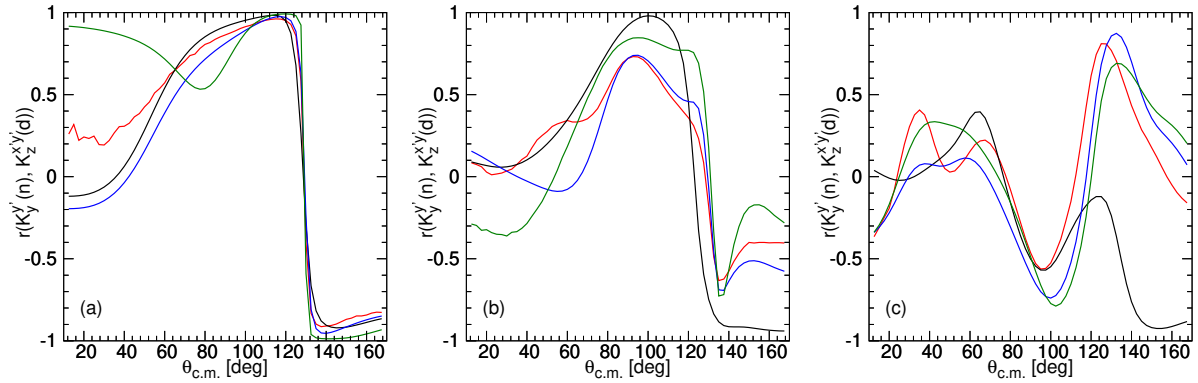

Figure 6.42: The angular dependence of the correlations coefficients between the nucleon to nucleon spin transfer coefficient $K_y^{y'}(n)$ and the nucleon to deuteron tensor spin transfer coefficient $K_z^{x'y'}(d)$ for the incoming neutron laboratory energies $E_{\rm lab} = 13$ MeV (a), $E_{\rm lab} = 65$ MeV (b) and $E_{\rm lab} = 135$ MeV (c) in the elastic neutron-deuteron scattering. Curves are as in Figure 6.33.

linear dependence of the observables on potential parameters. In addition, using partial-wave decomposition, i.e. splitting the genuine chiral LEC to their PWD substitutions makes this relationship even more hidden. Also, our method of calculating r, which is based on a sample of only 50 predictions, introduces additional uncertainty. Thus at this stage, our description of the correlation coefficients and subsequent conclusion should be treated only qualitatively. However, tests performed for the 2N system, and the fact that the use of different potentials (therefore different samples of parameters) lead to similar conclusions about the strength of correlations, assure us of the correctness of the obtained picture.

- In most cases, there is a similarity of correlation coefficients for pairs of observables at N^{4}LO and N^{4}LO$^+$, although there are also pairs of 3N observables for which they are mutually shifted for $120^\circ < \theta_{c.m.} < 150^\circ$, especially at $E_{\rm lab} = 13$ MeV. They are: $(C_{xx}, K_y^{y'}(n))$, $(C_{zz}, K_z^{z'}(d))$, $(K_y^{y'}(n), K_x^{z'}(n))$, $(K_y^{y'}(n), K_y^{y'}(d))$, $(K_y^{y'}(n), K_z^{z'}(d))$, $(K_y^{y'}(n), K_x^{x'y'}(d))$, and $(K_y^{y'}(n), K_z^{x'y'}(d))$.

- At $E_{\rm lab} = 13$ MeV 3N observables are usually strongly correlated in the case of the chiral N^{4}LO$^+$ SMS potential at $\theta_{c.m.} < 120^\circ$, and they become moderately or weakly correlated or even no correlation is observed above this angle up to $\theta_{c.m.} \approx 150^\circ$ where again a strong correlation is seen.

- Besides the complex behavior of r with the scattering angle, observed for all observables, in some cases, there are sudden changes of correlation coefficients. For example, in Figure 6.38 at $\theta_{c.m.} \in (125^\circ, 135^\circ)$ we observe a rapid fall of r, which reaches a minimum at $\theta_{c.m.} \approx 130^\circ$ (N^{4}LO predicts here $r = 0.28$). Note, that both for $K_y^{y'}(n)$ (see Figure 5.19) and $K_x^{z'}(n)$ (see Figure 5.21) there is a peak with maximum at $\theta_{c.m.} \approx 130^\circ$ equal 0.9530 ± 0.0006 [4] and 0.8969 ± 0.0004, respectively, when using the N^{4}LO SMS potential. The observed minimum of r indicates that both observables become independent or dependent nonlinearly. This, in turn, may suggest that in this angular range at least one observable depends strongly on some potential parameter (or parameters) or partial wave, which does not affect the second observable significantly. More insight into the origin of structures seen in angular dependence could be obtained by studying the dependence of given observables on individual low-energy constants.

- In the case of the N^{2}LO SMS force at all considered energies the correlation coefficient undergoes stronger changes with the scattering angle than the correlation coefficients computed with other potentials. The observed stabilization at higher orders shows that restricting calculations to the third order of chiral expansion can be misleading for some correlation coefficients at studied here energies.

- With increasing energy, the magnitude of the correlation coefficient drops to zero which indicates weak correlation or even no correlation, with rare exceptions of $(C_{xx}, K_y^{y'}(n))$ (Figure 6.36) and $(C_{zz}, K_y^{y'}(d))$ (Figure 6.37) pairs at $E_{\rm lab} = 65$ MeV. For other pairs at $E_{\rm lab} = 65$ and 135 MeV a strong/moderate correlation appears only at specific intervals of scattering angles. This is true for any potential, except the chiral N^{2}LO SMS force.

All the SMS chiral force based results in Figures 6.33 – 6.42 were obtained with the regularization parameter $\Lambda = 450$ MeV. It is also interesting to study the sensitivity of correlation coefficient to that cutoff parameter. Figure 6.43 demonstrates this dependence at N^{4}LO$^+$ using three values of Λ: 450, 500, and 550 MeV for the pairs (C_{xx}, C_{yy}) (top row) and $(A_y, {\rm iT}_{11})$ (bottom row). There is a cutoff dependence of the (C_{xx}, C_{yy}) correlation coefficient for $E_{\rm lab} = 13$ and 135 MeV, and for $E_{\rm lab} = 65$ MeV all predictions overlap. At $E_{\rm lab} = 13$ MeV (Figure 6.43(a)) all potentials give a strong correlation below $\theta_{c.m.} \approx 60^\circ$ but for $\Lambda = 500$ and 550 MeV, it gets moderate/weak in the range of $\theta_{c.m.} \in (75^\circ, 115^\circ)$ for $\Lambda = 500$ MeV and $\theta_{c.m.} \in (75^\circ, 100^\circ)$ for $\Lambda = 550$ MeV. For interval $\theta_{c.m.} \in (75^\circ, 150^\circ)$ we also observe difference between these two predictions compared to the result based on $\Lambda = 450$ MeV. For the higher energies (Figure 6.43(b) and (c)) all predictions are almost close to each other and, in particular, they practically overlap, for $\Lambda = 450$ MeV and $\Lambda = 550$ MeV.

[4] $\Delta_{68\%}$ statistical uncertainty.

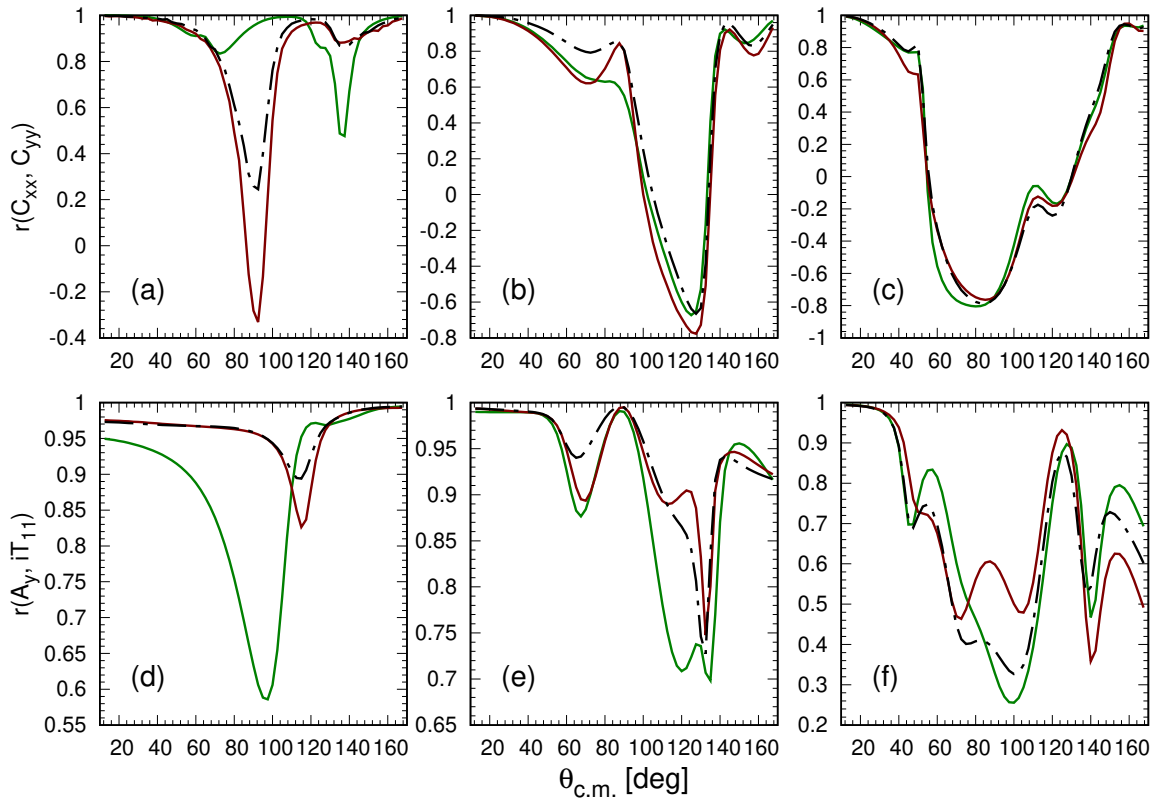

Figure 6.43: The angular dependence of correlation coefficients between (C_{xx}, C_{yy}) (top) and $(A_y, \mathrm{i}T_{11})$ (bottom) for different cutoff values (450 MeV — green solid curve, 500 MeV — maroon solid curve, and 550 MeV — black dot-dashed curve) for the SMS force at N^{4}LO$^+$ order and at the incoming neutron laboratory energies $E_{\mathrm{lab}} = 13$ MeV (left), $E_{\mathrm{lab}} = 65$ MeV (center) and $E_{\mathrm{lab}} = 135$ MeV (right) in the elastic neutron-deuteron scattering.

A relatively strong correlation occures also between the neutron vector and the deuteron tensor analyzing powers A_y and iT_{11} at $E_{\mathrm{lab}} = 13$ and 65 MeV, see bottom row of Figure 6.43. For $\Lambda = 550$ MeV there is a strong correlation in the whole range of $\theta_{c.m.}$, decreasing only to $r \approx 0.9$ at $\theta_{c.m.} = 112.5°$ and the same is for $\Lambda = 500$ MeV but reaching a minimum $r \approx 0.83$ at at $\theta_{c.m.} = 115°$. At $E_{\mathrm{lab}} = 13$ MeV the cutoff $\Lambda = 450$ MeV provides a gradual decreasing of r from 0.95 at $\theta_{c.m.} = 12.5°$ to $r \approx 0.58$ at $\theta_{c.m.} = 97.5°$, but starting $\theta_{c.m.} \approx 100°$ A_y and iT_{11} correlate more strongly with increasing $\theta_{c.m.}$. Moreover, the correlation between A_y and iT_{11} becomes stronger at $E_{\mathrm{lab}} = 65$ MeV in comparison to this at $E_{\mathrm{lab}} = 13$ MeV. At $E_{\mathrm{lab}} = 135$ MeV a strong correlation between these observables is observed just for $\Lambda = 550$ MeV for most $\theta_{c.m.}$. For the remaining cutoff values a strong or moderate correlation at specific interval of $\theta_{c.m.}$ occures.

Another interesting case of dependence between observables is so-called Phillips line [84], [148] expressing a correlation between the ^{3}H binding energy and the nucleon-deuteron doublet scattering length, $^2\mathrm{a}_{\mathrm{nd}}$. The Phillips line was observed in the past both in calculations with and without 3NF. As seen from Figure 6.44 we reproduce the Phillips line using chiral N^{3}LO, N^{4}LO and N^{4}LO$^+$ SMS interactions at $\Lambda = 450$ MeV. The correlation coefficient between these observables takes values of 0.75, 0.71 (after removing 3 outliers r is 0.97), 0.98, and 0.96 obtained at N^{2}LO, N^{3}LO, N^{4}LO, and N^{4}LO$^+$, respectively. With increasing chiral order, the values of these two observables change little in comparison with the experimental data ($E(^3H) = -8.4820 \pm 0.0001$ MeV [73] and

$^2a_{nd} = 0.65 \pm 0.04$ fm [149]). The observed discrepancy with the data is not surprising as it is well-known that ^{3}H binding energy and $^2a_{nd}$ are strongly influenced by 3NF.

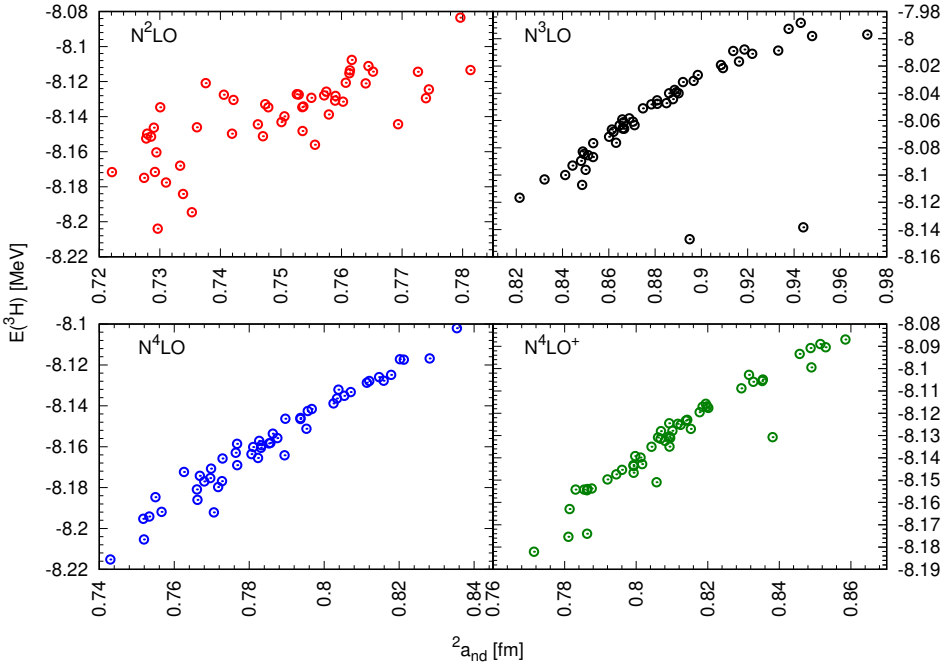

Figure 6.44: Order-by-order results (N^2LO–N^4LO^+ with $\Lambda = 450$ MeV) for the Phillips line.

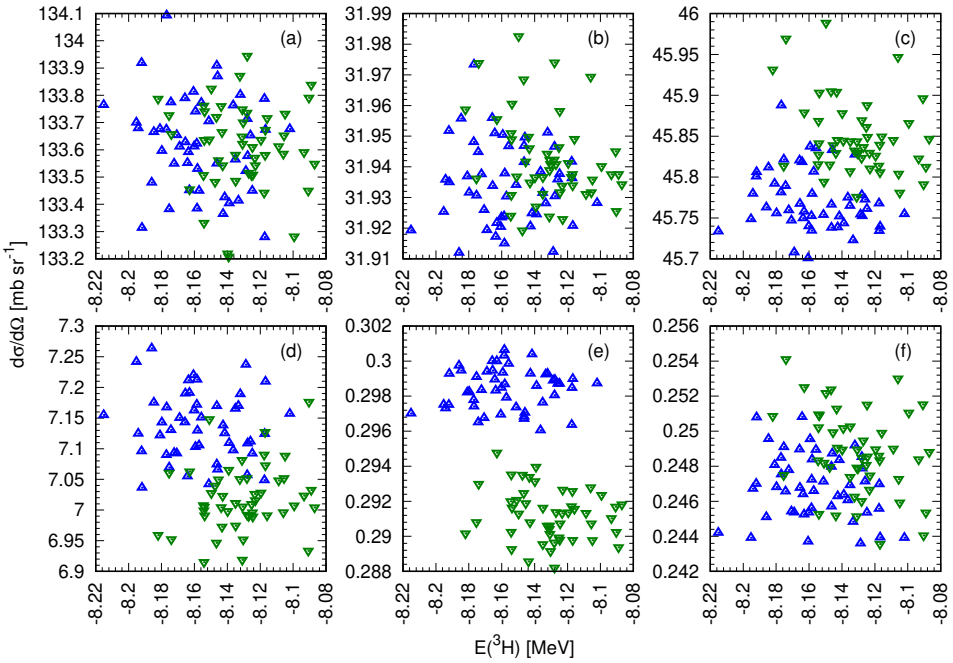

Figure 6.45: The scatter plot between the *nd* elastic differential cross section $d\sigma/d\Omega$ and the triton binding energy $E(^3H)$ at the c.m. scattering angle $\theta_{c.m.} = 30°$ (left), $\theta_{c.m.} = 90°$ (middle), and $\theta_{c.m.} = 150°$ (right) and at the incoming neutron laboratory energy $E_{\rm lab} = 13$ MeV (top) and $E_{\rm lab} = 135$ MeV (bottom). Description of symbols is as in Figure 6.25.

As mentioned in Chapter 3.2, the differential cross section at medium energy and the ^{3}H binding energy are nowadays used to fix parameters of the 3NF in the chiral SMS model. Now I'm able to check if these two observables are uncorrelated. This is done in Figure 6.45. Indeed, presented scatter plots confirm no correlation between the two observables. $r(d\sigma/d\Omega, E(^3H)$ remains small for both energies and all scattering angles and is within the range ($\min|r| = 0.05$ and $\max|r| = 0.28$). For not shown here energy 65 MeV $|r(d\sigma/d\Omega, E(^3H)|$ doesn't exceed $|r| \approx 0.3$. I expect that this picture will not change for complete predictions comprising 3NF.

Summarizing, I showed that it is possible to analyze the correlation among various 3N observables using the correlation matrices for potential parameters provided with the models of NN interaction from the Granada and Bochum-Bonn groups. My results demonstrate a complex dependence of correlation coefficients on scattering angle for all pairs of 3N observables and in the whole range of studied energies. This reflects the dependence of observables on potential parameters. Results obtained for various models of NN interaction proof that it is possible, at least on a qualitative level, to point correlated/uncorrelated observables.

It was also demonstrated that for the chiral interaction the angular behaviour of the correlation coefficients depends on the order of chiral expansion as well as on value of the cutoff parameter. Specifically, for some pairs of spin correlations, spin transfer coefficients, and analyzing powers, there is a strong dependence on the cutoff parameter. It is interesting that a strong correlation appears at specific intervals of scattering angles, what can indicate sensitivity of the transition amplitude on specific partial waves.

Chapter 7

Summary

In the presented thesis, the high-quality chiral NN potential with the semilocal regularization in momentum space at different orders of chiral expansion up to N^4LO^+ have been implemented for the calculation of neutron-proton and neutron-deuteron elastic scattering and the neutron-induced deuteron breakup reactions at energies up to 200 MeV. The first results of the application of the OPE-Gaussian force to 3N reactions are also given. In the present study, we have neglected the three-nucleon and Coulomb interactions. The formalism of the Faddeev equation has been used to obtain 3N observables.

I focused on two applications of the covariance matrix of NN potential parameters. They are: 1) the study of statistical uncertainties of 3N observables and 2) the study of correlations among 2N and 3N observables. In the main part of the thesis, I present an in-depth assessment of various theoretical uncertainties in the *ab initio* type calculations based on the chiral NN SMS force in describing three-nucleon processes. I used the correlation matrix of parameters of that NN potential to study the propagation of uncertainties from these parameters to Nd scattering observables. I compared the obtained uncertainty to other theoretical errors, i.e., to the cutoff dependence and to the truncation errors. The latter is estimated using two different approaches: the prescription from reference [14] and the Bayesian approach from references [15] and [61].

I found that the statistical errors remain relatively small in the nucleon-deuteron scattering independently from the employed NN force model. Namely, the statistical uncertainties of the chiral predictions have similar magnitudes and energy dependence as those from the semi-phenomenological OPE-Gaussian potential. Only at low energies and at N^4LO truncation errors become smaller than statistical uncertainties, for all *nd* elastic scattering observables (the differential cross section and a whole set of polarization observables). The estimated magnitudes of all types of uncertainties remain small, usually in the range 0.5%–4%, depending on the energy and the observable. The fact that various contributions to the theoretical uncertainty are so small points to the high quality of the theoretical input in the SMS interaction. It is worth mentioning that theoretical uncertainties remains usually much smaller than experimental errors.

My analysis of theoretical uncertainties in the neutron–deuteron scattering confirms that the SMS chiral potential belongs to the first-rate models of nuclear forces. It also demonstrates that, with ongoing progress in the derivation, regularization, and inclusion of higher-order contributions to the nuclear interaction, theoretical uncertainties, obtained with the chiral interaction, would be reduced to the limit dependent only on the quality of experimental data which influence the uncertainty of potential parameters. The Nd data description delivered by the chiral SMS force is similar to that based on the

older versions of the chiral potential from the Bochum–Bonn group. The omitted three-nucleon interaction is the main reason for observed discrepancies between predictions and the data at energies above about 60 MeV. However, while the dominant contributions to the 3NF arising at N^2LO usually reduce these discrepancies they are not able to explain them fully [61], [150], and [86]. It is expected that only after using consistent 3NF up to at least N^3LO a satisfactory data description will be achieved. It would be interesting to check if the results presented in this thesis will remain valid when three-nucleon interaction is taken into account in calculations. Such a study is planned as soon as the consistent SMS 3NF at N^3LO is available.

In Chapter 3.2 the limitations of procedure used to fit potential parameters to scattering observables or bound states in 2N or 3N systems, which are not sensitive enough to the NN/3N interaction in some partial waves are formulated. They call for careful analysis of dependencies between observables and parameters. Thereby, I wanted to point out the importance of the possible existence of correlations among two- and three-nucleon observables as well as their sensitivity to potential parameters acting in specific partial waves. This is important for future investigation within the general χEFT framework, in order to confidently eliminate any ambiguities in the determination of the LECs, especially for 3NF beyond N^3LO.

Systematic analysis of the correlation coefficients among 2N and 3N observables is given in the second part of my thesis. I demonstrated that it is possible to analyze the correlation among various 2N and 3N observables using the correlation matrices of potential parameters provided with the models of NN interactions from the Granada and Bochum-Bonn groups. Consequently, I showed that there are pairs of 2N spin observables for which an almost linear relationship exists. It happens both for the chiral SMS force (at N^3LO and beyond) and the OPE-Gaussian potential. For some pairs of 2N observables, the angular dependence of the correlation coefficients depends strongly on the order of chiral expansion as well as on the scattering energy. It is interesting that a strong correlation appears at specific intervals of scattering angles. This could indicate a sensitivity of the transition amplitude to specific parameters or partial waves.

The same is true for elastic neutron-deuteron scattering. I studied selected correlations among 3N observables. All angular dependences of correlation coefficient reveal a complex behavior of correlation coefficients r with scattering angles and the existence of regions with $|r| > 0.8$. It was also demonstrated that when using the chiral interaction the angular dependence of the correlation coefficients depends on the order of chiral expansion as well as on the scattering energy. In addition for some pairs of spin correlation and spin transfer coefficients, as well as analyzing powers, there is a strong dependence on the cutoff parameter. It is interesting that a strong correlation appears at specific intervals of scattering angles.

The presented thesis includes innovative elements that have not been used to study 2N and 3N systems before. They are:

- the usage of the covariance matrix of the potential parameters for the new generation of the chiral interaction derived up to N^4LO^+ of the chiral expansion using the semilocal regularization in momentum space and the OPE-Gaussian potential;

- sampling various sets of potential parameters from the multivariate normal distribution (in space of parameters) with a given covariance matrix to obtain new versions of the NN potential and resulting 2N and 3N observables;

- establishing statistical errors for 3N scattering observables and studying their dependence on energy, scattering angle, potential, and cutoff parameters;
- gathering information about the correlations among 2N and 3N observables;
- investigation, in the case of the chiral interaction, the dependence of correlation coefficient on the order of chiral expansion and regulator value.

The presented study is in line with modern efforts to construct a precise model of nuclear interaction comprising two- and many-body forces. The fixing free parameters of such a model is an important part of the whole derivation and has to be done carefully using the proper statistical methods. To this end, the knowledge of theoretical uncertainties as well as correlations between observables and sensitivity of observables to model parameters have to be taken into account. Of course, I aware that our search for a correlated/uncorrelated set of observables is only the first step towards an optimal set of observables. The next step is to study the sensitivity of the selected observables to the magnitude of the parameters, using suitable statistical techniques to measure and interpret relationships between numerous dependent variables (LECs) and one dependent variable (e.g., 2N or 3N observable). Nevertheless, my results reveal the usefulness of the covariance matrix of NN potential parameters for studies the neutron-proton and the neutron-deuteron elastic scatterings, and the deuteron breakup reaction observables. They may be also extended to other systems.

Appendix A

Sampling 50 sets of the chiral potential parameters at different orders in the chiral expansion

We have been equipped by the authors of Ref. [9] with the mean values of the NN potential parameters and their correlation matrix for the chiral interaction at each order of chiral expansion. This allows us to sample 50 sets of potential parameters, LECs, from the multivariate normal distribution and obtain new versions of the corresponding NN force.

The Mathematica script given below shows how I perform such sampling in practice. After reading in the central values of parameters (variables `ExpValuesLECs*`) and covariance matrices (variables `CovMatrix*`) I use the `RandomVariate` function, taking as its argument `MultinormalDistribution` which is nothing but a multivariate normal distribution. Having generated 50 samples of LEC's at each chiral order, the next step is to write data in the format as used in the subroutine code of chiral SMS potential in "for" loop and subsequent export parameters to a file.

```
In[ ]:= SetDirectory[NotebookDirectory[]];
        files = FileNames["Covariance-Matrix*.dat", NotebookDirectory[]];
```

Imports data :
the covariance matrices of parameters at
different orders (LO, NLO, N^2 LO, N^3 LO, N^4 LO and N^4 LO^+)
in the chiral expansion with cutoff Λ = 450 MeV)

```
In[ ]:= (*cut2 means Λ = 450 MeV *)
        (*LO*)
        CovMatrixLOCut2 = Import[files[[1]]];
        (*N2LO*)
        CovMatrixN2LOCut2 = Import[files[[2]]];
        (*N3LO*)
        CovMatrixN3LOCut2 = Import[files[[3]]];
        (*N4LO++*)
        CovMatrixN4LOPlusCut2 = Import[files[[4]]];
        (*N4LO*)
        CovMatrixN4LOCut2 = Import[files[[5]]];
        (*NLO*)
        CovMatrixNLOCut2 = Import[files[[6]]];
```

Gives the correlation matrix for the corresponding covariance matrix

```
In[ ]:= ρ1 = Correlation[CovMatrixLOCut2] // MatrixForm;
        ρ2 = Correlation[CovMatrixN2LOCut2] // MatrixForm;
        ρ3 = Correlation[CovMatrixN3LOCut2] // MatrixForm;
        ρ4 = Correlation[CovMatrixN4LOCut2] // MatrixForm;
        ρ5 = Correlation[CovMatrixN4LOPlusCut2] // MatrixForm;
        ρ6 = Correlation[CovMatrixNLOCut2] // MatrixForm;
```

The central values of the chiral LO, NLO,
N^2 LO, N^3 LO, N^4 LO and N^4 LO^+ SMS (Λ = 450 MeV)
potential parameters (low – energy constants, LEC's)

In[ ]:=
```
(*LEC's LO, Λ = 450 MeV (cut=2)*)
ExpValuesLECsLOCut2 =
  {-0.075582417864592744, -0.084738448787523735, -0.075392863895045389};
(*LEC's NLO, Λ = 450 MeV (cut=2)*)
ExpValuesLECsNLOCut2 =
  {-0.077938124413691717, 0.49496052083734010,
   0.64254690467392583, -0.12511487702236343, 0.36594848141466652,
0.12623389878766889, 0.11094128292763249, 0.28092810466022505,
   -0.33914945155602533, -0.075567405693055242};
(*LEC's N2LO, Λ = 450 MeV (cut=2)*)
ExpValuesLECsN2LOCut2 =
  {0.0073531853, 0.199222330, 0.37773895, -0.031018587, 0.18918091, 0.31853848,
 0.53970847, 0.76404881, -0.044238698, 0.0098588308};
(*LEC's N3LO, Λ = 450 MeV (cut=2)*)
ExpValuesLECsN3LOCut2 =
  {0.049440144478154625, -0.067851120626338163, 3.5107105027204075,
   0.87440686294802017, 0.016628629038027941, 0.95653559359427653,
   0.034616530856821981, -0.17370940139736049, 5.2796498528876699,
   0.41431770066015017, -0.023286178402950435, 1.6742777866499625,
0.82843006226903082, 0.51697470296182158, 1.1390323508502656, -0.24808743784999177,
   0.33562748273714116, -0.77188034815936479, -0.18197158903775518,
   0.50421327948104999, -0.089674005079767929, 0.051770603265125580};
(*LEC's N4LO, Λ = 450 MeV (cut=2)*)
ExpValuesLECsN4LOCut2 =
  {0.010596572607727553, 0.090666804874369164, 2.9617749120040253, 0.75140537198508639,
   -0.057107861359049959, 0.22510248577682418, 0.0081122609433074335,
   -0.0079985206224870431, 2.8364705496272742, 0.37676863022591578,
   0.0017534709116716980, 1.3010338412251252, 0.60503657235297026,
   1.0800863507008038, 0.85084310989652090, 0.35107833086177215, 0.12559984040349559,
   -0.44161518729421245, -0.16108047872821163, 0.21999587983184971,
   -0.15826534216162522, 0.012072334371911570, 0.12627105733936761};
```

Checking

In[ ]:=
```
CovMatrixN2LOCut2;
CovMatN2LOCut2 = (CovMatrixN2LOCut2 + Transpose[CovMatrixN2LOCut2]) / 2.0;
CovMatN2LOCut2 // MatrixForm;
CovMatrixN2LOCut2 - Transpose[CovMatrixN2LOCut2] // MatrixForm;
CovMatrixN2LOCut2 - Transpose[CovMatrixN2LOCut2] // Flatten // Abs // Max;
CovMatN2LOCut2 == Transpose[CovMatN2LOCut2] // MatrixForm;
CovMatrixN2LOCut2 - CovMatN2LOCut2 // Flatten // Abs // Max
CovMatrixN2LOCut2 // Flatten // Abs // Max
```

Out[ ]= 7.64091×10^{-17}

Out[ ]= 0.000231166

Actions for LO ($\Lambda = 450$ MeV)

In[ ]:=
```
CovMatLOCut2 = (CovMatrixLOCut2 + Transpose[CovMatrixLOCut2]) / 2.0;
CovMatrixLOCut2 // MatrixForm;
CovMatrixLOCut2 - Transpose[CovMatrixLOCut2] // MatrixForm;
CovMatrixLOCut2 - Transpose[CovMatrixLOCut2] // Flatten // Abs // Max;
CovMatLOCut2 == Transpose[CovMatLOCut2] // MatrixForm
```

Out[ ]//MatrixForm=

True

Actions for NLO ($\Lambda = 450$ MeV)

```
CovMatNLOCut2 = (CovMatrixNLOCut2 + Transpose[CovMatrixNLOCut2]) / 2.0;
CovMatrixNLOCut2 // MatrixForm;
CovMatrixNLOCut2 - Transpose[CovMatrixNLOCut2] // MatrixForm;
CovMatrixNLOCut2 - Transpose[CovMatrixNLOCut2] // Flatten // Abs // Max;
CovMatNLOCut2 == Transpose[CovMatNLOCut2] // MatrixForm
```

Actions for N^2LO ($\Lambda = 450$ MeV)

In[ ]:=
```
CovMatN2LOCut2 = (CovMatrixN2LOCut2 + Transpose[CovMatrixN2LOCut2]) / 2.0;
CovMatrixN2LOCut2 // MatrixForm;
CovMatrixN2LOCut2 - Transpose[CovMatrixN2LOCut2] // MatrixForm;
CovMatrixN2LOCut2 - Transpose[CovMatrixN2LOCut2] // Flatten // Abs // Max;
CovMatN2LOCut2 == Transpose[CovMatN2LOCut2] // MatrixForm
```

Out[ ]//MatrixForm=

True

Actions for N^3LO ($\Lambda = 450$ MeV)

In[ ]:=
```
CovMatN3LOCut2 = (CovMatrixN3LOCut2 + Transpose[CovMatrixN3LOCut2]) / 2.0;
CovMatrixN3LOCut2 // MatrixForm;
CovMatrixN3LOCut2 - Transpose[CovMatrixN3LOCut2] // MatrixForm;
CovMatrixN3LOCut2 - Transpose[CovMatrixN3LOCut2] // Flatten // Abs // Max;
CovMatN3LOCut2 == Transpose[CovMatN3LOCut2] // MatrixForm
```

Out[ ]//MatrixForm=
```
True
```

Actions for N^4LO ($\Lambda = 450$ MeV)

In[ ]:=
```
CovMatrixN4LOCut2;
CovMatN4LOCut2 = (CovMatrixN4LOCut2 + Transpose[CovMatrixN4LOCut2]) / 2.0;
CovMatN4LOCut2 // MatrixForm;
CovMatrixN4LOCut2 - Transpose[CovMatrixN4LOCut2] // MatrixForm;
CovMatrixN4LOCut2 - Transpose[CovMatrixN4LOCut2] // Flatten // Abs // Max;
CovMatN4LOCut2 == Transpose[CovMatN4LOCut2] // MatrixForm
```

Out[ ]//MatrixForm=
```
True
```

Lack Transpose[ExpValuesLECs] , CovMat is symmetrized.
Represents a multivariate normal (Gaussian) distribution with the vectors of central values of potential parameters and covariance matrices.

In[ ]:=
```
SamplesLOCut2 =
  RandomVariate[MultinormalDistribution[ExpValuesLECsLOCut2, CovMatLOCut2], 50];
SamplesNLOCut2 = RandomVariate[
   MultinormalDistribution[ExpValuesLECsNLOCut2, CovMatNLOCut2], 50];
SamplesN2LOCut2 = RandomVariate[MultinormalDistribution[
    ExpValuesLECsN2LOCut2, CovMatN2LOCut2], 50];
SamplesN3LOCut2 = RandomVariate[MultinormalDistribution[
    ExpValuesLECsN3LOCut2, CovMatN3LOCut2], 50];
SamplesN4LOCut2 = RandomVariate[MultinormalDistribution[
    ExpValuesLECsN4LOCut2, CovMatN4LOCut2], 50];

(*Preparation before export*)
```

In[ ]:=
```
out = "";
For[iset = 1 , iset ≤ Dimensions[SamplesLOCut2][[1]] , iset = iset + 1 ,
  out = out <> "&!=\nSOMETHING" <> ToString[iset] <> "\n";
  For[ii = 1 , ii ≤ Dimensions[SamplesLOCut2][[2]] , ii = ii + 1,
   out = out <> ToString[SamplesLOCut2[[iset , ii]], FormatType → FortranForm] <> ", ";
   If[Mod[ii , 6] == 0,
    out = out <> "&!=\n";
   ];
  ];
  ];
```

```
(*Export[NotebookDirectory[]<>"SamplesN3LOCut2.dat" , out , "Text"];*)
```

```
(*Export["SamplesN3LOCut2LECs.dat",SamplesN3LOCut2]*)
```

```
Export["SamplesNewSetsLOCut2LECs.dat", Partition[SamplesLOCut2, 1]]
```

```
SamplesNewSetsLOCut2LECs.dat
```

Appendix B

Bayesian truncation errors of 3N observables

This appendix contains additional figures presenting the dependence of the chiral predictions with truncation errors using the Bayesian approach with respect to the order of chiral NN potential. Similarly to examples given in Chapter 5 in all cases we observe rapid decreasing of truncation errors with growing order of chiral expansion. As expected, moving to higher energies makes truncation errors at given order bigger.

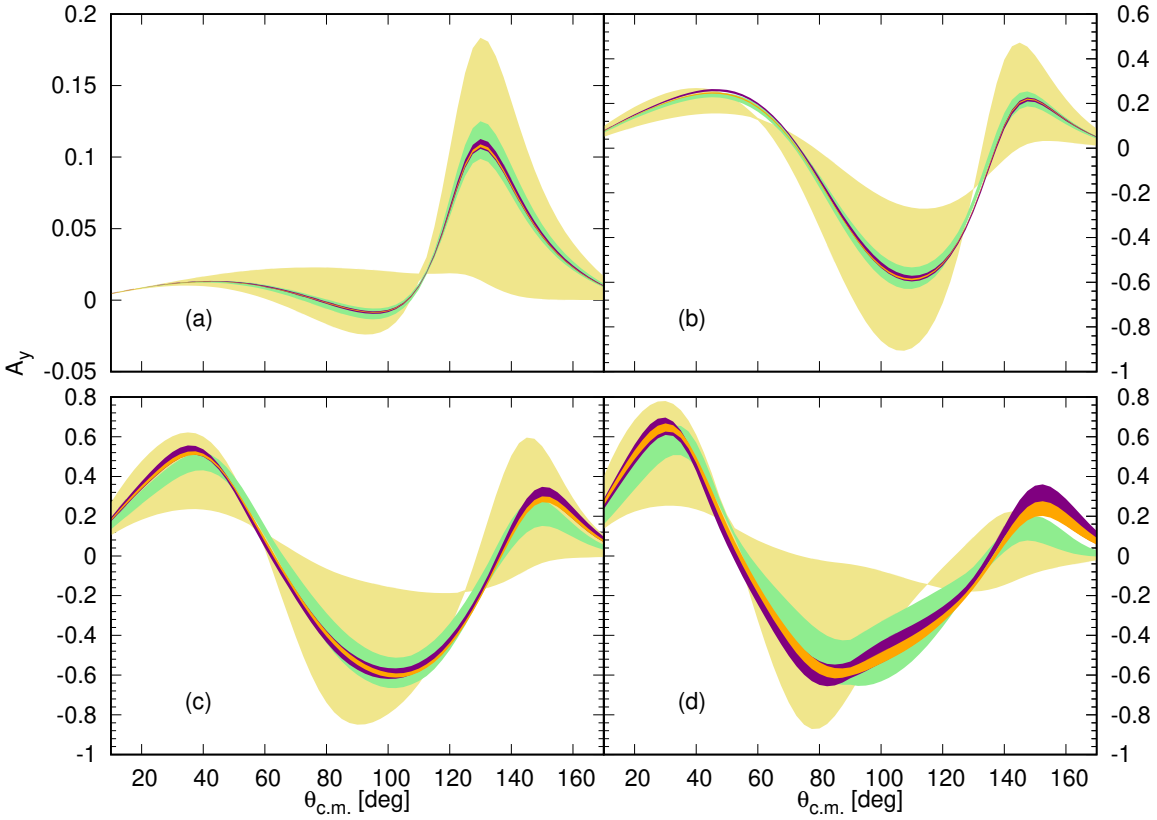

Figure B1: The neutron vector analyzing power A_y for the elastic nd scattering process at the incoming neutron laboratory energy (a) $E_{\rm lab} = 13$ MeV, (b) $E_{\rm lab} = 65$ MeV, (c) $E_{\rm lab} = 135$ MeV and (d) $E_{\rm lab} = 200$ MeV as a function of the c.m. scattering angle $\theta_{c.m.}$. The light-shaded brown, green and blue, purple and orange bands depict 68% DoB intervals using the Bayesian model $\bar{C}^{650}_{0.5-10}$ based on the chiral NLO, N^{2}LO, N^{3}LO and N^{4}LO ($\Lambda = 450$ MeV) SMS potentials, respectively.

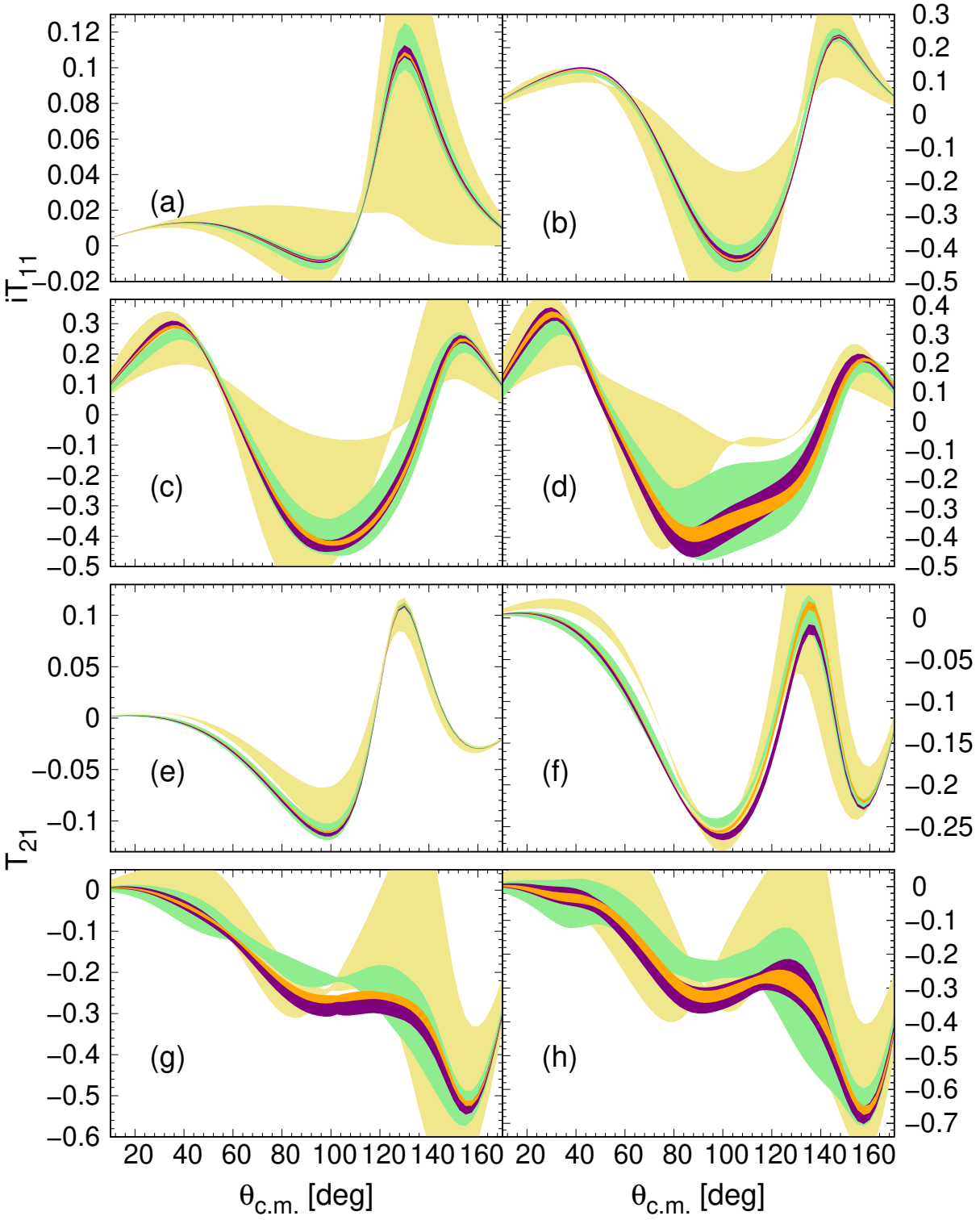

Figure B2: The deuteron vector analyzing power iT_{11} and the deuteron tensor analyzing power T_{21} for the elastic *nd* scattering process at the incoming neutron laboratory energy (a, e) $E_{\rm lab} = 13$ MeV, (b, f) $E_{\rm lab} = 65$ MeV, (c, g) $E_{\rm lab} = 135$ MeV and (d, h) $E_{\rm lab} = 200$ MeV as a function of the c.m. scattering angle $\theta_{c.m.}$. Bands are as in Fig. B1.

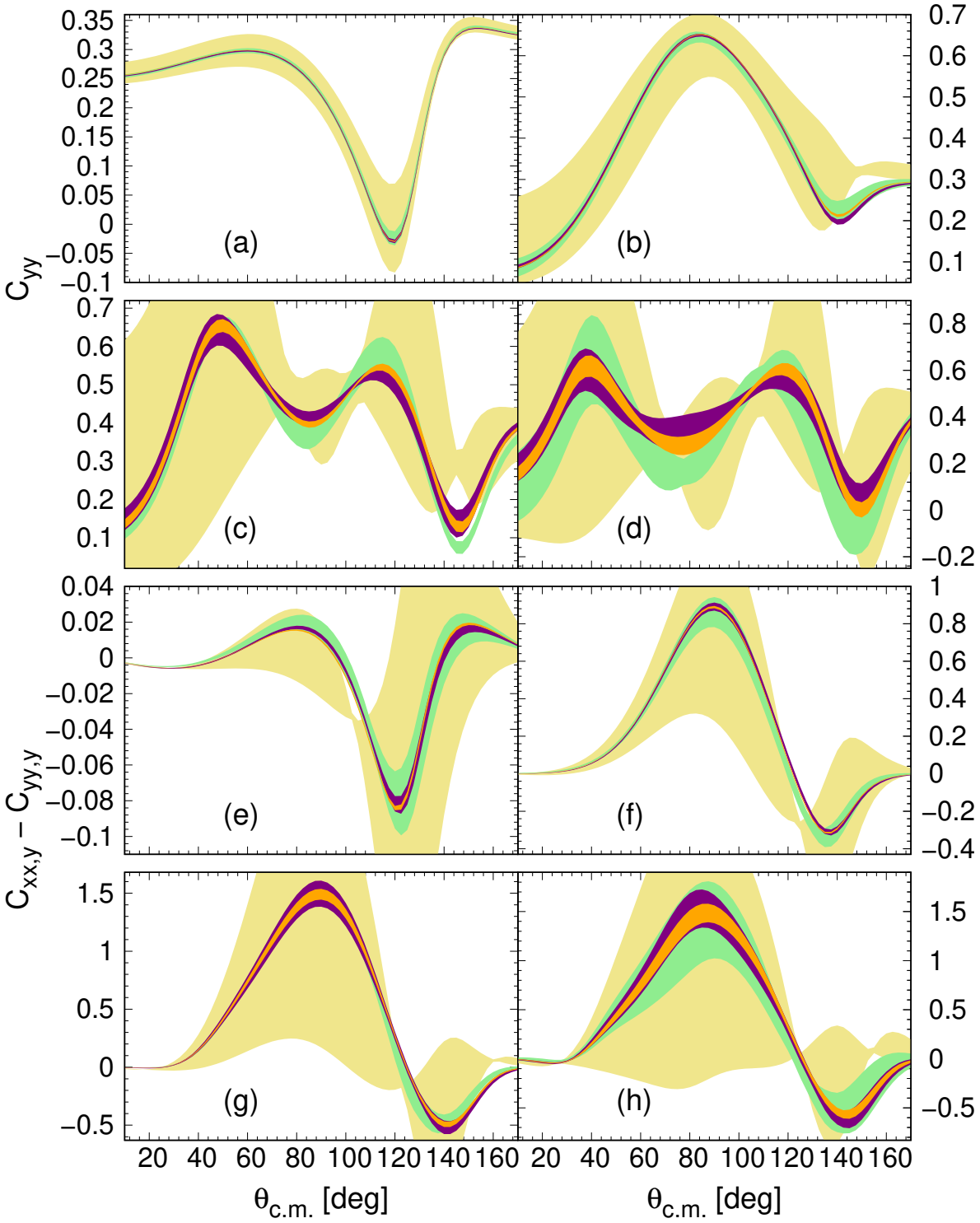

Figure B3: The spin correlation coefficients C_{yy} and $C_{xx,y} - C_{yy,y}$ for the elastic nd scattering process at the incoming neutron laboratory energy (a, e) $E_{\rm lab} = 13$ MeV, (b, f) $E_{\rm lab} = 65$ MeV, (c, g) $E_{\rm lab} = 135$ MeV and (d, h) $E_{\rm lab} = 200$ MeV as a function of the c.m. scattering angle $\theta_{c.m.}$. Bands are as in Fig. B1.

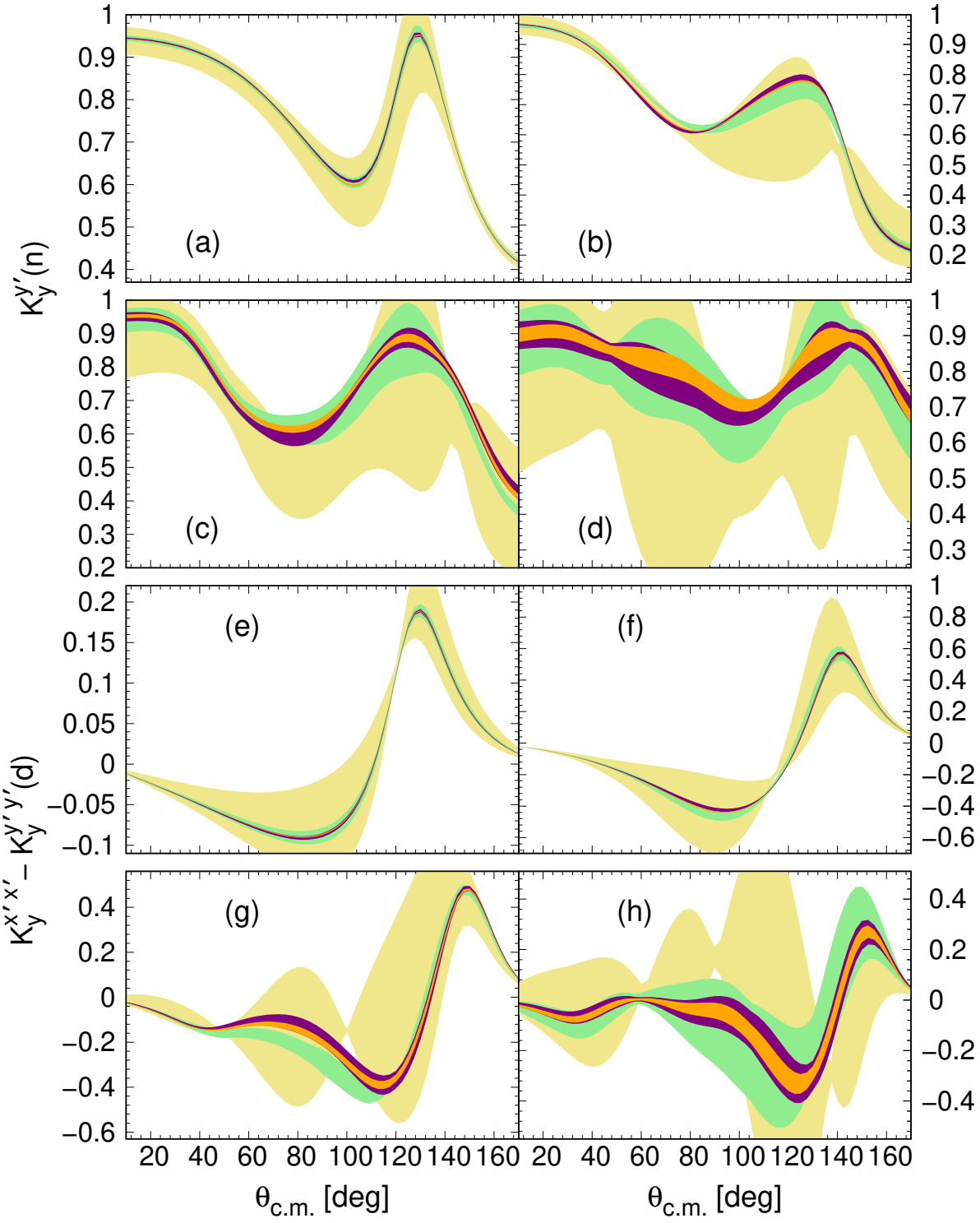

Figure B4: The nucleon to nucleon spin transfer coefficient $K_y^{y'}(n)$ and the neutron-deuteron tensor spin transfer coefficient $K_y^{x'x'} - K_y^{y'y'}(d)$ for the elastic nd scattering process at the incoming neutron laboratory energy (a, e) $E_{\rm lab} = 13$ MeV, (b, f) $E_{\rm lab} = 65$ MeV, (c, g) $E_{\rm lab} = 135$ MeV and (d, h) $E_{\rm lab} = 200$ MeV as a function of the c.m. scattering angle $\theta_{c.m.}$. Bands are as in Fig. B1.

Appendix C

Below I give values of LECs of the NN interactions up to N^4LO^+ with their uncertainties. The latter ones are square roots of diagonal elements of suitable covariance matrix delivered by the Bochum-Bonn group.

LEC	N^2LO	N^3LO	N^4LO	N^4LO^+
$\tilde{C}_{1S0}^{np}$	0.007±0.000	0.049±0.000	0.011±0.000	0.010±0.000
C_{1S0}^{np}	0.199±0.001	-0.679±0.006	0.091±0.013	0.121±0.013
D_{1S0}		3.511±0.224	2.962±0.162	2.579±0.151
C_{1P1}	0.378±0.015	0.875±0.019	0.751±0.014	0.753±0.013
D_{1P1}		0.166±0.280	-0.057±0.124	-0.056±0.118
D_{1D2}		0.957±0.012	0.225±0.008	0.218±0.008
$\tilde{C}_{3S1}$	-0.310±0.001	0.346±0.004	0.008±0.002	0.011±0.002
C_{3S1}	0.189±0.004	-0.174±0.034	-0.008±0.016	-0.024±0.017
D_{3S1}		5.280±0.404	2.836±0.186	2.660±0.175
C_{ε_1}	0.318± 0.009	0.414±0.024	0.377±0.014	0.410±0.014
D_{ε_1}		-0.233±0.47	0.002±0.202	-0.330±0.200
D_{3D1}		1.674±0.265	1.301±0.121	1.525±0.119
C_{3P0}	0.540±0.005	0.828±0.006	0.605±0.005	0.591±0.005
D_{3P0}		0.517±0.076	1.08±0.059	0.813±0.053
C_{3P1}	0.764±0.004	1.139±0.005	0.851±0.003	0.828±0.003
D_{3P1}		-0.248±0.077	0.351±0.057	0.215±0.053
C_{3P2}	-0.442±0.001	0.336±0.002	0.126±0.001	0.127±0.001
D_{3P2}		-0.772±0.010	-0.442±0.008	-0.449±0.008
D_{ε_2}		-0.182±0.007	-0.161±0.006	-0.219±0.007
D_{3D2}		0.504±0.045	0.22±0.022	0.186±0.022
D_{3D3}		-0.897±0.052	-0.158±0.022	0.140±0.030
$\tilde{C}_{1S0}^{pp}$	0.010±0.000	0.0518±0.000	0.012±0.000	0.012±0.000
$C_{1S0}^{pp/nn}$			0.126±0.005	0.133±0.005
E_{3F2}				2.290±0.130
E_{1F3}				2.161±0.275
E_{3F3}				1.319±0.172
E_{3F4}				0.278±0.067

Table C1: The central values and uncertainties of LECs of the NN contact interactions at N^2LO, N^3LO, N^4LO, and N^4LO^+ chiral orders for the cutoff value of $\Lambda = 450$ MeV.

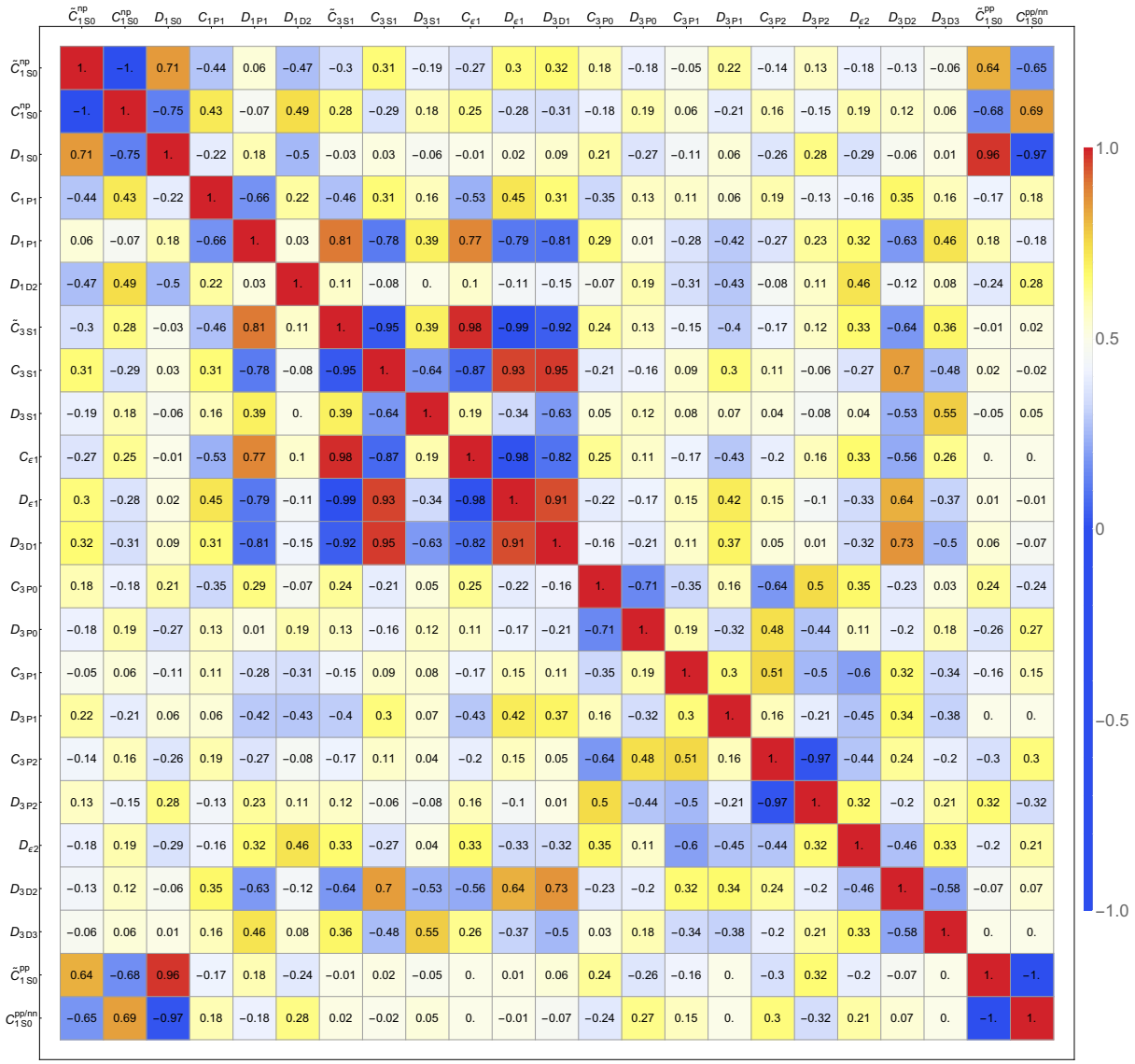

Figure C1: The correlation matrix between the various potential parameter (LECs) for the case of the chiral N^{4}LO SMS potential with $\Lambda = 450$ MeV.

Bibliography

[1] H. Witała, W. Glöckle, J. Golak, A. Nogga, H. Kamada, R. Skibiński, and J. Kuroś-Żołnierczuk. Nd elastic scattering as a tool to probe properties of 3N forces. *Phys. Rev. C*, 63(2):12, 2001.

[2] W. Glöckle, H. Witała, D. Hüber, H. Kamada, and J. Golak. The three-nucleon continuum: achievements, challenges and applications. *Physics Reports*, 274:107–285, 1998.

[3] C.R. Howell, W. Tornow, H.R. Setze, R.T. Braun, D.E.Gonzalez Trotter, C.D. Roper, R.S. Pedroni, S.M. Grimes, C.E. Brient, N. Al-Niemi, F.C. Goeckner, and G. Mertens. Resolution of discrepancy between backward angle cross-section data for neutron-deuteron elastic scattering. *Few-Body Systems*, 16(3):127–142, 1994.

[4] St. Kistryn, E. Stephan, A. Biegun, K. Bodek, A. Deltuva, E. Epelbaum, K. Ermisch, W. Glöckle, J. Golak, N. Kalantar-Nayestanaki, H. Kamada, M. Kiš, B. Kłos, A. Kozela, J. Kuroś-Znierczuk, M. Mahjour-Shafiei, U. G. Meißner, A. Micherdzińska, A. Nogga, P. U. Sauer, R. Skibiński, R. Sworst, H. Witała, J. Zejma, and W. Zipper. Systematic study of three-nucleon force effects in the cross section of the deuteron-proton breakup at 130 MeV. *Phys. Rev. C*, 72(4):1–25, 2005.

[5] B. V. Przewoski, H. O. Meyer, J. T. Balewski, W. W. Daehnick, J. Doskow, W. Haeberli, R. Ibald, B. Lorentz, R. E. Pollock, P. V. Pancella, F. Rathmann, T. Rinckel, Swapan K. Saha, B. Schwartz, P. Thörngren-Engblom, A. Wellinghausen, T. J. Whitaker, and T. Wise. Analyzing powers and spin correlation coefficients for $p+d$ elastic scattering at 135 and 200 MeV. *Phys. Rev. C*, 74(6):1–21, 2006.

[6] G.J. Weisel, W. Tornow, A.S. Crowell, J.H. Esterline, G.M. Hale, C.R. Howell, P.D. O'Malley, J.R. Tompkins, and H. Witała. Neutron-deuteron analyzing power data at $E_n = 22.5$ MeV. *Phys. Rev. C*, 89(5):1–7, 2014.

[7] K. Sekiguchi, H. Witała, T. Akieda, D. Eto, H. Kon, Y. Wada, A. Watanabe, S. Chebotaryov, M. Dozono, J. Golak, H. Kamada, S. Kawakami, Y. Kubota, Y. Maeda, K. Miki, E. Milman, A. Ohkura, H. Sakai, S. Sakaguchi, N. Sakamoto, M. Sasano, Y. Shindo, R. Skibiński, H. Suzuki, M. Tabata, T. Uesaka, T. Wakasa, K. Yako, T. Yamamoto, Y. Yanagisawa, and J. Yasuda. Complete set of deuteron analyzing powers from d - p elastic scattering at 190 MeV/nucleon. *Phys. Rev. C*, 96(6):1–8, 2017.

[8] Editorial: Uncertainty estimates. *Physical Review A - Atomic, Molecular, and Optical Physics*, 83(4):40001, 2011.

[9] P. Reinert, H. Krebs, and E. Epelbaum. Semilocal momentum-space regularized chiral two-nucleon potentials up to fifth order. *European Physical Journal A*, 54(5):1–49, 2018.

[10] R. Navarro Pérez, J.E. Amaro, and E. Ruiz Arriola. Statistical error analysis for phenomenological nucleon-nucleon potentials. *Phys. Rev. C*, 89(6):1–20, 2014.

[11] R. Skibiński, Yu. Volkotrub, J. Golak, K. Topolnicki, and H. Witała. Theoretical uncertainties of the elastic nucleon-deuteron scattering observables. *Phys. Rev. C*, 98(1):1–15, 2018.

[12] Yu. Volkotrub, J. Golak, R. Skibiński, K. Topolnicki, H. Witała, E. Epelbaum, H. Krebs, and P. Reinert. Uncertainty of three-nucleon continuum observables arising from uncertainties of two-nucleon potential parameters. *Journal of Physics G: Nuclear and Particle Physics*, 47(10):104001, 2020.

[13] S. Binder, A. Calci, E. Epelbaum, R.J. Furnstahl, J. Golak, K. Hebeler, H. Kamada, H. Krebs, J. Langhammer, S. Liebig, et al. Few-nucleon systems with state-of-the-art chiral nucleon-nucleon forces. *Phys. Rev. C*, 93(4):044002, 2016.

[14] S. Binder, A. Calci, E. Epelbaum, R.J. Furnstahl, J. Golak, K. Hebeler, T. Hüther, H. Kamada, H. Krebs, P. Maris, et al. Few-nucleon and many-nucleon systems with semilocal coordinate-space regularized chiral nucleon-nucleon forces. *Phys. Rev. C*, 98(1):014002, 2018.

[15] J.A. Melendez, S. Wesolowski, and R.J. Furnstahl. Bayesian truncation errors in chiral effective field theory: nucleon-nucleon observables. *Phys. Rev. C*, 96(2):024003, 2017.

[16] S.R. Beane, W. Detmold, K. Orginos, and M.J. Savage. Nuclear physics from lattice QCD. *Progress in Particle and Nuclear Physics*, 66(1):1–40, 2011.

[17] S. Aoki. Hadron interactions in lattice QCD. *Progress in Particle and Nuclear Physics*, 66(4):687–726, 2011.

[18] S.R. Beane, E. Chang, S.D. Cohen, W. Detmold, H.W. Lin, T.C. Luu, K. Orginos, A. Parreño, M.J. Savage, and A. Walker-Loud. Light nuclei and hypernuclei from quantum chromodynamics in the limit of SU(3) flavor symmetry. *Physical Review D - Particles, Fields, Gravitation and Cosmology*, 87(3):1–20, 2013.

[19] K. Orginos, A. Parreno, M.J. Savage, S.R. Beane, E. Chang, W. Detmold, NPLQCD Collaboration, et al. Two nucleon systems at $m_\pi \sim 450$ MeV from lattice QCD. *Physical Review D*, 92(11):114512, 2015.

[20] Ning Li, S. Elhatisari, E. Epelbaum, Dean Lee, Bing-Nan Lu, and Ulf-G Meißner. Neutron-proton scattering with lattice chiral effective field theory at next-to-next-to-next-to-leading order. *Phys. Rev. C*, 98(4):044002, 2018.

[21] W. Leidemann and G. Orlandini. Modern *ab initio* approaches and applications in few-nucleon physics with A $\geq$ 4. *Progress in Particle and Nuclear Physics*, 68:158–214, 2013.

[22] A. Nogga, H. Kamada, and W. Gloeckle. Modern nuclear force predictions for the α particle. *Phys. Rev. Lett*, 85(5):944, 2000.

[23] J. Carlson, S. Gandolfi, F. Pederiva, Steven C. Pieper, R. Schiavilla, K.E. Schmidt, and Robert B. Wiringa. Quantum monte carlo methods for nuclear physics. *Reviews of Modern Physics*, 87(3):1067, 2015.

[24] P. Navrátil, S. Quaglioni, G. Hupin, C. Romero-Redondo, and A. Calci. Unified *ab initio* approaches to nuclear structure and reactions. *Physica Scripta*, 91(5):053002, 2016.

[25] P. Maris, M.A. Caprio, and J.P. Vary. Emergence of rotational bands in *ab initio* no-core configuration interaction calculations of the Be isotopes. *Phys. Rev. C*, 91(1):014310, 2015.

[26] T. Fukui, L. De Angelis, Y.Z. Ma, L. Coraggio, A. Gargano, N. Itaco, and F.R. Xu. Realistic shell-model calculations for p-shell nuclei including contributions of a chiral three-body force. *Phys. Rev. C*, 98(4):044305, 2018.

[27] E. Epelbaum, J. Golak, K. Hebeler, T. Hüther, H. Kamada, H. Krebs, P. Maris, Ulf-G Meißner, A. Nogga, R. Roth, et al. Few-and many-nucleon systems with semilocal coordinate-space regularized chiral two-and three-body forces. *Phys. Rev. C*, 99(2):024313, 2019.

[28] S.K. Bogner, R.J. Furnstahl, and A. Schwenk. From low-momentum interactions to nuclear structure. *Progress in Particle and Nuclear Physics*, 65(1):94–147, 2010.

[29] H. Hergert, S.K. Bogner, T.D. Morris, A. Schwenk, and K. Tsukiyama. The in-medium similarity renormalization group: A novel *ab initio* method for nuclei. *Physics Reports*, 621:165–222, 2016.

[30] A. Kievsky, S. Rosati, M. Viviani, L.E Marcucci, and L. Girlanda. A high-precision variational approach to three-and four-nucleon bound and zero-energy scattering states. *Journal of Physics G: Nuclear and Particle Physics*, 35(6):063101, 2008.

[31] L.E. Marcucci, A. Kievsky, L. Girlanda, S. Rosati, and M. Viviani. N-d elastic scattering using the hyperspherical harmonics approach with realistic local and nonlocal interactions. *Phys. Rev. C*, 80(3):034003, 2009.

[32] L.E. Marcucci, J. Dohet-Eraly, L. Girlanda, A. Gnech, A. Kievsky, and M. Viviani. The hyperspherical harmonics method: a tool for testing and improving nuclear interaction models. *arXiv preprint arXiv:1912.09751*, 2019.

[33] L.D. Faddeev. Scattering theory for a three-particle system. In *Fifty Years of Mathematical Physics: Selected Works of Ludwig Faddeev*, pages 37–42. World Scientific, 2016.

[34] O.A. Rubtsova, V.N. Pomerantsev, V.I. Kukulin, and A. Faessler. Three-body breakup within the fully discretized Faddeev equations. *Phys. Rev. C*, 86(3):034004, 2012.

[35] A.C. Fonseca and A. Deltuva. Numerical exact *ab initio* four-nucleon scattering calculations: from dream to reality. *Few-Body Systems*, 58(2):46, 2017.

[36] A. Deltuva, A.C. Fonseca, and P.U. Sauer. Coulomb force effects in few-nucleon systems. *Few-Body Systems*, 60(2):29, 2019.

[37] R. Lazauskas. Solution of the n-He^4 elastic scattering problem using the Faddeev-Yakubovsky equations. *Phys. Rev. C*, 97(4):044002, 2018.

[38] J.E. Drut, R.J. Furnstahl, and L. Platter. Toward ab initio density functional theory for nuclei. *Progress in Particle and Nuclear Physics*, 64(1):120 – 168, 2010.

[39] J. Dobaczewski. Current developments in nuclear density functional methods. *Journal of Physics: Conference Series*, 312(9):092002, sep 2011.

[40] A.V. Afanasjev, S.E. Agbemava, D. Ray, and P. Ring. Nuclear landscape in covariant density functional theory. *Physics Letters B*, 726(4):680 – 684, 2013.

[41] W. Nazarewicz. Challenges in nuclear structure theory. *Journal of Physics G: Nuclear and Particle Physics*, 43(4):044002, 2016.

[42] C.W. Johnson, K.D. Launey, N. Auerbach, S. Bacca, B.R. Barrett, C. Brune, M.A. Caprio, P. Descouvemont, W.H. Dickhoff, Ch. Elster, et al. From bound states to the continuum. *arXiv preprint arXiv:1912.00451*, 2019.

[43] H. Yukawa. On the interaction of elementary particles. I. *Proceedings of the Physico-Mathematical Society of Japan. 3rd Series*, 17:48–57, 1935.

[44] W.N. Cottingham, M. Lacombe, B. Loiseau, J.M. Richard, and R. Vinh Mau. Nucleon-nucleon interaction from pion-nucleon phase-shift analysis. *Physical Review D*, 8(3):800, 1973.

[45] R. Machleidt, K. Holinde, and Ch. Elster. The Bonn meson-exchange model for the nucleon—nucleon interaction. *Physics Reports*, 149(1):1–89, 1987.

[46] V.G.J. Stoks, R.A.M. Klomp, M.C.M. Rentmeester, and J.J. De Swart. Partial-wave analysis of all nucleon-nucleon scattering data below 350 MeV. *Phys. Rev. C*, 48(2):792, 1993.

[47] R. Machleidt. Nuclear forces. *Scholarpedia*, 9(1), 2014.

[48] Mohammad Naghdi. Nucleon-nucleon interaction: A typical/concise review. *Physics of Particles and Nuclei*, 45(5):924–971, 2014.

[49] V.I. Zhaba. Deuteron: properties and analytical forms of wave function in coordinate space. *arXiv preprint arXiv:1706.08306*, 2017.

[50] R. Machleidt. Historical perspective and future prospects for nuclear interactions. *International Journal of Modern Physics E*, 26(11):1730005, 2017.

[51] V. Somà. From the liquid drop model to lattice QCD: A brief history of nuclear interactions. *European Physical Journal Plus*, 133(10):1–22, 2018.

[52] R.B. Wiringa, V.G.J. Stoks, and R. Schiavilla. Accurate nucleon-nucleon potential with charge-independence breaking. *Phys. Rev. C*, 51(1):38–51, 1995.

[53] R. Machleidt. High-precision, charge-dependent Bonn nucleon-nucleon potential. *Phys. Rev. C*, 63(2):32, 2001.

[54] R. Navarro Pérez, J.E. Amaro, and E. Ruiz Arriola. Coarse-grained potential analysis of neutron-proton and proton-proton scattering below the pion production threshold. *Phys. Rev. C*, 88(6):1–31, 2013.

[55] S. Weinberg. Nuclear forces from chiral lagrangians. *Physics Letters B*, 251(2):288–292, 1990.

[56] S. Weinberg. Effective chiral lagrangians for nucleon-pion interactions and nuclear forces. *Nuclear Physics B*, 363(1):3–18, 1991.

[57] E. Epelbaum, H. Krebs, and P. Reinert. High-Precision Nuclear Forces From Chiral EFT: State-of-the-Art, Challenges, and Outlook. *Frontiers in Physics*, 8(April):1–30, 2020.

[58] E. Epelbaum, H. Krebs, and U. G. Meißner. Improved chiral nucleon-nucleon potential up to next-to-next-to-next-to-leading order. *European Physical Journal A*, 51(5), 2015.

[59] D. R. Entem, R. Machleidt, and Y. Nosyk. High-quality two-nucleon potentials up to fifth order of the chiral expansion. *Phys. Rev. C*, 96(2):1–19, 2017.

[60] R.J. Furnstahl, N. Klco, D.R. Phillips, and S. Wesolowski. Quantifying truncation errors in effective field theory. *Phys. Rev. C*, 92(2), 2015.

[61] E. Epelbaum, J. Golak, K. Hebeler, H. Kamada, H. Krebs, U-G. Meißner, A. Nogga, P. Reinert, R. Skibiński, K. Topolnicki, et al. Towards high-order calculations of three-nucleon scattering in chiral effective field theory. *European Physical Journal A*, 56(3):1–14, 2020.

[62] E. Epelbaum. Nuclear forces from chiral effective field theory: a primer. *arXiv preprint arXiv:1001.3229*, 2010.

[63] E. Epelbaum. Few-nucleon forces and systems in chiral effective field theory. *Progress in Particle and Nuclear Physics*, 57(2):654–741, 2006.

[64] E. Epelbaum, H.W. Hammer, and Ulf.G. Meißner. Modern theory of nuclear forces. *Reviews of Modern Physics*, 81(4):1773–1825, 2009.

[65] E. Epelbaum, H. Krebs, and U. G. Meißner. Precision Nucleon-Nucleon Potential at Fifth Order in the Chiral Expansion. *Phys. Rev. Lett*, 115(12):1–5, 2015.

[66] R. Machleidt and D.R. Entem. Chiral effective field theory and nuclear forces. *Physics Reports*, 503(1):1–75, 2011.

[67] R. Machleidt. Nuclear Forces from Chiral Effective Field Theory: Achievements and Challenges. *Few-Body Systems*, 54(1-4):5–10, 2013.

[68] R. Machleidt and F. Sammarruca. Chiral EFT based nuclear forces: Achievements and challenges. *Physica Scripta*, 91(8), 2016.

[69] R. Machleidt. Consistent, high-quality two-nucleon potentials up to fifth order of the chiral expansion. *Journal of Physics: Conference Series*, 966(1), 2018.

[70] J.R. Bergervoet, P.C. Van Campen, W.A. Van Der Sanden, and J.J. De Swart. Phase shift analysis of 0-30 MeV pp scattering data. *Phys. Rev. C*, 38(1):15–50, 1988.

[71] A. Nogga, D. Hüber, H. Kamada, and W. Glöckle. Triton binding energies for modern nn forces and the π-π exchange three-nucleon force. *Physics Letters B*, 409(1-4):19–25, 1997.

[72] A. Nogga, A. Kievsky, H. Kamada, W. Glöckle, L.E. Marcucci, S. Rosati, and M. Viviani. Three-nucleon bound states using realistic potential models. *Phys. Rev. C*, 67(3):034004, 2003.

[73] R. Navarro Pérez, E. Garrido, J.E. Amaro, and E. Ruiz Arriola. Triton binding energy with realistic statistical uncertainties. *Phys. Rev. C*, 90(4):047001, 2014.

[74] D.R. Entem, R. Machleidt, and H. Witała. Chiral NN model and A_y-puzzle. *Phys. Rev. C*, 65(6):064005, 2002.

[75] H. Witała and W. Glöckle. On the discrepancies in the low-energy neutron-deuteron breakup. *Journal of Physics G: Nuclear and Particle Physics*, 37(6):064003, 2010.

[76] H. Witała and W. Glöckle. The *nn* quasifree *nd* breakup cross section: Discrepancies with theory and implications for the $^1S_0$ nn force. *Phys. Rev. C*, 83(3):034004, 2011.

[77] S.A. Coon, M.D. Scadron, P.C. McNamee, Bruce R. Barrett, D.W.E. Blatt, and B.H.J. McKellar. The two-pion-exchange three-nucleon potential and nuclear matter. *Nuclear Physics A*, 317(1):242–278, 1979.

[78] S.A. Coon and W. Glöckle. Two-pion-exchange three-nucleon potential: Partial wave analysis in momentum space. *Phys. Rev. C*, 23(4):1790, 1981.

[79] S.A. Coon and H.K. Han. Reworking the tucson-melbourne three-nucleon potential. *Few-Body Systems*, 30(1-2):131–141, 2001.

[80] B.S. Pudliner, V.R. Pandharipande, J. Carlson, S.C. Pieper, and Robert B. Wiringa. Quantum Monte Carlo calculations of nuclei with A$<\tilde{}$ 7. *Phys. Rev. C*, 56(4):1720, 1997.

[81] E. Epelbaum, H. Kamada, A. Nogga, H. Witała, W. Gloeckle, and Ulf-G. Meissner. Three-and four-nucleon systems from chiral effective field theory. *Phys. Rev. Lett*, 86(21):4787, 2001.

[82] R. Skibiński, J. Golak, K. Topolnicki, H. Witała, E. Epelbaum, W. Glöckle, H. Krebs, A. Nogga, and H. Kamada. Triton with long-range chiral N3LO three-nucleon forces. *Phys. Rev. C*, 84(5):054005, 2011.

[83] L. Girlanda, A. Kievsky, and M. Viviani. Subleading contributions to the three-nucleon contact interaction. *Phys. Rev. C*, 84(1):014001, 2011.

[84] A.C. Phillips. Consistency of the low-energy three-nucleon observables and the separable interaction model. *Nuclear Physics A*, 107(1):209–216, 1968.

[85] K. Sekiguchi, H. Sakai, H. Witała, W. Glöckle, J. Golak, M. Hatano, H. Kamada, H. Kato, Y. Maeda, J. Nishikawa, et al. Complete set of precise deuteron analyzing powers at intermediate energies: comparison with modern nuclear force predictions. *Phys. Rev. C*, 65(3):034003, 2002.

[86] P. Maris, E. Epelbaum, R. J. Furnstahl, J. Golak, K. Hebeler, T. Hüther, H. Kamada, H. Krebs, Ulf-G. Meißner, J. A. Melendez, A. Nogga, P. Reinert, R. Roth, R. Skibiński, V. Soloviov, K. Topolnicki, J. P. Vary, Yu. Volkotrub, H. Witała, and T. Wolfgruber. Light nuclei with semilocal momentum-space regularized chiral interactions up to third order. *Phys. Rev. C*, 103:054001, May 2021.

[87] A. Ekström, G. Baardsen, C. Forssén, G. Hagen, M. Hjorth-Jensen, G.R. Jansen, R. Machleidt, W. Nazarewicz, T. Papenbrock, J. Sarich, et al. Optimized chiral nucleon-nucleon interaction at next-to-next-to-leading order. *Phys. Rev. Lett*, 110(19):192502, 2013.

[88] R. Navarro Pérez, J.E. Amaro, and E. Ruiz Arriola. Low-energy chiral two-pion exchange potential with statistical uncertainties. *Phys. Rev. C*, 91(5):054002, 2015.

[89] V.G.J. Stoks, R.A.M. Klomp, M.C.M. Rentmeester, and J.J. De Swart. Partial-wave analysis of all nucleon-nucleon scattering data below 350 MeV. *Phys. Rev. C*, 48(2):792–815, 1993.

[90] E. Arriola Ruiz and R. Navarro Pérez. *Private communication*, 2017.

[91] R. Navarro Pérez, J. E. Amaro, and E. Ruiz Arriola. Erratum: Coarse-grained potential analysis of neutron-proton and proton-proton scattering below the pion production threshold (Phys. Rev. C - Nuclear Physics (2013) 88 (064002)). *Phys. Rev. C*, 91(2):24–26, 2015.

[92] F. Gross and A. Stadler. Covariant spectator theory of np scattering: Phase shifts obtained from precision fits to data below 350 MeV. *Phys. Rev. C*, 78(1):014005, 2008.

[93] R. Navarro Pérez, E. Garrido, J.E. Amaro, and E. Ruiz Arriola. Triton binding energy with realistic statistical uncertainties. *Phys. Rev. C*, 90(4):1–5, 2014.

[94] M. Hoferichter, Jacobo R. de Elvira, B. Kubis, and Ulf-G Meißner. Matching pion-nucleon roy-steiner equations to chiral perturbation theory. *Phys. Rev. Lett*, 115(19):192301, 2015.

[95] Wolfram Research, Inc. Mathematica, Version 11.3. Champaign, IL, 2018.

[96] E. Epelbaum, A. Nogga, W. Glöckle, H. Kamada, Ulf-G. Meißner, and H. Witała. Three-nucleon forces from chiral effective field theory. *Phys. Rev. C*, 66:064001, Dec 2002.

[97] R. Navarro Pérez, A. Nogga, J. E. Amaro, and E. Ruiz Arriola. Binding in light nuclei: Statistical NN uncertainties vs Computational accuracy. *Journal of Physics: Conference Series*, 742(1), 2016.

[98] J. Kirscher, H.W. Grießhammer, D. Shukla, and H.M. Hofmann. Universal correlations in pion-less eft with the resonating group method: Three and four nucleons. *European Physical Journal A*, 44(2):239–256, 2010.

[99] A. Kievsky, M. Viviani, D. Logoteta, I. Bombaci, and L. Girlanda. Correlations imposed by the unitary limit between few-nucleon systems, nuclear matter, and neutron stars. *Phys. Rev. Lett*, 121(7):072701, 2018.

[100] J.A. Tjon. Bound states of 4He with local interactions. *Physics Letters B*, 56(3):217 – 220, 1975.

[101] R.A. Fisher. Frequency distribution of the values of the correlation coefficient in samples from an indefinitely large population. *Biometrika*, 10(4):507–521, 1915.

[102] R.A. Fisher. On the 'probable error' of a coefficient of correlation deduced from a small sample. *Metron*, 1:1–32, 1921.

[103] B. Eforn. Bootstrap methods: another look at the jackknife. *The Annals of Statistics*, 7:1–26, 1979.

[104] A.J. Bishara and J.B. Hittner. Confidence intervals for correlations when data are not normal. *Behavior research methods*, 49(1):294–309, 2017.

[105] O.Ikpotokin and I.W.Edokpa. Correlation analysis: the bootstrap approach. *Int. Journal of Scientific & Engineering Research (IJSER)*, 4(5):1695–1702, 2013.

[106] A.R. Edmonds. The angular momentum in quantum mechanics. *Princeton University Press*, 1960.

[107] C. Van Der Leun and C. Alderliesten. The deuteron binding energy. *Nuclear Physics A*, 380(2):261–269, 1982.

[108] E. Anderson, Z. Bai, C. Bischof, S. Blackford, J. Demmel, J. Dongarra, J. Du Croz, A. Greenbaum, S. Hammarling, A. McKenney, and D. Sorensen. LAPACK users' guide. 1999.

[109] L. Wolfenstein. Possible triple-scattering experiments. *Phys. Rev.*, 96:1654–1658, Dec 1954.

[110] W. Glöckle. The quantum mechanical few-body problem. 1983.

[111] Ch. Elster. Lectures on few-body systems. Available online at http://www.phy.ohio.edu/ elster/phys755/index.html.

[112] H. Kamada, W. Glöckle, H. Witała, J. Golak, and R. Skibiński. Determination of Wolfenstein parameters in NN scattering directly from observables. *Few-Body Systems*, 50(1-4):231–234, 2011.

[113] H.P. Stapp, T.J. Ypsilantis, and N. Metropolis. Phase-Shift Analysis of 310 Mev proton-proton scattering experiments. *Phys. Rev.*, 105:302–310, Jan 1957.

[114] H. Witała, W. Glöckle, and Th. Cornelius. Nucleon-induced deuteron breakup: analysis of 14.1 MeV data by rigorous Faddeev calculations with meson-exchange NN interactions. *Phys. Rev. C*, 39(2):384, 1989.

[115] H. Witała, J. Golak, R. Skibiński, K. Topolnicki, E. Epelbaum, K. Hebeler, H. Kamada, H. Krebs, U.-G. Meißner, and A. Nogga. Role of the total isospin 3/2 component in three-nucleon reactions. *Few-Body Systems*, 57(12):1213–1225, 2016.

[116] A. Deltuva, A.C. Fonseca, and P.U. Sauer. Momentum-space treatment of the coulomb interaction in three-nucleon reactions with two protons. *Phys. Rev. C*, 71:054005, May 2005.

[117] S. Shimizu, K. Sagara, H. Nakamura, K. Maeda, T. Miwa, N. Nishimori, S. Ueno, T. Nakashima, and S. Morinobu. Analyzing powers of $p + d$ scattering below the deuteron breakup threshold. *Phys. Rev. C*, 52:1193–1202, Sep 1995.

[118] H. Rühl, B. Dechant, J. Krug, W. Lübcke, G. Spangardt, M. Steinke, M. Stephan, D. Kamke, J. Balewski, K. Bodek, et al. Analyzing power in $n + d$ elastic scattering at 67 MeV. *Nuclear Physics A*, 524(3):377–390, 1991.

[119] K. Sekiguchi, H. Sakai, H. Witała, W. Glöckle, J. Golak, K. Hatanaka, M. Hatano, K. Itoh, H. Kamada, H. Kuboki, Y. Maeda, A. Nogga, H. Okamura, T. Saito, N. Sakamoto, Y. Sakemi, M. Sasano, Y. Shimizu, K. Suda, A. Tamii, T. Uesaka, T. Wakasa, and K. Yako. Resolving the discrepancy of 135 MeV *pd* elastic scattering cross sections and relativistic effects. *Phys. Rev. Lett.*, 95:162301, Oct 2005.

[120] N. Sakamoto, H. Okamura, T. Uesaka, S. Ishida, H. Otsu, T. Wakasa, Y. Satou, T. Niizeki, K. Katoh, T. Yamashita, et al. Measurement of the vector and tensor analyzing powers for the dp elastic scattering at $E_d = 270$ MeV. *Physics Letters B*, 367(1-4):60–64, 1996.

[121] K. Sekiguchi, H. Sakai, H. Witała, W. Glöckle, J. Golak, K. Hatanaka, M. Hatano, K. Itoh, H. Kamada, H. Kuboki, Y. Maeda, A. Nogga, H. Okamura, T. Saito, N. Sakamoto, Y. Sakemi, M. Sasano, Y. Shimizu, K. Suda, A. Tamii, T. Uesaka, T. Wakasa, and K. Yako. Resolving the discrepancy of 135 MeV *pd* elastic scattering cross sections and relativistic effects. *Phys. Rev. Lett.*, 95:162301, Oct 2005.

[122] K. Ermisch, H.R. Amir-Ahmadi, A.M. van den Berg, R. Castelijns, B. Davids, A. Deltuva, E. Epelbaum, W. Glöckle, J. Golak, M.N. Harakeh, M. Hunyadi, M.A. de Huu, N. Kalantar-Nayestanaki, H. Kamada, M. Kiš, M. Mahjour-Shafiei, A. Nogga, P.U. Sauer, R. Skibiński, H. Witała, and H.J. Wörtche. Systematic investigation of three-nucleon force effects in elastic scattering of polarized protons from deuterons at intermediate energies. *Phys. Rev. C*, 71:064004, Jun 2005.

[123] R.E. Adelberger and C.N. Brown. $p - d$ elastic cross section and polarization at 198 MeV. *Phys. Rev. D*, 5:2139–2142, May 1972.

[124] G. Igo, J.C. Fong, S.L. Verbeck, M. Goitein, D.L. Hendrie, J.C. Carroll, B. McDonald, A. Stetz, and M.C. Makino. Large-angle elastic scattering of deuterons from hydrogen: $T_k = 433$, 362 and 291 MeV. *Nuclear Physics A*, 195(1):33–56, 1972.

[125] J. Cub, E. Finckh, H. Friess, G. Fuchs, K. Gebhardt, K. Geissdörfer, R. Lin, and J. Strate. Analyzing power for elastic $n - d$ scattering at 13 MeV. *Few-Body Systems*, 6(3):151–156, 1989.

[126] B. v Przewoski, H.O. Meyer, J.T. Balewski, W.W. Daehnick, J. Doskow, W. Haeberli, R. Ibald, B. Lorentz, R.E. Pollock, P.V. Pancella, et al. Analyzing powers and spin correlation coefficients for $p + d$ elastic scattering at 135 and 200 MeV. *Phys. Rev. C*, 74(6):064003, 2006.

[127] R.V. Cadman, J. Brack, W.J. Cummings, J.A. Fedchak, B.D. Fox, H. Gao, W. Glöckle, J. Golak, C. Grosshauser, R.J. Holt, C.E. Jones, H. Kamada, E.R. Kinney, M.A. Miller, W. Nagengast, A. Nogga, B.R. Owen, K. Rith, F. Schmidt, E.C. Schulte, J. Sowinski, F. Sperisen, E.L. Thorsland, R. Tobey, J. Wilbert, and H. Witała. Evidence for a three-nucleon-force effect in proton-deuteron elastic scattering. *Phys. Rev. Lett.*, 86:967–970, Feb 2001.

[128] S.P. Wells, S.W. Wissink, A.D. Bacher, S.M. Bowyer, S. Chang, J. Lisantti, J. Liu, C. Olmer, A.K. Opper, T. Rinckel, et al. An in-beam polarimeter for intermediate energy protons using $p + d$ elastic scattering. *Nuclear Instruments and Methods in Physics Research Section A: Accelerators, Spectrometers, Detectors and Associated Equipment*, 325(1-2):205–215, 1993.

[129] H. Witała, W. Glöckle, L.E. Antonuk, J. Arvieux, D. Bachelier, B. Bonin, A. Boudard, J.M. Cameron, H.W. Fielding, M. Garçon, et al. Complete set of deuteron analyzing powers in deuteron-proton elastic scattering: Measurement and realistic potential predictions. *Few-Body Systems*, 15(2):67–85, 1993.

[130] E. Stephan, R. Sworst, A. Biegun, K. Bodek, I. Ciepał, A. Deltuva, E. Epelbaum, A. Fonseca, W. Glöckle, J. Golak, et al. Vector and tensor analyzing powers of elastic deuteron-proton scattering at 130 MeV deuteron beam energy. *Phys. Rev. C*, 76(5):057001, 2007.

[131] H. Mardanpour, H.R. Amir-Ahmadi, A. Deltuva, K. Itoh, N. Kalantar-Nayestanaki, T. Kawabata, H. Kuboki, Y. Maeda, J.G. Messchendorp, S Sakaguchi, et al. Precision measurement of vector and tensor analyzing powers in elastic deuteron-proton scattering. *European Physical Journal A*, 31(3):383–391, 2007.

[132] M. Allet, K. Bodek, W. Hajdas, J. Lang, R. Müller, S. Navert, O. Naviliat-Cuncic, J. Sromicki, J. Zejma, L. Jarczyk, et al. Proton-induced deuteron breakup at $E_p^{lab} = 65$ MeV in quasi-free scattering configurations. *Few-Body Systems*, 20(1):27–40, 1996.

[133] J. Zejma, M. Allet, K. Bodek, J. Lang, R. Müller, S. Navert, O. Naviliat-Cuncic, J. Sromicki, E. Stephan, L. Jarczyk, et al. Cross sections and analyzing powers A_y in the breakup reaction ^{2}H$(p \rightarrow, pp)n$ at 65 MeV: Star configurations. *Phys. Rev. C*, 55(1):42, 1997.

[134] W. Pairsuwan, J.W. Watson, M. Ahmad, N.S. Chant, B.S. Flanders, R. Madey, P.J. Pella, and P.G. Roos. Analyzing powers for the ^{2}H(p$\rightarrow$,pn)^{1}H reaction at 200 MeV. *Phys. Rev. C*, 52(5):2552, 1995.

[135] N. Boukharouba, F. B. Bateman, C. E. Brient, A. D. Carlson, S. M. Grimes, R. C. Haight, T. N. Massey, and O. A. Wasson. Measurement of the n-p elastic scattering angular distribution at $E_n = 10$MeV. *Phys. Rev. C*, 65:014004, Dec 2001.

[136] G. Fink, P. Doll, T.D. Ford, R. Garrett, W. Heeringa, K. Hofmann, H.O. Klages, and H. Krupp. Backward angle *np* differential cross sections from 22 to 50 MeV. *Nuclear Physics A*, 518(3):561–571, 1990.

[137] A. Bol, C. Dupont, P. Leleux, P. Lipnik, P. Macq, and A. Ninane. Measurement of the backward-to-90° neutron-proton elastic cross section ratio between 40 and 75 MeV. *Phys. Rev. C*, 32:308–310, Jul 1985.

[138] D. Holslin, J. McAninch, P.A. Quin, and W. Haeberli. New test of nucleon-nucleon potential models. *Phys. Rev. Lett.*, 61:1561–1564, Oct 1988.

[139] G.S. Mutchler and J.E. Simmons. Polarization in $n-p$ scattering from 11 to 29.6 MeV. *Phys. Rev. C*, 4:67–73, Jul 1971.

[140] R.A. Eldred, B.E. Bonner, and T.A. Cahill. Polarization in neutron-proton scattering at 29.6 MeV. *Phys. Rev. C*, 12:1717–1722, Dec 1975.

[141] A. Langsford, P.H. Bowen, G.C. Cox, G.B. Huxtable, and R.A.J. Riddle. A measurement of polarization in neutron-proton scattering in the energy range 20–120 MeV. *Nuclear Physics*, 74(2):241 – 260, 1965.

[142] A.M. Shirokov, J.P. Vary, A.I. Mazur, and T.A. Weber. Realistic nuclear Hamiltonian: *Ab exitu* approach. *Physics Letters B*, 644(1):33–37, 2007.

[143] A.M. Shirokov, V.A. Kulikov, P. Maris, and J.P. Vary. Nucleon-nucleon and three nucleon interactions, edited by ld blokhintsev and ii strakovsky. *Nova Science*, page 231, 2014.

[144] E. Dikmen, A.F. Lisetskiy, B.R. Barrett, P. Maris, A.M. Shirokov, and J.P. Vary. *Ab initio* effective interactions for *sd*-shell valence nucleons. *Phys. Rev. C*, 91(6):064301, 2015.

[145] R. Skibiński, J. Golak, K. Topolnicki, H. Witała, Yu. Volkotrub, H. Kamada, A.M. Shirokov, R. Okamoto, K. Suzuki, and J.P. Vary. Nucleon-deuteron scattering with the JISP16 potential. *Phys. Rev. C*, 97(1):014002, 2018.

[146] J. Bystricky, F. Lehar, and P. Winternitz. Formalism of nucleon-nucleon elastic scattering experiments. *Journal de Physique*, 39(1):1–32, 1978.

[147] J. Lefrançois, R.A. Hoffman, E.H. Thorndike, and R. Wilson. Quasifree proton-neutron and proton-proton scattering at 140 MeV. *Phys. Rev.*, 131:1660–1670, Aug 1963.

[148] V. Efimov and E.G. Tkachenko. Explanation of the Phillips line in the three-nucleon problem. *Physics Letters B*, 157(2):108 – 114, 1985.

[149] W. Dilg, L. Koester, and W. Nistler. The neutron-deuteron scattering lengths. *Physics Letters B*, 36(3):208 – 210, 1971.

[150] H. Witala, J. Golak, R. Skibinski, K. Topolnicki, E. Epelbaum, H. Krebs, and P. Reinert. Comprehensive investigation of the symmetric space-star configuration in the nucleon-deuteron breakup. *arXiv preprint arXiv:2102.09863*, 2021.

Acknowledgments

During the years of my doctoral studies I was fortunate to meet many wonderful people, without whom this *Thesis* would have never been created. I would like to thank each of them for their support, inspiration and friendship.

First of all, I am especially thankful for my supervisor dr hab. Roman Skibiński for giving me the opportunity to work with him. I am very grateful to him for his unwavering support and constructive criticism, as well as for his guidance during the preparation and correction of this manuscript and me when I was wrong, and for the simple explanation of the most difficult things. Completion of the dissertation would have been impossible without his guidance and constant feedback.

I convey my special gratitude to prof. dr hab. Jacek Golak, prof. dr hab. Henryk Witała and dr Kacper Topolnicki, who also advised me on many issues, always motivating me to improve my research and presentation skills, and showed how easy it is to solve technical problems.

I am grateful to prof. dr hab. Bogusław Kamys for allowing me to join research in the Cluster of Nuclear Physics Departments. I also thank my colleagues: Anjali Aggarwal, Arshiya Anees Ahmed, Shivani Choudhary, Neha Chug, Alessandro Grassi, Vahagn Ivanyan, Krzysztof Nowakowski, Juhi Raj, Udai Singh, Volodymyr Soloviov, Vitalii Urbanevych, dr Sushil Sharma — thank you for all the conversations during coffee and various meetings outside the university.

I would like to thank prof. Evgeny Epelbaum, dr Patrick Reinert for providing me with a potential chiral interaction subroutine, and prof. Enrico Ruiz Arriola and dr Rodrigo Navarro Pérez for sending me the parameter sets for the OPE-Gaussian potential. Without their materials, this study would have been impossible. I am also grateful to all of them for fruitful discussions. The presented *Thesis* is a part of the LENPIC project and was supported by the Polish National Science Center under Grant No. 2016/22/M/ST2/00173.

I also would like to thank my friends particularly, dr Kacper Topolnicki, Karthik Balasubramanaiam, Narendra Rathod, Akshay Malige, dr Oleksii Potiienko, dr Oleksandr Rundel and Vlad Zhuk for their friendship and emotional support through all these last years.

I am thankful as well to people who taught me in Odesa National Polytechnic University in Ukraine for the knowledge they have transferred to me. Among them, I want to mention dr. Igor Sharph, prof. dr. Viktor Tarasov, prof. dr. Vitalii Rusov, Oleksandr Berezovski, and Volodymyr Smolyar.

Finally, I am grateful to my two aunts, Olena and Olga, and two brothers Igor and Andrii for their love, for their endless patience and endless support, not only with Ph.D. studies and this *Thesis* but throughout my life. I am especially grateful to my girlfriend Anna Poplavskaia for understanding and support in difficult times.